ÉCOLE DOCTORALE N°104 SCIENCES DE LA MATIÈRE DU RAYONNEMENT ET DE L'ENVIRONNEMENT

UNITÉ DE SERVICE ET RECHERCHE CNRS USR 3290 MINIATURISATION POUR LA SYNTHÈSE, L'ANALYSE ET LA PROTÉOMIQUE

THÈSE

Présentée par : **Sergui MANSOUR**

Pour l'obtention du titre de

DOCTEUR DE L'UNIVERSITÉ DE LILLE

Titre de la Thèse

Methodological development in proteomics and lipidomics applied to the analysis of cultural heritage samples. Photochemical synthesis of metallic nanoparticles in flow.

Développement méthodologique en protéomique et lipidomique appliquées à l'analyse d'échantillons du patrimoine culturel. Synthèse photochimique de nanoparticules métalliques en flux.

Soutenue publiquement le 14 Décembre 2018

Jury :

Pr. Caroline TOKARSKI, Université de Lille, Directrice de thèse

Dr. Christian ROLANDO, Université de Lille, Co-directeur de thèse

Dr. Daniela COMELLI, Rapporteur, Politecnico di Milano, Présidente de Jury

Pr. Matthew COLLINS, Rapporteur, University of Copenhagen

Dr. Ali ABOU-HASSAN, Examinateur, Sorbonne Université, Paris

Dr. Maël PENHOAT, Examinateur, Université de Lille

ACKNOWLEDGMENTS

Once again,

Table of content

Chapter I: Introduction to mass spectrometry

Chapter II: Proteomics applied to the study of Archaeological ceramics

Chapter III: Lipidomics applied for the analysis of cross-linked polymer in oil art paintings

Chapter IV: Photochemical synthesis of metallic nanoparticles in flow

General introduction

Cultural heritage is defined as all material and immaterial goods of artistic and/or historical significance that belong to either a private or a public entity. This group of cultural properties is generally preserved, restored, safeguarded and shown to the public. The so-called "material" heritage consists mainly of built landscapes, architecture and urban planning, archaeological and geological sites, certain developments in agricultural or forest areas, objects of art and furniture, industrial heritage (tools, instruments, machinery, buildings, etc.).

Heritage draws on the idea of an inheritance bequeathed from generations that preceded us, and that we must transmit it intact or ameliorated to next generations, as well as building a heritage for the future. It belongs to the public and common good.

The science of conservation is therefore the discipline studying cultural heritage properties. Science plays a key role in the conservation of our cultural heritage since that it makes it possible to identify the materials and therefore the techniques formerly used by artists, to understand the natural mechanisms of alteration and destruction: as scientists helped to safeguard and restore the works, monuments and remains from the past. It must not be forgotten that cultural heritage 'samples' are unique goods endowed with inestimable values. Thus, the scientific examination must in no way cause the degradation of the sample. Analytical techniques in the science of conservation must therefore be non-destructive or micro-destructive. The use of non-destructive methods makes it possible to obtain analytical information without causing the slightest damage to the object whereas the micro-destructive techniques do not cause visible damage, so the sample remains intact. Consequently, micro-analysis methods, such as infrared and Raman micro-spectrometers, have the advantage of being non-invasive, non-destructive and allowing the study of small samples, and have proven to be perfectly suited for the study of Cultural Heritage properties.

However, vibrational spectroscopy can offer primary information about the nature of the organic material (protein, lipid, sugar…) present in the cultural heritage sample. On the other hand, chromatographic techniques are widely used in the field of cultural heritage analysis, especially gas chromatography. However, this technique allows the analysis of small volatile organic molecules (amino acids, esterified fatty acids and others). Mass spectrometry is a powerful

analytical technique with high mass accuracy and high sensibility capabilities which make it a suitable technique for the analysis of cultural heritage samples.

However, cultural heritage samples present huge analytical challenges due to the minute quantity of available sample. Usually, this kind of samples is highly complex, referred to its composition of different types of molecules, the possibility of contamination, as well as chemical modifications and material degradation caused by aging and environmental conditions during sample preservation.

Therefore, it is necessary to develop experimental protocols that confine the type of samples we aim to study allowing us to obtain maximum information on the sample with minimal invasiveness. Also, it is essential to establish efficient methods for data treatment that permit us to acquire maximum results from the analysis.

In this perspective, my PhD project aims to develop different analytical methods in proteomics for the study of archeological samples and in lipidomics to analyze oil art paintings.

In the first chapter, I described the theory and the functioning mode of different mass spectrometry techniques used in this work.

The second chapter of this thesis is dedicated to describe the development of a proteomic bottom-up strategy for fish species identification from proteins residues trapped into archeological ceramics. This sample is a Dressel 14 amphora that was preserved in very unfavorable environment: the submarine context. The amphora dates from 116 AD. Another challenge is linked to the lack of protein databases suitable to this sample, involving consequently the study of unsequenced species via de novo experiments.

In the third chapter, we aim to develop a methodology in lipidomics in order to study the structure of molecular networks of oil paints, the phenomena of degradation of paint films as well as the interaction between pigments and oil based binder. We developed an analytical strategy based on soft depolymerization of paint films followed by an analysis with high-resolution mass spectrometry (FTICR) and a data treatment methodology for the identification and characterization of the network structure formed after oil polymerization. This new analytical methodology was applied on a real art oil painting dating from the 19th century.

In the last chapter, we developed a photochemical flux synthesis of mono and bimetallic nanoparticles (silver, gold and palladium,) in organic solvents. The synthesized silver nanoparticles are used in the design of antibacterial paints.

Chapter I: Introduction to mass spectrometry

Table of Contents

List of figures

I. Introduction on mass spectrometry

Mass spectrometry was introduced at the end of the XIXth-beginning of the XXth centuries.[2] It is only in 1990 that mass spectrometry has started to be applied on biological macromolecules analysis due to the implementation of soft ionization sources such as MALDI (Matrix Assisted Laser Desorption Ionization)[3] and ESI (Electro-Spray Ionization).[4] Nowadays, mass spectrometry is considered as the main analytical technique for the identification and the quantification of molecules present in pure or complex samples. During this process, molecules present in samples are converted into gaseous ions with or without fragmentation, that are identified upon their mass-to-charge ratio (m/z) and relative abundances. The mass spectrometry technology is based on three major components. The first part consists of an ionization source, which allows the formation of gaseous ions from studied samples. In the second part, the ions are separated according to their mass-to-charge ratio in the first analyzer, and selected ions can be fragmented thus those fragments can be separated according to (m/z) values in a second analyzer. The last part is the detector system, where emerged ions are detected, and relative abundance of ions is measured. The resulted electric signals are sent to a computer where they will be treated and transformed to a mass spectrum.
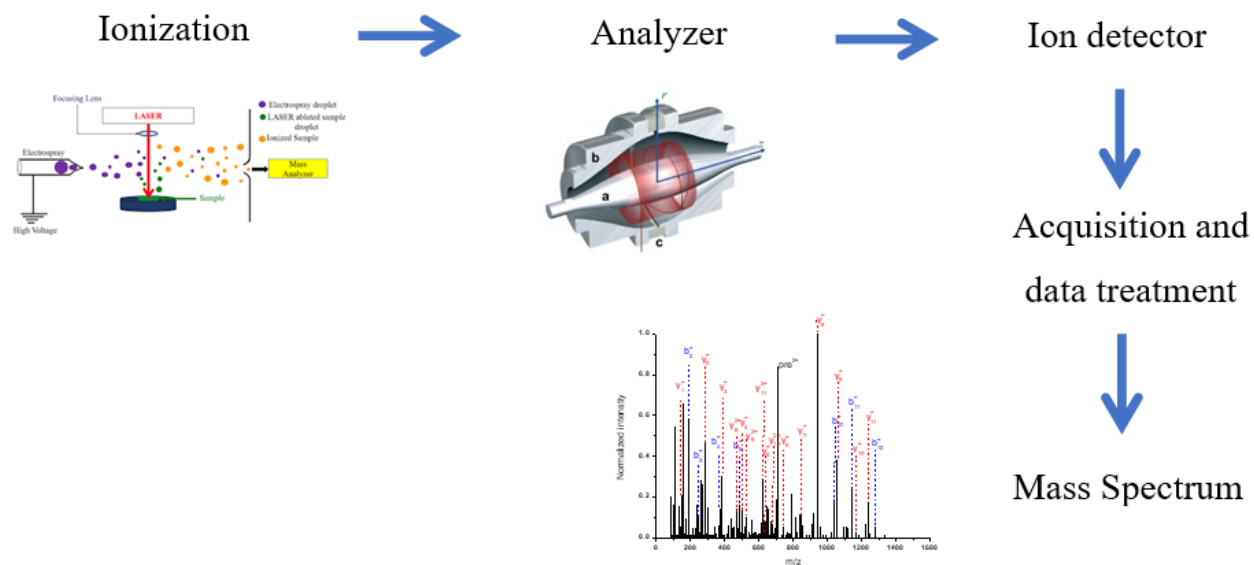
Figure 1. Schematic representation of different constituents of a mass spectrometer

II.   Ionization sources

Several ions sources were developed for mass spectrometry with different technical characteristics and diverse methods for ionization. The choice of the ionization source depends on the types of analytes and different parameters should be taken in consideration as volatility and thermal stability of the sample, chemical lability, molecular weight, quantity of analyte and the solvent. Among others, the most commonly used ionization sources are: Electrospray ionization sources (ESI) well adapted to analyze polar compounds with high molecular weight, Atmospheric-Pressure Chemical Ionization applied for the analysis of compounds with low polarity, Electronic Impact more used in GC/MS for the analysis of small volatile molecules, and Matrix-Assisted Laser Desorption/Ionization (MALDI) applied in the ionization of both low and high molecular weight non-volatile compounds.

1.   ESI source (Electrospray ionization)

Developed by Fenn et al (Nobel Prize of Chemistry in 2002), electrospray is one of the most used ionization technique and its use rapidly expanded to other analyses. ESI source is dedicated to the analysis of liquid phase, which allows its coupling with liquid chromatography or capillary electrophoresis. The source disperses the solution containing the analytes to form aerosol by evaporating the solvent, the reason why analytes are more often dispersed in mixtures of water and organic solvents as methanol and acetonitrile. Agents of ionization like formic acid can be added to the mixtures to help the protonation or the deprotonation of the analytes and facilitate the ionization process. ESI is considered as a soft method of ionization, which can generate ions without molecular fragmentation. The ionization mechanism with electrospray can be divided into three steps.[4]

First step is nebulization and droplets formation. The heated flow of inert gas as nitrogen allows the nebulization of the liquid into fine droplets. A potential difference (between 1.5 and 2 kV) applied between the capillary (generally a glass needle coated with a conductive alloy, based on gold and palladium) and the counter electrode forms an electric field and causes polarization of the solvent containing the analytes. Solvent at the end of the capillary takes the shape of a cone (Taylor cone) because of charge accumulation.[5]Then solvent evaporation reduces droplets size and increases the coulombic repulsion forces to overcome the surface tension forces (Rayleigh limit),

which releases a jet of smaller electrically charged droplets from the end of the capillary.[4,6] The produced ions can be mono- or multi-charged depending on the number of ionizable sites in the molecule. Obtaining multi-charged molecules allows the analysis of those of high molecular weight (greater than 100,000 Da). This process can be performed in positive or negative mode depending on the formation of positively or negatively charged ions. Change of polarity of the electrodes makes it possible to pass from the positive to the negative mode.
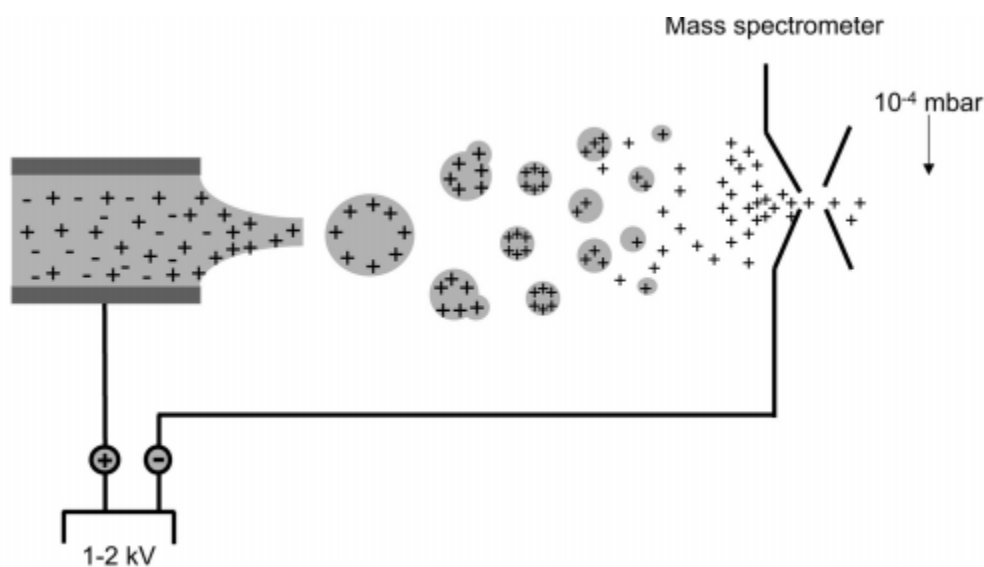
Figure 2. Representation of nano-flow ESI process in positive ion mode[7-8]

III.   Analyzers

1. Orbitrap

Orbitrap was developed at the beginning of the 2000s by Alexander A. MAKAROV[9-11] and commercialized by Thermo Fisher Scientific society. Orbitrap analyzer is composed of an external hollow electrode in cylinder shape and a central electrode. Ions are introduced into the trap tangentially to the central electrode, in packets after being accumulated in a linear trap (C-Trap). Trapped ions preform a harmonic oscillation, rotate around the central electrode and move in an axial movement along this same electrode, with a frequency that depends on their m/z ratio. The axial oscillations of the ions generate an induced current recorded by the external electrodes and converted into spectra by Fourier transform, which allows to calculate the axial oscillation

frequency of the ions, and gives access to their m/z ratio thanks to the electric field curvature equation.

a. Theory of orbitrap

Orbitrap is an ion trap, in which ions are put in their orbits at the frequency according to their mass on charge (m/z). The Orbitrap consists of an external hollow electrode and a coaxially placed central electrode, in the form of a spindle (Figure 1). The latter is brought to an alternating voltage with the opposite polarity to ions. The particular shape of the electrodes is indeed inspired by that of the electric field where the ions are tangentially injected. Since orbitrap is also an ion trap, ion stability is also governed by the solution of Mathieu's equation. The electrostatic field in the orbitrap cell is described by the following equation.

Equation 1: $U(r,z) = \frac{k}{2}(z^2 - \frac{r^2}{2}) + \frac{k}{2}(R_m)^2 \ln\left[\frac{r}{R_m}\right] + C$

Where r and z are cylindrical coordinates, R_m is characteristic radius, R1 is central electrode radius, R2 is hollow electrode radius, C is a constant, and k is a parameter determined by the shape of the center electrode and the applied voltage
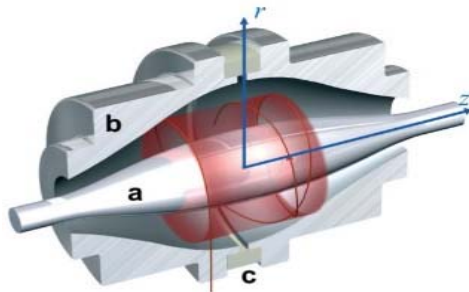
Figure 3. Schematic representation of Orbitrap[10]

The movement of ions in the orbitrap adopts a spiral trajectory around the central electrode, decomposed into a circular motion which is not exploitable, and an axial movement, the frequency of which is exploited to measure the mass by the transformation of Fourier. The axial movement

of ions is completely independent of the initial properties of ions at the moment of injection, it is described by the following equation.

$$\text{Equation 2: } z(t) = z_0 \cos(\omega t) + \left(\frac{2E_z}{k}\right)^{\frac{1}{2}} \sin(\omega t)$$

Where z_0 is the initial axial amplitude, and E_z is the initial kinetic energy in z direction

$$\text{Equation 3: } \omega = \sqrt{\frac{k}{m/z}}$$

Where k is the electric field curvature.

According to equation 3, the axial frequency of ions depends only on m/z. The movement of ions along the z axis generates an induced current recorded by the detector placed on the hollow electrodes. The image of the induced current is a transient signal, which is then transformed into a frequency spectrum by the Fourier transform, and then the frequency spectrum is easily converted into the spectrum of m/z by equation 3.

Produced ions in ESI sources are guided by a funnel and a quadrupole until C-trap. C-trap is a curved linear trap which allows ions accumulation in packages before ions injections in orbitrap. Then by rapidly ramping down trapping RF voltages, ions are rapidly injected inside the orbitrap where they are concentrated and accelerated.[11]

b. Inductive ion detection

This detection mode is well suited to ions whose m/z ratio is obtained from the frequency measurement of periodic movements in a magnetic field or in a particular electric field (orbitrap). The physical principle of this detection is based on the electrical effects induced in a metallic conductor when a charged particle approaches to the surface. A pack of ions approaching periodically to two parallel metal plates and generates in the conductive plates periodic currents and voltages of the same frequency.[9]
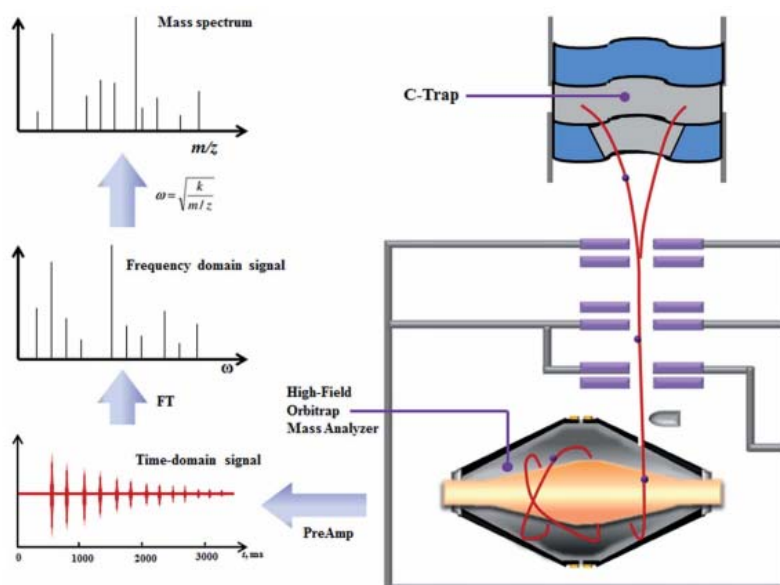
Figure 4. Signal detection by an Orbitrap analyzer and transformation of the signal into a mass spectrum[1]

2. Fourier-Transform Ion Cyclotron Resonance (FT-ICR)

The use of cyclotron ion resonance (ICR for Ion Cyclotron Resonance) with spectrometry was developed by Sommer in 1949 but it was only in the 1970s that Fourier transform mass spectrometry was described by Comisarow and Marshall[12-13]. This technique has shown great capabilities in terms of resolution (up to 10 000 000) and mass accuracy and it became a powerful tool for the analysis of complex mixtures.
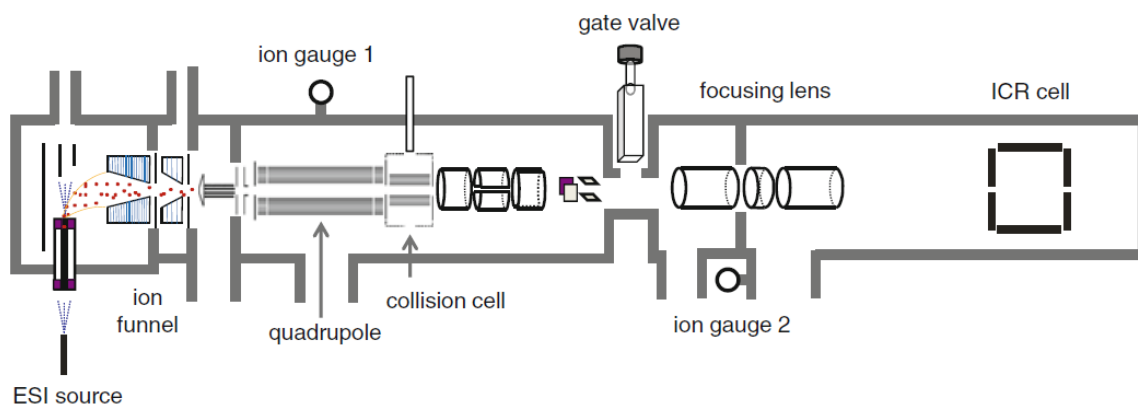
Figure 5. Schematic representation of 15 T FT-ICR[14]

The principle of ion detection is based on the measurement of ions cyclotron movement in an intense magnetic field and calculating their frequencies to end-up in converting of this information into mass spectrum. Ions are introduced into the FT-ICR through different types of ionization sources as MALDI,[15] ESI,[16] APPI (Atmospheric Pressure Photoionization)[17] and others… Plus, FT-ICR mass spectrometer contains ions trap,[18] and it can contain quadrupole ion trap[19] as well for external selection of ions. Different modes of fragmentation can be used in the FT-ICR as CID (Collision-Induced Dissociation),[20] IRMPD (Infrared Multiphoton Dissociation),[21] ECD (Electron-Capture Dissociation),[22] ETD (Electron-Transfer Dissociation)[23] and others…

a. FT-ICR cell

FT-ICR cell is placed inside a magnet that generates a uniform magnetic field B and it is composed of plates for excitation and others for detection (Figure 4). The combination of the magnetic field B and the electric constant field traps respectively ions radially and axially inside the ICR cell. The excitation and the detection of ions will be carried out in the same cell. The magnetic field traps the ions in a circular trajectory which is called cyclotronic movement. The frequency of the cyclotron movement and its angular velocity depend both on the magnetic field and on the m/z ratio of trapped ions.
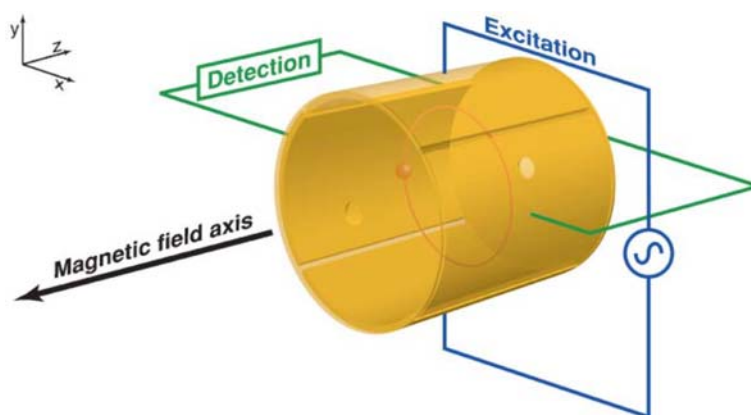
Figure 6. Schematic representation of a cylindrical FT-ICR analyzer cell[24]

When ions enter to the ICR cell with velocity v, ions are subjected to a magnetic field and they adopt a uniform circular motion perpendicular to the magnetic field due to Lorentz force as shown in Figure 5. The angular rotation speed of an ion ω_c depends on the magnetic field B, the charge q of the ion and its mass m (Equation 4).[24]
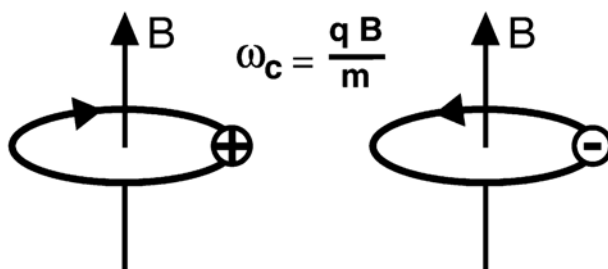
$$\omega_c = \frac{q\,B}{m}$$

Figure 7. Cyclotronic motion of positive and negative ions in a magnetic field[25]

$$\text{Equation 4: } \omega_c = \frac{qB}{m}$$

$$\text{Equation 5: } f_c = \frac{qB}{2\pi m}$$

The cyclotron frequency f_c is directly proportional to the magnetic field, inversely proportional to m/z and independent of the initial velocity of the ion (Equation 5). The measurement of ions cyclotron frequencies subjected to a magnetic field B allow the determination of their m/z ratio[24].
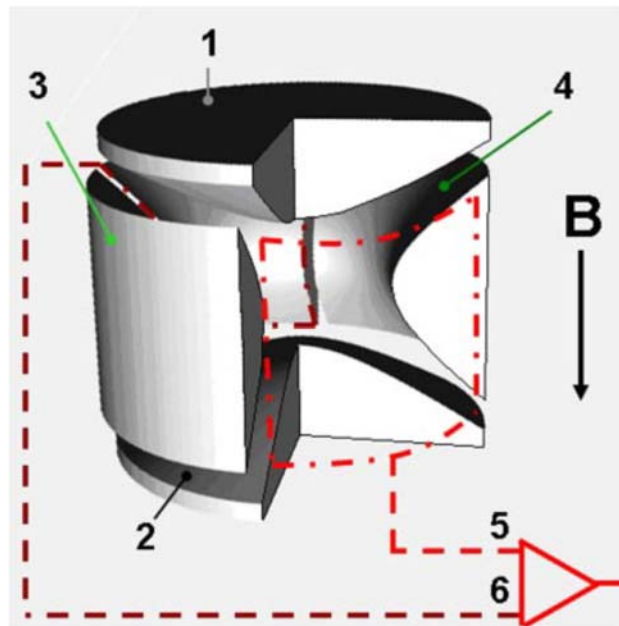
Figure 8. Hyperbolic ICR cell. 1,2: trapping electrodes; 3,4: excitation electrodes and 5,6: detection electrodes[26]

In order to trap ions inside the ICR cell, an electrostatic potential is superimposed on the magnetic field. A repulsive electric potential is applied on two perpendicular plates to the z axis, called "trapping plate" (Figure 8). This process is called Panning trap[27] and it results in confining ions in the trap center. Trapped ions between the two plates perform an oscillation movement with a ν_t frequency called trapping frequency (Equation 6). The ions are trapped in the xy plane thanks to the magnetic field, and along the z axis thanks to the electric field.

$$\text{Equation 6: } \nu_t = \frac{1}{2\pi}\sqrt{\frac{2qV_{trap}\alpha}{ma^2}}$$

Where V_{trap} is trapping potential, α is geometric factor, a is the distance between the plates. This frequency is independent of the initial kinetic energy of ions.

In result, the trapped particles in the cell undergo three types of oscillations as it is shown in Figure 9). The first type is an axial oscillation ν_T, and two oscillations in the radial plane, the second type is a reduced cyclotron oscillation ν_+ or ν_c (application of an electrostatic field reduces the cyclotronic frequency as shown in Equation 7) corresponding to the circular orbit of the particle within the trap and the third type is a magnetron oscillation ν_- or ν_m (Equation 8) corresponding to the rotation of the particle on itself.

The application of an electrostatic field reduces the cyclotronic frequency.

$$\text{Equation 7: } \nu_+ = \frac{\nu_c}{2} + \sqrt{\left(\frac{\nu_c}{2}\right)^2 - \left(\frac{\nu_T}{2}\right)^2}$$

$$\text{Equation 8: } \nu_- = \frac{\nu_c}{2} - \sqrt{\left(\frac{\nu_c}{2}\right)^2 - \left(\frac{\nu_T}{2}\right)^2}$$
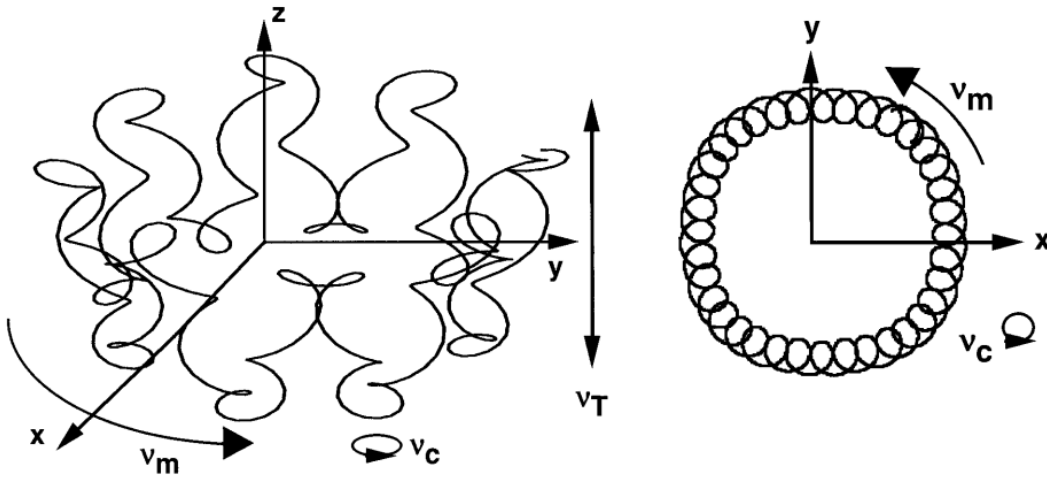
Figure 9. Three ion motional modes and their frequencies inside ICR cell (cyclotron rotation, magnetron rotation, and trapping oscillation)[28]

For ions with low m/z ratios, the reduced cyclotron frequency ν_+ is very close to the cyclotronic frequency ν_c. Nevertheless, in the case of those with high m/z ratios (or low frequencies), the situation is different where the trapping frequency becomes higher.

b. FT-ICR signal measurement

Ions with equal m/z can have distinct initial kinetic energies and can be produced at different times, which results in a wide spatial distribution. It is therefore necessary to pass ions of the same m/z from an incoherent overall motion to a coherent overall movement. This step, called the excitation phase, consists in applying an electric current between two opposite plates and results not only in putting ions of the same ratio m/z in phase, but also in causing a path passing near the perpendicular wall to orbit. During the excitation of an ion at its cyclotronic frequency with a voltage V_0 applied for a duration T_{exc}, the radius of the orbit is given by the equation

$$r = \frac{V_0 T_{exc}}{B_0}$$

Where r is cyclotron radius, V_0 is the applied voltage, T_{exc} is excitation time and B_0 is the magnetic field.

There are different methods of excitation (Figure 10):

- The Rectangular pulse excitation that relies on the application of an excitation frequency corresponding to only a population of ions with the same m/z ratio.
- The "broadband" excitation, which allows the excitation of the whole range of frequencies of interest. Two approaches exist: the method called "chirp" (Frequency-sweep)[29] and the "SWIFT" method (Stored waveform inverse Fourier transform waveforms).[30]
    - The Chirp method uses a sinus function where the linear frequency is a function of time over a frequency range determined a priori. The shortcomings of this method lie to the homogeneity of the amplitude of the frequency over the frequency range and the lack of selectivity at the limits of the frequency range (Figure 10 c).
    - The Fourier Transform stored-waveform (SWIFT) method excites ions by means of a radio frequency signal calculated by inverse Fourier transform to a rectangular signal containing the frequency range of interest. The desired signal is therefore defined in the frequency domain, generally of constant amplitude

over the range corresponding to the possible cyclotron frequencies (Figure 10 d, e).
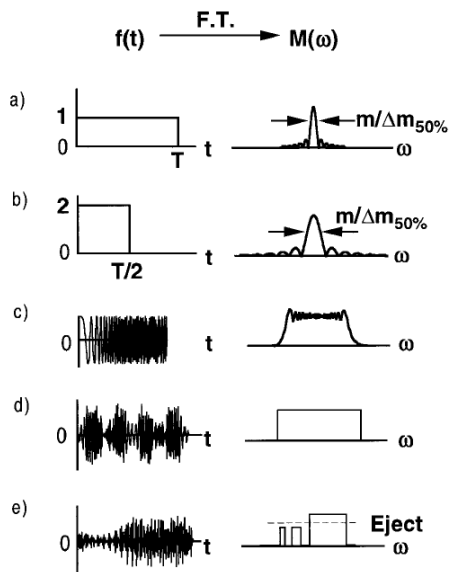
Figure 10. Time-domain (left) and frequency-domain (right) excitation waveforms. (a), (b) Rectangular pulses. (c) Frequency-sweep (''chirp''), (d), (e) Stored waveform inverse Fourier transform (''SWIFT'') wave-forms[28]

c. Ion detection

Coherent rotation of ions in a wide orbit creates an induced current on both opposite detection plates detectable by suitable electronics. The induced current is described by the following equation:

$$\varDelta Q = - \frac{2zev_y}{d}$$

Where $\varDelta Q$ corresponds to the induced current, v_y is the ions velocity along the y axis and d is the distance between the detection plates.

The induced current depends on the post excitation cyclotron radius, since the velocity increases by increasing the cyclotron radius and it is proportional to the number of ions present in the coherent ion package. However, the induced current is independent of the intensity of the magnetic field. The detected signal is called a free induced decay (FID), transient, interferogram or time-domain and its intensity increases with the number of ions charge.

12

The collision of ions during the measurement time cause reduction of ions velocity and their radius which leads to a loss of coherence of the ion pack and thus a loss of the signal. As a result, the signal obtained corresponds to an exponentially damped sinusoid. But the precision in mass is directly related to the accuracy on the measurement of ion cyclotron rotation frequency trapped. Accurate mass measurement will require the lowest possible pressure in the cell (10^{-10} mbar).

The induced current measured on the detection plates corresponds to an interferogram (FID) where the sinusoids damped of all ions present in the cell are added to each other. The digitization of this signal, followed by Fourier transform makes it possible to convert this interferogram into a spectrum representing the signal magnitude in function of cyclotron frequencies of ions present. And since the cyclotron frequency is related to the m/z, the spectrum containing the frequency information is converted into a spectrum representing the signal magnitude that correspond to ion abundance in the sample in function of m/z. By adding several successive detections, it is possible to improve the signal-to-noise ratio of the transformed spectrum. Various methods of Digital signal treatment are also accessible to improve its quality. We can quote in particular the zero-filling which allows an interpolation between the points drawing the spectrum (interpolation of Shannon) and the apodization that allows the refinement of the peaks present on the spectrum.
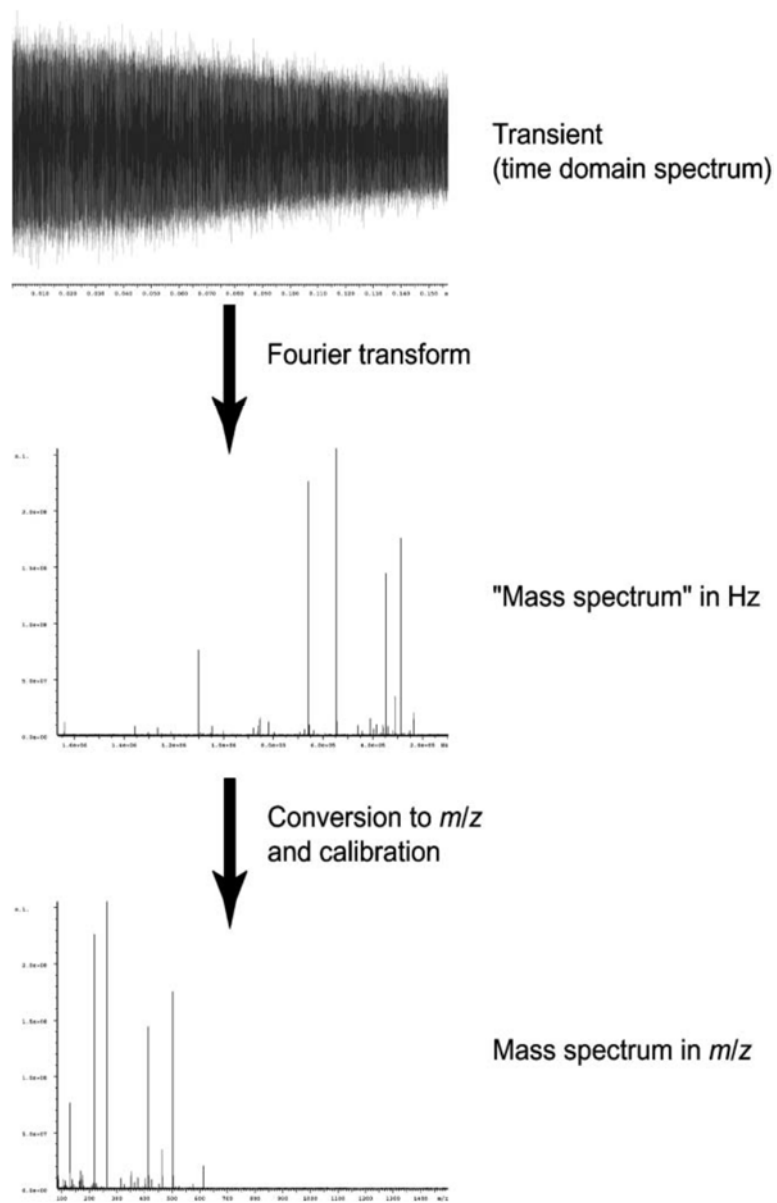
Figure 11. Illustration of the processing of raw data. A Fourier transform is performed on time-domain data to convert it to frequency domain, and this resulting spectrum is then calibrated in terms of m/z[24]

3. ICR cells

Different shapes of FT-ICR cells were developed as (a) cubic; (b) cylindrical; (c) infinity trap is an end cap segmented to linearize excitation potential; (d) and (e) open-ended, without or with capacitive RF coupling between the three sections; (f) dual and (g) "matrix-shimmed".
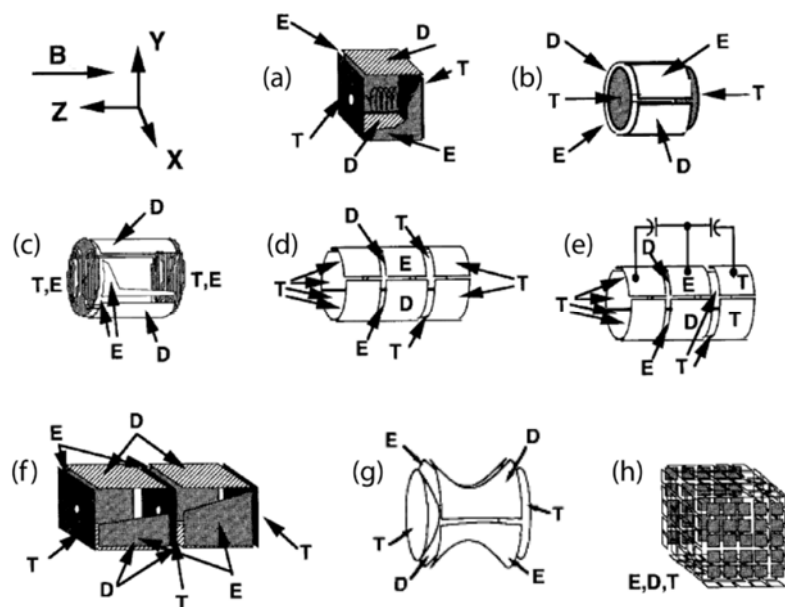
Figure 12. Different types of FT-ICR cells[28]

a. Harmonized cell

The inhomogeneity of the magnetic field in its axial direction prevails over inhomogeneity in others directions and should be considered the main factor influencing the synchronous motion of the cloud of ions. The inhomogeneity leads to a dependence of the frequency of cyclotron on the amplitude of the axial oscillation in the well potential of the ion trap. As a result, ions in an ion cloud become out of phase, resulting in signal attenuation and reduced power of resolution. The cyclotron frequency of the ion is also affected by the radial component of the electric field. Therefore, by appropriately adjusting the electric field, it is possible to compensate for the inhomogeneity of the magnetic field and to align the cyclotron frequency throughout the range of amplitudes of the oscillations z. The harmonized cell compensates for the inhomogeneity of the magnetic field by adding additional electrodes in the cell so that the

medium electric field created by these electrodes produces a counterforce to forces caused by the inhomogeneous magnetic field (Figure 13) [31]. The development of the harmonized FT-ICR cell has shown a higher resolution for masses ranging 500-1000 Da (typically peptides), as well as for masses up to 200 kDa as proteins[30, 32].
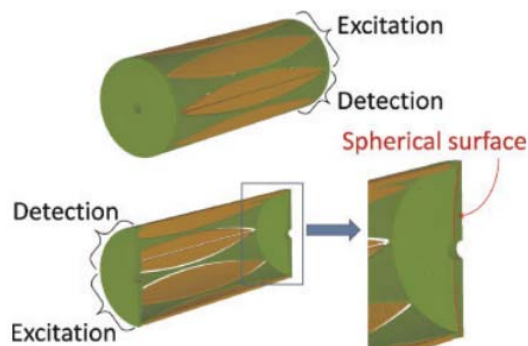
Figure 13. Design of Harmonized FT-ICR cell[33]

IV.   Fragmentation modes

Tandem mass spectrometry (MS/MS) allows the determination of the structure of an ion based on its fragmentation profile. The generated ions from the ionization source will be first analyzed in the first MS analyzer and ions are selected in function of their m/z. In the next step, ions are fragmented in the collision cell. Then, fragmented ions are analyzed and detected in the second MS. The development of MS/MS techniques has allowed to increase its areas of application, particularly in life sciences [34-35].

Figure 14 Principle of tandem mass spectrometry (MS / MS).

Various modes of fragmentation exist, permitting the obtainment of different types of fragments, such as Collision Induced Dissociation (CID), Electron Capture Dissociation (ECD), Electron Transfer Dissociation (ETD), Higher energy Collisional Dissociation (HCD) and Multiphoton Infrared Dissociation (IRMPD).

In 1990, Roepstorff and Biemann proposed nomenclature for different types of fragments generated during peptide fragmentation. Biemann nomenclature classes peptides fragments in two categories: The first category regroups the fragments "a, b and c" extending from the N-terminal of peptide precursor, while the second group regroups "x, y and z" fragments extending from the C-terminal side of peptide precursor.
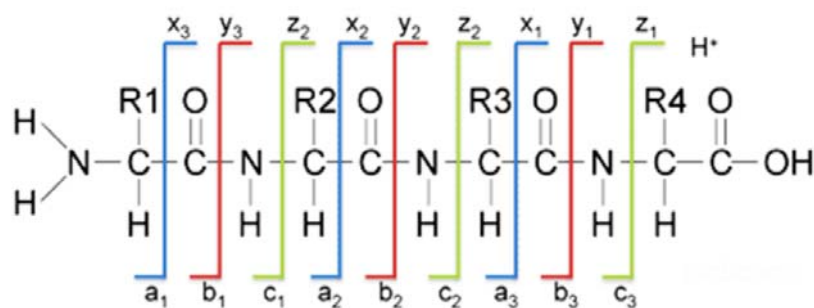
Figure 15. Schematic representation of Biemann nomenclature of peptide fragments

1. Higher energy Collisional Dissociation (HCD)

HCD (Higher energy Collisional Dissociation) is a fragmentation mode originally described by Olsen in an LTQ Orbitrap device.[36] This mode of fragmentation is very close to the CID (Collision-Induced Dissociation). Indeed, the dissociation of parent ions is done by collision with an inert gas and allows to obtain fragment ions b and y. However, unlike the CID that occurs in a linear ion trap, HCD fragmentation takes place in a specially designed octopolar collision cell, in order to increase the fragmentation energy. This has two main consequences. First, with respect to the CID, fewer fragment ions are observed on the spectrum. Second, the CID limit, called the "low-mass cutoff", is characterized by the absence of low-mass fragments (less than a third of the precursor ion) on conventional CID spectra. Unlike the CID, the HCD makes it possible to observe these fragments.

2. Multiphoton Infrared Dissociation (IRMPD)

Multiphoton Infrared Dissociation (IRMPD) is a technique used in mass spectrometry to break molecules in the gas phase.[37] An infrared laser is directed through a window into the vacuum of the mass spectrometer, where ions are present. The fragmentation mechanism comprises the absorption by an ion of several infrared photons from the laser beam. The parent ion becomes excited in more vigorous vibratory states until one or more bonds are fragmented in the gas phase. In the case of powerful laser pulses, dissociation takes place by the inner valence of electron ionization.[38-39] IRMPD fragmentation is most commonly used in FT-ICR mass spectrometers[40] and allows fragmentation of peptides or proteins by forming b and y type fragment ions such as CID fragmentation.[41] Recently this method has been implemented in an Orbitrap type mass spectrometer.[42] Lisa A. Vasicek et al modified an Orbitrap with IRMPD fragmentation within the HCD cell to allow fragmentation of peptides or proteins.

References

1.   Lin, L.; Lin, H.; Zhang, M.; Dong, X.; Yin, X.; Qu, C.; Ni, J., Types, principle, and characteristics of tandem high-resolution mass spectrometry and its applications. *RSC Advances* **2015,** *5* (130), 107623-107636.

2.   Thomson, J. J., *Rays of positive electricity and their application to chemical analyses*. Longmans, Green and Company: 1921; Vol. 1.

3.   Tanaka, K.; Waki, H.; Ido, Y.; Akita, S.; Yoshida, Y.; Yoshida, T.; Matsuo, T., Protein and polymer analyses up to m/z 100 000 by laser ionization time-of-flight mass spectrometry. *Rapid communications in mass spectrometry* **1988,** *2* (8), 151-153.

4.   Fenn, J. B.; Mann, M.; Meng, C. K.; Wong, S. F.; Whitehouse, C. M., Electrospray ionization for mass spectrometry of large biomolecules. *Science* **1989,** *246* (4926), 64-71.

5.   Aebersold, R.; Mann, M., Mass spectrometry-based proteomics. *Nature* **2003,** *422* (6928), 198.

6.   Bruins, A. P., Mechanistic aspects of electrospray ionization. **1998,** *794*, 345-357.

7.   Ganem, B.; Henion, J. D., Going gently into flight: analyzing noncovalent interactions by mass spectrometry. *Bioorganic & medicinal chemistry* **2003,** *3* (11), 311-314.

8.   Van Den Bremer, E. T.; Heck, A. J.; Press, A., Mass spectrometry: Protein conformational analysis and molecular recognition. *Biotechnol: Pharm Aspects* **2005,** *3*, 435-464.

9.   Perry, R. H.; Cooks, R. G.; Noll, R. J., Orbitrap mass spectrometry: instrumentation, ion motion and applications. *Mass spectrometry reviews* **2008,** *27* (6), 661-699.

10.   Scigelova, M.; Makarov, A., Orbitrap Mass Analyzer – Overview and Applications in Proteomics. **2006**, 16-21.

11.   Perry, R. H.; Hu, Q.; Salazar, G. A.; Cooks, R. G.; Noll, R. J., Rephasing ion packets in the orbitrap mass analyzer to improve resolution and peak shape. *Journal of the American Society for Mass Spectrometry* **2009,** *20* (8), 1397-1404.

12.   Comisarow, M. B.; Marshall, A. G., Fourier transform ion cyclotron resonance spectroscopy. *Chemical physics letters* **1974,** *25* (2), 282-283.

13.   Marshall, A. G.; Comisarow, M. B.; Parisod, G., Relaxation and spectral line shape in Fourier transform ion resonance spectroscopy. *The Journal of Chemical Physics* **1979,** *71* (11), 4434-4444.

14.   Park, K. H.; Kim, M. S.; Baek, S. J.; Bae, I. H.; Seo, S.-W.; Kim, J.; Shin, Y. K.; Lee, Y.-M.; Kim, H. S., Simultaneous molecular formula determinations of natural compounds in a plant extract using 15 T Fourier transform ion cyclotron resonance mass spectrometry. *Plant methods* **2013,** *9* (1), 15.

15.   Castro, J. A.; Köster, C.; Wilkins, C.; Cotter, R., Matrix-assisted laser desorption/ionization of high-mass molecules by Fourier-transform mass spectrometry. *Rapid communications in mass spectrometry* **1992,** *6* (4), 239-241.

16.   Henry, K. D.; Williams, E. R.; Wang, B. H.; McLafferty, F. W.; Shabanowitz, J.; Hunt, D. F., Fourier-transform mass spectrometry of large molecules by electrospray ionization. *Proceedings of the National Academy of Sciences* **1989,** *86* (23), 9075-9078.

17.   Purcell, J. M.; Hendrickson, C. L.; Rodgers, R. P.; Marshall, A. G., Atmospheric pressure photoionization Fourier transform ion cyclotron resonance mass spectrometry for complex mixture analysis. *Analytical Chemistry* **2006,** *78* (16), 5906-5912.

18.   Senko, M. W.; Hendrickson, C. L.; Emmett, M. R.; Shi, S. D.; Marshall, A. G., External accumulation of ions for enhanced electrospray ionization Fourier transform ion cyclotron resonance mass spectrometry. *Journal of the American Society for Mass Spectrometry* **1997,** *8* (9), 970-976.

19.   Belov, M. E.; Nikolaev, E. N.; Anderson, G. A.; Auberry, K. J.; Harkewicz, R.; Smith, R. D., Electrospray ionization-Fourier transform ion cyclotron mass spectrometry using ion preselection and

external accumulation for ultrahigh sensitivity. *Journal of the American Society for Mass Spectrometry* **2001,** *12* (1), 38-48.

20.	Solouki, T.; Paša-Tolić, L.; Jackson, G. S.; Guan, S.; Marshall, A. G., High-resolution multistage MS, MS2, and MS3 matrix-assisted laser desorption/ionization FT-ICR mass spectra of peptides from a single laser shot. *Analytical chemistry* **1996,** *68* (21), 3718-3725.

21.	Little, D. P.; Speir, J. P.; Senko, M. W.; Connor, P. B. O.; Mclafferty, F. W., Infrared Multiphoton Dissociation of Large Multiply Charged Ions for Biomolecule Sequencing. **1994,** *66*, 2809-2815.

22.	Cooper, H. J.; Håkansson, K.; Marshall, A. G., The role of electron capture dissociation in biomolecular analysis. *Mass spectrometry reviews* **2005,** *24* (2), 201-222.

23.	Kaplan, D. A.; Hartmer, R.; Speir, J. P.; Stoermer, C.; Gumerov, D.; Easterling, M. L.; Brekenfeld, A.; Kim, T.; Laukien, F.; Park, M. A., Electron transfer dissociation in the hexapole collision cell of a hybrid quadrupole-hexapole Fourier transform ion cyclotron resonance mass spectrometer. *Rapid Communications in Mass Spectrometry: An International Journal Devoted to the Rapid Dissemination of Up-to-the-Minute Research in Mass Spectrometry* **2008,** *22* (3), 271-278.

24.	Barrow, M. P.; Burkitt, W. I.; Derrick, P. J., Principles of Fourier transform ion cyclotron resonance mass spectrometry and its application in structural biology. *Analyst* **2005,** *130* (1), 18-28.

25.	Marshall, A. G.; Hendrickson, C. L., Fourier transform ion cyclotron resonance detection: principles and experimental configurations. *International Journal of Mass Spectrometry* **2002,** *215* (1-3), 59-75.

26.	Nikolaev, E. N.; Kostyukevich, Y. I.; Vladimirov, G. N., Fourier transform ion cyclotron resonance (FT ICR) mass spectrometry: Theory and simulations. *Mass spectrometry reviews* **2016,** *35* (2), 219-258.

27.	Penning, F. M., Die Glimmentladung bei niedrigem Druck zwischen koaxialen Zylindern in einem axialen Magnetfeld. *physica* **1936,** *3* (9), 873-894.

28.	Marshall, A. G.; Hendrickson, C. L.; Jackson, G. S., Fourier transform ion cyclotron resonance mass spectrometry: A primer. *Mass Spectrometry Reviews* **1998,** *17* (1), 1-35.

29.	Marshall, A. G.; Roe, D. C., Theory of Fourier transform ion cyclotron resonance mass spectroscopy: Response to frequency-sweep excitation. *The Journal of Chemical Physics* **1980,** *73* (4), 1581-1590.

30.	Popov, I.; Nagornov, K. O.; Vladimirov, G., Twelve Million Resolving Power on 4.7 T Fourier Transform Ion Cyclotron Resonance Instrument with Dynamically Harmonized Cell-Observation of Fine Structure in Peptide Mass Spectra. **2014**.

31.	Boldin, I. A.; Nikolaev, E. N., Fourier transform ion cyclotron resonance cell with dynamic harmonization of the electric field in the whole volume by shaping of the excitation and detection electrode assembly. *Rapid Communications in Mass Spectrometry* **2011,** *25* (1), 122-126.

32.	Li, H.; Wolff, J. J.; Van Orden, S. L.; Loo, J. A., Native top-down electrospray ionization-mass spectrometry of 158 kDa protein complex by high-resolution Fourier transform ion cyclotron resonance mass spectrometry. *Analytical chemistry* **2013,** *86* (1), 317-320.

33.	Boldin, I. A.; Nikolaev, E. N., Fourier transform ion cyclotron resonance cell with dynamic harmonization of the electric field in the whole volume by shaping of the excitation and detection electrode assembly. **2011**, 122-126.

34.	McLafferty, F. W., Tandem mass spectrometry. *Science* **1981,** *214* (4518), 280-287.

35.	McLafferty, F. W., Mass spectrometry across the sciences. *Proceedings of the National Academy of Sciences* **2008,** *105* (47), 18088-18089.

36.	Olsen, J. V.; Macek, B.; Lange, O.; Makarov, A.; Horning, S.; Mann, M., Higher-energy C-trap dissociation for peptide modification analysis. *Nature methods* **2007,** *4* (9), 709.

37.	Little, D. P.; Speir, J. P.; Senko, M. W.; O'Connor, P. B.; McLafferty, F. W., Infrared multiphoton dissociation of large multiply charged ions for biomolecule sequencing. *Analytical Chemistry* **1994,** *66* (18), 2809-2815.

38.   Talebpour, A.; Bandrauk, A.; Yang, J.; Chin, S., Multiphoton ionization of inner-valence electrons and fragmentation of ethylene in an intense Ti: sapphire laser pulse. *Chemical Physics Letters* **1999,** *313* (5-6), 789-794.

39.   Talebpour, A.; Bandrauk, A.; Vijayalakshmi, K.; Chin, S., Dissociative ionization of benzene in intense ultra-fast laser pulses. *Journal of Physics B: Atomic, Molecular and Optical Physics* **2000,** *33* (21), 4615.

40.   Laskin, J.; Futrell, J. H., Activation of large Ions in FT-ICR mass spectrometry. *Mass spectrometry reviews* **2005,** *24* (2), 135-167.

41.   Crowe, M. C.; Brodbelt, J. S., Infrared multiphoton dissociation (IRMPD) and collisionally activated dissociationof peptides in a quadrupole ion trapwith selective IRMPD of phosphopeptides. *Journal of the American Society for Mass Spectrometry* **2004,** *15* (11), 1581-1592.

42.   Vasicek, L. A.; Ledvina, A. R.; Shaw, J.; Griep-Raming, J.; Westphall, M. S.; Coon, J. J.; Brodbelt, J. S., Implementing photodissociation in an Orbitrap mass spectrometer. *Journal of the American Society for Mass Spectrometry* **2011,** *22* (6), 1105-1108.

Chapter II: Proteomics applied to the study of archaeological ceramics

Table of content

List of figures

List of tables

Introduction

I.   Archaeological materials

Archaeology is the discipline destined to study human evolution through different eras in various regions of the world. In their studies, archeologists focus on objects such as stone tools, ceramics, arms, coins, jewelry, clothing, footprints, traces, paintings, buildings, infrastructures, fossils, bones, skin, teeth, hair and others. To understand the historical context of the archaeological remains, both inorganic and organic parts are chemically analyzed to reveal their composition. Among organic remains can be found lipids, polysaccharides and proteins. In particular, proteins are a source of information.

They can be adsorbed to the surface of an archaeological material (such as stone tools), impregnated (e.g. ceramics), or proteins can be constitutive of a material (e.g. textiles, leathers and others).

II.   Proteins detection in archaeological samples

1.   Staining methods applied to archaeological samples

Protein staining is a common technique used to detect proteins in biological samples. Different methods of staining are widely applied in biological research based on visible dyes (e.g. Coomassie blue) or fluorescent dyes (SYPRO Ruby). For example, mercurochrome[1] was applied on fossil teeth of Cretaceous mammals, embedded in an epoxy resin. This dye reacts with sulfhydryl groups and protein disulfide bridges.[2] The results showed that the staining of fossil teeth was more pronounced near the pulp cavity, indicating the presence of proteins in dentin.[1] Colorimetric tests were also used for proteins detection on prehistoric tools. Ninhydrin reagent reacts with proteins amino groups and indicates a pink-violet color. Another type of coloration is OPA (o-Phthalaldehyde) which reacts with the primary amino groups of proteins and produces a fluorescent blue color.[3] Blood residue from several animal species have been discovered on the surface of prehistoric chert, basalt and obsidian tools (1000 to 6000 years old) in outdoor sites on the west coast and Canada's boreal forest.[3] In the late 1990s, a colorimetric test that detected the blood in the urine, Hemastix, was applied to detect the presence of blood residues on stone artefacts from

Çayönü Tepasi archaeological excavations in Turkey.[4] The test is based on the peroxidase activity of hemoglobin which cleaves oxygen molecules from the hydroperoxide and catalyzes the transformation of 3,3 ', 5,5'-tetramethylbenzidine (clear, colorless yellow) in its oxidized form (orange to green), at very high concentrations of blood. More recently, Hemastix® presumptive blood test, in addition to EDTA was tested on archaeological samples in order to identify the presence of blood residues.[5] The use of sodium ethylenediaminetetraacetic acid (EDTA), increases the solubility of residues, enhances the specificity of the test and decreases the false positive.

2. Spectroscopic techniques applied to archaeological samples

Vibrational spectroscopy techniques such as spectroscopy Infra-Red (IR) and Raman spectroscopy represent relevant methods to obtain simultaneous molecular information on mineral and organic phases.

These two analysis techniques use energies associated with vibrational movements of chemical bonds inside a molecule. In IR spectroscopy, the frequencies absorbed by a sample positioned in the path of an IR beam are measured (transmission or reflection mode), while the Raman technique consists of measuring the light scattered by a sample previously excited by a laser. Infrared and Raman spectroscopy are considered among the most favorable techniques to analyze cultural heritage samples due to their non-destructive utilization and their sensitivity to both organic and inorganic compounds.

a. Infrared spectroscopy

Infrared spectroscopy has been applied on archaeological and palaeontological samples for proteins detection and understanding their states of degradation.[6] Synchrotron infrared microscopy was used to study the state of degradation of different layers of an Egyptian mummy skin (epidermis, dermis) using protein related vibrational bands as amide A (3300 cm^{-1}), amide B (3030 cm^{-1}), amide I (1650 cm^{-1}), and amide II (1540 cm^{-1}).[7] Moreover, the IR technique was used in the investigation of preservation state of collagen in archaeological bones. Another example is the study of the preservation state of a bone dating from 5,000 years from the Neolithic site of the Chalain lake.[8] The Authors succeeded to analyze the bone composition and defining its degradation state at microscale level by using synchrotron radiation micro-Fourier transform infrared spectroscopy (SR micro-FTIR) imaging in transmission mode. In order to analyze heavily altered and degraded fossil

bones by SR-FTIR micro-spectroscopy, a procedure for sample preparation based on PMMA resin impregnation was applied in order to obtain larger thin sections and to preserve their histological structure.[9] Near Infrared Hyperspectral Chemical Imaging (NIR-HCI) was also applied to determine the degradation state of collagen in archaeological bones. The NIR-HCI analysis was followed by a chemometric model based on the Partial Least Squares Discriminant Analysis (PLS-DA) to allow samples discrimination and comparison based on the presence of collagen and its degradation state.[10] Furthermore, FTIR imaging allowed the study of archaeological hairs from the medieval burial of Marie de Bretagne (XVth century). Analysis shows the good preservation of the fibrillin keratin contained inside the hair, with potential structure modifications (e.g., oxidative degradation of disulfide bridges leading to formation of cysteic acid at 1040 cm^{-1} and cysteine-S-sulfonate at 1022 cm^{-1}). The study identified the presence of copper and lead, which can be the cause of the exceptional preservation of the sample. This work has proposed a multi-analytical approach by combining synchrotron XRF, µXRF, µFTIR, and µSAXS techniques.[11] FT-IR spectroscopy was used to investigate residues from archaeological pottery suspected to be containers for cosmetics. FT-IR analysis proved the presence of lipids, vegetable resins, and proteins as well as the presence of inorganic compounds like calcite.[12] This study combine application of different techniques as FT-IR (spectroscopy), XRD and thermogravimetric (TGA) analyses.

Collagen degradation and mineral fossilization in archaeological bones were also studied by a combination of different analytical techniques as FT-IR (spectroscopy), X-ray diffraction (XRD) and thermogravimetric (TGA) analyses. FT-IR techniques allow the determination of crystallinity degree by calculating the splitting factor (SF) or the crystallinity index using two vibrations bands at 565 and 605 cm^{-1} corresponding for $\nu_4(PO_4)^{3-}$ (Figure 1). The higher value of SF indicates the higher degree of crystallinity which means higher degree of bones mineralization.[13]
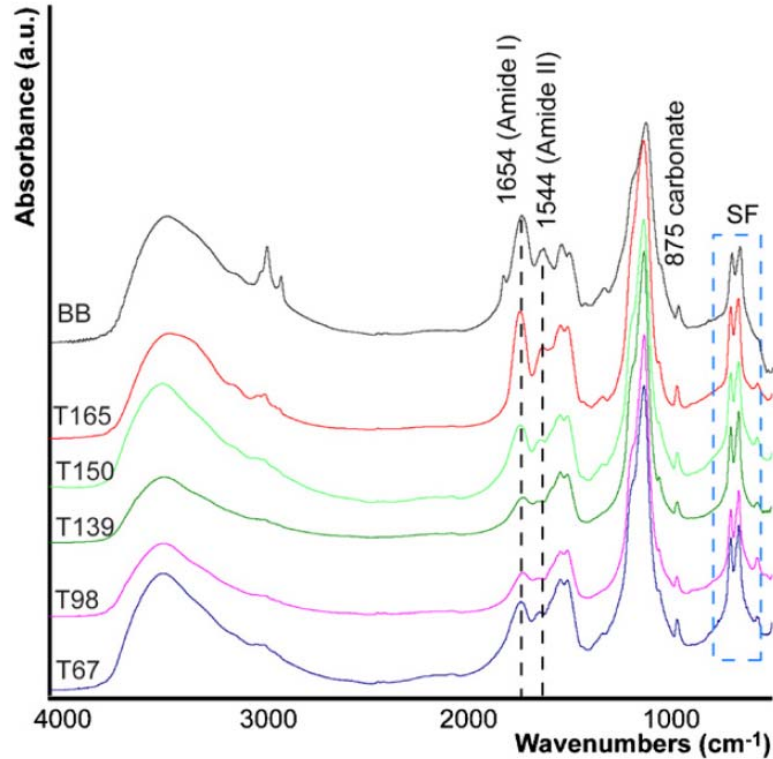
Figure 1. FTIR spectra of archaeological bone samples (T67, T98, T139, T150 and T165) and bovine bone [13]. The proteic bands amide I and amide II, and the carbonatic band are indicated. The phosphate bands used for the splitting factor (SF) calculation are squared[13]

b. Raman spectroscopy

Raman spectroscopy is also a common technique used for analysis and the characterization of archaeological samples.[14] For example, collagen preservation in bones was studied by measuring the ratio of peak intensity between the inorganic part of the bone (hydroxyapatite band at 960 cm^{-1}) and the band belonging to collagen protein (at 1636 cm^{-1}) which corresponds to amide I bond. The collagen in bones is considered well preserved when the ratio is higher than 19.4 (Figure 2).[15] Moreover, Raman spectroscopy can be applied for preliminary dating human skeletal remains. The analysis of five ancient molar teeth with different burial time (150-6000 years) showed that the intensity ratio I_{2941}/I_{960} of the stretching mode ν_s CH$_2$ of the organic component and $\nu_1(PO_4)^{3-}$ of the inorganic component decreases when the burial period increases.[16] Fourier transform-Raman spectroscopy was applied as well in order to identify mammalian ivory[17] and to partially discriminate between ancient ivory specimens.[18] The amid I and III bands represented an indication for the proteins in Egyptian mummies skin (ca. 2000   BC).[19] Fourier transform-Raman

spectroscopy was applied to study Keratin proteins from modern and ancient hair belonging to human remains from a stone-lined cist grave in a sand beach at Towyn y Capel, Anglesey, UK, dating from 630-780 A.D. The study showed the degradation of keratin proteins in the ancient sample, for example the band of the disulfide bond at 510 cm⁻¹ found in the modern sample was absent in the ancient sample. As well the band at 165 cm⁻¹ that corresponds to the α-helical amide I was also absent in the ancient sample of hair.[20]

The spectroscopic techniques allowed the detection of proteins in the ancient sample, as well the possibility to study their degradation states.
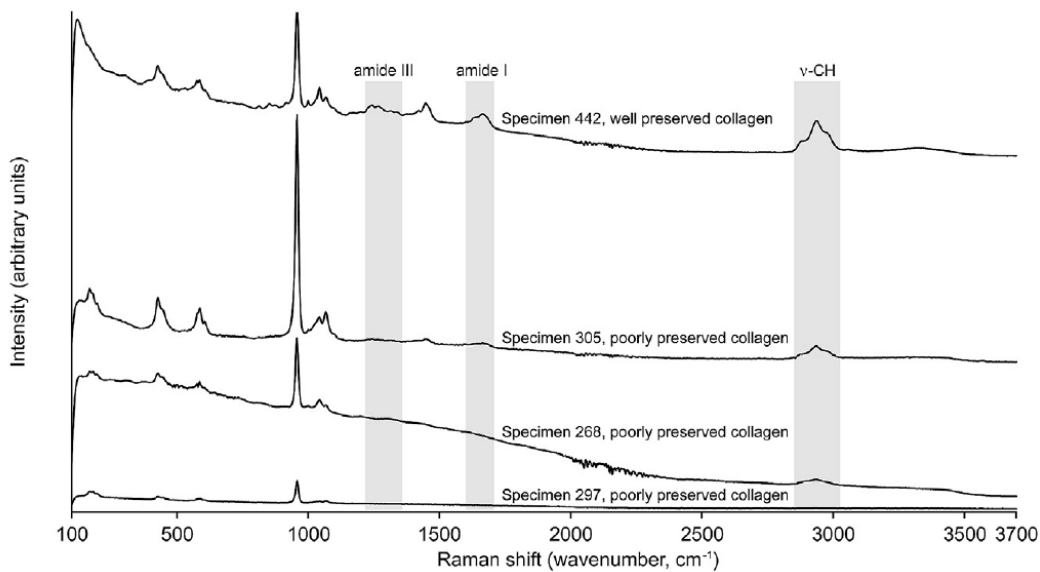
Figure 2 Raman spectra of well- and poorly -preserved collagen in bones[15]

3. TOF-SIMS

TOF-SIMS (Time of Flight Secondary Ion Mass Spectrometry) is an analytical technique that permits the analysis of both organic and inorganic phases. The principle of this technique relies on the analysis of secondary ions emitted following surface irradiation of the sample with a primary ion beam.

TOF-SIMS analyses were performed on mummy skin by studying ions of amino acids (leucine, valine ...) and fatty acids (palmitic acid, oleic acid). TOF-SIMS analysis allowed to evidence

keratin and collagen degradation (following ions of amino acids), and the repartition of lipids present in the skin.[21]

TOF-SIMS analysis of a fossilized soft tissue dating from the middle of Triassic age (-252.2 ± 0.5 and -201.3 ± 0.2 million years) allowed the identification of specific ions of glycine, alanine, proline, lysine, hydroxyproline and hydroxylysine.[22] The presence of blood residues was also detected in African artifacts by combining different analytical methods as TOF-SIMS and µFT-IR. TOF-SIMS was applied to identify the blood biomarkers in the case of proteins degradation (Figure 3). X-ray microfluorescence (µXRF) and X-ray absorption near-edge microspectroscopy (µXANES) were applied to detect the presence of iron in the area of proteins.[23-24]
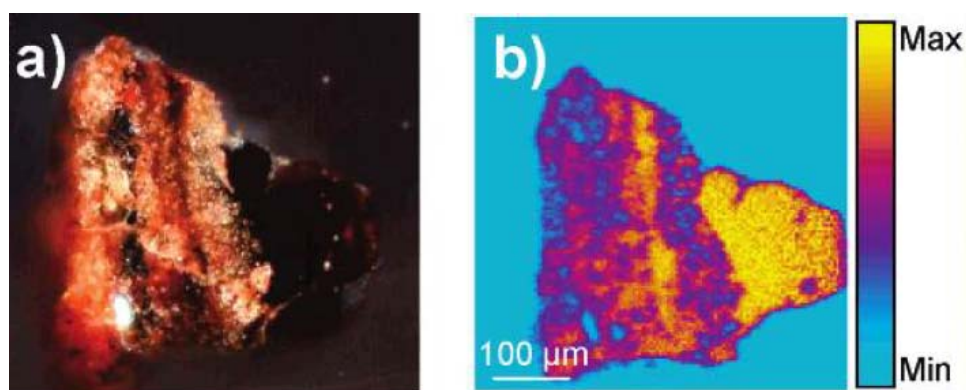
Figure 3. Proteins localization (a) microscopic view of the cross section, (b) TOF-SIMS spatial distribution of the proteins (sum of amino acids)[24]

4. Amino acid analysis and separation using chromatographic methods

The first chromatographic method allowed the analysis of amino acids using chromatography on paper. The technique is based on the separation of adsorbed amino acids on a cellulose paper using a solvent rising by capillarity. The detection of amino acids is carried out using ninhydrin staining. Egyptian archaeological samples[25] have been subjected to chromatography on paper analysis and amino acids were separated and identified.

A second method is cation exchange chromatography. In this method, the absorbance of amino acids is measured after their derivatization with ninhydrin. This technique was applied on glass jars from Ethiopia.[26] Proteins extracted from fossil bones of a 150-million-year-old sauropod dinosaur were separated and identified by reversed phase HPLC.[27] Furthermore, RP-HPLC has been used to isolate ten amino acids present in archaeological bone collagen as aspartic acid, glutamic acid,

serine, threonine, glycine, arginine, proline, hydroxyproline and leucine.[28] Moreover, reverse phase HPLC method was reported for the identification of the ratios of D- and L- amino acids isomers extracted from fossils.[29]

The mainstream technique used for identification of proteins in cultural heritage samples is based on gas chromatography and amino acid composition. Before analysis, archaeological samples require a pretreatment procedure consisting of extracting proteins and hydrolyzing them into amino-acids with strong acid or base. Then amino acids are derived (using alkyl chloroformates or trifluoroacetamide or alkylsilyl acetamide) to make them volatile for GC analysis.

This technique allowed to identify the amino acid composition of fossils from Pleistocene to Jurassic fossils (201.3 to 145 million years).[30] The use of gas chromatography with pyrolysis coupled with Mass Spectrometry (Py-GC/MS) is also a highly used technique for the study of old samples. Samples are heated (50-310 °C) and pyrolysis products are analyzed by MS. For example, 2.5-diketopiperazines produced upon the pyrolysis of the cyclohydroxyproline precursor allowed identification of collagen in archaeological bones.[31]

5. Immunological Methods

Immunological methods using specific antibodies are used for the analysis of proteins contained in old samples since the early 1960s. Among these immunological techniques are used the RIA (Radioimmunoassay), based on the use of radioactively labeled antigens, and ELISA (enzyme-linked immunosorbent assay),[66] based on an antigen-antibody reaction by means of a colored reaction produced by the action on a substrate of an enzyme attached to the antibody. Immunological techniques as enzyme-linked immunosorbent assay[66] (ELISA) and radioimmunoassay (RIA) were applied for the analysis of skull fragments fossils dating from 1.6 million years ago, found in south of Spain. The analysis showed the presence of human albumin in the skull fragments and provided an evidence of human presence in the Andalusia 1.6 million years ago.[32] These techniques have been also used to detect traces of blood on archaeological objects.[33-35] However, the immunological approach is limited by the identification of targeted proteins only.

III. Proteomics

1. Definition

The term of proteome appeared for the first time in a scientific publication in 1995, and was referred to the term genome that was used to define the entire collection of genes in an organism.[36] The proteome represents the entire proteins present in a studied biological sample. A single genome can generate different proteomes under different conditions depending on the stages of the cell cycle, the response to different biological or physical signals and the physiopathological status. Moreover, a protein is chemically modified by post-translational modifications or by external factors (e.g. UV exposure, heating…). All these factors increase the complexity of the proteome, and the study of the proteome allows a global understanding of a given biological system in specific context. Proteomics is the large-scale study of proteins. This discipline has grown strongly during last years, due to the exponential increase of available genome sequences and on the other hand to the progress of mass spectrometry. The proteomic classical approach analysis is divided into several stages and consists, in a first step, of proteins extraction from the studied medium (biological fluid, cell, plant ...). Then, protein analysis performed according to two different strategies called 'top-down' and 'bottom-up'.

2. Bottom-up strategy

Bottom-up strategy is the most common approach applied for proteins analysis and is based on the enzymatic digestion of proteins before their analysis by mass spectrometry. This approach depends on the reliability and the robustness of the protein extraction, solubilizing, and digestion methods. Extraction of proteins depends on the type of sample. It can be based on mechanic homogenization, ultrasonication, freeze-thaw cycles, osmotic lysis, etc. The next step after proteins extraction is protein solubilization. pH and salt concentration of solutions can be modified to enhance protein solubility and to break the hydrophobic interactions. Before protein digestion, disulfide bonds between cysteine amino acids are treated by reducing agents such dithiothreitol (DTT) to prevent disulfide bonds reformation, thiol function of cysteine amino acids are protected with alkylating agents such as iodoacetamide, 2-chloroacetamide or 4-vinylpyrolidine.[37-39]

The addition of chaotropic agents, detergents and reducing agents helps to increase proteins solubility. Before protein analysis, contaminants should be removed; e.g. detergents and salts removed by dialysis. After the purification steps, extracted proteins can be separated by mono- or 2-dimensional gel electrophoresis or liquid chromatography.

Trypsin is one of the mostly used enzyme for protein digestion due its efficiency and specificity. It cleaves the amino acid chain after arginine and a lysine in the C-terminal generating relatively small peptides with high tendency for ionization (dozens of amino acids).[40] Other enzymes can be used for protein digestion as LysC, which cleaves after a lysine in C-terminal, and AspN which digests after an aspartate in N-terminal.[39] The resulted peptides from digestion are separated and analyzed by liquid chromatography coupled to mass spectrometry (LC-MS/MS). The soft sources of ionization such as MALDI and ESI allow peptides ionization without any fragmentation. The MS spectrum for all peptides is called the peptide mass fingerprint. Then each peptide can be selected and fragmented in the collision cell, the resulted MS/MS spectrum identify the amino acid chain as well as different chemical modifications. By comparing the generated MS and MS/MS spectra with databases, proteins identification is obtained.

Different methods of protein digestion were developed as the classical digestion in gel[41] and FASP Filter Aide Sample Preparation (FASP).[42] The enhanced Filter-Aided Sample Preparation (e-FASP) incorporates alternative reagents to the ones used in the FASP approach that lead to a better sensitivity, recovery, and proteomic coverage for processed samples.[43] Other digestion methods were developed as well for example Gel-aided sample preparation (GASP),[44] In Stage Tips method,[45] or a combination of different digestion methods as In Stage Tips and FASP.[46]

3. Proteins Data-Bases and bio-informatics

MS/MS spectra are compared with protein databases for identification. Several databases are existing. Among the databased can be cited NCBI (National Center for Bio-technology Information), which lists protein sequences from genomic libraries. This exhaustive bank contains redundancies. Another databases is UniProt (Universal Protein Ressource). The UniProtKB database includes the bank SwissProt (verified and annotated) and the bank TrEMBL (annotated automatically, unvalidated experimentally).

There are different search algorithms that can identify proteins from fragmentation spectra like Mascot,[47] which was used during this project. But many other algorithms have been developed as Protein prospector,[48] Sequest,[49] Andromeda,[50] ProbID,[51] X! Tandem,[52] OMSSA,[53] ProSight[54] and Inspect.[55] These algorithms compare fragmentation spectra obtained by mass spectrometry, from peptide mixtures of digested proteins, to the theoretical fragmentation spectra of the peptides from all proteins present in the databases. All these algorithms integrate different search parameters such as post-translational modifications, the mass error of the spectrometer, the different databases, and also the different taxa of living organisms. The final result is the identification of proteins through peptides fragmented by mass spectrometry and the obtainment of a score that can filter the data. Each search engine calculates a score and a statistical probability. The score obtained is a statistical score indicating the extent to which the experimental data corresponds to the sequence of the database. Most often this score is accompanied by a statistical probability called E-value for Mascot that represents the probability that a result will occur by chance. This comparison between experimental and theoretical MS/MS spectra can also be done using a library of MS/MS spectra of peptides acquired and identified previously. This tool is integrated in softwares like MyProMS[56] or Proteome discoverer 2.1 with the MSPepSearch tool.[57] The software assigns a score that measures the similarity degree between the experimental spectrum and the theoretical spectrum. This identification score depends on the used bank and the mass tolerance that also allows to filter the identifications.

4. Identification strategy of non-sequenced species. *De novo* sequencing.

De novo sequencing consists in directly interpreting a fragmentation spectrum to deduce the primary sequence of the peptide, without referring to a database of sequences data. The interpretation of an MS/MS spectrum allows the identification of amino acids which constitute the primary peptide sequence. Softwares have been designed to facilitate the task such as PEAKS,[58] PepNovo,[59] Novor[60] or DenoGui[61] which is an interface that groups together several *de novo* algorithms.

De novo peptide sequences are compared to proteins sequences in the database. This task can be carried out by a sequence similarity search using the MS Local Basic Alignment Search Tool (MS BLAST) algorithm. Thus, if a protein in the databank contains peptides similar to the *de novo* peptides sequences, then the studied protein is most likely a homologue of this protein in the library.

In this way, *de novo* proteins are identified by sequence homology to same proteins but belonging to another species and most often a close species. The main advantage of this methodology is that the comparison is done based on the characters of sequences and not on their masses. BLAST MS allows the detection of one or more amino acids mutations (depending on the stringency or phylogenetic proximity between the two organisms). In order to obtain reliable results by *de novo* sequencing approach followed by a BLAST, it is essential to work with good of quality data but results must also be validated on the basis of the score, the sequence length and the length of the match. SPIDER software is based on an algorithm that takes in consideration both *de novo* sequencing errors, and homology mutations between the analyzed proteins sequences and the proteins sequences present in the database.[62-63]

IV.   Proteomics in Archaeological and Paleontological samples

Proteomics is an extremely sensitive method. Recent developments in the miniaturization of soft ionization techniques and the nanoscale chromatography allowed to apply it to very small sample amounts. Proteomic methodology was adapted to analyze proteins from different types of archaeological samples like ceramics, textiles, egg shell, mummy skins, fossil and ancient bones.[64-65] The proteomics protocols depend on the type of the archaeological sample, for example the protocol and especially the extraction procedure can change between proteins trapped inside the ceramics and proteins extracted from bones.

The first attempt to analyze proteins present in archaeological samples was at the end of 2000s. Proteins were successfully identified from organic remains present in Iñupiat potsherd fragment[66] dating from 1200-1400 AD excavated in Point Borrow in Alaska. Analytical procedure was optimized on ceramics models impregnated with muscle tissues and blubbers of harbor seal (*P. vitulina*), gray seal (*H. grypus*), ringed seal (*P. hispida*), and beluga whale (*D. leucas*), which were essential components of the Eskimo diet. First, proteins were extracted from 25 mg of impregnated potsherd ceramic with 1% TFA and ultrasound sonication, then extracted proteins were submitted to several steps of denaturation (guanidine), reduction (dithiothreitol), alkylation (iodoacetamide), and hydrolysis (trypsin). In the next step, proteins were analyzed by nanoLC coupled to a high-resolution mass spectrometry and were identified by Matrix Science software with the help of SwissProt and NCBInr databases. Due to the lack of databases, proteins were identified by sequence homology to other species, and they succeeded to identify species specific peptides. The

developed methodology was then applied to 250 mg of archaeological potsherd, and they succeeded to identify four species specific peptides corresponding to harbor seal myoglobin including a peptide specific to cetacean and pinniped species and another peptide specific to seal species.

identified protein	identified sequences	species					peptide position	retention time (min)	precursor ions mass/charge		mean error MS/MS/MS	
		baikal seal (*P. sibirica*)	gray seal (*H. grypus*)	harbor seal (*P. vitulina*)	other marine species	other species						
myoglobin[a]	SHPETLEKFDKFK	X	X	X			36−48	30.3	803.417	2+	<1	<1
	YKELGFHG		X	X	[b]	[c]	147−154	29.6	475.740	2+	<1	<1
	HPAEFGADAQAAMK	X	X	X		[d]	120−133	30.4	722.338	2+	<1	<1
	VETDLAGHGQEVLIR		X	X		[e]	18−32	34.3	818.936	2+	<1	<1

[a] Decoy 0, false positive rate 0%. [b] Amazon dolphin (*I. geoffrensis*), Atlantic bottle-nosed dolphin (*T. truncatus*), beluga whale (*D. leucas*), Black Sea dolphin (*D. delphis*), bridled dolphin (*S. attenuata*), Dall's porpoise (*P. dalli dalli*), goose-beaked whale (*Z. cavirostris*), harbor porpoise (*P. phocoena*),Hubb's whale (*M. carlhubbsi*), Killer whale (*O. orca*), long-finned pilot whale (*G. melaena*), Longman's beaked whale (*I. pacificus*), melon-headed whale (*P. electra*), and Stejneger's beaked whale (*M. stejnegeri*). [c] Black-lipped pika (*O. curzoniae*). [d] African elephant (*Loxodonta Africana*), weasel lemur (*Lepilemur mustelinus*). [e] African wild dog (*Lycaon pictus*), bat-eared fox (*Otocyon megalotis*), cape fox (*Vulpes chama*), and dog (*Canis familiaris*).

Figure 4. Identification of 4 peptides of myoglobin as species 'markers' from 1200-1400 AD sample including 1 peptide (YKELGFHG) specific to 17 pinnipeds and cetaceans; and 1 peptide (SHPETLEKFDKFK) specific to 3 Phoca species (*Phoca sibirica*, *Halichoerus grypus*, *Phoca vitulina*)[66]

In another study, fish proteins were identified from non-visible remains in potsherds and species could be discriminated.[67] An extraction protocol was implemented to extract trapped proteins inside model ceramics that were impregnated with anchovy (*Engraulis encrasicolus*) and bonito (*Sarda sarda*) fish species. The extraction solution was composed of urea and thiourea for denaturation, and dithiothreitol as a detergent and a reduction agent. In this work, they succeeded to identify around 200 proteins from bonito and anchovy fish species. The identified proteins contain 73 peptides specific for fish species, among them *de novo* peptides specific to anchovy (*Engraulis encrasicolus*) and bonito (*Sarda sarda*) fish species which were identified by sequence homology to other fish species contained in databases. The sequence alignment of *de novo* peptides against fish proteins from databases using Blastp software showed amino acid substitution in comparison to the same peptides in other species. Other extraction protocols were developed to extract proteins from ceramics as for example the use of microwave-assisted enzymatic digestion (trypsin),[68] and it was optimized by using extraction solution made of SDS or hydrofluoric acid.[69] Peptides from alpha and beta casein were extracted and identified from archaeological pottery (500−300 BC), by using an extraction solution containing PBS as an extraction reagent and they succeeded to demonstrate that milk proteins can be identified from archaeological samples as well as discriminating their origin.[70]

In 2014, proteins were also identified in remnants of bread found in China[71] on an archaeological site dating from 500 to 300 BC revealing manufacturing receipe. To realize this identification, they

extracted proteins from the sample, separated them using SDS-PAGE gel technique and finally they analyzed each band by nanoLC-MS/MS.

Collagen is the main protein present in bones and it can be efficiently preserved due to the protective effects of bones mineral phase. Collins *et al.*[72] have developed a robust and straightforward PMF (Peptide Mass Fingerprint) method called ZooMS based on the identification of collagen peptides that represent markers of animal species. It consists of proteins extraction from bones, digestion and peptides purification and MALDI-TOF/TOF analysis. The peptide species markers were identified using available protein databases and also from homemade databases that included various animal species. For example 92 peptides markers belonging to 32 different mammal species were used to identify species (Figure 5).[73] The proposed ZooMS method allowed for example the differentiation of sheep and goat bones.[74] Collagen fingerprint was used also for the discrimination between different species of rodents.[75]
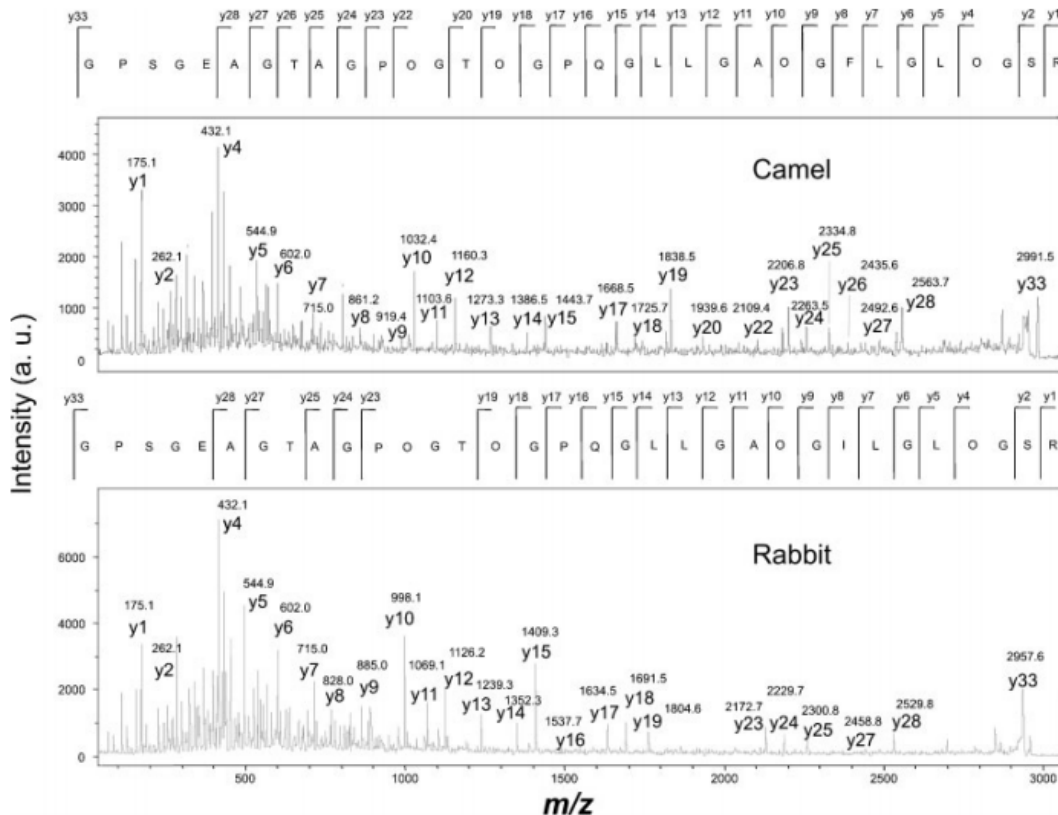
Figure 5. MS/MS spectra showing the *de novo* sequencing interpretation of a known rabbit collagen peptide at m/z 2957 (COL1A2T62) and the identification of the analogous camel peptide at m/z 2991.[73]

A proteomic approach was also used to characterize hair from mummies.[76] This method, requiring 500 μg of sample, allowed the identification of this mummy hair keratin and evaluated, hair molecular preservation by a proteomic approach. Chemical modifications such as deamidation of glutamines and asparagines were studied and compared to results obtained for modern hair.

Bottom-up proteomics was also used for archaeological proteins identification from other types of samples such as teeth[77] or the skin of mummies.[78]

V. Amphorae

The Greek word "amphoreus" originated the Latin word "amphora". Mentioned by the poet Homer, amphorae appeared in the Greek world from the 6th century BC. Amphora is a terracotta vase, manufactured with clay and water and used for transportation and storage of many products, mainly food products such as wine, oil, fish in brine, olives, honey, dried fruits (almonds, dates ...), etc. The amphora was therefore the packaging of a large number of products to circulate by land, river and maritime. The first classification was done by the German archaeologist and epigraph Heinrich Dressel (1845-1920) who wrote a typology listing 45 types of amphorae. These amphorae, listed from Dressel 1 to 45, dated between the 1st century BC and the 4th century AD. They have been classified depending on their content, their origin, and their date of manufacture. 3 main types of amphorae can be distinguished: wine amphorae, oil amphorae and fish products (*Garum, Hallec, Muria, Liquamen*) amphorae.[79]

Dressel 14 amphorae are produced mainly in Lusitania, Portugal, between the first half of the 1st century and the end of the 2nd-early 3rd century AD. They were intended to carry mainly *Liquamen*, of various qualities, as evidenced by the known painted inscriptions.[80]

Several elements allow to obtain information on the craftsman who shaped the amphora, the trader, and sometimes its content and its place of origin. First, the amphorae present specific forms that depend on 3 variables: the content, the region of production and the date of production. Secondly, inscriptions and stamps that are printed on the amphorae are of interest. Third, organic matters may be conserved and studied, even in the absence of visual organic biomolecules residues that can be trapped inside ceramics.

Figure 6. Different types of amphorae

VI.   Fish sauces

Fish processing industry was very prospered during the Roman empire,[81] salted fish (*Salsamenta*)[82-83] and fish sauces were the main products produced and exported across the empire.[84] Salted fish or *Salsamenta* was made from fish meat slices covered with layers of salts to conserve it.[82-83]

Fish sauces were among the most common condiment consumed during that era. Roman produced 4 different sauces: *Garum*, *Liquamen*, *Allec* and *Muria.*[85] *Garum* was first produced by the Greeks. The highest quality of *Garum* in Greece was produced from the innards and the blood of Bluefin Tunas.[83] It was also prepared from whole small fishes as sardine, anchovy or from the innards of bigger fishes as mackerel[82] and herring[86] in the presence of salt excess and fermented during several months.[71] *Liquamen* is a similar sauce to *Garum*, has the same production procedure as *Garum* and was made initially from mackerel. *Muria* is the solid residue produced during *Garum* fabrication. *Allec* is a salty solution obtained during preparation of salted fish.[85] The analysis of fish products remains from archaeological amphorae or from fish processing sites reveals invaluable historical, socioeconomic, and cultural information beside evaluation of trade routes during the antiquity.[87-88]

VII.   Fish species authentication in Food-omics

Since the antiquity, fish is considered as a major food source in human nutrition. Fish contains high nutritional values for human diet. It is well known for its high content of polyunsaturated fatty acid, especially ω-3 fatty acids, which can help in preventing cardiovascular, neurological and inflammatory diseases. Fish is rich in proteins, vitamins (A, D, E, B1, B6 and B12) and minerals (Fe, I, P, Na, Ca and K) as well. In order to respond to the grown demand for fish products,

36

production of fish processed food increased in the last decades worldwide. These evolutions have caused the increase of risks that may come from fish species substitutions, contaminations and allergens. In response to those concerns, a robust, sensitive, accurate, fast analytical method is a must, to assure the quality control and detect any potential risks on human health, as well as the authentication of fish species.

The food-omics combine different types of omics (as genomics, metabolomics, and proteomics) that are used to analyze and study food quality and its effects on human health. Among those different disciplines, proteomics play an important role to protect the consumer and to ensure food quality especially for fish products. Proteomics is considered a reliable technical approach for fish species authentication, and is also used to detect allergens and pathogen microorganisms, as well as it can reveal any change in fish quality during processing or storage.[89-90]

Fish species authentication represents the main challenge. After fish processing, fish species identification becomes impossible by conventional methods as anatomical and morphological examination. Therefore, different techniques were adapted to perform this task at molecular level. Electrophoretic and immunological protein-based methods were among the most used methods for fish species identification. An indirect enzyme-linked immunosorbent assay (ELISA) technique was developed for specific identification of Grouper, Wreck fish, and Nile perch using polyclonal antibodies against muscle soluble proteins of grouper (anti-GSP), wreck fish (anti-WSP), and Nile perch (anti-PSP) respectively.[91] Isoelectric focusing (IEF)[92] and two-dimensional electrophoresis (2-DE) have been developed in order to distinguish different fish species profiles as in the case of commercial flat fish.[93] Due to the modifications that can occur on proteins during food processing, these techniques become limited and they are time-consuming regarding preparations.

Genomics and PCR-based studies can be an alternative for fish species authentication. DNA barcoding method is considered as an efficient technique for species identification. Most often, a partial sequence of the mitochondrial Cytochrome c Oxidase I[94] gene is used to distinguish different fish species. However, DNA-based procedures still facing many challenges, where food processing under high temperature and pH variation can affect DNA sequences and cause their degradation leading to non-specific identifications.

Proteomics proposes a fast, accurate and sensitive alternative methodology for fish species identification. Matrix assisted laser desorption ionization time-of-flight mass spectrometry

(MALDI-TOF-MS) represents a fast and common tool for species identification. MALDI-TOF-MS can generate a spectrum presenting a finger print of the studied sample, which is compared and matched with other spectra from known sources found in the databases. After proteins separation with a 2-DE gel, spots corresponding to proteins of interest are digested and peptides are recovered and analyzed with MALDI-TOF/MS. For example parvalbumin beta protein was selected as a target in studies related to species differentiation for *Merluccius* and *Macruron* genera as well as hake species identification.[95] Triose phosphate isomerase protein has been also studied and analyzed by 2-DE-MALDI-TOF PMF for the discrimination between three tuna species (*Thunnus thynnus, T. albacares and T. alalunga*).[96] A method based on MALDI-TOF/MS analysis was developed for the discrimination of 25 fish species without any previous time-consuming separation by 2-D gel. Intact Parvalbumin proteins showed molecular weight variation regarding fish species, for example for sole m/z = 11975.21, for European plaice m/z = 11351.73 and 11763.63 , and for Greenland halibut species m/z = 11432.38.[97] Another recent study established a protein fingerprint database of 56 common fish species with MALDI-TOF/MS that allows a fast identification of fish species present in processed seafood.[98]

Tandem mass spectrometry coupled to liquid chromatography (LC-MS/MS) is the main technology applied in proteomics, and more precisely in the bottom-up approach based on the analysis of recovered peptides from proteins digested with enzymes (mainly trypsin), allowing the identification and the quantification of thousands of proteins from a complex sample. However, proteins identification is limited by the presence of genomic sequences in the databases which not the case when dealing with fishes. Only few fish species have sequenced genomes such as *Danio rerio* species.[99] A majority of fishes references few proteins in databased such as mitochondrial cytochrome c oxidase I [94] and cytochrome b (two regions often used for DNA barcoding). Therefore, the identification of species specific peptides from an unknown sample requires *de novo* sequencing. D*e novo* sequencing of 25 new PRVB isoforms belonging to different species of the unsequenced *Merlucciidae* family were for example investigated. In their study, they combined different MS techniques and proteomics strategies, as bottom-up approach, FT-ICR for intact proteins detection with high accuracy and selected MS/MS ion monitoring (SMIM). SMIM strategy allowed the fast identification of 11 species specific peptides from the Parvalbumin beta proteins belonging to the *Merlucciidae* family present in seafood products.[100]

Alternative method for species identification from an unknown sample was proposed based on bottom-up approach and analysis with tandem mass spectrometry (MS/MS). In the first step, a database containing the MS/MS spectra was created for each fish species interesting to study. In the next step, MS/MS spectra generated from the unknown sample were compared and matched with the MS/MS spectra present in the created database with the help of specific programs as compareMS2, SpectraST and SEQUEST. This method allowed the identification of fish species from both fresh and processed samples. The identification of species, genus or family levels can be performed, and the percentage of matched spectra allows the determination of phylogenetic tree for studied species.[101-103]

VIII.   Fish remains analysis from archaeological samples

The analysis of the organic residue in archaeological ceramics is considered as a real challenge due to the degradation phenomena and leaching of hydrophilic molecules. Most common analytical approaches deal with lipidic remains[104] especially in case of fish which have characteristic lipids profile rich in long chain n-3 polyunsaturated fatty acids.[105] The detection of $C_{17:1}$ and $C_{19:1}$ fatty acids with GC-MS indicated the presence of fish and seafood in an Anglo-Saxon potsherd dating from the seventh to the ninth century.[106] Nevertheless, GC/MS techniques were used to analyze fish sauce remains in an amphora from Pompeii, Italy. The profile of amino acids obtained from the archaeological sample showed a similarity with the modern fish sauce from Italy and Asia which is mainly composed of glutamate amino acids.[107]

Recently, DNA based approaches are being widely applied for fish species discrimination in Archaeology. This method provides many advantages as robustness and high specificity of the analysis. For example, the study of ancient DNA from fish vertebrates allowed the identification of salmon species present in the archaeological site at Dionisio Point, British Columbia, Canada.[108-110] Lately, stable isotope ratio analysis has also been applied in archaeological studies, most often bone collagen was isolated and analyzed especially for stable carbon and nitrogen isotopes.[111] Two different methods exist to isolate collagen from bones for carbon and nitrogen analyses. The first technique, consists of bones demineralization (e.g. HCl), and it was applied for recent or well reserved bones. Isotopic analysis of poorly preserved bones includes several preparation steps including demineralization, gelatinization (heating at 70°C) and ultra-filtration in order to isolate high molecular weight components. The proteins were combusted to N_2 and CO_2 and analyzed in

an automated carbon and nitrogen analyzer coupled to a continuous-flow isotope ratio mass spectrometer. Furthermore, isotopic analysis allows the identification of organic samples or even the definition of the diet or the mobility of those samples.[112] Besides proteins,[113] fatty acids extracted from archaeological samples have been investigated by carbon isotope analysis in order to identify the animal origin of the organic remain.[114-115]

Proteomics was adapted to provide structural information on proteins from archaeological[64-65], paleontological[116] and artwork samples[117-118] as well. ZooMS strategy based on collagen fingerprinting method was used for the discrimination between archaeological specimens from marine mammal.[119] Based on collagen PMF approach, ZooMS method was used for the identification of fish archaeological specimens.[120] Collagen PMF allowed the species discrimination between modern fish samples and spectra obtained from archaeological samples. Collagen PMF also led to the identification on species, genus and subfamily/tribe levels from bones samples from whales.

Results and discussion

The aim of this work was to identify fish proteins and species from ceramics preserved in an unfavorable context: a submarine context. The studied sample was provided by Dr Franca Cibbeccini, *Département de Recherches Archéologiques Subaquatiques et Sous-Marines (DRASSM), Marseille, France*.

The amphora sampled was found in a shipwreck located in the harbor of Marseille city in south of France at 49-50 m deep and dating from 116 AD. It is a Dressel 14 (Dr. 14) (Figure 7). The Dressel amphorae from types 7 to 14 have a streamlined shape and a pointed bottom; the Dr. 14 has a narrow-mouth aperture. Dr. 14 amphorae were produced mainly in Lusitania, Portugal, between the first half of the 1st century and the early 3rd century AD. They are suspected to have carried processed fish products mainly *Liquamen*, of various qualities, as testify the known painted inscriptions. *Liquamen* was a product similar to *Garum*, until the late 2nd century AD. However, from the 3rd century AD., *Liquamen* became the generic name for all kinds of fish sauces. Fish sauces were made initially from small fishes as sardines but also bigger fishes such as mackerel; innards of bigger fishes were also used. Bigger fishes such as mackerel or tuna were also used for elaboration of *Salsamenta* (salted fishes).

It can be pointed out that the identification of fish species from processed fishes remains a difficult task. Commonly it is based on ancient texts and the *titulus pictus* on amphorae. The Dr. 14 amphora studied in this work did not have any "*titulus pictus*". The objectif is thus here to bring a new light and a direct evidence of the content of Dr. 14 amphorae.

A methodology based on proteomics has been optimized here for fish species identification, from residues trapped in this archaeological ceramics. The study was based on the identification of species-specific peptides obtained from different model fish sauces made from both sardines and mackerel fishes. Due to the lack of fish proteins in databases, proteins from various fish species were analyzed.

Figure 7. The studied Dressel 14 provided by Dr Franca Cibbeccini, Département de recherches archéologiques subaquatiques et sous-marines (DRASSM, Marseille).

I.   Samples and fish protein extraction

Old recipes described *Garum* and *Liquamen* to be made from fermented small fishes such as sardines, from sections of bigger fishes or from innards of bigger fishes especially mackerels (i.e. *Liquamen* of "higher quality"). As mentioned before, *Garum* and *Liquamen* were produced in a similar way. Tuna species was described to be mainly used in production of salted fishes known as *Salsamenta*, and its use for fish sauce production was mentioned in ancient Greece.[121]

This proteomics work aiming to identify proteins and their species is based on the use of both public databases and home-made protein database due to the lack of fish proteins databases for numerous species. The Table 1 is showing several fish species that we have included in our work to build the database. In particular 7 different fish species were considered to be of main interest in this study in view of the ancient practices for fish sauce preparation and salted fish production. The Table 3 is showing the phylogenetic tree of the studied fish species.

Table 1. List of extracted fish species

Species	Family	Common name	Origin
Sardina pilchardus	*Clupeidae*	European pilchard	Mediterranee
Sardina pilchardus	*Clupeidae*	European pilchard	Nord-Est Atlantic
Scomber scombrus	*Scombridae*	Atlantic mackerel	Nord-Est Atlantic
Auxis thazard	*Scombridae*	Melva	Mediterranee
Ehthynnus alletteratus	*Scombridae*	Little tunny	Mediterranee
Thunnus thynnus	*Scombridae*	Atlantic bluefin tuna	Mediterranee
Thunnus alalunga	*Scombridae*	Albacore	Pacific-Tahiti

The bottom up proteomic protocol was derived and optimized from a previous work.[122] In details, 50 mg of fish muscles were extracted using a buffer extraction solution and stirred in a tube containing metallic beads. The extraction solution contained high amounts of denaturant agent (urea), reducing agent (DTT) and detergents (SDS, CHAPS) in addition to DCA in order to increase proteins solubility. In the next step, the recovered solution was extracted with chloroform and methanol to remove lipids and SDS. Finally, the proteins were dosed with a NOVO-peptides, and 50 µg of proteins were extracted and digested following the eFASP method (see experimental section). Peptides were analyzed using LC-MS/MS. Raw data generated were treated with Peaks software for protein identification and *de novo* sequencing. Table 2 shows the MS and MS/MS results. The interrogation of raw data was performed against our fish protein database and fish proteins described in the nrNCBI public database.

Proteins from fish samples were identified by sequence homology to other species. As example of results, 1569 proteins were identified for *Scomber scombrus* from data regrouping 7889 MS scans and 49329 MS/MS scans. Focusing on tropomyosin from *Scomber scombrus,* 75% of sequence coverage was achieved. The protein was identified by sequence homology to *Thunnus thynnus* species and contains 5 peptides with amino acids substitutions. As an example, MS/MS spectrum (Figure 8) of the doubly charged ion at m/z 619.816 Da, allows the identification of YSG$\underline{A}$LKD$\underline{V}$QEK sequence using the y fragments (y_1^+- y_{10}^+) and b fragments (b_1^+- b_{10}^+) corresponding to the peptide 60-70 of tropomyosin (sequence homology to *Thunnus thynnus*). This spectra highlights the substitution of the forth residue, asparagine by alanine and the substitution of the eighth amino acid alanine by valine.

Table 2. Table summarizing the LC-MS/MS result obtained for fish samples (Peaks software)

	Sardina pilchardus (Mediterranean)	*Sardina pilchardus (Atlantic)*	*Scomber scombrus*	*Auxis thazard (Melva)*	*Euthynnus alletteratus (thonine)*	*Thunnus thynnus*	*Thunnus alalunga*
Number of MS scans	7460	7729	7889	7664	8111	7584	7762
Number of MS/MS scans	49735	49427	49329	49526	49144	49608	49526
Peptide-Spectrum Matches	19281	18444	19388	18589	22700	24635	23454
Peptide sequences	10226	9970	9804	9499	11596	12435	11068
Protein groups	512	521	490	441	522	609	428
Proteins	1381	1388	1569	941	1240	1252	774
Proteins (>2 Unique Peptides)	745	754	83	539	679	685	403
Missed Cleavages = 0	6290	6229	6711	6266	7493	8268	7405
Missed Cleavages = 1	2775	2629	2394	2446	3013	3101	2780
Missed Cleavages = 2	866	834	575	660	890	869	741
Missed Cleavages = 3	259	242	112	117	179	173	131

Table 3. Phylogenetic tree of the studied fish species

Class	Order	Family	Genus	Species

Actinopterygii

Clupeiformes — Clupeidae — *Sardina* — *Sardina pilchardus*

Perciformes — Scombridae

Scomber — *Scomber scombrus*

Auxis — *Auxis thazard*

Euthynnus — *Ehthynnus alletteratus*

Thunnus — *Thunnus thynnus* / *Thunnus alalunga*
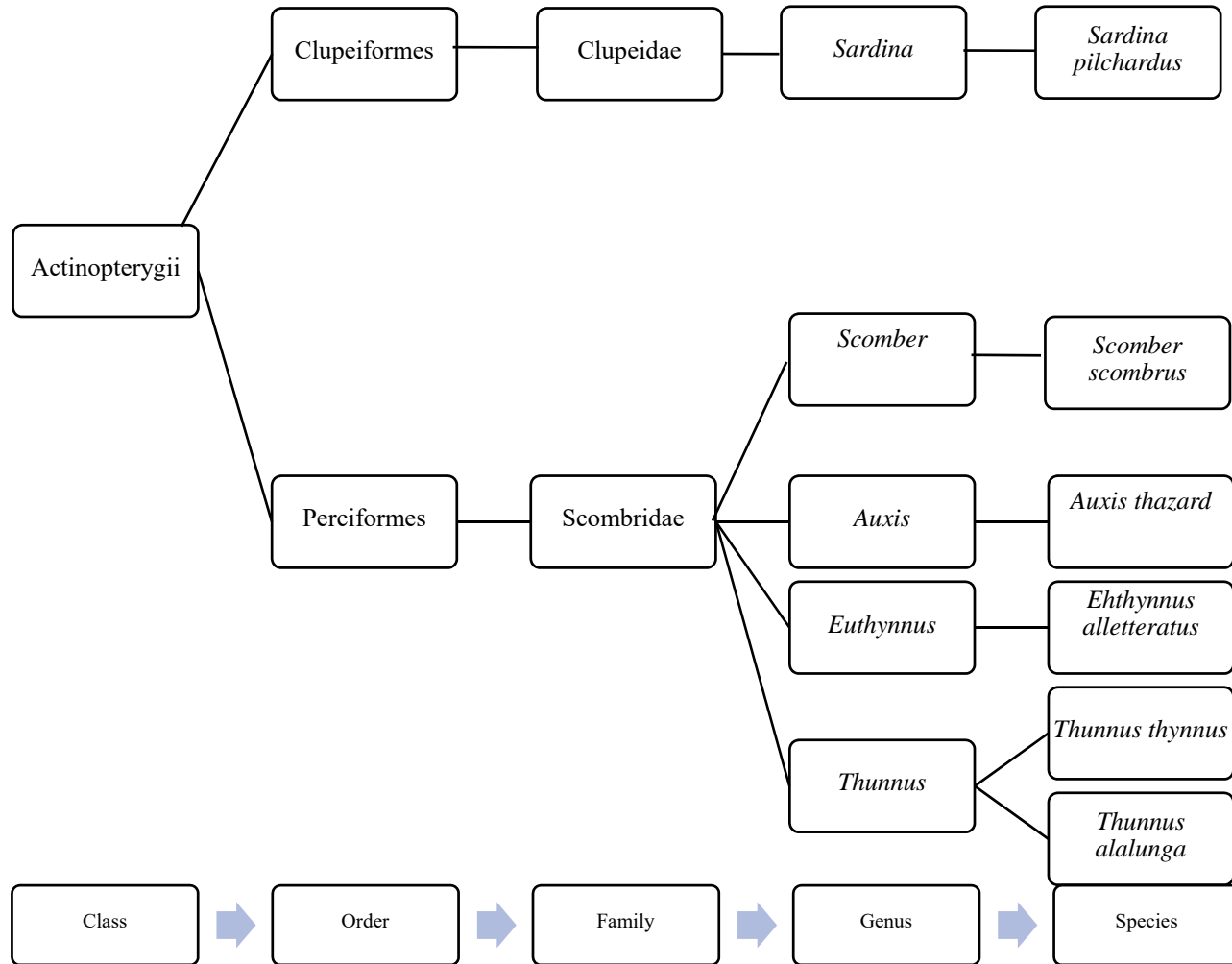
Few proteins of fish species are referenced in databases; e.g. *Danio rerio* (Swiss-Prot: 3072; TrEMBL: 59291; NCBI: 88160*)* is for example used as a model organism for biological, genetic, environmental and toxicological studies, and is referenced in databanks. In our studies, we focused on fish species belonging to Clupeidae and Scombridae families since they are most probably used in fish sauces production. However, most of the species of interest are unsequenced and their proteomic databases are limited as it is shown in Table 4: for example 13 and 78 proteins are respectively referenced in SwissProt Databases for Clupeidae and Scombridae; and NCBI databank contains 36836 and 9736 proteins respectively. Considering species, SwissProt describes 16 proteins fot *Thunnus thynnus* and 325 and 687 are described in TrEMBL and NCBI.

Figure 8. MS/MS spectrum of the doubly charged ion at m/z: 619.816 (Δm = 0.3 ppm) presenting y and b fragments of the peptide sequence YSGALKDVQEK of tropomyosin protein from hydrolysis extract of *Scomber scombrus* fresh fish.

Table 4. Number of sequenced proteins from different fish species present in the databases

	Swiss-Prot (database July 2018)	TrEMBL	NCBI
Actinopterygii (Class)	5343	1469565	3858321
Clupeiformes (Order)	14	3966	41668
Perciformes (Order)	208	67597	118224
Clupeidae (Family)	13	2274	36836
Engraulidae (Family)	-	1503	4165
Scombridae (Family)	68	3425	9736
Sardina **(Genus)**	1	253	1507
Clupea **(Genus)**	16	703	30480
Scomber **(Genus)**	22	1635	1920
Auxis **(Genus)**	1	191	605
Euthynnus **(Genus)**	-	133	271
Thunnus **(Genus)**	50	1347	3188
Sardina pilchardus **(Species)**	1	96	323
Scomber scombrus **(Species)**	4	207	694
Auxis thazard **(Species)**	-	6	261
Euthynnus alletteratus **(Species)**	-	-	131
Thunnus thynnus **(Species)**	16	325	687
Thunnus alalonga **(Species)**	2	109	436

II. Methodological development on model fish sauces samples

The first question to solve was related to the occurrence of proteins in fish sauces not fully hydrolyzed into amino-acids. Next step were focused on the identification of proteins and their biological species. Specific peptides identified from fish model sauces were compared and matched with species specific peptides identified from fresh fish samples and public databases.

Three different samples of model fish sauces were used in our study in order to develop and optimize our methodology. The first sauces were made by Emmanuel Botte (Centre Camille Jullian, Aix Marseille Université and Centre J. Bérard, Naples) from sardine fishes (*Sardina pilchardus*) following an old recipe (E. Botte. PhD 2008, Lyon 2, *Salaisons et sauces de poissons*), the second sauce from Mackerel innards (Mackerel-1) and the third one from Mackerel fishes (Mackerel-2).

We carried out a bottom-up approach for the proteome analysis in the fish sauces. The analytical protocol was applied to 50 µl of model fish sauces samples. Table 5 is showing the identification of proteins in fish sauces, confirming thus that proteins were not fully hydrolyzed into amino acids in-situ. For example Sardines-based garum showed 1409 proteins identified. The sauce made from innards and mackerel blood has shown more identified proteins (1311) than the other mackerel sauce (176), however the last contains a higher percentage of muscle proteins. The details of these analysis is shown in the following paragraphs.

Table 5. Table summarizing the LC-MS/MS results obtained for fish sauces (Peaks software)

	Garum (Sardine)	*Garum (Mackerel-1)*	*Garum (Mackerel-2)*
Number of MS scans	9298	12963	28642
Number of MS/MS scans	33616	13320	17730
Peptide-Spectrum Matches	11418	2580	2190
Peptide sequences	6676	2284	1789
Protein groups	464	320	102
Proteins	1409	1311	176
Proteins (>2 Unique Peptides)	716	631	101
Missed Cleavages = 0	5159	2010	425
Missed Cleavages = 1	1286	259	581
Missed Cleavages = 2	192	15	474
Missed Cleavages = 3	259	0	243

1. Sardine *Garum* model sauce

For sardines *Garum* sauce, 1409 proteins including 716 proteins with more than 2 unique peptides were successfully identified (Table 5). Among identified proteins, we found cell cytoskeleton proteins, muscle proteins (e.g. tropomyosin, myosin) and blood proteins (e.g. hemoglobin) (Table 6).

Table 6. Example of identified proteins from sardine *Garum* model sauce

Accession	Protein	Coverage %	Peptides	Unique peptides	Average mass Da	Function	Homology to species
229366368	Calmodulin	99	26	7	16939	Cytoplasmic protein	*Anoplomo fimbria*
37903435	Actin	85	106	12	41975	Muscle protein	*Danio rerio*
18859495	Troponin C	83	33	10	18211	Muscle protein	*Danio rerio*
348500102	Tropomyosin alpha-3	68	60	14	32773	Muscle protein	*Oreochromin niloticus*
7678756	Myosin light chain-2	66	23	9	19418	Muscle protein	*Sardinops melanosticus*
348527312	Beta-enolase	65	116	20	47565	Cytoplasmic protein	*Oreochromin niloticus*
221221958	Ribonuclease	58	13	4	14902	Cytoplasmic protein	*Salmo salar*
303657547	Hemoglobin	56	22	2	16112	Blood protein	*Salmo salar*
1644255	Beta-globin	55	23	4	16397	Blood protein	*Cyprinos carpio*

Clupeidae family that regroups sardine and herring species contains only 2274 protein in TrEMBL database, 13 in Swiss-Prot and 36836 in NCBI, majorly identified by sequence homology to other species. For example, troponin C type 2 (>gi|18859495) was identified with 83% sequence homology to *Danio rerio* species, and contains 2 peptides with amino acid substitutions. The sequence alignment against existing database confirms that both peptides are specific to fish species used in sauce preparation (sardine in our case).

As an example, the MS/MS spectrum (Figure 9) of the doubly charged ion at m/z 11180.0439 Da, allows the identification of V<u>F</u>D<u>D</u>NGDGYIDRDEFAEIIR sequence using y fragments (y_1^+- y_{18}^+) and b fragments (b_2^+- b_{19}^+) corresponding to the peptide 103-121 of Troponin C type 2 (sequence homology to *Danio-Rerio*) highlighting the substitution of the second residue, leucine, by phenylalanine and the mutation of the fourth amino acid lysine to aspartic acid. This peptide is not referenced in current databases.
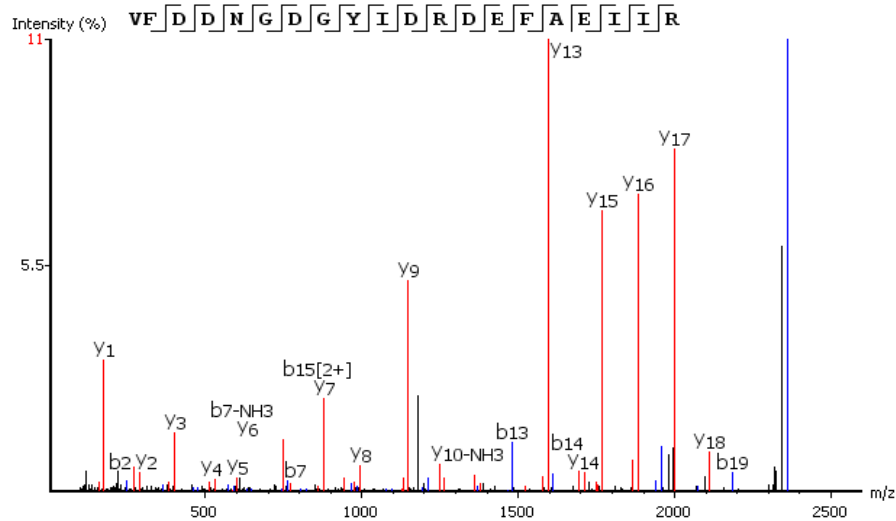
Figure 9. MS/MS spectrum of the doubly charged ion at m/z: 1180.0439 (Δm = 0.3 ppm) presenting y and b fragments of the peptide sequence VFDDNGDGYIDRDEFAEIIR of troponin C protein from hydrolysis extract of sardine *Garum* model sauce.

In the next step, we aimed to validate the species matching between *Garum* sauce and fresh sardine fish (*Sardina pilchardus* species) from the Mediterranean Sea and the Atlantic Ocean. We have found 6 muscle proteins (e.g. myosin heavy chain) and a blood protein (e.g. beta-globin) in both sardine *Garum* sauce and fish represented in Table 7.

After a sequence alignments with BLASTp software, we succeeded to identify 8 peptides markers of *Sardina pilchardus* (Table 7, blue marks). For example, myosin light chain 2 was identified by sequence homology to *Dicentrarchus labrax* in both *Garum* and sardine fish samples. Among the 32 sequenced peptides, 13 peptides were common to many species, 19 peptides were specific to fish species, only a unique specific peptide NLWAAFPPDVTGNVDYK has been found in both fresh sardine and *Garum* sauce (Table 8). This specific peptide is located at the position (142-158) identified by (y_1^+-y_{15}^+) ions and (b_1^+-b_6^+) ions as shown in the MS/MS spectrum (Figure 10).

Figure 10. MS/MS spectrum of the doubly charged ion at m/z 953.971 (Δm= 0.4 ppm) presenting y and b fragments of the peptide sequence NLWAAFPPDVTGNVDYK of myosin light chain 2 from *Garum* and sardine fish samples.Figure 10, highlighting the substitution of the eleventh residue alanine by threonine. We verified that this peptide can be used as a biomarker for sardine fish species present in *Garum* sauce by comparing it with the same protein and the same peptide in *Thunnus thynnus* fish. The peptide NMWAAFPPDVAGNVDYK at the position (140-156) identified by (y_1^+-y_{14}^+) ions and (b_2^+-b_6^+) ions is shown in the MS/MS spectrum Figure 11. The peptides found in *Garum* sauce and sardine differ from the peptide in tuna fish by 2 amino acids; the second amino acid lysine (b_2^+) and the eleventh amino acid threonine (y_6^+-y_7^+) in sardine fish were substituted by methionine and alanine respectively in tuna fish. Moreover, this peptide can be used to discriminate between two different sardine species as *Sardinops melanostictus* known as the Japanese pilchard (sequenced in the public database) and *Sardina pilchardus* known as the European pilchard (our samples), by the replacement of the second asparagine with glutamine (Table 8).
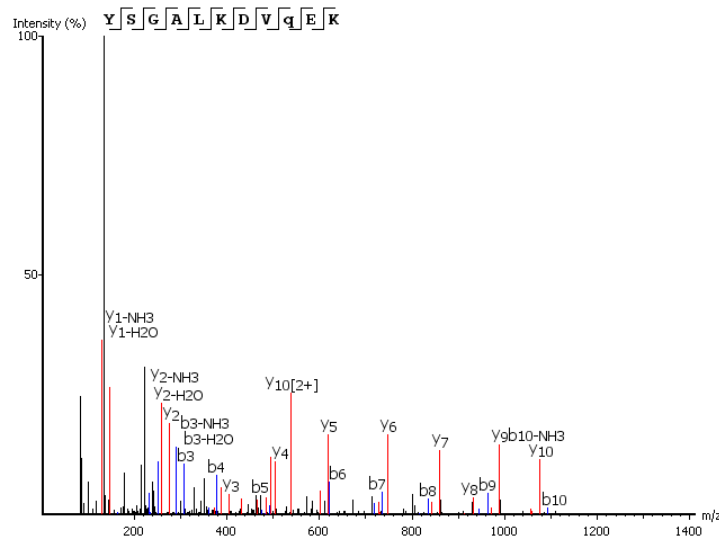

Figure 10. MS/MS spectrum of the doubly charged ion at m/z 953.971 (Δm= 0.4 ppm) presenting y and b fragments of the peptide sequence NLWAAFPPDVTGNVDYK of myosin light chain 2 from *Garum* and sardine fish samples.

Figure 11. MS/MS spectrum of the doubly charged ion at m/z 947.9438 (Δm= 0.6 ppm) presenting y and b fragments of the peptide sequence NMWAAFPPDVAGNVDYK of myosin light chain 2 of *Thunnus thynnus* fish

Table 7. Proteins identified in both sardine *Garum* sauce (G) and sardine fresh fish (F) and peptides with amino acid substitutions showing differences between both samples

Acc[1]	Proteins	Taxonomy	MW[2] (Da)	Coverage %	# Peptides[3]	# Unique[4]	Peptides with A.A substitutions	Position	A.A. substitutions			Exp. mass Z=2	Theo mass Z=1	Δ[5] (ppm)	G[6]	F[7]	O[8]
9971579	Myosin heavy chain	*Pennahia argentata*	221207	31% (G) 37% (F)	131 (G) 106 (F)	5 (G) 3 (F)	IEAQTKPF EAK	25-35	T→I (29)	E→D (33)		631.344	1261.679	1.3	X		
							LLPVLYPP VVEDTNG NK	655-631	D→E (626)	N→G (628)	N→K (630)	623.344 Z=3	1868.0193	1.1	X		
							SAETEKEL ANLK	837-848	L→M (847)			666.854	1332.701	1.1	X	X	
12657354	Myosin heavy chain	*Notothenia coriiceps*	222053	22% (G) 27% (F)	78 (G) 73 (F)	6 (G) 3 (F)	DTEIFAM(ox)[9]NPPK	73-83	A→P (78)			639.805	1278.602	-1.0	X	X	
							SVSDNAY QFM(ox)L QDR	156-169	V→I (157)			845.381	1689.753	0.3	X		X
							GYM(ox)Q NFLVIHQL R	680-692	Y→L (681)			817.927	1634.846	-0.5	X		X
1644255	Beta-globin	*Cyprinus carpio*	16397	55% (G) 26% (F)	23 (G) 4 (F)	4 (G) 2 (F)	LLADNITV C(c)[10]VAM (ox)K	106-118	N→C (110)			488.592 Z=3	1707.856	1.5	X		X

Accession number [1]	Protein	Species	Molecular weight [2]	Coverage	Identified peptides [3]	Unique peptides [4]	Peptide	Position	Mutation	Mutation	Mass	Mass	MS error [5]	Sardine garum sauce [6]	Sardine fish [7]	Other species [8]
317419364	Myosin light chain 2	*Dicentrarchus labrax*	19231	50% (G) 48% (F)	13 (G) 10 (F)	3 (G) 3 (F)	FGPSGFSP DAQEAW (ox)QK	119-134	S→A (125)	A→V (128)	884.339	1767.792	-3.7	X	X	
							NLWAAFP PDVTGNV PYK	142-158	T→A (152)		953.971	1889.962	0.4	X	X	
3668187	Myosin heavy chain	*Gadus chalcogrammus*	146468	23% (G) 32% (F)	63 (G) 57 (F)	5 (G) 7 (F)	SAETEKEL ANLK	844-855	L→M (854)		666.855	1332.701	1.1	X	X	
326678010	Myosin heavy chain, fast skeletal muscle-like	*Danio rerio*	16232	29% (G) 37% (F)	88 (G) 71 (F)	3 (G) 2 (F)	TVKEDEA FPM(ox)NP PK	70-83	A→V (76)		809.893	1618.773	0.1	X	X	
							VTFQLSD ER	275-283	D→A (281)		547.775	1094.548	-3.7	X		X
333108579	Slow skeletal muscle myosin heavy chain	*Siniperca chuatsi*	105985	29% (G) 24% (F)	65 (G) 26 (F)	11 (G) 5 (F)	SVSDNAY QFM(ox)L QDR	157-170	V→I (158)		845.381	1689.783	0.3	X		X
							VTFQVSD ER	275-283	D→A (281)		547.775	1080.532	-3.7	X		X

[1] Accession number. [2] Molecular weight. [3] Number of identified peptides. [4] Number of unique peptides. [5] MS error. [6] Sardine garum sauce. [7] Sardine fish. [8] Other species

Table 8. Myosin peptide (light chain 2) allowing discrimination between various fish species

gi[1]	Proteins	Taxonomy	MW[2] (Da)	Coverage %	# peptides[3]	# Unique[4]	Common peptides with A.A substitution	Position	A.A. substitution	Exp mass Z=2	Theor mass Z=1	Δ[5] (ppm)	Samples
317419364	Myosin light chain 2	*Dicentrarchus labrax*	19231	50%	13	3	NLWAAFPPDVTGNVDYK	142-158	T→A (152)	953.9707	1889.962	0.4	*Garum* sardine
317419364	Myosin light chain 2	*Dicentrarchus labrax*	19231	48%	10	3	NLWAAFPPDVTGNVDYK	142-158	T→A (152)	953.9691	1889.962	-1.2	*Sardina pilchardus*
7678756	Myosin light chain 2	*Sardinops melanostictus*	19418	66%	23	9	NLWAAFPPDVTGQVDYK	140-156	x	x	x	x	Database
68132178	Myosin light chain 2	*Thunnus thynnus*	17284	75%	32	2	NMWAAFPPDVAGNVDYK	140-156	-	947.9438	1905.957	0.6	*Thunnus thynnus*

[1] Accession number. [2] Molecular weight. [3] Number of identified peptides. [4] Number of unique peptides. [5] MS error.

2. **Mackerel-1** *Garum* **model sauce**

The developed methodology was applied on more complex *Garum* sauce prepared from blood and fish Mackerel intestines. In this study, we investigated blood proteins identification due to the lack of muscle proteins in this sample. Following the strategy mentioned previously, 1311 proteins including 631 proteins with more than 2 unique peptides had been identified successfully, among them blood proteins as hemoglobin alpha and beta chain proteins with 34% and 28% sequence coverage respectively, by sequence homology to *Thunnus thynnus*. As mentioned before, only 468 sequenced proteins belonging to Scombrini-Mackerels species were present in TrEMBL database, 6 in Swiss-Prot, and 1741 in NCBI. Identified peptides are IDDLTT<u>M</u>LGDLSELHA<u>S</u>K belonging to hemoglobin alpha chain at the position 76-93 with the substitution of the seventh amino acid glycine by methionine, and the peptide YFGAYGDLST<u>Q</u>DAIK present in hemoglobin beta chain at the position 42-56 with the substitution of eleventh amino-acid proline by glutamine (Figure 12). Those 2 peptides were also identified in *Scomber scombrus* fish by sequence homology to *Thunnus thynnus* indicating that those peptides are species markers (Table 9).
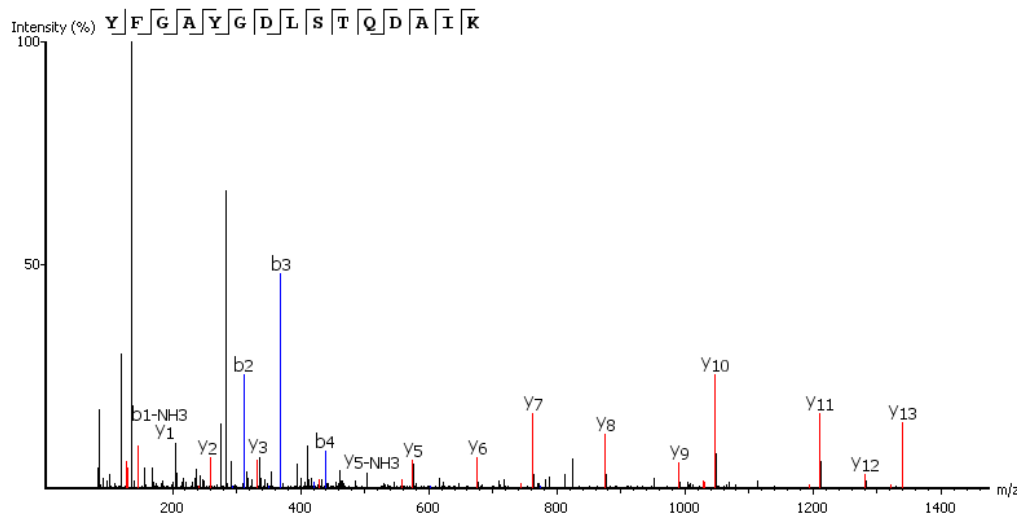
Figure 12. MS/MS spectrum of the doubly charged ion at m/z 824.8960 (Δm= 0.3 ppm) presenting y and b fragments of the peptide sequence YFGAYGDLSTQDAIK of hemoglobin beta chain of *Scomber scombrus* fish

3. Mackerel-2 *Garum* model sauce

We studied also another *Garum* made from *Scomber scombrus*. However, in this sauce fewer number of proteins were detected (only 176 proteins) among which 101 contain more than 2 specific peptides. Proteins from *Garum* mackerel sauce was compared to proteins identified from *Scomber scombrus* fishes. We found tropomyosin protein present in both samples and it was identified with a good coverage (74%) by sequence homology to *Thunnus thynnus* species. We detected 4 species specific peptides with amino substitutions as shown in Table 10.

For example, the specific peptide LEEAEKVADESER is located at the position (113-125) identified by (y_1^+-y_{12}^+) ions and (b_1^+-b_{10}^+) ions as shown in the MS/MS spectrum (Figure 13), representing the substitution of the seventh amino acid alanine by valine deducted from the difference of m/z value between (y_7^+-y_6^+) ions and (b_7^+-$_6^+$) ions.
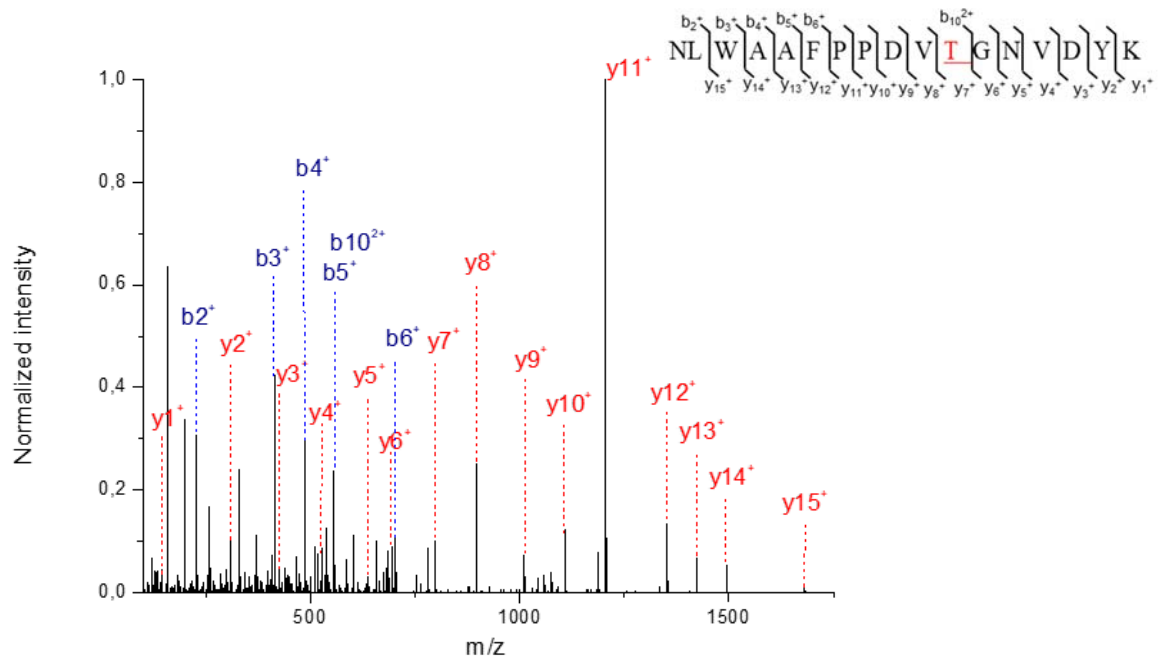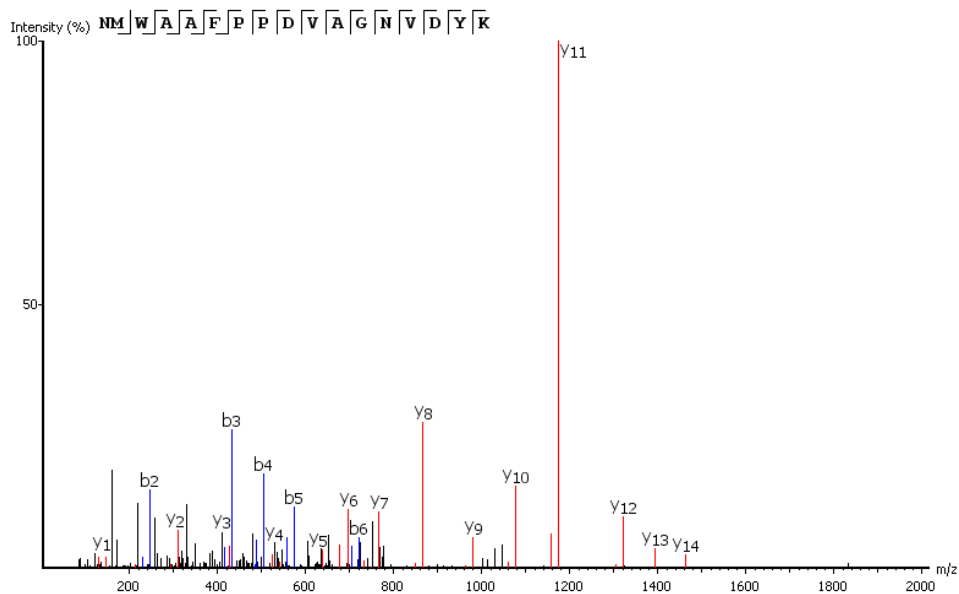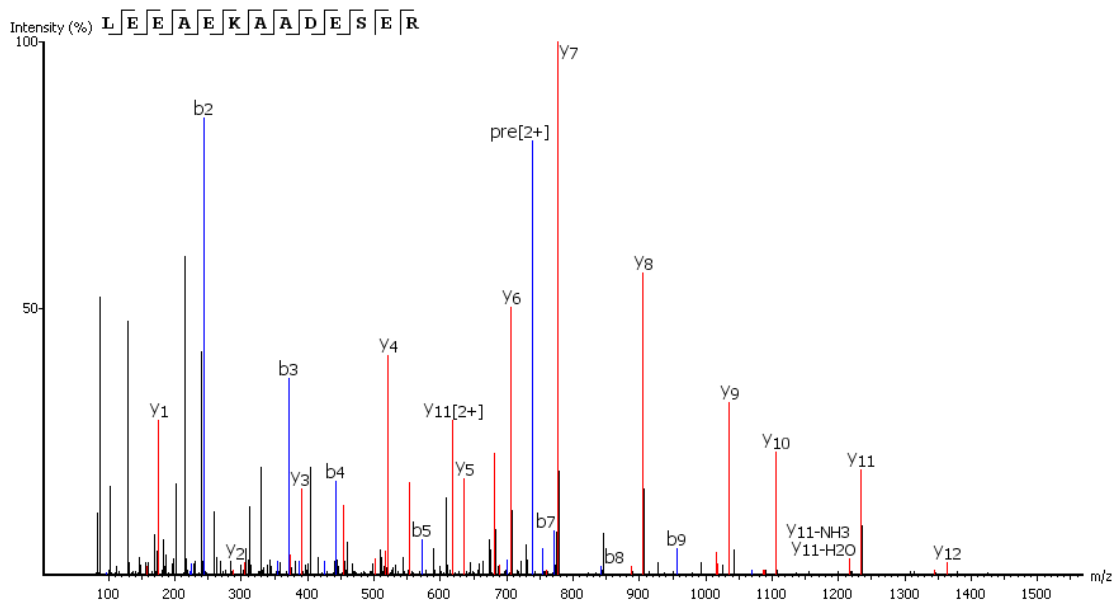

Figure 13. MS/MS spectrum of the doubly charged ion at m/z 738.8475 (Δm= 0.5 ppm) presenting y and b fragments of the peptide sequence LEEAEKVADESER of tropomyosin of *Scomber scombrus* fish

To summarize.

The developed workflow, including proteins extraction, trypsin digestion and data treatment were optimized on model fish sauces which were made from two different fish species (*Scomber scombrus and Sardina pilchardus)*. Due to the lack of fish proteins sequences in proteomic/genomic databases, most of the proteins were identified using sequence homology to other fish species (e.g. *Danio renio*, etc.). *De novo* sequencing allowed the identification of new unsequenced peptides from muscular and blood proteins and several peptides could be used to discriminate the different fish species. On the other hand, Spider algorithms allowed proteins identification by sequence homology to other fish species as well as by the determination of amino acids mutations sites. Furthermore, by comparing the identified *de novo* species specific peptides in model fish sauces samples to their analogues in fish references samples, we were able to determine the exact fish species of sauces samples and to discriminate between the different species as well. This methodology was thus applied on archaeological ceramics belonging to the Dressel 14 amphorae which was carrying fish derivative products, in order to determine the fish species.

Table 9. Common proteins identified in both mackerel-1 *Garum* sauce and *Scomber scombrus* fresh fish

gi[1]	Proteins	Taxonomy	MW[2] (Da)	Coverage %	# peptides [3]	# Unique [4]	Peptides with A.A substitutions	Position	A.A. substitution	Exp. mass Z=2	Theor mass Z=1	Δ[5] (ppm)	G [6]	F [7]	O [8]
23978920	Hemoglobin beta chain	*Thunnus thynnus*	16313	28% (G) 27% (F)	6 (G) 5 (F)	2 (G) 3 (F)	YFGAYGDLSTQ DAIK	42-56	Q→P (52)	824.8 974	1648.7 85	1.4	X	X	
23978926	Hemoglobin alpha chain 1	*Thunnus thynnus*	15563	34% (G) 25% (F)	6 (G) 4 (F)	5 (G) 3 (F)	IDDLTTMLGDL SELHASK	76-93	M→G (82) S→F (92)	653.6 627 z=3	1959.9 77	-0.2	X	X	

Table 10. Common protein identified in both mackerel-2 *Garum* sauce and *Scomber scombrus* fresh fish

gi[1]	Proteins	Taxonomy	MW[2] (Da)	Coverage %	# peptides[3]	# Unique[4]	Peptides with A.A substitution	Position	A.A. substitution	Exp. mass Z=2	Theor mass Z=1	Δ[5] (ppm)	G [6]	F [7]	O [8]
301017128	Tropomyosin	*Thunnus thynnus*	32762	74% (G) 75% (F)	71 (G) 40 (F)	32 (G) 12 (F)	TKQLEDDLVDMQK	36-48	D→A	789.8 870	1562.7 730	0.8	x	x	
							YSGALKDVQ(d)EK	60-70	A→N V→A	619.8 16	1236.3 77	0.3	x	x	
							QATDAEGDVASLNR	77-90	Q→S	482.8 99	1428.4 65	1.1	x	x	
							LEEAEKVADESER	113-125	V→A	725.8 59	1504.7 125	1.2	x	x	

[1] Accession number. [2] Molecular weight. [3] Identified peptides number. [4] Number of unique peptides. [5] MS error. [6] Sardine *Garum* sauce. [7] Sardine fish. [8] Other species

III.   Archaeological sample

The Dressel 14 amphora was obtained from the wreck of the Tiboulen of Maïre, which is located in the bay of Marseille at 49-50 m depth and dated to 116 AD. This wreck has been the subject of several search campaigns since 1977 which allowed to have a clear vision of its cargo. More than 400 amphorae have been documented; their vast majority is composed of oil amphorae type Dr. 20 from Baetica (70%), followed by amphorae containing fish products also from Baetica, type Beltran IIA and IIB (14%) and small batches of wine amphorae Gauloise 4 (4%), Dr. 28 (3%), Dr.2-4 of Tarraconaise (3%). As well, this wreck contained also 4 Dr. 14 amphorae (2%), including the one concerned in our studies.

Dr. 14 amphorae were mainly produced in Lusitania, Portugal, between the first half of the 1st century and the end of the 2nd-early 3rd century AD. They are intended to carry mainly *Liquamen*, of various qualities, as testify the known painted inscriptions.

Until the late 2nd century AD, *Liquamen* appeared as a sauce distinct from that of *Garum*. From the 3rd century AD. After JC, *Liquamen* became the generic name for all kinds of fish sauces. On the tituli picti known on the amphorae, *Liquamen* is described in different ways, i.e. *Flos Excellens*, *Flos primum*, *Primum*, *Flos Flos floris*), *Flos optimum*, *Flos excellens scombri*, *optimum*, *optimum scombri*, which indicate that it was mainly produced from mackerel fish.[123] However, in our case the studied amphora does not contain any inscription.

Figure 14. Archaeological ceramic sample crushed into fine powder

Proteins were extracted from the crushed archaeological ceramics (Figure 14) and then prepared to analysis following the eFASP protocol detailed in the experimental section. The resulting peptides were separated by nanochromatography and analyzed in-line with nanoESI-Orbitrap MS/MS. Raw data generated by Orbitrap were analyzed with Peaks software for proteins identification. Table 11 shows the MS and MS/MS results. The raw data interrogation was done against a database created with the only sequenced fish proteins that recover all fish species present in NCBI database and the data were also compared to our internal databases.

Table 11. Table summarizing the LC-MS/MS results obtained from the archaeological sample (Peaks software)

	Archaeological sample
Number of MS scans	25609
Number of MS/MS scans	33291
Peptide-Spectrum Matches	1721
Peptide sequences	701
Protein groups	39
Proteins	198
Proteins (>2 Unique Peptides)	157
Missed Cleavages = 0	531
Missed Cleavages = 1	152
Missed Cleavages = 2	23
Missed Cleavages = 3	1

Following those analyses, 157 proteins were identified, with 2 or more unique peptides, including muscle tissue proteins, as myosin light chain 1, 2 and 3 with 40%, 68%, 47% coverage respectively and tropomyosin with 61% of coverage (homology to *Thunnus thynnus* species).

In order to identify the species specific peptides of those muscular proteins, two parallel sequences alignments were done for the obtained peptides: the first alignment was done against all the database excluding the Actinopterygii class that regroups ray-finned fishes, and the second was performed only on Actinopterygii database. This study allows the identification of 12 proteins belonging to fishes and consisting of two blood proteins and 10 muscle proteins, among which 4

muscle proteins and a blood protein represent specific peptides for Scombridae family as shown in Table 12.

Despite the fact that, the genome of tuna fish more precisely the pacific bluefin tuna was studied,[124-125] only 3425 sequenced proteins that belong to Scombridae family species are present in TrEMBL database, 68 in Swiss-Prot, and 9736 in NCBI. Considering Clupeidae family, it's respectively 2274, 13 and 36836. Due to the limitation in fish databases, proteins identification by sequence homology to other species was performed. Species specific peptides identified in the archaeological sample were compared to their analogues extracted from fresh fish samples (our internal database).

Table 12. Identified muscular proteins from the archaeological ceramics

gi⁻¹	Proteins	Taxonomy	MW₂ (Da)	Cover age %	# peptid es	# Unique	peptides	Position	Exp mass Z=2	Theor mass Z=1	Δ (ppm)	Fish	*Scombr idae*
90025055	myosin heavy chain	*Dicentrarchus labrax*					QADSVAELGEQIDNLQR	1193-1209	943.467	1885.925	1.2	x	
							GEVDDTVQEAR	1567-1577	609.783	1218.559	0.1	x	
							VQLELNQIK	1558-1566	542.822	1084.636	0.7	x	
							INEM(ox)LDTK	439-446	409.242	979.472	0.3	x	
							DIDDLELTIAK	950-960	623.332	1245.657	0.0	x	
38347761	myosin heavy chain	*Lethenteron camtschaticum*					QADSVAELGEQIDNLQR	1194-1210	943.467	1885.925	1.2	x	
							DIDDLELTIAK	951-961	623.332	1245.657	0.0	x	
							LQGEVEDLM(ox)IDVER	1423-1436	831.406	1661.800	0.5	x	
							NLQQEISDLTEQIGETGK	1506-1523	668.336 z=3	2003.996	0.2	x	
							DAQLHLDDAVR	1654-1664	626.819	1252.628	2.0	x	
							VAEQELVDASER	1703-1714	673.333	1345.659	0.1	x	
							VQHELEEAQER	1901-1911	684.331	1367.655	0.6	x	

7209643	myosin heavy chain	*Seriola dumerili*						QADSVAELGQQIDNLQR	1200-1216	943.4 67	1884.9 41	1.2	x
								LQGEVEDLMIDVER	1425-1438	831.4 06	1645.8 10	0.5	x
								NLQQEISDLTEQIGETGK	1508-1525	668.3 36	2003.9 96	0.2	x
156229670	myosin heavy chain fast skeletal type 1	*Saurida wanieso*						QADSVAELGQQIDNLQR	1197-1213	943.4 673	1884.9 17	1.2	x
								LQGEVEDLMIDVER	1422-1432	832.4 06	1660.7 97	0.5	x
160332467	myosin heavy chain fast skeletal type 3	*Hypophthalmich thys molitrix*						NLTEEMTSQDESLAK	976-990	848.3 91	1694.7 67	0.2	x
								M(ox)EIDDLSSNM(ox)EA VAK	1225-1239	842.8 74	1683.7 33	0.8	x
7678720	myosin light chain 1	*Scombridae: Thunnus thynnus*	213 00	40	11	3		LLGM(ox)PSAEDM(ox) [126] [125 126 127 126 125 127] TNK	98-110	719.8 31	1438.6 55	-0.96		x
								LQTIINSPNK	121-130	564.3 25	1126.6 35	0.6	x
								ALGQNPTNKDVAK	85-97	678.3 68	1354.7 21	1.2	x
								AGYEDYVEGLR	131-141	636.2 99	1270.5 83	0.6	x
7678724	myosin light chain 2	*Scombridae: Thunnus thynnus*	190 00	68	16	4		VLDPDATGTIKK	108-119	419.9 06 z=3	1257.7 049	-0.96		x
								AAAGEGGSSNVF	10-21	533.7 43	1066.4 80	0.4		x
7678	myosin light chain 3		185 00	47	12	6		ALGQNPTNKDVHK	59-71	711.3 79	1421.7 495	0.26		x

	Scombridae				ILGNPTADDM(ox)ANK	72-84	688.3 29	1374.6 45	0.5	x
	Thunnus									
	thynnus				VGDNQVAFNQ	43-52	546.2 59	1090.5 04	0.1	x
348502222	myosin-binding protein C	*Oreochromis niloticus*				SAHPSEYEK	273-281	524.2 42	1046.4 67	2.9	x
23978926	hemoglobin alpha chain 1	*Scombridae* *Thunnus* *thynnus*				SADAIGADALGR	22-33	558.7 85	1115.5 57	0.9	x
						M(ox)LAVYPQTK	34-42	533.7 83	1065.5 53	2.1	x
50513935	hemoglobin beta chain	*Scombridae* *Thunnus* *thynnus*	161 82	22	5	4	ANLNYEDIGPK	16-26	617.3 09	1233.6 109	0.4	x
							GDLSTPDAIK	46-55	508.7 67	1015.5 18	1.2	x
301017128	tropomyosin	*Scombridae:* *Thunnus* *thynnus*	327 00	61	24	10	M(ox)EM(ox)QDVQLK	141-149	577.2 65	11532. 5227	-0.23	x
							SATDAEGDVASLNR	77-90	703.3 31	1405.6 554	0.1	x
							YSGNLKDAQEK	60-70	626.8 11	1252.6 17	-2.00	x

The first evaluation was done against *Sardina pichardus* species that belongs to Clupeidae family. Sardine fish was used for the preparation of *Garum* sauce.[84] Two specific peptides referring to 2 muscular proteins (myosin light chain 1 and 2) were found in both *Sardina pichardus* fish and archaeological sample (Table 13) that show sequence differences. For example, in the archaeological sample, the peptide VLDPDATGTIKK was identified in myosin light chain 2 at the position (108-119) and belongs to *Thunnus thynnus* species. This peptide has also been found in fresh sardine fish, VMDPEGTGAIKK at the position (108-119) corresponding to myosin light chain 2 protein of *Sparus aurata* species (sequence homology) (Figure 15). These 2 peptides are differing by 4 amino acids resulting in a similarity of 67%. Lysine, second aspartate, alanine and the second threonine in the peptide of *Thunnus thynnus* are replaced by methionine, glutamate, glycine and alannine in the peptide found in fresh sardine fish.

Figure 15. Above the MS/MS spectrum of the triply charged ion at m/z 419.9064 (Δm= 0.1 ppm) presenting y and b fragments of the peptide sequence VLDPADATGTIKK of myosin light chain 2 of *Thunnus thynnus* fish species from the archaeological sample, and below the MS/MS spectrum of 2+ ion at m/z 559.2809 (Δm= 1.1 ppm) presenting y and b fragments of the peptide sequence VMDPEGTGAIKK of myosin light chain 2 of *Sardina pilchardus* fish species

Table 13. Common protein identified in both archaeological sample and Sardine fresh fish

gi[1]	Proteins	Taxonomy	MW[2] (Da)	Coverage %	# peptides [3]	# Unique [4]	Common peptides with A.A substitution	Position	Exp mass Z=2	Theor mass Z=1	Δ[5] (ppm)	sample
7678720	myosin light chain 1	*Scombridae: Thunnus thynnus*	21300	40	11	3	LLGM(ox)PSAED M(ox)TNK	98-110	719.831	1438.655	-0.96	Archaeological sample
7678752	myosin light chain 1	*Sardinops melanostictus*	21837	88	27	19	HILGNPST(P)ED MT(A)GK	97-110	750.3614	1498.698	0.3	*Sardina pichardus*
7678724	myosin light chain 2	*Scombridae: Thunnus thynnus*	19000	68	16	4	VLDPDATGTIKK	108-119	419.906 z=3	1257.7049	-0.96	Archaeological sample
5852838	myosin light chain 2	*Sparus aurata*	19079	63	31	9	VM(L)DPEG(A)TG AIKK	108-119	415.880 z=3	19079	0.9	*Sardina pichardus*

[1] Accession number. [2] Molecular weight. [3] Identified peptides number. [4] Number of unique peptides. [5] MS error

The following focus was given to *Scomber* genus and *Thunnus* genus (Scombridae family). Among the identified proteins in the archaeological sample only myosin light chain 1 and 3 proteins have been sequenced for *Scomber japonicus* in the public database. De novo peptides from the archaeological sample were searched against existing database of *Scomber* and *de novo* sequenced proteins from our *Scomber scombrus* fish, we found 7 peptides illustrating the difference between *Thunnus thynnus* species present in the archaeological sample and the mackerel fish (Table 14).

For example, myosin light chain 2 presents a specific peptide allowing species discrimination between the two samples. VLDPDATGTIKK is a specific peptide belonging to myosin light chain 2 at the position (108-119) (*Thunnus thynnus)* fish species found in the archaeological sample. The same peptide (VLDP<u>E</u>A(subG)TG<u>S</u>IK) at the position (107-117) was extracted from mackerel fish and identified by sequence homology to *Decapterus maruads* species, with a glycine substituted by an alanine. The difference between the two peptides is highlighted by the second aspartate and the second threonine present in the peptide extracted from the archaeological sample were replaced by a glutamate and a serine in the peptide from mackerel fish (Figure 16).

In another example, the peptide SG<u>N</u>LKD<u>A</u>QEK located at the position 61-70 of tropomyosin protein recovered from the amphora has been identified by homology to *Thunnus thynnus* species. This peptide differs from its analogue YSGA(subN)LKD<u>V</u>(subA)Q(d)EK located at the position 60-70 of tropomyosin protein extracted from mackerel fish and identified by sequence homology to *Thunnus thynnus* species. This peptide highlights the substitution of the first asparagine by an alanine and the substitution of the alanine by a valine in the case of *Scomber scombrus* fish (Figure 17). This peptide represents another example of the comparison between peptides from the archaeological sample and *de novo* sequenced peptides from *Scomber scombrus* fish sample. After this study, we have deduced that extracted proteins from the archaeological sample differ from proteins of *Scomber scombrus* species; however they may belong to Scombridae family. We limited our research to Thunnini tribe and more specifically to genera that live in Mediterranean and Atlantic coasts near to Spain and Portugal, such as *Auxis, Euthynnus* and *Thunnus* genera.
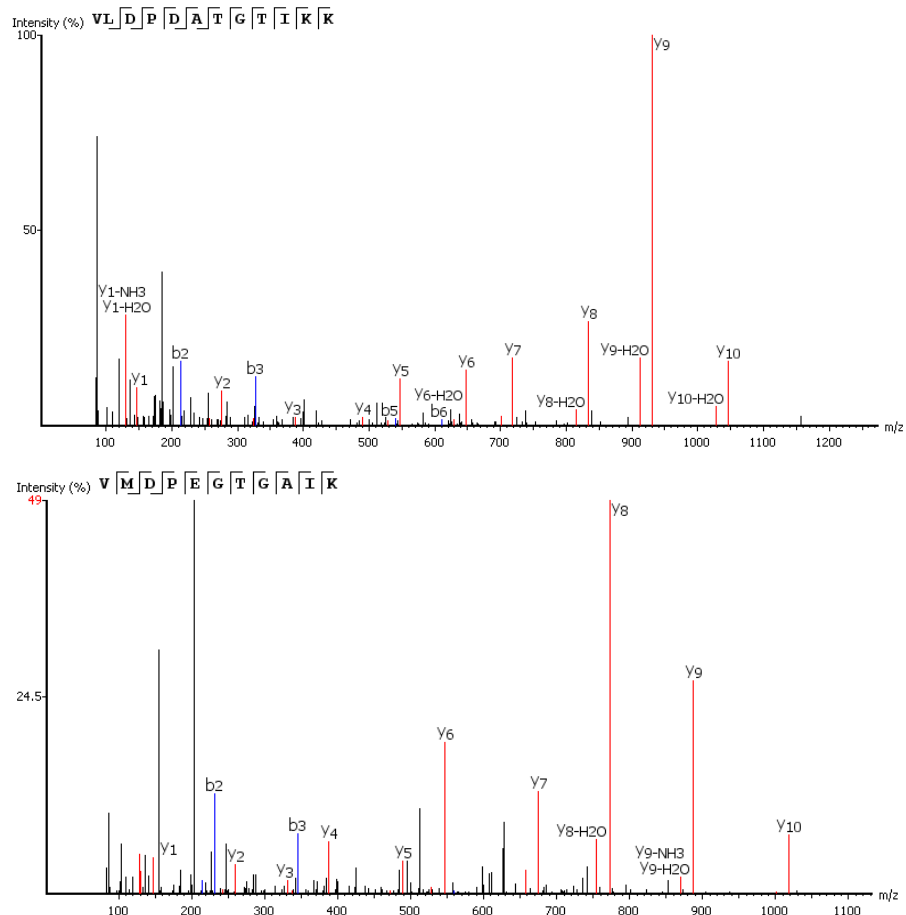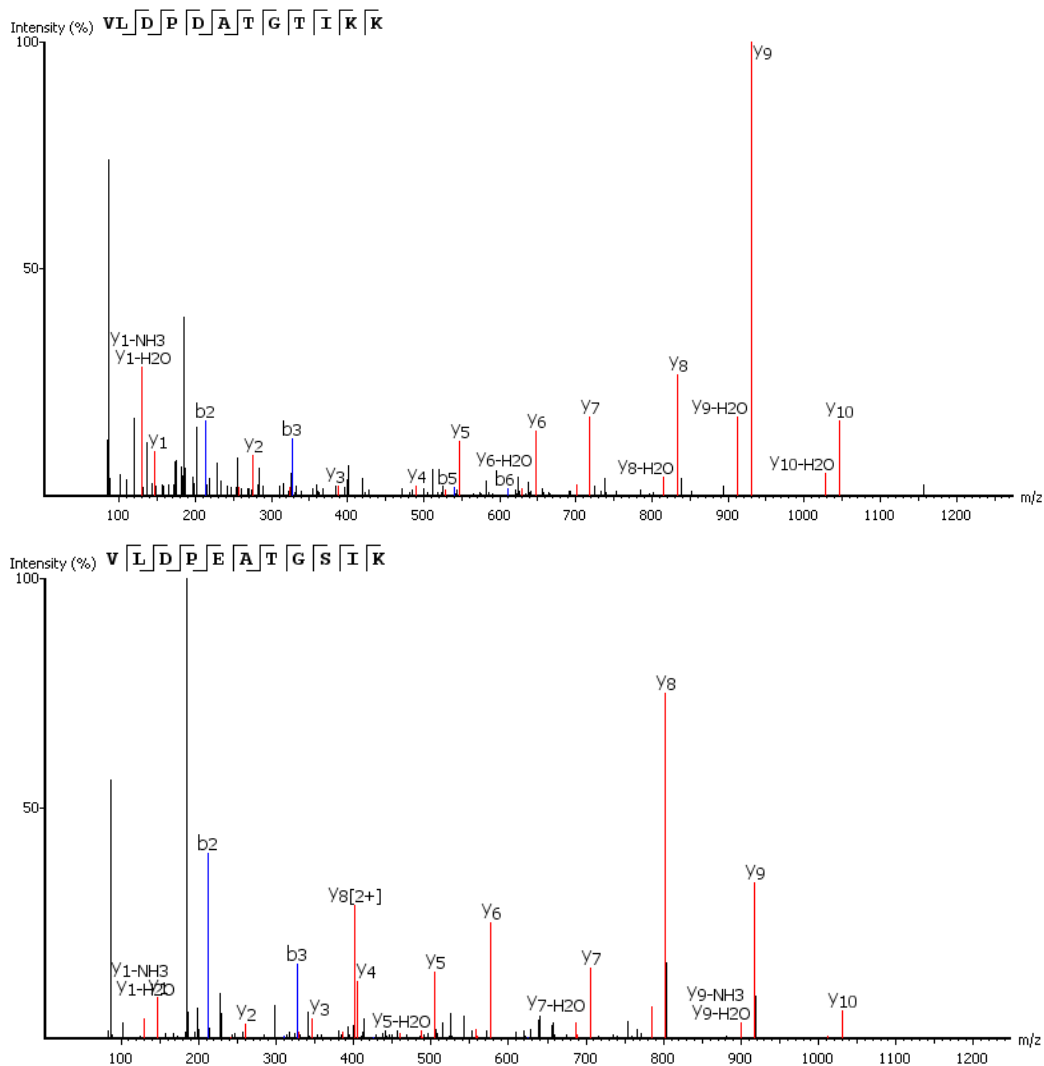
Figure 16. MS/MS spectrum of the triply charged ion at m/z 419.9064 (Δm= 0.1 ppm) presenting y and b fragments of the peptide sequence VLDPADATGTIKK of myosin light chain 2 of *Thunnus thynnus* fish species (full homology) from the archaeological sample, and below the MS/MS spectrum of the doubly charged ion at m/z 565.309 (Δm= 0.7 ppm) presenting y and b fragments of the peptide sequence VLDPEATGSIK of myosin light chain 2 of *Scomber scombrus* fish species
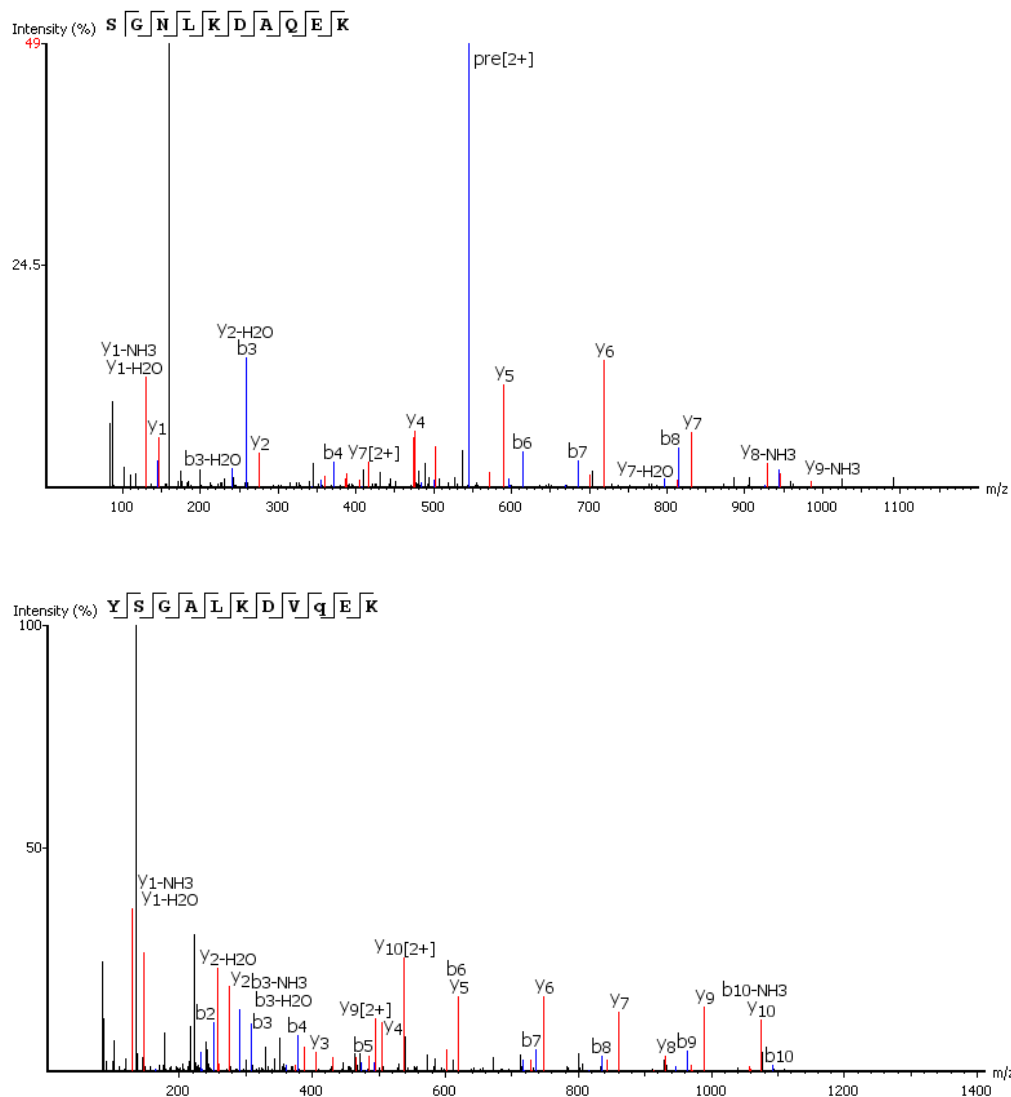
Figure 17. MS/MS spectrum of the doubly charged ion at m/z 545.280 (Δm= 0.4 ppm) presenting y and b fragments of the peptide sequence SGNLKDAQEK of tropomyosin of *Thunnus thynnus* fish species (full homology) from archaeological sample, and below the MS/MS spectrum of the doubly charged ion at m/z 619.816 (Δm= 0.3 ppm) presenting y and b fragments of the peptide sequence YSGALKDVQEK specific to tropomyosin of *Scomber scombrus* fish species

Table 14. Common protein identified in both archaeological sample and mackerel fresh fish and peptides showing amino acid substitutions.

gi[1]	Proteins	Taxonomy	MW[2] (Da)	Coverage %	# peptides[3]	# Unique[4]	Common peptides with A.A substitutions	Position	Exp mass Z=2	Theor mass Z=1	Δ[5] (ppm)	samples
50513935	hemoglobin beta chain	*Scombridae Thunnus thynnus*	16182	22	5	4	GDLSTPDAIK	47-56	508.767	1015.518	1.2	Archaeological sample
23978920	hemoglobin beta chain	*Thunnus thynnus*	16313	7	5	3	YFGAYGDLSTQ(sub P)DAIK	42-56	824.8974	1648.769	0.3	Mackerel fish (*Scomber scombrus*)
7678720	myosin light chain 1	*Scombridae: Thunnus thynnus*	21300	40	11	3	LLGM(ox)PSAEDM(ox)TNK	98-110	719.831	1438.655	-0.96	Archaeological sample
16117365	myosin light chain 1	*Scomber japonicus*	-	-	-	-	LLGNPSADDMNSK	98-110	-	1361.635	-	*Scomber japonicus* NCBI Database
7678724	myosin light chain 2	*Scombridae: Thunnus thynnus*	19000	68	16	4	VLDPDATGTIKK	108-119	419.906 z=3	1257.7049	-0.96	Archaeological sample
16117359	myosin light chain 2	*Decapterus maruads*	18991	95	27	2	VLDPEA(subG)TGSIK	107-117	565.309	1129.258	0.7	Mackerel fish (*Scomber scombrus*)
7678722	myosin light chain 3	*Scombridae: Thunnus thynnus*	18556	47%	12	6	ALGQNPTNKDVHK	59-71	711.379	1421.7495	0.26	Archaeological sample

[1]			[2]		[3]	[4]					[5]	
16117367	Myosin light chain 3	*Scomber japonicus*	18398	63%	21	12	ALGQNPTNKDVHA	59-71	455.5 684 z=3	1364.6 917	0.7	*Garum* (Mackerel)
7678722	Myosin light chain 3	*Thunnus Thunnus*	18556	47%	12	6	QVDTFQK-GTYDDYVEGLR	97-114	443.2 243 ——— 644.2 941	865.44 1 1287.5 85	0 -3.3	Archaeological sample
16117367	Myosin light chain 3	*Scomber japonicus*	18398	63%	21	12	TVDTYPKGTYDDYVEGLR	97-114	698.0 01 Z=3	2092.9 90	1.1	*Garum* (Mackerel)
301017128	tropomyosin	*Scombridae: Thunnus thynnus*	32700	61	24	10	SGNLKDAQEK	61-70	545.2 806	1089.5 54	0.4	Archaeological sample
301017128	tropomyosin	*Scombridae: Thunnus thynnus*	32762	75	40	12	YSGA(subN)LKDV(subA)Q(d)EK	60-70	619.8 16	1236.3 77	0.3	Mackerel fish (*Scomber scombrus*)
301017128	tropomyosin	*Scombridae: Thunnus thynnus*	32700	61	24	10	SATDAEGDVASLNR	77-90	703.3 31	1405.6 554	0.1	Archaeological sample
301017128	tropomyosin	*Scombridae: Thunnus thynnus*	32762	75	40	12	Q(subS)ATDAEGDVASLNR	77-90	482.8 99	1428.4 65	1.1	Mackerel fish (*Scomber scombrus*)

[1] Accession number. [2] Molecular weight. [3] Identified peptides number. [4] Number of unique peptides. [5] MS error.

We extracted and analyzed proteins from *Thunnus* genus (*Thunnus Thynnus* and *Thunnus alalunga* species), *Auxis* genus (*Auxis thazard*) and *Euthynnus* genus (*Euthynnus alletteratus*).

We compared the identified proteins from these fish species with proteins recovered from the archaeological sample. The peptide YSG<u>N</u>LKDAQEK at the position 60-70 of tropomyosin in the archaeological sample showed to differ between different *Thunnini* species and other fish species studied in this work, e.g. *Auxis thazard* and *Euthynnus alletteratus* (Table 15 & Table 16) but also *Scomber scombrus* discussed previously (underlined in the Figure 18). MS/MS spectra presented in the Figure 20 show (i) similar sequence for archaeological sample and *Thunnus alalunga* species (spectrum not shown for *Thunnus thynnus* species as the sequence is referenced in database) and (ii) dissimilarities with *Auxis thazard* species (YSG<u>A</u>(subN)LKDAQEK, position 60-70) and *Euthynnus alletteratus* species (YSG<u>A</u>(subN)LKDAQEKLEVAEK, position 60-76) for which a substitution of asparagine by alanine was identified using fragment ions b_4^+ to b_{10}^+ and y_8^+ to y_{10}^+ for *Auxis thazard* and y_{14}^+ to y_{16}^+ for *Euthynnus alletteratus* (sequence homology to *Thunnus thynnus* species). Truncated forms of the peptide YSG<u>N</u>LKDAQEK was also found in the archaeological sample; i.e. the spectrum corresponding to SG<u>N</u>LKDAQEK sequence is shown on the Figure 21. It can be mentioned that truncated forms of peptides (C-terminus side) were identified for several proteins identified in the archaeological samples (not in our fresh model samples).

>Analyzed sample: Archaeological sample
>gi|301017128|dbj|BAJ11924.1| tropomyosin [*Thunnus thynnus*]
MEAIKKKMQM LKLDKENALD RAEQSESDKK AAEDRTKQLE DDLVAMQKRL KGTEDELEKY SGNLKDAQEK
LEVAEKSATD AEGDVASLNR RIQLVEEELD RAQERLATAL TKLEEAEKAA DESERGMKVI ENRNMKDEEK
MEMQDVQLKE AKNIAEEADR KYEEVARKLV VIESDLERTE ERAELSESKC SELEEESKTV TNNLKSLEAQ
AEKYTQKEDK YEEEIKVLTD KLKEAETRAE FAERSVAKLE KTIDDLEDEL YAQKQKFKSI SEELDHALND MTSI

> Analyzed sample: *Thunnus alalunga*
>gi|301017128|dbj|BAJ11924.1| tropomyosin [*Thunnus thynnus*]
MEAIKKKMQM LKLDKENALD RAEQSESDKK AAEDRTKQLE DDLVAMQKRL KGTEDELEKY SGNLKDAQEK
LEVAEKSATD AEGDVASLNR RIQLVEEELD RAQERLATAL TKLEEAEKAA DESERGMKVI ENRNMKDEEK
MEMQDVQLKE AKNIAEEADR KYEEVARKLV VIESDLERTE ERAELSESKC SELEEESKTV TNNLKSLEAQ
AEKYTQKEDK YEEEIKVLTD KLKEAETRAE FAERSVAKLE KTIDDLEDEL YAQKQKFKSI SEELDHALND MTSI

> Analyzed sample: *Thunnus thynnus*
>gi|301017128|dbj|BAJ11924.1| tropomyosin [*Thunnus thynnus*]
MEAIKKKMQM LKLDKENALD RAEQSESDKK AAEDRTKQLE DDLVAMQKRL KGTEDELEKY SGNLKDAQEK
LEVAEKSATD AEGDVASLNR RIQLVEEELD RAQERLATAL TKLEEAEKAA DESERGMKVI ENRNMKDEEK
MEMQDVQLKE AKNIAEEADR KYEEVARKLV VIESDLERTE ERAELSESKC SELEEESKTV TNNLKSLEAQ
AEKYTQKEDK YEEEIKVLTD KLKEAETRAE FAERSVAKLE KTIDDLEDEL YAQKQKFKSI SEELDHALND MTSI

> Analyzed sample: *Scomber Scombrus*
>gi|301017128|dbj|BAJ11924.1| tropomyosin [Thunnus thynnus]
MEAIKKKMQM LKLDKENALD RAEQSESDKK AAEDRTKQLE DDLV**D**MQKRL KGTEDELEKY SG**A**LKD**V**QEK
LEVAEK**Q**ATD AEGDVASLNR RIQLVEEELD RAQERLATAL TKLEEAEK**V**A DESERGMKVI ENRNMKDEEK
MEMQDVQLKE AKNIAEEADR KYEEVARKLV VIESDLERTE ERAELSE**T**KC SELEEESKTV TNNLKSLEAQ
AEKYTQKEDK YEEEIKVLTD KLKEAETRAE FAERSVAKLE KTIDDLEDEL YAQKQKFKSI SEELDHALND MTSI

> Analyzed sample: *Auxis thazard*
>gi|301017128|dbj|BAJ11924.1| tropomyosin [Thunnus thynnus]
MEAIKKKMQM LKLDKENALD RAEQSESDKK AAEDRTKQLE DDLVAMQKRL KGTEDELEKY SG**A**LKDAQEK
LEVAEKSATD AEGDVASLNR RIQLVEEELD RAQERLATAL TKLEEAEKAA DESERGMKVI ENRNMKDEEK
MEMQDVQLKE AKNIAEEADR KYEEVARKLV VIESDLERTE ERAELSESKC SELEEESKTV TNNLKSLEAQ
AEKYTQKEDK YEEEIKVLTD KLKEAETRAE FAERSVAKLE KTIDDLEDEL YAQKQKFKSI SEELDHALND MTSI

> Analyzed sample: *Euthynnus alletteratus*
>gi|301017128|dbj|BAJ11924.1| tropomyosin [*Thunnus thynnus*]
MEAIKKKMQM LKLDKENALD RAEQSESDKK AAEDRTKQLE DDLVAMQKRL KGTEDELEKY SG**A**LKDAQEK
LEVAEKSATD AEGDVASLNR RIQLVEEELD RAQERLATAL TKLEEAEKAA DESERGMKVI ENRNMKDEEK
MEMQDVQLKE AKNIAEEADR KYEEVARKLV VIESDLERTE ERAELSESKC SELEEESKTV TNNLKSLEAQ
AEKYTQKEDK YEEEIKVLTD KLKEAETRAE FAERSVAKLE KTIDDLEDEL YAQKQKFKSI SEELDHALND MTSI

Figure 18. Sequences of tropomyosin identified in several of the studied samples. The peptides underlined in yellow were identified in our spectra. The amino acids in red are showing substitutions from one species versus another. The peptide underlined is discussed in this paragraph.

4. Phylogenetic study

Based on tropomyosin identification results, a phylogenetic study was performed to observe the divergence of tropomyosin protein between the archaeological sample and the analyzed samples from different species of *Scombridae* family (Figure 19) using the online tool "phylogeny".[127] First, the protein sequences of tropomyosin were aligned with the MUSCLE 3.7 (MUltiple Sequence

Comparison by Log-Expectation) tool. Then PhyML 3.0 tool, which is a phylogeny software based on the maximum similarity principle, processed the input data. It calculates the similarity between sequences (and evaluates a hypothesis on the history of evolution in terms of probability). Then the phylogenetic tree was created using TreeDyn 198.3.
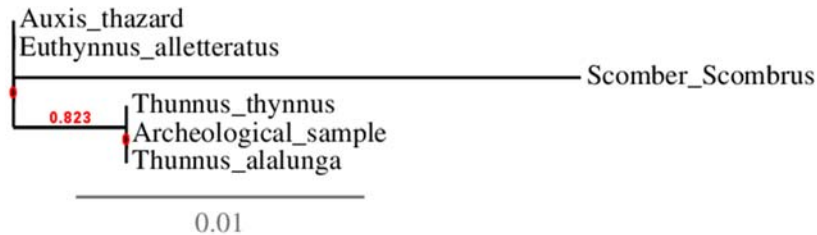
Figure 19. Phylogeny of the sequences of tropomyosin protein between the archaeological sample and *Scombridae* fish samples obtained using tools from the site http://phylogeny.lirmm.fr/phylo_cgi/index.cgi

As observed in Figure 19, the tropomyosin sequence shows similarities between *Thunnus* genera and the archaeological sample and differs from *Auxis thazard* and *Euthynnus alletteratus* species. It can be also pointed out here the difference between the tropomyosin from the amphora and that from *Scomber scombrus*. These results were already pointed out in the previous paragraph.

To summarize,

This study concludes that muscle proteins identified in the archaeological sample differ in their sequences from proteins of *Sardina pichardus* (*Clupeidae*) and *Scomber scombrus* (*Scombridae*); these species were initially suspected to be present in the sample. The detected traces of proteins tends to be attributed to *Thunnus* genus, excluding *Auxis thazard* and *Euthynnus alletteratus* species in favor to *Thunnus thynnus* and *Thunnus alalunga*; however, this last result has to be taken with caution because it is based on a unique informative peptide.

76

A
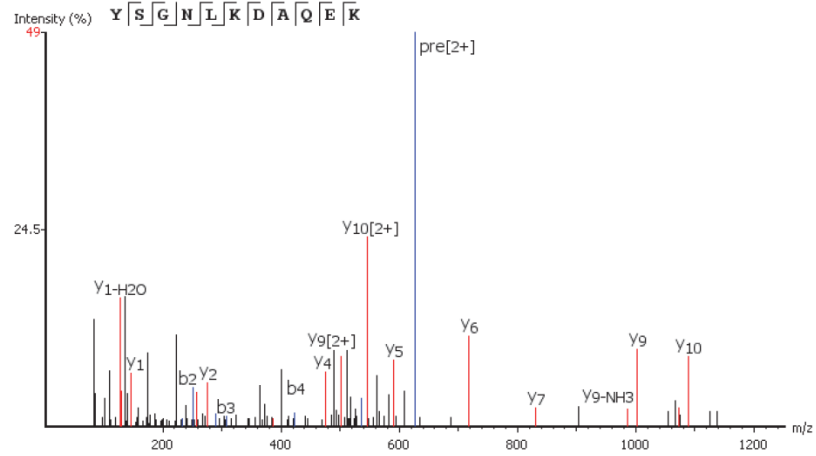
B
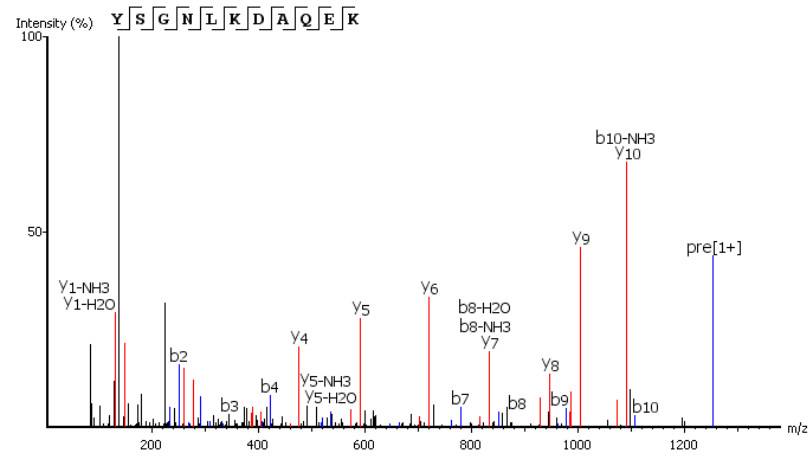
C
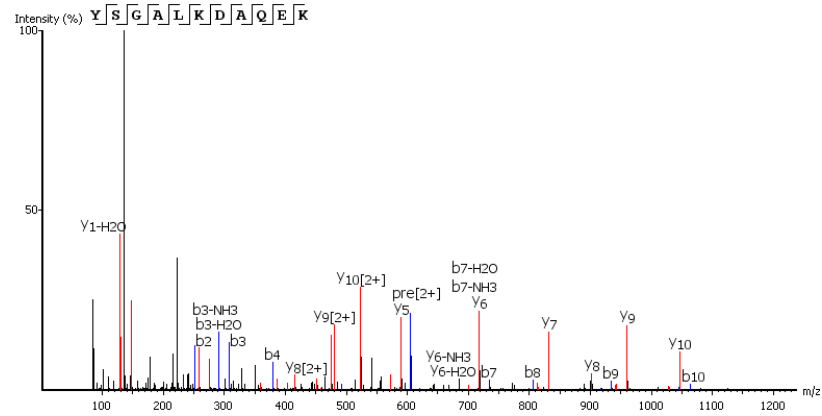
D
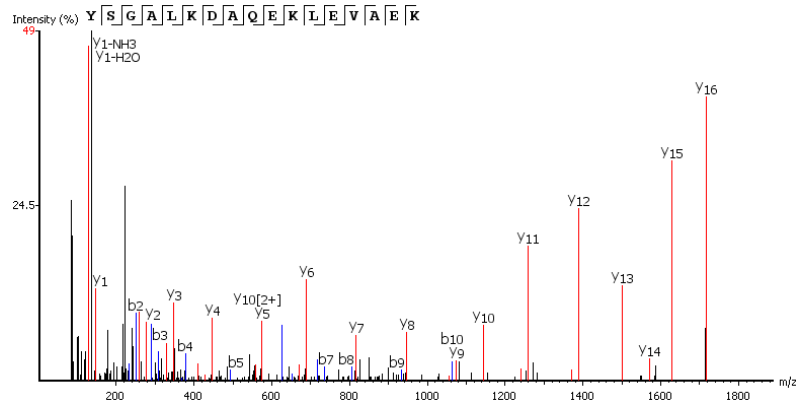
Figure 20. (A) MS/MS spectrum of the doubly charged ion at m/z 545.280 (Δm= 0.4 ppm) presenting y and b fragments of the peptide sequence YSGNLKDAQEK of tropomyosin of *Thunnus thynnus* fish species (full homology) from the archaeological sample, (B) MS/MS spectrum of the doubly charged ion at m/z 626.811 (Δm= 2.5 ppm) presenting y and b fragments of the peptide sequence YSGNLKDAQEK of tropomyosin of *Thunnus thynnus* fish species (full homology) from *Thunnus alalunga* sample; (C) MS/MS spectrum of the doubly charged ion at m/z 605.308 (Δm= 1.6 ppm) presenting y and b fragments of the peptide sequence YSGALKDAQEK of tropomyosin of *Auxis thazard* fish species and (D) MS/MS spectrum of the triply charged ion at m/z 626.999 (Δm= 1.4 ppm) presenting y and b fragments of the peptide sequence YS-GALKDAQEKLEVAEK of tropomyosin of *Euthynnus alletteratus* fish species
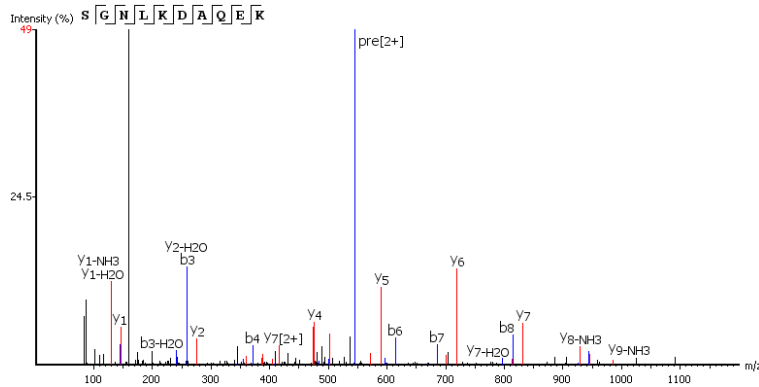
Figure 21. MS/MS spectrum of the doubly charged ion at m/z 545.280 (Δm= 0.4 ppm) presenting y and b fragments of the truncated sequence SGNLKDAQEK of tropomyosin from the archeological sample (sequence homology to *Thunnus thynnus* fish species)

.

Table 15. Common protein identified in both archaeological sample and *Auxis thazard* fresh fish

gi[1]	Proteins	Taxonomy	MW[2] (Da)	Coverage %	# peptides[3]	# Unique[4]	Common peptides with A.A substitution	Position	Exp mass Z=2	Theor mass Z=1	Δ[5] (ppm)	sample
301017128	tropomyosin	*Scombridae: Thunnus thynnus*	32700	61	24	10	YSG<u>N</u>LKD<u>A</u>QEK	60-70	626.811	1252.617	2.5	Archaeological sample
301017128	tropomyosin	*Scombridae: Thunnus thynnus*	32762	75	40	12	YSG<u>A</u>(subN)LKDAQEK	60-70	605.308	1209.303	1.6	*Auxis thazard*

[1] Accession number. [2] Molecular weight. [3] Identified peptides number. [4] Number of unique peptides. [5] MS error

Table 16. Common protein identified in both archaeological sample and *Euthynnus alletteratus* fresh fish

gi[1]	Proteins	Taxonomy	MW[2] (Da)	Coverage %	# peptides[3]	# Unique[4]	Common peptides with A.A substitution	Position	Exp mass Z=2	Theor mass Z=1	Δ[5] (ppm)	sample
301017128	tropomyosin	*Scombridae: Thunnus thynnus*	32700	61	24	10	YSG<u>N</u>LKD<u>A</u>QEK	60-70	626.811	1252.617	2.5	Archaeological sample
301017128	tropomyosin	*Scombridae: Thunnus thynnus*	32762	75	40	12	YSG<u>A</u>(subN)LKDAQEKLEVAEK	60-76	626.999 z=3	1209.303	1.6	*Euthynnus alletteratus*

[1] Accession number. [2] Molecular weight. [3] Identified peptides number. [4] Number of unique peptides. [5] MS error

Conclusion

A strategy based on proteomics was established for fish species authentication from traces of fish products trapped into archaeological ceramics preserved in unfavorable context. The developed workflow, including protein extraction, trypsin digestion and data treatment were first optimized on model fish sauces. Due to the lack of fish protein sequences in proteomic/genomic databases, we build our own proteins database from 8 different fish species that were suspected to be used in fish sauces preparation during the Roman era. Most of the proteins were identified using sequence homology to other sequenced fish species (e.g. *Danio renio*, etc.). *De novo* sequencing allowed the identification of new unsequenced peptides from muscular and blood proteins and several peptides could be used to discriminate different fish species.

To summarize, 157 proteins (≥ 2 unique peptides) were identified in the archeological sample among them 10 muscle proteins and 2 blood proteins with fish specific peptides obtained from 1721 peptides-spectrum matches and 707 peptides sequences. Considering the 10 muscle proteins identified, 32 peptides were specific for fish among 377 peptides-spectrum matches and 7 for *Scombridae*. Considering the 2 blood proteins, 4 specific peptides for fish were identified among 7 peptides in total and 2 were specific for *Scombridae*.

Considering peptides allowing the discrimination between the fish species contained in archaeological sample and our fish references (and/or public databases): 2 peptides were used considering *Sardina pichardus*, 6 peptides considering *Scomber scombrus*, 1 peptide considering *Auxis thazard* & *Euthynnus alletteratus*, and in the current state of databases (and considering our analytical results), no peptide of archaeological sample showed dissimilarity with *Thunnus thynnus* and *Thunnus allalunga*.

Our study showed that several fish species were (suprinsingly) not constitutive of the studied samples such as *Sardina pichardus* and *Scomber scombrus* (respectively Clupeidae and Scombridae families) which were suspected by historic sources. Considering the Scombridae family and several selected fish species (genera that live in Mediterranean and Atlantic coasts near near Spain and Portugal), the trace of proteins identified in the archaeological sample excluded the *Auxis thazard* and *Euthynnus alletteratus* species and showed similarities with *Thunnus thynnus* and *Thunnus allalunga* species (via a muscle protein, the tropomyosin) indicating thus a receipe similar to a *Garum sociorum* sauce.[121]. However this result focusing to these 2 Thunnus species have to be taken with caution considering the important lack of fish databases and the trace level of organic component detected in the amphorae.

Materials and Methods

I.   Proteins extraction from fish

Our fish samples were washed with distilled water and then 50 mg of fish muscles were inserted to a tube containing metal beads and 1 ml of buffer solution made with 6M urea, 100 mM Ammonium Bicarbonates (ABC) pH 8.8, DTT (1.4-dithiothreitol) 50 μm, 0.1% DCA (deoxycholic acid), 4% SDS (sodium dodecyl sulfate), 2% CHAPS (3-[(3-cholamidopropyl)dimethylammonio]-1-propanesulfonate) and stirred for 60 sec, on the BeadBug system. Then our samples were incubated for 2 hours at 4 ° C with stirring. In the next step, the proteins were delipidated, by taking 200 μl of sample and adding 200 μl of chloroform, 400 μl of methanol and 300 μl of H2O, then the mixture was stirred for 30 minutes. The upper phase was removed and the chloroform phase and the protein pellet were kept in the tube. After this, 50 μl of methanol were added, the mixture was agitated and centrifuged for 20 min at 13000 rpm to eliminate the liquid phase without touching the formed pellet. At the end, the pellet is dissolved with 150 μl of 8 M urea, 100 mM ABC pH 8.8, and the mixture was stirred for 2 h at room temperature.

Archaeological sample

The archaeological sample is a piece of ceramic belonging to an analyzed amphora type Dressel 14 found in a shipwreck (Tiboulen wreck of Maïre), which is located in the harbor of Marseille by 49-50 m of depth and dating from 116 AD.

Figure 22. Shipwreck location

50 mg of the archaeological sample were ground in a mortar frosted glass. Then obtained powder were placed in 100 μL of eFASP lysis buffer (8 M urea, 4% SDS, 0.2% DCA, 50 mM DTT, 100

mM ammonium bicarbonate pH 8.8) to perform the bottom-up analysis, then the mixture was stirred at 4 ° C overnight.

II.   Digestion eFASP With Passivated Ultra filtration Unit

UF filters from Microcon UF units (YM-3 3 kDa cutoff limit; Millipore, Billerica, MA) were incubated overnight with 5% v/v TWEEN-20 (T20, Sigma-Aldrich P7949). Following incubation, the filter units were rinsed thoroughly by three immersions in MS-grade water. eFASP digestion[42-43] was realized on 50 µl of *Garum* sauce or 50 mg of archaeological sample. These samples were mixed in 50 µL of solubilizing and reducing buffer A (4% SDS, 0.2 % DCA, 50 mM DTT, 200 mM ABC) overnight at 4°C. Samples were centrifuged at 13,000 g at 20°C for 15 min. Supernatants were mixed with 200 µL of SDS exchange buffer (8 M urea, 0.2 % DCA, 100 mM ABC, pH 8) and were transferred into Microcon UF units (YM-3 3 kDa cutoff limit; Millipore, Billerica, MA). After 30 min of centrifugation at 13000 rpm, the filtrate was discarded, an additional 200 µL of exchange buffer A was deposited in each unit, and centrifugation resumed for 30 more minutes. This buffer addition/centrifugation step was repeated twice more. The reduced proteins were alkylated within the filter unit by adding alkylation buffer A (8 M urea, 50 mM iodoacetamide, and 100 mM ABC, pH 8) and incubating at 37°C for 1 h with shaking in the dark. After 30 min of centrifugation at 13000 rpm, the filtrate was discarded, an additional 200 µL of exchange buffer A was deposited in each unit, and centrifugation resumed for 30 more minutes. This buffer addition/centrifugation step was repeated one more. After three exchanges with eFASP digestion buffer (50 mM ABC, 0.2% DCA pH 8) were performed. eFASP digestion buffer (100 µL) was added to each UF device, followed by 1 µg of trypsin (1:50 w/w). Digestion proceeded for 16 h at 37°C. Peptides were recovered by transferring the UF filter to a new collection tube and spinning at 13000 rpm for 20 min. To complete peptides recovery, filters were rinsed twice with 50µL of 50 mM ABC that was collected by centrifugation.

III.   Phase Transfer

200 µL of ethyl acetate was added to peptides containing filtrate that was transferred to a 2 mL tube. After 2.5 µL TFA was added and was quickly vortexed. White thread like precipitate may be visible for large quantities of peptides. Peptides precipitate was mixed with 800 µL of ethyl acetate and was centrifuged at 13 000 rpm for 10 minutes. The organic supernatant was discarded and this

step was repeated twice more, with respect to careful removal of the upper organic layer as much as possible without disturbing the boundary layer. Uncovered sample tube was placed in a thermomixer at 60°C, in a fume hood, for 5 minutes to remove residual ethyl acetate. Residual organic and volatile salts were removed by vacuum drying in a SpeedVac, repeated two times with 50% methanol.

IV.   Nano HPLC Q-Exactive Plus

A nanoflow HPLC instrument (U3000 RSLC Thermo Fisher Scientific) was coupled in-line to a Q Executive Plus (Thermo Scientific) with a Nano electrospray ion source. 1 µL of peptides mixture (corresponding to 200 ng of proteins) was loaded onto the preconcentrating trap (Thermo Scientific, Acclaim PepMap100 C18, 5 µm, 300 µm i.d x 5 mm) using partial loop injection, for 5 min at a flow rate of 10 µL.min^{-1} with buffer A (5% acetonitrile and 0.1% formic acid) then separated on column (Acclaim PepMap100 C18, 3 µm, 75 mm i.d. × 500 mm) with a linear gradient of 5–50% buffer B (75% acetonitrile and 0.1% formic acid) at a flow rate of 250 nL.min^{-1} and temperature of 45 °C. The total time for an LC MS/MS run lasted about 240 min and each sample was injected tree times for statistical treatment.

V.   Mass spectrometry

MS data was acquired on Q Executive Plus (Thermo Scientific) using a data-dependent top 20 method dynamically choosing the most abundant precursor ions from the survey scan (400–1600 m/z) for HCD fragmentation.[128] Dynamic exclusion duration was 60 sec. Isolation of precursors was performed with a 1.6 m/z window and MS/MS scans were acquired with a starting mass of 80 m/z. Survey scans were acquired at a resolution of 70,000 at m/z 400 (AGC set to 106 ions with a maximum fill time of 180 ms). Resolution for HCD spectra was set to 35,500 at m/z 200 (AGC set to 105 ions with a maximum fill time of 120 ms). Normalized collision energy was 28 eV. The underfill ratio, which specifies the minimum percentage of the target value likely to be reached at maximum fill time, was defined as 0.3%. The instruments were run with peptide recognition mode (i.e. from 2 to 8 charge), exclusion of singly charged and of unassigned precursor ions were enabled.

VI.   Data Analysis

The acquired raw files were analyzed with PEAKS 7 studio software (Bioinformatics Solutions Inc., Waterloo, Canada) with MASCOT 2.5 search engine against the NCBI and Swissprot created fish database. The maximum mass error for peptides was set at 5 ppm in MS and 0.005 Da in MS / MS. PEAKS.DB[129] were used to perform *de novo* sequencing, database searches, PTM analyses to detect modifications as the oxidation of methionine, tryptophan, histidine, deamination of asparagine and glutamine, carbamidomethylation of cysteine, phosphorylation of tyrosine, serine, threonine and pyro-Glu formation. On the other hand, SPIDER algorithm allows the matching of *de novo*-obtained amino acid sequences with homologous protein sequences in the database.[62] After the PEAKS analyses the resulting list of proteins was filtered using a peptide false discovery rate of 0.1% and only proteins identified with a minimum of 2 peptides are reported.

For the archaeological sample the acquired raw files were analyzed with proteome Discoverer 2.0 (Thermo Scientific) using the Sequest HT search engine against the same fish databaseas well as PEAKS/SPIDER. The peptide mass tolerance was set to 10 ppm and 0.02 Da for MS/MS. Various modifications were included as follows: Oxidation of methionine, tryptophan, histidine, deamidation of asparagine, glutamine, carbamidomethylation of cysteine, phosphorylation of tyrosine, serine, threonine, pyro-Glu. For high-confidence peptides identification a FDR (False Discover Rate) of 1% and a minimum of 2 ranked peptides were used for peptide filtering.

References

1.   Fosse, G.; Justesen, N.-P. B.; Wesenberg, G. B. R., Microstructure and chemical composition of fossil mamalian teeth. *Calcified Tissue International* **1981,** *528*, 521-528.

2.   Cowden, R. R.; Curtis, S. K., Demonstration of protein-bound sulfhydryl and disulfide groups with fluorescent mercurials. *Histochemie* **1970,** *22*, 247-255.

3.   Loy, T. H., Prehistoric blood residues: Detection on tool surfaces and identification of species of origin. *Science* **1983,** *220*, 1269-1271.

4.   Loy, T. H.; Wood, A. R., Blood Residue Analysis at Cayonii Tepesi , Turkey. **1987**, 451-460.

5.   Matheson, C. D.; Veall, M. A., Presumptive blood test using Hemastix®with EDTA in archaeology. *Journal of Archaeological Science* **2014,** *41*, 230-241.

6.   Bobroff, V.; Chen, H. H.; Javerzat, S.; Petibois, C., What can infrared spectroscopy do for characterizing organic remnant in fossils? *TrAC - Trends in Analytical Chemistry* **2016,** *82*, 443-456.

7.   Cotte, M.; Walter, P.; Tsoucaris, G.; Dumas, P., Studying skin of an Egyptian mummy by infrared microscopy. *Vibrational Spectroscopy* **2005,** *38*, 159-167.

8.   Reiche, I.; Lebon, M.; Chadefaux, C.; Müller, K.; Le Hô, A. S.; Gensch, M.; Schade, U., Microscale imaging of the preservation state of 5,000-year-old archaeological bones by synchrotron infrared microspectroscopy. *Analytical and Bioanalytical Chemistry* **2010,** *397*, 2491-2499.

9.   Lebon, M.; Müller, K.; Bahain, J. J.; Fröhlich, F.; Falguères, C.; Bertrand, L.; Sandt, C.; Reiche, I., Imaging fossil bone alterations at the microscale by SR-FTIR microspectroscopy. *Journal of Analytical Atomic Spectrometry* **2011,** *26*, 922-929.

10.   Vincke, D.; Miller, R.; Stassart, É.; Otte, M.; Dardenne, P.; Collins, M.; Wilkinson, K.; Stewart, J.; Baeten, V.; Fernández Pierna, J. A., Analysis of collagen preservation in bones recovered in archaeological contexts using NIR Hyperspectral Imaging. *Talanta* **2014,** *125*, 181-188.

11.   Bertrand, L.; Vichi, A.; Doucet, J.; Walter, P.; Blanchard, P., The fate of archaeological keratin fibres in a temperate burial context: Microtaphonomy study of hairs from Marie de Bretagne (15th c., Orléans, France). *Journal of Archaeological Science* **2014,** *42*, 487-499.

12.   Kremer, B.; Owocki, K.; Królikowska, A.; Wrzosek, B.; Kazmierczak, J., Mineral microbial structures in a bone of the Late Cretaceous dinosaur Saurolophus angustirostris from the Gobi Desert, Mongolia - a Raman spectroscopy study. *Palaeogeography, Palaeoclimatology, Palaeoecology* **2012,** *358-360*, 51-61.

13.   Adamiano, A.; Fabbri, D.; Falini, G.; Belcastro, M. G., A complementary approach using analytical pyrolysis to evaluate collagen degradation and mineral fossilisation in archaeological bones: The case study of Vicenne-Campochiaro necropolis (Italy). *Journal of analytical and applied pyrolysis* **2013,** *100*, 173-180.

14.   Łydżba-Kopczyńska, B.; Madariaga, J. M., Applications of Raman spectroscopy in art and archaeology. *Journal of Raman Spectroscopy* **2016,** *47* (12), 1404-1407.

15.   France, C. A. M.; Thomas, D. B.; Doney, C. R.; Madden, O., FT-Raman spectroscopy as a method for screening collagen diagenesis in bone. *Journal of Archaeological Science* **2014,** *42*, 346-355.

16.   Bertoluzza, A., Preliminary Results in Dating Human Skeletal Remains by Raman Spectroscopy. **1997,** *28*, 185-188.

17.   Edwards, H. G. M.; Farwell, D. W.; Holder, J. M.; Lawson, E. E., Fourier-transform Raman spectra of ivory III : identification of mammalian specimens. **1997**.

18.   Edwards, H. G. M.; Brody, R. H.; Hassan, N. F. N.; Farwell, D. W.; O'Connor, S., Identification of archaeological ivories using FT-Raman spectroscopy. *Analytica Chimica Acta* **2006,** *559*, 64-72.

19.   Petersen, S.; Nielsen, O. F.; Christensen, D. H.; Edwards, H. G. M.; Farwell, D. W.; David, R.; Lambert, P.; Gniadecka, M.; Wulf, H. C., Near-infrared Fourier transform Raman spectroscopy of skin samples from the 'Tomb of the Two Brothers,' Khnum-Nakht and Nekht-Ankh, XIIth Dynasty Egyptian mummies (ca 2000 BC). *Journal of Raman Spectroscopy* **2003,** *34*, 375-379.

20.   Edwards, H. G. M.; Wilson, A. S.; Hassan, N. F. N.; Davidson, A.; Burnett, A., Raman spectroscopic analysis of human remains from a seventh century cist burial on Anglesey , UK. **2007**, 821-828.

21.   Cersoy, S.; Richardin, P.; Walter, P.; Brunelle, A., Cluster TOF-SIMS imaging of human skin remains: analysis of a South-Andean mummy sample. *Journal of Mass Spectrometry* **2012,** *47* (3), 338-346.

22.   Surmik, D.; Rothschild, B. M.; Pawlicki, R., Unusual intraosseous fossilized soft tissues from the Middle Triassic Nothosaurus bone. *The Science of Nature* **2017,** *104* (3-4), 25.

23.   Mazel, V.; Richardin, P.; Touboul, D.; Brunelle, A.; Walter, P.; Laprévote, O., Chemical imaging techniques for the analysis of complex mixtures: New application to the characterization of ritual matters on African wooden statuettes. *Analytica Chimica Acta* **2006,** *570* (1), 34-40.

24.   Mazel, V.; Richardin, P.; Debois, D.; Touboul, D.; Cotte, M.; Brunelle, A.; Walter, P.; Laprévote, O., Identification of ritual blood in African artifacts using TOF-SIMS and synchrotron radiation microspectroscopies. *Analytical chemistry* **2007,** *79* (24), 9253-9260.

25.   Nicholson, P. T.; Peltenburg, E., Egyptian Faience. *Ancient Egyptian Materials and Technology* **2010**, 177-194.

26.   Von Endt, D. W., Amino-acid analysis of the contents of a vial excavated at Axum, Ethiopia. *Journal of Archaeological Science* **1977,** *4*, 367-376.

27.   Gurley, L. R.; Valdez, J. G.; Spall, W. D.; Smith, B. F.; Gillette, D. D., Proteins in the fossil bone of the dinosaur, Seismosaurus. *Journal of protein chemistry* **1991,** *10*, 75-90.

28.   O'Connell, T. C.; M., H. R. E., Isolation and Isotopic Analysis of Individual Amino Aids from Archaeological Bone Collagen: A New Method Using RP-HPLC. **2001,** *43*, 421-438.

29.   Kaufman, D. S.; Manley, W. F., A new procedure for determining DL amino acid ratios in fossils using reverse phase liquid chromatography. *Quaternary Science Reviews* **1998,** *17*, 987-1000.

30.   Akiyama, M.; Wyckoff, R. W., The total amino acid content of fossil pecten shells. *Proceedings of the National Academy of Sciences* **1970,** *67* (3), 1097-1100.

31.   Fabbri, D.; Adamiano, A.; Falini, G.; De Marco, R.; Mancini, I., Analytical pyrolysis of dipeptides containing proline and amino acids with polar side chains. Novel 2, 5-diketopiperazine markers in the pyrolysates of proteins. *Journal of analytical and applied pyrolysis* **2012,** *95*, 145-155.

32.   Borja, C.; García-Pacheco, M.; Olivares, E. G.; Scheuenstuhl, G.; Lowenstein, J. M., Immunospecificity of albumin detected in 1.6 million-year-old fossils from Venta Micena in Orce, Granada, Spain. *American Journal of Physical Anthropology: The Official Publication of the American Association of Physical Anthropologists* **1997,** *103* (4), 433-441.

33.   Wilson, A., Protein stability in preserved biological remains: II. Modification and aggregation of proteins in an 8-year-old sample of dried blood. *International Journal of Biochemistry* **1971,** *2* (11), 558-568.

34.   Wilson, A., Protein stability in preserved biological remains: I. Survival of biologically active proteins in an 8-year-old sample of dried blood. *International Journal of Biochemistry* **1971,** *2* (11), 545-557.

35.   Downs, E. F.; Lowenstein, J. M., Identification of archaeological blood proteins: A cautionarynote. *Journal of Archaeological Science* **1995,** *22* (1), 11-16.

36.   Anderson, N. L.; Anderson, N. G., Proteome and proteomics: new technologies, new concepts, and new words. *Electrophoresis* **1998,** *19* (11), 1853-1861.

37.   Bodzon-Kulakowska, A.; Bierczynska-Krzysik, A.; Dylag, T.; Drabik, A.; Suder, P.; Noga, M.; Jarzebinska, J.; Silberring, J., Methods for samples preparation in proteomic research. *Journal of Chromatography B* **2007,** *849* (1-2), 1-31.

38.   Feist, P.; Hummon, A. B., Proteomic challenges: sample preparation techniques for microgram-quantity protein analysis from biological samples. *International journal of molecular sciences* **2015,** *16* (2), 3537-3563.

39.   Zhang, Y.; Fonslow, B. R.; Shan, B.; Baek, M.-C.; Yates III, J. R., Protein analysis by shotgun/bottom-up proteomics. *Chemical reviews* **2013,** *113* (4), 2343-2394.

40.   Olsen, J. V.; Ong, S.-E.; Mann, M., Trypsin cleaves exclusively C-terminal to arginine and lysine residues. *Molecular & Cellular Proteomics* **2004,** *3* (6), 608-614.

41.   Shevchenko, A.; Tomas, H.; Havli, J.; Olsen, J. V.; Mann, M., In-gel digestion for mass spectrometric characterization of proteins and proteomes. *Nature protocols* **2006,** *1* (6), 2856.

42.   Wiśniewski, J. R.; Zougman, A.; Nagaraj, N.; Mann, M., Universal sample preparation method for proteome analysis. *Nature methods* **2009,** *6* (5), 359.

43.   Erde, J.; Loo, R. R. O.; Loo, J. A., Enhanced FASP (eFASP) to increase proteome coverage and sample recovery for quantitative proteomic experiments. *Journal of proteome research* **2014,** *13* (4), 1885-1895.

44.   Fischer, R.; Kessler, B. M., Gel-aided sample preparation (GASP)—A simplified method for gel-assisted proteomic sample generation from protein extracts and intact cells. *Proteomics* **2015,** *15* (7), 1224-1229.

45.   Kulak, N. A.; Pichler, G.; Paron, I.; Nagaraj, N.; Mann, M., Minimal, encapsulated proteomic-sample processing applied to copy-number estimation in eukaryotic cells. *Nature methods* **2014,** *11* (3), 319.

46.   Wiśniewski, J. R.; Zougman, A.; Mann, M., Combination of FASP and StageTip-based fractionation allows in-depth analysis of the hippocampal membrane proteome. *Journal of proteome research* **2009,** *8* (12), 5674-5678.

47.   Perkins, D. N.; Pappin, D. J.; Creasy, D. M.; Cottrell, J. S., Probability-based protein identification by searching sequence databases using mass spectrometry data. *ELECTROPHORESIS: An International Journal* **1999,** *20* (18), 3551-3567.

48.   Jiménez, C.; Huang, L.; Qiu, Y.; Burlingame, A., Searching sequence databases over the internet: protein identification using MS-Fit. *Current protocols in protein science* **1998,** *14* (1), 16.5. 1-16.5. 6.

49.   Eng, J. K.; McCormack, A. L.; Yates, J. R., An approach to correlate tandem mass spectral data of peptides with amino acid sequences in a protein database. *Journal of the American Society for Mass Spectrometry* **1994,** *5* (11), 976-989.

50.   Cox, J.; Neuhauser, N.; Michalski, A.; Scheltema, R. A.; Olsen, J. V.; Mann, M., Andromeda: a peptide search engine integrated into the MaxQuant environment. *Journal of proteome research* **2011,** *10* (4), 1794-1805.

51.   Zhang, N.; Aebersold, R.; Schwikowski, B., ProbID: a probabilistic algorithm to identify peptides through sequence database searching using tandem mass spectral data. *Proteomics* **2002,** *2* (10), 1406-1412.

52.   Craig, R.; Beavis, R. C., TANDEM: matching proteins with tandem mass spectra. *Bioinformatics* **2004,** *20* (9), 1466-1467.

53.   Fenn, J. B.; Mann, M.; Meng, C. K.; Wong, S. F.; Whitehouse, C. M., Electrospray ionization for mass spectrometry of large biomolecules. *Science* **1989,** *246* (4926), 64-71.

54.   Zamdborg, L.; LeDuc, R. D.; Glowacz, K. J.; Kim, Y.-B.; Viswanathan, V.; Spaulding, I. T.; Early, B. P.; Bluhm, E. J.; Babai, S.; Kelleher, N. L., ProSight PTM 2.0: improved protein identification and characterization for top down mass spectrometry. *Nucleic acids research* **2007,** *35* (suppl_2), W701-W706.

55.   Tanner, S.; Shu, H.; Frank, A.; Wang, L.-C.; Zandi, E.; Mumby, M.; Pevzner, P. A.; Bafna, V., InsPecT: identification of posttranslationally modified peptides from tandem mass spectra. *Analytical chemistry* **2005,** *77* (14), 4626-4639.

56.   Poullet, P.; Carpentier, S.; Barillot, E., myProMS, a web server for management and validation of mass spectrometry-based proteomic data. *Proteomics* **2007,** *7* (15), 2553-2556.

57.   Stein, S. E.; Scott, D. R., Optimization and testing of mass spectral library search algorithms for compound identification. *Journal of the American Society for Mass Spectrometry* **1994,** *5* (9), 859-866.

58.   Ma, B.; Zhang, K.; Hendrie, C.; Liang, C.; Li, M.; Doherty-kirby, A.; Lajoie, G., PEAKS : powerful software for peptide de novo sequencing by tandem mass spectrometry. **2003**, 2337-2342.

59.   Frank, A.; Pevzner, P., PepNovo: de novo peptide sequencing via probabilistic network modeling. *Analytical chemistry* **2005,** *77* (4), 964-973.

60.   Ma, B., Novor: real-time peptide de novo sequencing software. *Journal of the American Society for Mass Spectrometry* **2015,** *26* (11), 1885-1894.

61.   Muth, T.; Weilnböck, L.; Rapp, E.; Huber, C. G.; Martens, L.; Vaudel, M.; Barsnes, H., DeNovoGUI: an open source graphical user interface for de novo sequencing of tandem mass spectra. *Journal of proteome research* **2014,** *13* (2), 1143-1146.

62.   Grossmann, J.; Fischer, B.; Baerenfaller, K.; Owiti, J.; Buhmann, J. M.; Gruissem, W.; Baginsky, S., A workflow to increase the detection rate of proteins from unsequenced organisms in high-throughput proteomics experiments. *Proteomics* **2007,** *7* (23), 4245-4254.

63.   Han, Y.; Ma, B.; Zhang, K. In *SPIDER: software for protein identification from sequence tags with de novo sequencing error*, Proceedings. 2004 IEEE Computational Systems Bioinformatics Conference, 2004. CSB 2004., IEEE: 2004; pp 206-215.

64.   Dallongeville, S.; Garnier, N.; Rolando, C.; Tokarski, C., Proteins in Art , Archaeology , and Paleontology : From Detection to Identi fi cation. **2016**.

65.   Vinciguerra, R.; De Chiaro, A.; Pucci, P.; Marino, G.; Birolo, L., Proteomic strategies for cultural heritage: From bones to paintings. *Microchemical Journal* **2016,** *126*, 341-348.

66.   Solazzo, C.; Fitzhugh, M. W. W.; Rolando, C.; Tokarskl, C., Identification of Protein Remains in Archaeological Potsherds by Proteomics. **2008,** *80*.

67.   Dallongeville, S.; Garnier, N.; Casasola, D. B.; Bonifay, M.; Rolando, C.; Tokarski, C., Dealing with the identification of protein species in ancient amphorae. **2010**.

68.   Stevens, S. M.; Wolverton, S.; Venables, B.; Barker, A.; Seeley, K. W.; Adhikari, P., Evaluation of microwave-assisted enzymatic digestion and tandem mass spectrometry for the identification of protein residues from an inorganic solid matrix: implications in archaeological research. *Analytical and bioanalytical chemistry* **2010,** *396* (4), 1491-1499.

69.   Barker, A.; Venables, B.; Stevens, S. M.; Seeley, K. W.; Wang, P.; Wolverton, S., An optimized approach for protein residue extraction and identification from ceramics after cooking. *Journal of Archaeological Method and Theory* **2012,** *19* (3), 407-439.

70.   Hong, C.; Jiang, H.; Lü, E.; Wu, Y.; Guo, L.; Xie, Y.; Wang, C.; Yang, Y., Identification of milk component in ancient food residue by proteomics. *PloS one* **2012,** *7* (5), e37053.

71.   Shevchenko, A.; Yang, Y.; Knaust, A.; Thomas, H.; Jiang, H.; Lu, E.; Wang, C.; Shevchenko, A., Proteomics identifies the composition and manufacturing recipe of the 2500-year old sourdough bread from Subeixi cemetery in China. *Journal of Proteomics* **2014,** *105*, 363-371.

72.   Collins, M.; Buckley, M.; Gruny, H. H.; Thomas-Oates, J.; Wilson, J.; van Doorn, N., ZooMS: the collagen barcode and fingerprints. *Spectroscopy Europe* **2010,** *22*, 6-10.

73.   Buckley, M.; Collins, M.; Thomas-Oates, J.; Wilson, J. C., Species identification by analysis of bone collagen using matrix-assisted laser desorption/ionisation time-of-flight mass spectrometry. *Rapid communications in mass spectrometry* **2009,** *23*, 3843-3854.

74.   Buckley, M.; Whitcher Kansa, S.; Howard, S.; Campbell, S.; Thomas-Oates, J.; Collins, M., Distinguishing between archaeological sheep and goat bones using a single collagen peptide. *Journal of Archaeological Science* **2010,** *37*, 13-20.

75.   Buckley, M.; Gu, M.; Shameer, S.; Patel, S.; Chamberlain, A. T., High-throughput collagen fingerprinting of intact microfaunal remains; A low-cost method for distinguishing between murine rodent bones. *Rapid Communications in Mass Spectrometry* **2016,** *30*, 805-812.

76.   Fresnais, M.; Richardin, P.; Sepúlveda, M.; Leize-Wagner, E.; Charrié-Duhaut, A., Omics for Precious Rare Biosamples: Characterization of Ancient Human Hair by a Proteomic Approach. *OMICS: A Journal of Integrative Biology* **2017,** *21*, 361-370.

77.   Stewart, N. A.; Molina, G. F.; Mardegan Issa, J. P.; Yates, N. A.; Sosovicka, M.; Vieira, A. R.; Line, S. R. P.; Montgomery, J.; Gerlach, R. F., The identification of peptides by nanoLC-MS/MS from human surface tooth enamel following a simple acid etch extraction. *RSC Advances* **2016,** *6*, 61673-61679.

78.   Corthals, A.; Koller, A.; Martin, D. W.; Rieger, R.; Chen, E. I.; Bernaski, M.; Recagno, G.; Dávalos, L. M., Detecting the immune system response of a 500 year-Old Inca Mummy. *PLoS ONE* **2012,** *7*.

79.   Lévêque, P., *Céramiques hellénistiques et romaines*. Presses Univ. Franche-Comté: 1980; Vol. 3.

80.   Quevedo Sanchéz, A., Lusitanian Amphorae in Carthago Nova (Cartagena, Spain): Distribution and Research Questions. **2016**.

81.   Curtis, R. I., Sources for production and trade of Greek and Roman processed fish. *Ancient fishing and fish processing in the Black Sea region* **2005**, 31-46.

82.   Curtis, R. I., Spanish trade in salted fish products in the 1st and 2nd centuries. **1988**, 205-210.

83.   Di Natale, A., The ancient distribution of bluefin tuna fishery: how coins can improve our knowledge. *Collect. Vol. Sci. Pap. ICCAT* **2014,** *70*, 2828-2844.

84.   Pitcher, T. J.; Lam, M. E., Fish commoditization and the historical origins of catching fish for profit. **2016**.

85.   Curtis, R. I., Umami and the foods of classical antiquity. *American Journal of Clinical Nutrition* **2009,** *90*, 712-718.

86.   Aquerreta, Y.; Astiasarán, I.; Bello, J., Use of exogenous enzymes to elaborate the Roman fish sauce 'garum'. *Journal of the Science of Food and Agriculture* **2002,** *82*, 107-112.

87.   Luca, R.; Miriello, D.; Pecci, A.; Domínguez-Bella, S.; Bernal-Casasola, D.; Cottica, D.; Bloise, A.; Crisci, G. M., Archaeometric study of mortars from the Garum Shop at Pompeii, Campania, Italy. *Geoarchaeology* **2015,** *30*, 330-351.

88.   Bonifay, M.; Botte, E.; Capelli, C.; Contino, A.; Panella, C.; Tchernia, A.; Bonifay, M.; Botte, E.; Capelli, C.; Contino, A.; Djaoui, D., Nouvelles hypothèses sur l ' origine et le contenu des amphores africaines Ostia LIX et XXIII To cite this version : HAL Id : hal-01461489. **2017**.

89.   Herrero, M.; Simó, C.; García-Cañas, V.; Ibáñez, E.; Cifuentes, A., Foodomics: MS-based strategies in modern food science and nutrition. *Mass spectrometry reviews* **2012,** *31* (1), 49-69.

90.   Cifuentes, A., Food analysis: present, future, and foodomics. *ISRN Analytical Chemistry* **2012,** *2012*.

91.   Asensio, L.; González, I.; Rodríguez, M. A.; Mayoral, B.; López-Calleja, I.; Hernández, P. E.; García, T.; Martín, R., Identification of grouper (Epinephelus guaza), wreck fish (Polyprion americanus), and Nile perch (Lates niloticus) fillets by polyclonal antibody-based enzyme-linked immunosorbent assay. *Journal of agricultural and food chemistry* **2003,** *51* (5), 1169-1172.

92.   Tepedino, V.; Berrini, A.; Borromeo, V.; Gaggioli, D.; Cantoni, C.; Manzoni, P.; Secchi, C., Identification of commercial fish species belonging to the orders pleuronectiformes and gadiformes: library of isoelectric focusing patterns. *Journal of AOAC International* **2001,** *84* (5), 1600-1607.

93.   Piñeiro, C.; Barros-Velázquez, J.; Sotelo, C. G.; Gallardo, J. M., The use of two-dimensional electrophoresis in the characterization of the water-soluble protein fraction of commercial flat fish species. *Zeitschrift für Lebensmitteluntersuchung und-Forschung A* **1999,** *208* (5-6), 342-348.

94.   Solanky, S. S.; Campistron, I.; Laguerre, A.; Pilard, J. F., Metathetic selective degradation of polyisoprene: low-molecular-weight telechelic oligomer obtained from both synthetic and natural rubber. *Macromolecular Chemistry and Physics* **2005,** *206* (10), 1057-1063.

95.   Carrera, M.; Cañas, B.; Piñeiro, C.; Vázquez, J.; Gallardo, J. M., Identification of commercial hake and grenadier species by proteomic analysis of the parvalbumin fraction. *Proteomics* **2006,** *6*, 5278-5287.

96.   Pepe, T.; Ceruso, M.; Carpentieri, A.; Ventrone, I.; Amoresano, A.; Anastasio, A., Proteomics analysis for the identification of three species of Thunnus. *Veterinary research communications* **2010,** *34* (1), 153-155.

97.   Mazzeo, M. F.; Giulio, B. D.; Guerriero, G.; Ciarcia, G.; Malorni, A.; Russo, G. L.; Siciliano, R. A., Fish authentication by MALDI-TOF mass spectrometry. *Journal of agricultural and food chemistry* **2008,** *56* (23), 11071-11076.

98.   Stahl, A., Development of a MALDI – TOF MS-Based Protein Fingerprint Database of Common Food Fish Allowing Fast and Reliable Identi fi cation of Fraud and Substitution. **2017**.

99.   Forné, I.; Abián, J.; Cerdà, J., Fish proteome analysis: Model organisms and non-sequenced species. *Proteomics* **2010,** *10*, 858-872.

100.   Carrera, M.; Canas, B.; Vázquez, J.; Gallardo, J. M., Extensive de novo sequencing of new parvalbumin isoforms using a novel combination of bottom-up proteomics, accurate molecular mass measurement by FTICR– MS, and selected MS/MS Ion monitoring. *Journal of proteome research* **2010,** *9* (9), 4393-4406.

101.   Carrera, M.; Canas, B.; López-Ferrer, D.; Pineiro, C.; Vázquez, J.; Gallardo, J. M., Fast monitoring of species-specific peptide biomarkers using high-intensity-focused-ultrasound-assisted tryptic digestion and selected MS/MS ion monitoring. *Analytical chemistry* **2011,** *83* (14), 5688-5695.

102.   Wulff, T.; Nielsen, M. E.; Deelder, A. M.; Jessen, F.; Palmblad, M., Authentication of fish products by large-scale comparison of tandem mass spectra. *Journal of proteome research* **2013,** *12* (11), 5253-5259.

103.   Nessen, M. A.; Zwaan, D. J. V. D.; Grevers, S.; Dalebout, H.; Staats, M.; Kok, E.; Palmblad, M., Authentication of Closely Related Fish and Derived Fish Products Using Tandem Mass Spectrometry and Spectral Library Matching. **2016**.

104.   Garnier, N.; Rolando, C.; Høtje, J. M.; Tokarski, C., Analysis of archaeological triacylglycerols by high resolution nanoESI, FT-ICR MS and IRMPD MS/MS: application to 5th century BC–4th century AD oil lamps from Olbia (Ukraine). *International Journal of Mass Spectrometry* **2009,** *284*, 47-56.

105.   Alasalvar, C.; Taylor, K. D. A.; Zubcov, E.; Shahidi, F.; Alexis, M., Differentiation of cultured and wild sea bass (Dicentrarchus labrax): total lipid content, fatty acid and trace mineral composition. *Food chemistry* **2002,** *79*, 145-150.

106.   Baeten, J.; Jervis, B.; De Vos, D.; Waelkens, M., Molecular evidence for the mixing of M eat, F ish and V egetables in A nglo-S axon coarseware from H amwic, UK. *Archaeometry* **2013,** *55* (6), 1150-1174.

107.   Smriga, M.; Mizukoshi, T.; Iwahata, D.; Eto, S.; Miyano, H.; Kimura, T.; Curtis, R. I., Amino acids and minerals in ancient remnants of fish sauce (garum) sampled in the "Garum Shop" of Pompeii, Italy. *Journal of food composition and analysis* **2010,** *23*, 442-446.

108.   Speller, C. F.; Yang, D. Y.; Hayden, B., Ancient DNA investigation of prehistoric salmon resource utilization at Keatley Creek, British Columbia, Canada. *Journal of Archaeological Science* **2005,** *32*, 1378-1389.

109.   Grier, C.; Flanigan, K.; Winters, M.; Jordan, L. G.; Lukowski, S.; Kemp, B. M., Using ancient DNA identification and osteometric measures of archaeological Pacific salmon vertebrae for reconstructing salmon fisheries and site seasonality at Dionisio Point, British Columbia. *Journal of Archaeological Science* **2013,** *40*, 544-555.

110.   Ewonus, P. A.; Cannon, A.; Yang, D. Y., Addressing seasonal site use through ancient DNA species identification of Pacific salmon at Dionisio Point, Galiano Island, British Columbia. *Journal of Archaeological Science* **2011,** *38*, 2536-2546.

111.   Sealy, J.; Johnson, M.; Richards, M.; Nehlich, O., Comparison of two methods of extracting bone collagen for stable carbon and nitrogen isotope analysis: comparing whole bone demineralization with gelatinization and ultrafiltration. *Journal of Archaeological Science* **2014,** *47*, 64-69.

112.   Makarewicz, C. A.; Sealy, J., Dietary reconstruction, mobility, and the analysis of ancient skeletal tissues: expanding the prospects of stable isotope research in archaeology. *Journal of Archaeological Science* **2015,** *56*, 146-158.

113.   Holstein, I. C. C. V.; Penkman, K. E. H.; Peacock, E. E.; Collins, M. J., Wet degradation of keratin proteins : linking amino acid , elemental and isotopic composition. **2014**, 2121-2133.

114.   Colonese, A. C.; Lucquin, A.; Guedes, E. P.; Thomas, R.; Best, J.; Fothergill, B. T.; Sykes, N.; Foster, A.; Miller, H.; Poole, K., The identification of poultry processing in archaeological ceramic vessels using in-situ isotope references for organic residue analysis. *Journal of Archaeological Science* **2017,** *78*, 179-192.

115.   Roffet-Salque, M.; Lee, M. R.; Timpson, A.; Evershed, R. P., Impact of modern cattle feeding practices on milk fatty acid stable carbon isotope compositions emphasise the need for caution in selecting reference animal tissues and products for archaeological investigations. *Archaeological and Anthropological Sciences* **2017,** *9* (7), 1343-1348.

116.   Cappellini, E.; Jensen, L. J.; Szklarczyk, D.; Fonseca, R. A. R.; Sta, T. W.; Holen, S. R.; Collins, M. J.; Orlando, L.; Willerslev, E.; Gilbert, M. T. P.; Olsen, J. V., Proteomic Analysis of a Pleistocene Mammoth Femur Reveals More than One Hundred Ancient Bone Proteins. **2012**, 917-926.

117.   Tokarski, C.; Martin, E.; Rolando, C.; Post-traductionnelles, M.; Cedex, A., Identification of Proteins in Renaissance Paintings by Proteomics John the Baptist , St . Sebastian (XVth century), and. **2006,** *78*, 1494-1502.

118.   Dallongeville, S.; Koperska, M.; Garnier, N.; Rolando, C.; Tokarski, C., Identification of Animal Glue Species in Artworks Using Proteomics : Application to a 18th Century Gilt Sample. **2011**, 9431-9437.

119.   Buckley, M.; Fraser, S.; Herman, J.; Melton, N. D.; Mulville, J.; Pálsdóttir, A. H., Species identification of archaeological marine mammals using collagen fingerprinting. *Journal of Archaeological Science* **2014,** *41*, 631-641.

120.   Richter, K. K.; Wilson, J.; Jones, A. K. G.; Buckley, M.; van Doorn, N.; Collins, M. J., Fish'n chips: ZooMS peptide mass fingerprinting in a 96 well plate format to identify fish bone fragments. *Journal of Archaeological Science* **2011,** *38*, 1502-1510.

121.   Di Natale, A., The ancient distribution of bluefin tuna fishery: how coins can improve our knowledge. *Collect. Vol. Sci. Pap. ICCAT* **2014,** *70* (6), 2828-2844.

122.   Dallongeville, S.; Garnier, N.; Casasola, D. B.; Bonifay, M.; Rolando, C.; Tokarski, C., Dealing with the identification of protein species in ancient amphorae. *Analytical and bioanalytical chemistry* **2011,** *399*, 3053-3063.

123.   Curtis, R.; Curtis, R. I., Garum and Salsamenta: Production and Commerce in Materia Medica {Studies in Ancient Medicine 3. *Leiden, EJ Brill* **1991**.

124.   Nakamura, Y.; Mori, K.; Saitoh, K.; Oshima, K.; Mekuchi, M.; Sugaya, T.; Shigenobu, Y.; Ojima, N.; Muta, S.; Fujiwara, A., Evolutionary changes of multiple visual pigment genes in the complete genome of Pacific bluefin tuna. *Proceedings of the National Academy of Sciences* **2013,** *110* (27), 11061-11066.

125.   Yasuike, M.; Fujiwara, A.; Nakamura, Y.; Iwasaki, Y.; Nishiki, I.; Sugaya, T.; Shimizu, A.; Sano, M.; Kobayashi, T.; Ototake, M., A functional genomics tool for the Pacific bluefin tuna: development of a 44K oligonucleotide microarray from whole-genome sequencing data for global transcriptome analysis. *Gene* **2016,** *576* (2), 603-609.

126.   Ma, H.; Yin, B.; Wang, S.; Jiao, Y.; Pan, W.; Huang, S.; Chen, S.; Meng, F., Synthesis of silver and gold nanoparticles by a novel electrochemical method. *ChemPhysChem* **2004,** *5* (1), 68-75.

127.   Dereeper, A.; Guignon, V.; Blanc, G.; Audic, S.; Buffet, S.; Chevenet, F.; Dufayard, J.-F.; Guindon, S.; Lefort, V.; Lescot, M., Phylogeny. fr: robust phylogenetic analysis for the non-specialist. *Nucleic acids research* **2008,** *36* (suppl_2), W465-W469.

128.   Sun, L.; Zhu, G.; Dovichi, N. J., Comparison of the LTQ-Orbitrap Velos and the Q-Exactive for proteomic analysis of 1–1000 ng RAW 264.7 cell lysate digests. *Rapid Communications in Mass Spectrometry* **2013,** *27* (1), 157-162.

129.   Zhang, J.; Xin, L.; Shan, B.; Chen, W.; Xie, M.; Yuen, D.; Zhang, W.; Zhang, Z.; Lajoie, G. A.; Ma, B., PEAKS DB: de novo sequencing assisted database search for sensitive and accurate peptide identification. *Molecular & Cellular Proteomics* **2012,** *11* (4), M111. 010587.

Chapter III: Lipidomics applied to the analysis of cross-linked polymers in oil paintings

Table of Contents

List of figures

List of tables

Introduction

I. Oil paintings

1. Definition

Paintings are composed of both organic and inorganic part phases. Pigments represent the main inorganic compounds, which impart color to paint. Oil that represents the organic part forms a solid film that can act as a binding medium, adhesive or varnish to protect and consolidate the fragile paintings.

Different types of binding media have been used in paintings in which they play a major role. The choice of materials initially depends on the technique used by the artist according to a given time and place. For example, beeswax was used as binding medium for the preparation of Encaustic painting. Tempera painting is composed from emulsions of some proteinaceous components such as eggs, gelatin, casein or their mixture. Polysaccharides (ex: Arabic gum) were also introduced, for example, in the composition of watercolors.

Oil painting was introduced in the early fifteenth century by the Flemish painter Van Eyck. Oils used in historic paintings are natural drying oils such as linseed oil. Triglycerides are the most abundant component of drying oils and they are mainly composed from unsaturated fatty acids such as linoleic acid and linolenic acid (C18 with 2 and 3 unsaturation). Oil drying is a chemical process that occurs spontaneously and it is considered as an auto-oxidation process followed by polymerization. This reaction happens in several stages. It begins with the auto-oxidation of the C = C double bonds of fatty acids into peroxides from a radical in the allylic position. Peroxides and hydro-peroxides decompose into free radicals that recombine to form a cross-linked structure. The phenomenon of auto-oxidation is strongly influenced by additives and pigments used in oil paints and by the pretreatment method of the oil.

Several methods and processes are used to produce oils with different qualities and properties, however there are specific stages of manufacture and treatment dedicated for oil paints. The extraction of oil can be done by two methods: cold pressing, or solvent extraction. A crude oil is obtained which contains many particles in suspension. It is then purified from its solid elements by

sedimentation, filtration or centrifugation to obtain a purified oil. The purified oil still contains a large amount of impurities, including mucilage (vegetable substances consisting of polysaccharides). Refining of the purified oil includes three main treatments: degumming, which eliminates mucilage, discoloration and neutralization which eliminate free fatty acids that can accelerate the oxidation process. Oils can undergo other treatments, such as heating with addition of metal salts, to improve their siccative property, that is to say their ability to form a solid film faster.

Table 1. Fatty acid compositions of some drying oils (wt%)[2]

Oil	Palmitic	Stearic	Oleic	Linoleic	Linolenic
Linseed	6-7	3-6	14-24	14-19	48-60
Walnut	3-7	0.5-3	9-30	57-76	2-16
Poppy seed	10	2	11	72	5
Tung	3	2	11	15	3

Table 2. Fatty acid composition of linseed oil[3]

Fatty acid	**% In freshly pressed oil**
18:3 linolenic acid	56-71
18:2 linoleic acid	12-18
18:1 oleic acid	10-22
18:0 stearic acid	2-3
16:0 palmitic acid	4-6

2. Pigments and dyes

Pigments or dyes are used to impart color to the paint. Pigments are usually metal salts or metal oxides, while dyes are organic compounds. For this reason, pigments are insoluble in the binder in opposition to dyes that are soluble and both pigments and dyes can be of natural or synthetic origin. The pigments need to be ground in the binder. It should be noted that grinding does not consist on reducing the size of the pigment particles, but on dispersing them in the binder. Dyes are used in the lacquer oil paint, which is obtained by fixing the dyestuff on a generally inorganic support, thereby making it possible to obtain an oil-insoluble compound.

3. Additives

Many and various additives may be incorporated into the paint, such as medium, solvents, driers or fillers and others.

The medium is an additional binder that can be added to the painting before its application to modify its properties (texture or siccativity for example). Many recipes of mediums have been developed over time: they can be for example based on oil, various resins and/or waxes.

The addition of solvent, for example gasoline turpentine or oil, will allow increasing the viscosity of the paint. The addition of oil drying agents, which are in particular metal oxides (lead oxide, manganese and cobalt), aims to accelerate the drying of the paint.

The fillers are inert, white mineral compounds with a low coloring power. They are added to bring material to the paint, which reduces the amount of pigment used, and therefore the cost of production of paints.

They also help to improve certain qualities of the paint (texture, opacity, saturation of the hue of the pigment) or to have a stabilizing effect. Calcium carbonate ($CaCO_3$) added especially in the form of chalk, gypsum ($CaSO_4.2H_2O$), barium sulfate ($BaSO_4$) and silicates such as talc (magnesium silicates hydrates) or clays (natural alumina silicates) hydrates) are the most commonly used fillers in oil painting. The fillers are crushed with the pigment in the oil to ensure their dispersion.

II.   Siccative oil polymerization

1. Mechanism

The drying, curing and aging of linseed oil is an auto-oxidative process. A complex cascade of reactions between the triglycerides and oxygen from the atmosphere lead to the polymerization of the linseed oil and the formation of a highly cross-linked structure. Triglycerides are the major component of linseed oil and they are composed mainly of polyunsaturated fatty acids. Linoleate and linolenate structures oxidize rapidly since they contain an allylic hydrogen between double bonds. The allylic hydrogen will lead to the formation of radical species. Subsequent reaction with oxygen generates hydroperoxide functions and lunch free radical-chain mechanisms. The radial chain reaction is composed from three steps: initiation, propagation and termination. This oxidation process is carried out in several stages:

1) Formation of hydroperoxides
2) Propagation of free radicals
3) Decomposition of hydroperoxides into free radicals
4) Free radical species react with each other to form cross-linked products

The organic material or substrate is represented by RH, where R is a hydrocarbon having a labile hydrogen atom H.

Initiation: $RH \rightarrow R* + H$

Propagation: $R* + O_2 \rightarrow ROO*$

$ROO* + RH \rightarrow ROOH + R*$

Hydroperoxide decomposition: $ROOH \rightarrow RO* + OH*$

$ROOH \rightarrow ROO* + H*$

Termination: $2RO* \rightarrow ROOR$

$2ROO* \rightarrow ROOR + O_2$

$2R* \rightarrow RR$

$RO* + R* \rightarrow ROR$
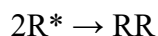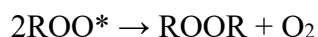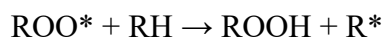
Factors such as temperature, oxygen concentration, moisture content, illumination, film thickness, concentration of antioxidants and catalysts, etc., affect the overall rate of autoxidation. Physical factors such as temperature, UV irradiation or transition metals increase the radical generation rate and by consequence increase the autoxidation rate. On the other hand, increasing the active sites and oxygen concentration initiates the reactivity of the autoxidizing material.
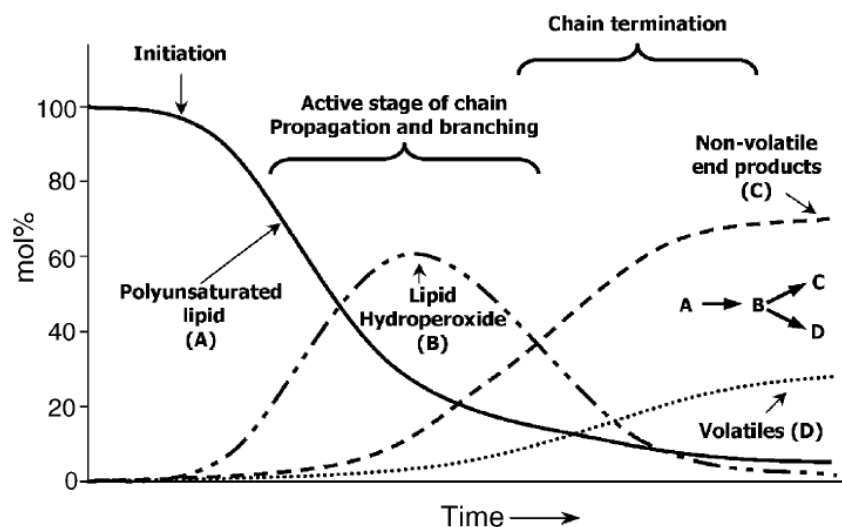
Figure 1. Schematic representation of fatty acids autoxidation during time[4]

Figure 1 represent the evaluation of lipid autoxidation; this scheme shows a decrease in the concentration of polyunsaturated fatty acids and increasing in hydroperoxide due to the loss of double bonds and the formation of hydroperoxide function when passing from the initiation step to the propagation step. During the propagation step, the rate of hydroperoxide formation attends its maximum then starts to decrease in favor of hydroperoxide decomposition and formation of volatile and non-volatile compounds. In the final step, hydroperoxide decomposition leads to the recombination of radical species to form cross-linked non-volatile compounds. On the other hand, radical species cause fatty acids degradation by β-scission mechanism and result in formation of oxygen containing products as alcohols, ketones, aldehydes and carboxylic acids.

2. Initiation

Drying oils are composed in majority of unsaturated fatty acids such as oleic, linoleic and linolenic acids. Allylic carbons are an attractive site to create radicals which are initiated by the presence of light and catalysts such as driers (e.g. cobalt salts) in the case of modern paints or pigments (e.g. lead white) in the case of art oil paintings (Reaction 1).

<u>**Reaction 1:**</u>

$$RH + M^{(n+1)+} \longrightarrow R* + M^{n+} + H^+$$

$M^{(n+1)+}$ is the higher oxidation state of the metal ions and M^{n+} is the lower oxidation state.

It exists three different classes of driers. The primary class of driers catalyzes the oxidation step and it includes Co^{2+}, Mn^{2+}, and Fe^{2+} metal salts. The second class of driers includes Pb^{2+}, Zr^{4+}, and Al^{3+} and catalyzes the polymerization step.[5] The oxidation states of iron, copper, manganese, nickel, Lead and cobalt are known to change through the single electron transfer.[6] Auxiliary driers like calcium and zirconium are used in combination with other driers in order to improve stability through drying and hardness.

3. Propagation

The free radicals produced in the previous step react easily with their environment. However, they have certain preferences. They react more easily with each other and this reactivity increases with the presence of oxygen atoms in their structure. At the beginning of the oxidation of lipids, the concentration of free radicals is too low for them to react with each other. The radicals then preferentially react with the oxygen of the air and optionally with the substrate, as shown in reaction R3 and R4 respectively. The hydroperoxide formed in reaction R4 can decompose into free radicals. Finally, these reactions generate new free radicals that will subsequently react with oxygen and between each other to create a cross-linked polymer.[7]

In the reaction 3, the electrons of the double bond of the active methylene group form a complex with an oxygen molecule before generating the hydroperoxide. The resulting complex is relatively stable because of the creation of a hydrogen bridge. Once the labile hydrogen of the methylene moiety moves to the oxygen molecule, rearrangement of the double bonds occurs. The hydroperoxide thus formed is conjugated with a cis-trans structure. (Figure 2) The double bonds

of the conjugated hydroperoxides can react under severe conditions with oxygen. Once the hydroperoxides are formed, they can decompose free radicals by mono or bimolecular decomposition.[8]
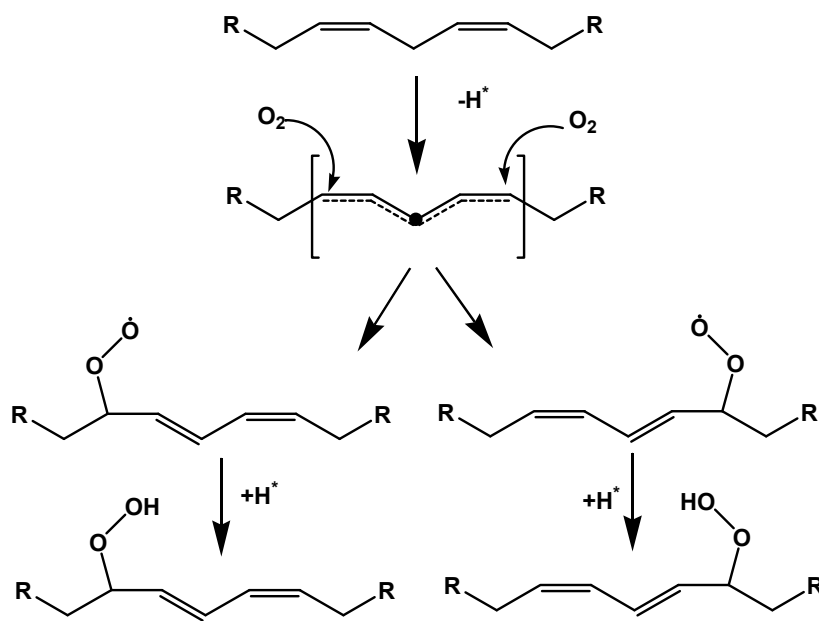
Figure 2. Hydroperoxide formation on the fatty acid chain during autoxidation

Reaction 3:

$+ O_2$
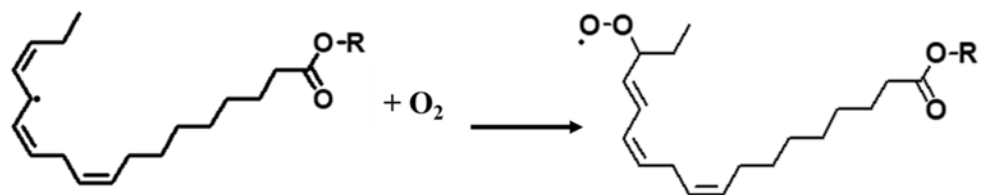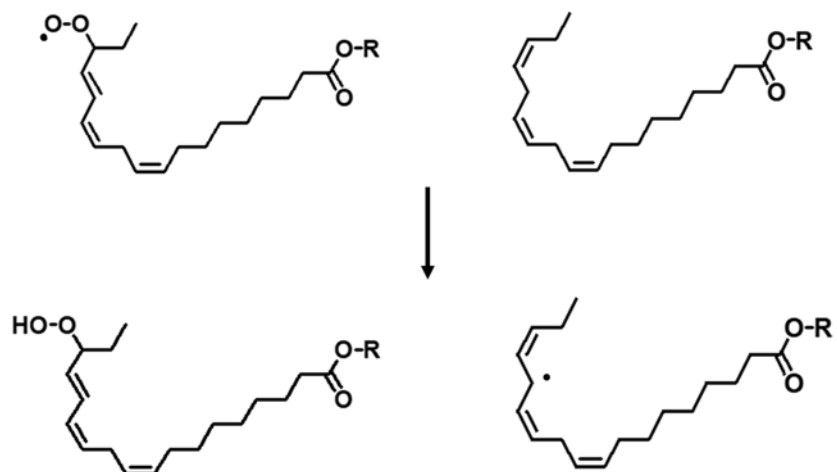
Reaction 4:

Reaction 5:
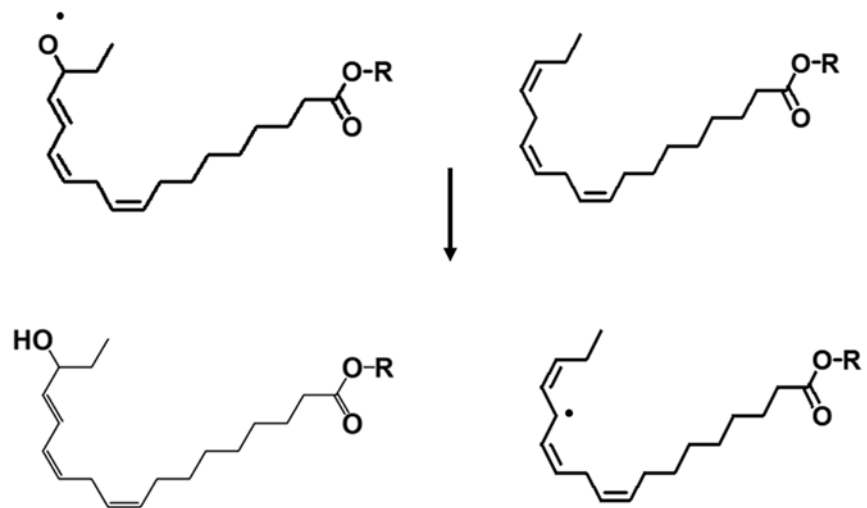
4. Hydroperoxide decomposition:

Hydroperoxide decomposition is initiated by the presence of driers such as Cobalt salts and lead to the generation of alkoxyl and peroxyl radicals which induce in their turn the propagation and the recombination steps. Hydrogen abstraction from the tertiary carbon with a hydroperoxide function leads to further product-formation, forming cross-linked (non-volatile) species and numerous other oxygen containing products such as alcohols, ketones, aldehydes and carboxylic acids.[9]

Reaction 6 :

$$ROOH + M^{(n+1)+} \rightleftharpoons [(ROOH)M]^{(n+1)+}$$

$$[(ROOH)M]^{(n+1)+} \longrightarrow ROO^* + M^{n+} + H^+$$

Reaction 7:

$$ROOH + M^{n+} \rightleftharpoons [(ROOH)M]^{n+}$$

$$[(ROOH)M]^{n+} \longrightarrow RO^* + [M^{(n+1)+}(OH^-)]^{n+}$$
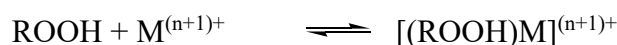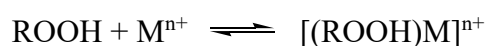
5. Termination

Once the free radicals are in appreciable quantity, they react with each other to form cross-linked products. The subsequent and successive reactions of cross-linked products with free radicals, gradually form a three-dimensional polymeric network, responsible for the solidification of the substrate, when the amount of the reactive sites is sufficiently high. (Reaction 6)

The bonds formed during this polymerization process may be carbon-carbon (-C-C-) (Figure 4), ether (-C-O-C-) (Figure 5) or peroxide (-C-O-O-C) (Figure 6). The nature of these bonds strongly influences the properties of the cross-linked products such as stability and strength. Generally, the best properties are found in polymers having a high carbon-carbon bond content. On the other hand, the flexibility of oxygen, ether and peroxide bonds generates polymers with low mechanical strengths.[10]

The type of polymeric linkages is defined primarily by three factors: the nature of the hydrocarbon or lipids, the oxygen concentration and the temperature. Various studies have shown that oxygen uptake by the substrate is greatly increased by the level of unsaturation in the chain. Under the same conditions, the contribution of ether and peroxide bonds to the polymerization of unsaturated

substrates (drying oils) is greater than that in saturated substrates (mineral oil). On the other hand, the contribution of carbon-carbon bonds is favored by relatively high temperatures and low oxygen concentrations. The polymerization process is often associated with a loss of unsaturation. Various studies have shown that during the formation and decomposition of hydroperoxides, double bonds are not usually consumed but rather restructured. This loss of unsaturation is therefore achieved during the polymerization step. The polymerization reactions responsible for the loss of unsaturation are shown in Figure 3.
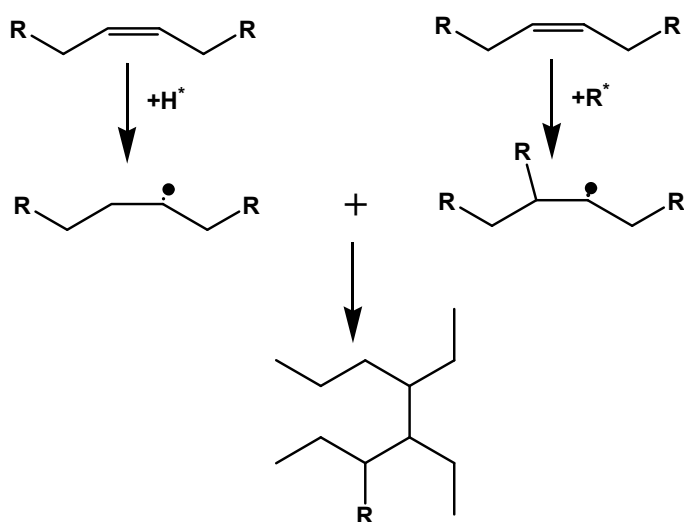
Figure 3. Reaction of polymerization between two free radicals and loss of unsaturation
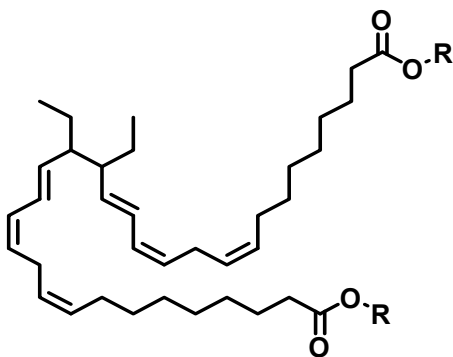
Figure 4 Dimer of two fatty acids with carbon-carbon bond
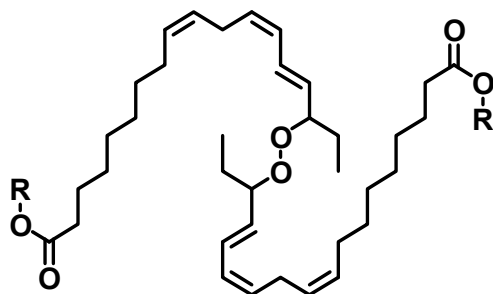
Figure 5. Dimer of two fatty acids with peroxide bond
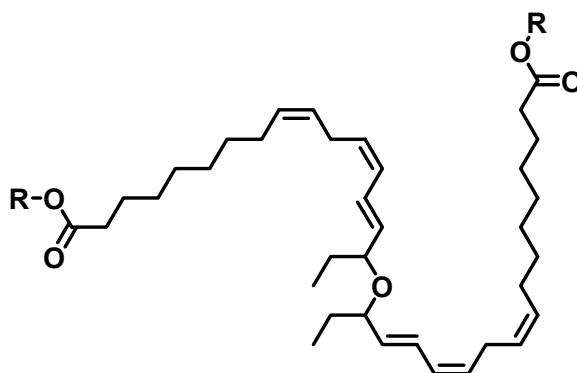
Figure 6. Dimer of two fatty acids with ether bond

Reaction 8:
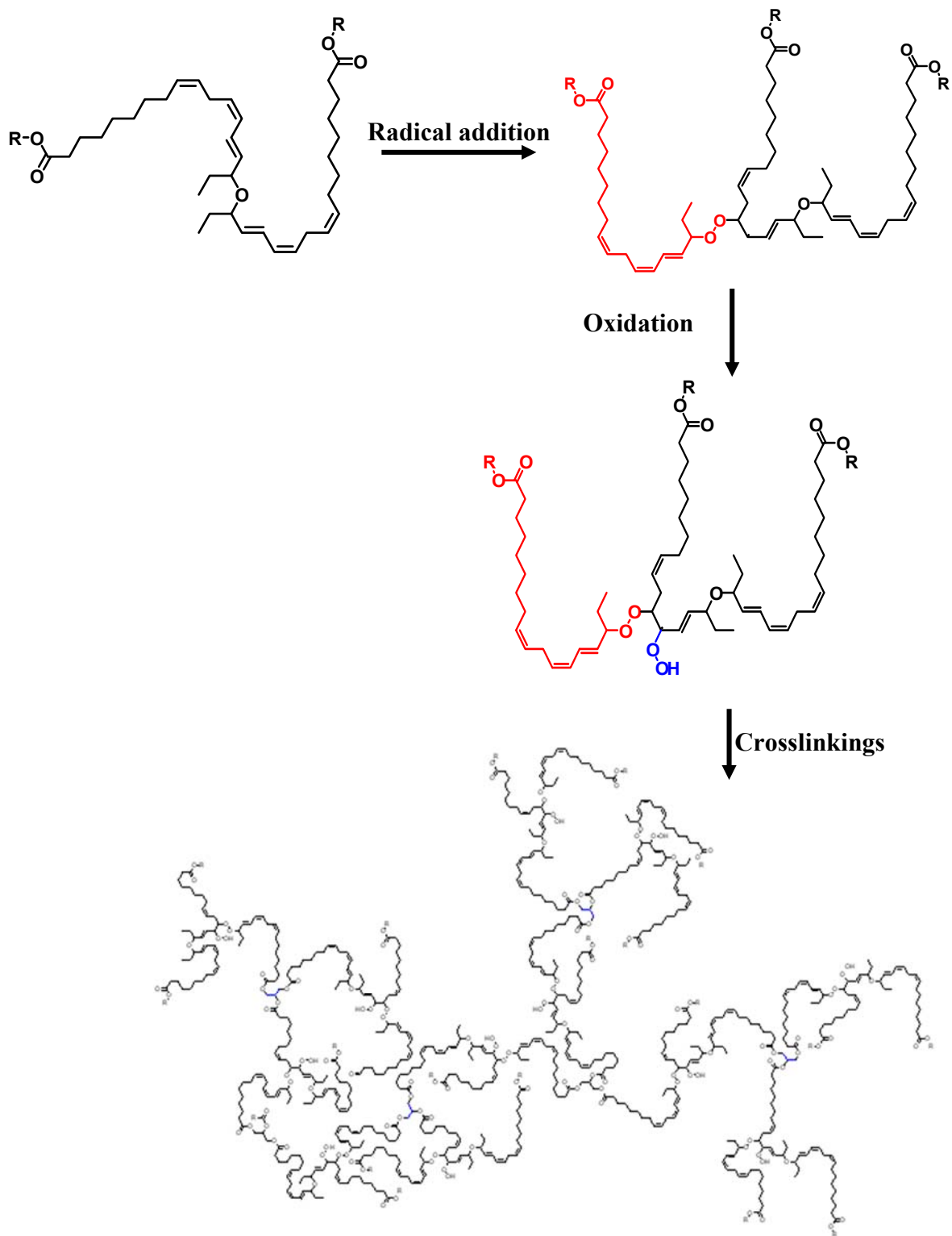
III. Oil paint degradation

1. β-scission degradation

During oil paint autoxidation and the formation of cross-linked polymer, fatty acid chains can be degraded and release low molecular weight volatile compounds at the same time. Those volatile compounds are behind the specific smell of an oil painting. Alkoxy radicals, RO•, are formed due to the homolytic cleavage of the hydroperoxides. These evolve by fragmentation of adjacent C-C and C-H bonds to produce aldehydes, ketones, alkyl and vinyl radicals which in turn react with H «and OH», and produce aldehydes or (un)saturated hydrocarbons. This is depicted in Reaction 9.

Reaction 9:
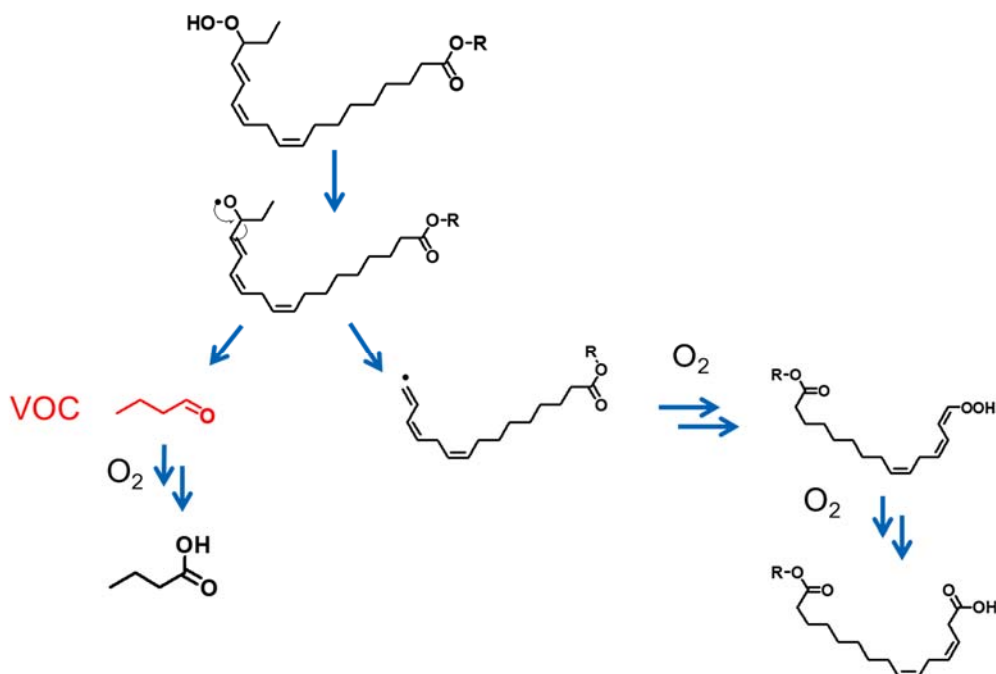
2. Metal soap formation

Metal soaps are complexes of metals and saturated fatty acids which grow in an underlying of painting and brake through the top surface in form of white protrusions (Figure 7). Metal soaps represent a real threat for oil art paintings and they are considered one of the main causes of oil paints degradations. Several research groups worked on the identification of metal soaps in many oil paintings and these studies show that lead[11] and zinc[12] compose the majority of metal soaps found in art oil paintings. Saturated free fatty acids such as palmitic acids (C16:0), stearic acid (C18:0) are not involved in the polymerization process. The hydrolysis of the ester bond between the fatty acids and the glycerol molecule lead to their release and they have more tendency to create complexes with the metallic ions. On the other hand, beta scission mechanism cause the degradation of fatty acids carbon chain and release saturated dicarboxylic acids as in the case of azelaic acid (nonanedioic acid, or di-C9:0).[2c, 13]

Figure 7. On the left, "Couple aux têtes pleines de nuage, Salvador Dali, 1936, Museum Boijmans van Beuningen.[12b] On the right, View on Delft, Johannes Vermeer, 1660-1661, Mauritshuis

Several analytical techniques were used to identify the metallic carboxylates. Fourier transform infrared spectroscopy (FTIR) allows the characterization of different types of metal soaps.[14] For example, the characteristic strong ν_a COO$^-$ band in the 1500-1600 cm^{-1} region allow the discrimination between lead and zinc palmitate, for the zinc soaps the band has a maximum around 1538 cm^{-1} and 1510 cm^{-1} in the case of lead soaps with a large peak at 1538 cm^{-1}.[15] Moreover, Raman spectroscopy technique allow the differentiation between the fatty acids chain length. The region between 1150 cm^{-1} and 1000 cm^{-1} which corresponds to the C-C stretching vibrations allows the discrimination of fatty acids carbon chain length. And the region between 1675 cm^{-1} and 1640

cm[-1] which corresponds to C=C stretching vibrations allows the detection of the unsaturated carbon chain.[14d] Secondary ion mass spectrometry (SIMS) is a complementary technique to other spectroscopic analytical methods. It allows the detection of both organic and inorganic compounds and their spatial distribution within the painting as well as the identification of metal soaps.[16] Solid-state nuclear magnetic resonance (ss-NMR) was applied to have a better understanding of metal soaps formation.[17]

IV.   Oil painting analysis

The different constituents of a painting can be identified through analytical techniques that can help unravel the history of the artwork. These techniques can help conservators to adopt the ideal conditions of restoration and conservation. However, works of art are usually of very high value, so the chemical analysis should preferably be micro or non-destructive, meaning that the sample available for analysis is very limited that work is not distorted from an aesthetic point of view. Thus, for decades, constant progress has been made in the field of analytical chemistry to propose techniques that are efficient and meet these criteria.

1.   Fourier transform infrared spectroscopy (FT-IR)

Fourier transform infrared spectroscopy (FTIR) analysis is an analytical technique that can characterize the chemical functions of organic, inorganic, crystalline or amorphous compounds.

The principle is to expose the sample to infrared radiation of different wavelengths. The molecules of the sample can absorb some of these radiations at wavelengths corresponding to the vibration frequencies of the chemical groups that constitute them.

The intensity of light absorbed at each wavelength is measured: a spectrum is obtained which is characteristic of the various chemical groups present. The comparison of the spectra with reference compounds makes it possible to identify certain substances. The advantage of this technique in the field of painting is the ability to obtain information on the type (s) of the organic compounds present (oil, wax, resin, proteins, metallic soaps, etc.). Derrick *et al* (1999), described the characteristics of the infrared spectra of various compounds found in the study of paint materials[18]. The FTIR

analysis also makes it possible to trace certain chemical modifications in the oil paintings during time or to study the influence of different conditions as heating, accelerated aging, restoration, etc.

FT-IR technique was also applied to study the autoxidation of linseed oil in order to understand the polymerization mechanism. Mallégol *et al.*[8, 19] investigated the long-term behavior of oil-based varnishes and paint as linseed and poppy-seed oil using the FT-IR technique. In their work, they focused on the formation of hydroperoxide group by observing the broad vibration band centered around 3425 cm^{-1}, the cis-double bond disappearance at 3010 cm^{-1} and 716 cm^{-1}, and the appearance of trans–trans conjugated double bonds at 987 cm^{-1} and trans–cis conjugated double bonds at 950 cm^{-1}.They also detected the formation of alcohols (nitrite band at 779 cm^{-1} after nitrogen monoxide treatment), aldehydes (bands at 2810 and 2717 cm^{-1} in gas phase), ketones (saturated and unsaturated at 1720 and 1698 cm^{-1}, respectively), carboxylic acids (saturated and unsaturated acid fluorides identified at 1843 and 1810 cm^{-1} after SF4 treatment), and peresters or γ-lactones (near 1770 cm^{-1}). In another study, the same group highlighted the role of transition metals such as cobalt in accelerating of the linseed oil autoxidation.[19b] Lazzari et *al.* explored the polymerization process and the degradation of linseed oil film, under both natural and accelerated weathering conditions.[2b] They remarked the decrease in the intensity of peaks at 2928 cm^{-1}, 2856 cm^{-1} and 727 cm^{-1}, attributed to unconjugated double bonds. At the same time, they observed the appearance of a broadband centered at 3430 cm^{-1}, due to hydroxyl groups, and of a weak absorption at 1633 cm^{-1} related to the formation of a conjugated double bond (Figure 9 & Figure 9).
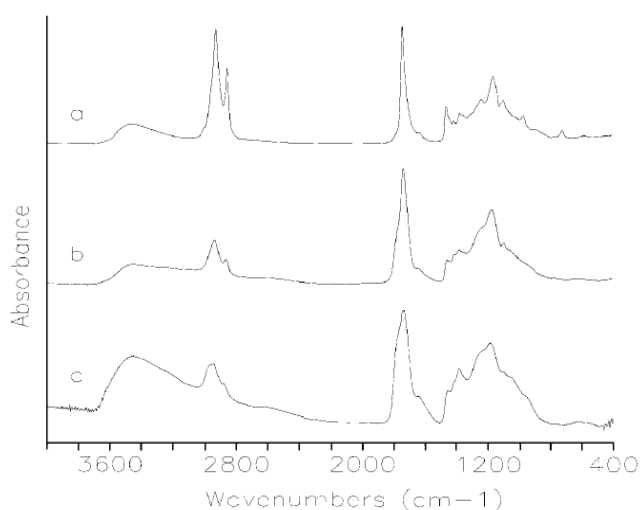
Figure 8. FTIR spectra of linseed oil photo-aged for (a) 7 h, (b) 487 h and (c) 1987 h[2b]
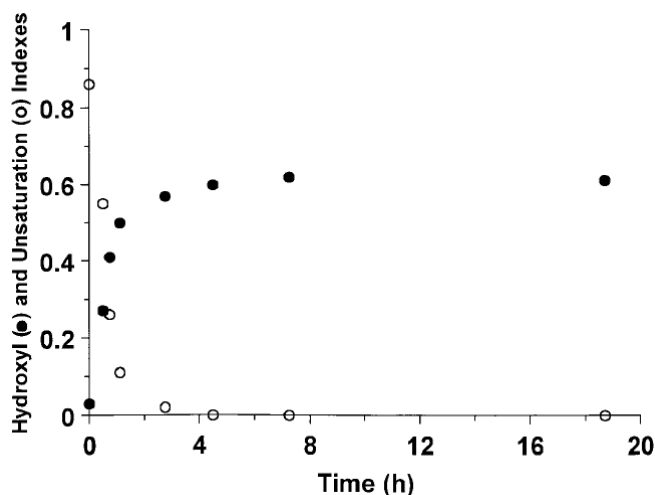
Figure 9. Variation of hydroxyl and unsaturation concentration during time in photo-aged linseed oil[2b]

On the other hand, FT-IR helped understanding the interaction between lead oxide and linseed oil during the polymerization process and showed that lead oxide accelerates the drying process and reduces the induction time, but without major change in the mechanisms involved and in the final composition.[20] Metal stearate was also detected by using FT-IR in oil paints. Metal soaps formation is characterized by the appearance of bands with COO⁻ antisymmetric and symmetric stretch at ~1550 cm^{-1} and 1400 cm^{-1} reflecting the ionized structure of the COO–metal bond.[21] FT-IR was applied in the studies of the degradation products formed due to ageing or deterioration of works of art.[22]

2. Raman spectroscopy

Raman spectroscopy is a non-destructive analytical technique, based on the physical phenomenon of Raman scattering. This phenomenon, highlighted by the Indian physicist Raman in 1928, is the inelastic diffusion of a monochromatic radiation (usually generated today by a laser) by a given material, generated by the coupling between the incident electromagnetic field and the vibration of molecules. This generates the emission of Stokes and anti-Stokes radiations, which are symmetrically offset with respect to the excitation wavelength. This offset corresponds to the vibration wavelength of the molecules. The Raman spectrum, obtained from the measurement of scattered intensity, constitutes a structural imprint of the studied material and gives information on the chemical composition, the structure and the molecular interactions of the material.

Raman spectroscopy is a very useful tool for the study of paints, because just like the XRF, XRD and FT-IR, it does not require any contact with the sample. An important asset of this analytical technique, especially in the case of hybrid materials such as paint, is that it can be used to characterize both amorphous and crystalline materials,[23] and organic[24] as well as mineral material. The identification of the binder is thus possible with Raman spectroscopy, but often difficult because of the changes caused by the aging of the paint. Raman spectroscopy proved its capability in monitoring the polymerization mechanism of linseed oil by following the formation and the disappearance of peroxide species and the evolution of the unsaturation values[1]. The comparison of obtained spectra of linseed oil before and after treatment by heating at 80 °C for 8 hours (Figure 10) shows the disappearance of peaks at 3010 and 1654 cm^{-1} corresponding for cis =C–H stretch and cis C=C stretch. The appearance of a broad band centered at 3472 cm^{-1} is also remarkable due to the presence of hydroxyl groups and the formation of the 987 and 971cm^{-1} peaks, which belong to trans-conjugated double bond and trans-out-of-plane C–H bend. Raman technique was used as well to study the difference in the oxidation reactions of fatty acids containing non-conjugated and conjugated double bonds in the presence of cobalt catalyst. And the study shows that the presence of allylic hydrogen contributes in the radical formation and the autoxidation mechanisms.[25]
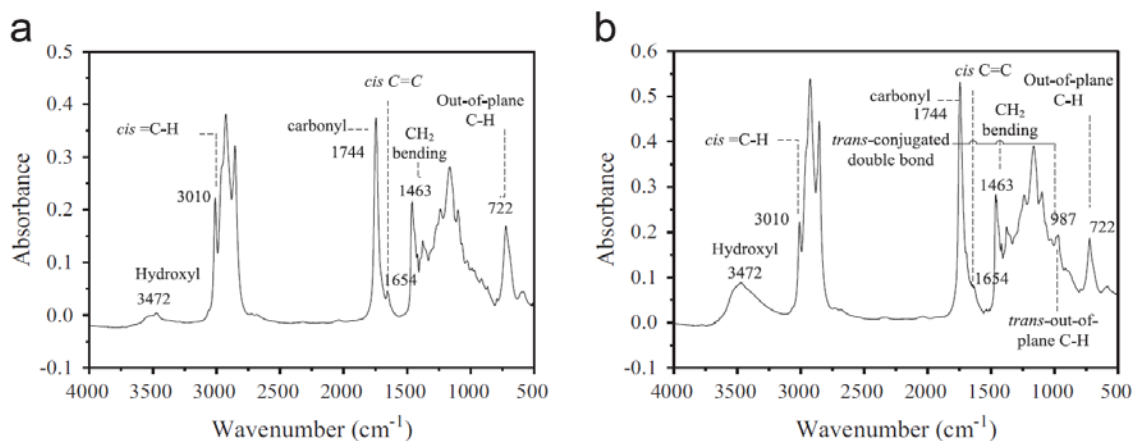
Figure 10. FTIR spectra of boiled linseed oil film (a) before reaction and (b) after 8h reaction at 80 °C[1]

An integrated approach based on chemometrics and Raman spectroscopy was also proposed to distinguish different aged binders of lipid paint such linseed oil, walnut oil and poppy-seed oil but also egg yolk,. Raman band around 2893 cm^{-1} corresponds to C–H stretching and allows the discrimination between different samples.[26]

3. X-ray fluorescence (XRF)

XRF is a non-destructive elemental analytical technique based on the interaction between an X-ray beam and the electronic procession of the atoms constituting the studied material. Under certain conditions, the interaction with an X-ray beam can cause the ejection of an E1 energy electron in a deep layer of the target atom, creating a gap in the atomic electron cortege. This generates an electronic reorganization allowing the return to equilibrium: the electronic gap is filled by an energy electron E2 originating from a more external layer. It is an electronic transition, accompanied by the release of excess energy, resulting in the emission of an X-ray energy E2 - E1, characteristic of the target atom. Depending on the electronic level to which the ejected electron belongs (main quantum number n = 1, 2 or 3), different emission lines will be detected (respectively emission lines called K, L or M).

The XRF analysis runs without contact with the object and therefore provides a knowledge of the elemental composition of the material by short-term analysis (of the order of a few minutes per tip). In many cases, this concept helps to obtain an idea on the pigments constituting the material, especially when the characteristic chemical elements of certain pigments are detected (for example the presence of mercury in vermilion or the joint presence of copper and arsenic in Veronese green). The color of the superficial layer is obviously an information to be taken into account. However, it is important to be careful with XRF analysis because some of the emissions detected do not come from the surface layer of paint, but from the underlying layers. This depends on the chemical elements and the thickness of the layers.

In several studies, XRF was combined with other techniques such as Raman spectroscopy, in order to determine the composition of some cultural heritage objects. For example, the analysis of a precious illuminated manuscript belonging to the Trivulziana library collection led to the identification of the original pigments and the overpainting layers.[27] The XRF mapping allows pigments identification as well their spatial distribution in the painting. Moreover, X-rays

penetration inside the paintings allows the identification of elements from different layers of the painting. More recently, XRF spectroscopy alongside other techniques were applied to the analysis of paintings present on an old Egyptian coffin. XRF analysis were done with a portable spectrometer (ELIO Spectrometer, XGlab srl, Milan, Italy). The analysis revealed the elemental composition of the different pigments. For example, the white area was composed mainly of calcium, the yellow pigments contained iron, while the green color was copper based.[28]

4. Nuclear magnetic resonance spectroscopy (NMR)

Nuclear magnetic resonance spectroscopy was also applied to the study of oil paintings dated to the early 20th and the late 17th century in order to investigate the hydrolysis and oxidation processes of the oil paint.[29] Proton NMR only allows the analysis of the "Mobile phase" of the oil paintings. "Mobile phase" of an oil paint sample is easily separated by solvent extraction from the insoluble part. It provides information about the change in oxidation levels that have occurred during aging of an oil painting. The comparison between fresh and aged linseed oil (Figure 11) shows that the number of unsaturation in the alkyl chain of fatty acid decreased in the aged oil. Moreover, the triglycerides content of paints extracts decreased with aging due to their hydrolysis into glycerol and free fatty acids.
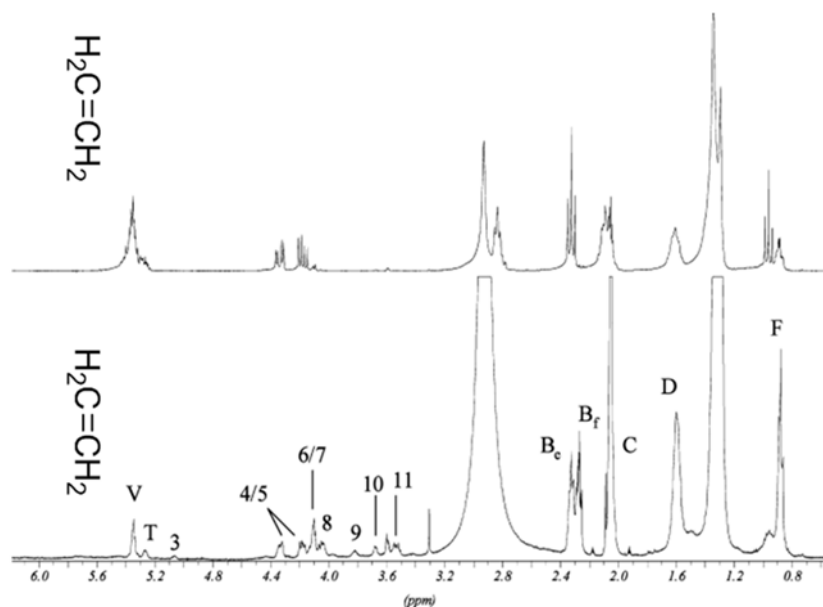
Figure 11. ^{1}H NMR spectra of fresh (top) and five-year-old (bottom) oil paint in acetone-d[29]

In another study, ^{13}C-labeled ethyl linoleate (^{13}C-EL) oxidation was monitored with ^{13}C NMR in order to follow the evolution of hydroperoxides (ROOH) and peroxy (ROOR) links. The ^{13}C-EL was chosen to be a model compound for alkyd paints. By comparing the ^{13}C NMR spectra of ^{13}C-EL, in the beginning and after three months of oxidation, the obtained results reveal the decrease of the non-conjugated cis- C=C peaks (127–132 ppm) and the formation of conjugated C=C peaks (132–136 ppm). Furthermore, there were a few other species formed including hydroperoxides (ROOH) and peroxides (ROOR).[25]
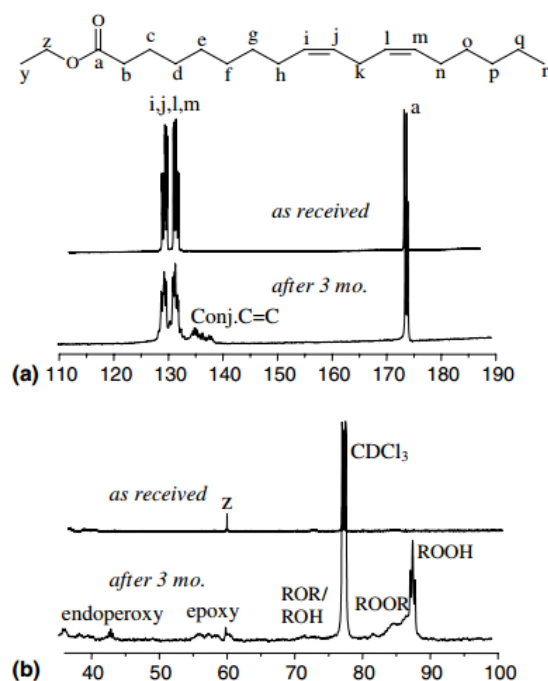
Figure 12. ^{13}C NMR spectra of the ^{13}C-ethyl linoleate in the beginning of oxidation and after 3 months without any catalyst[25]

On the other hand, solid-state NMR spectroscopy is capable of analyzing small semi-solid samples, and it was used to characterize the entire painting films.[30] ^{1}H-NMR spectra showed no difference between the soluble and the insoluble parts of oil paints. However, the comparison of ^{1}H-NMR spectra belonging to fresh and aged oils indicates a decrease in the intensity of double bonds signals. As a result, NMR spectroscopy proved to be an alternative technique for organic paint binders discrimination.[31]

5. Solid-state NMR spectroscopy (ssNMR).

Liquid NMR presented some limitations in the analysis of oil-based binders, due to the insolubility of the paint film. Solid-state NMR can be used as an alternative technique for the analysis of the solid paint film without destroying the sample. This technique is suitable for the analysis of both organic and inorganic components of paintings. However, low sensitivity is a main disadvantage which kept this technique limited to the analysis and detection of organic and metallic complexes known as metallic soaps.

Catalano *et al*. synthesized and analyzed different types of lead carboxylates metallic soaps such as lead stearate, lead palmitate, lead azelate, lead oleate and lead heptanoate. Based on the ^{207}Pb chemical-shift tensor, they succeeded to distinguish between lead azelate which has a span around 2640 ppm, a skew of 0.66, and an isotropic chemical shift at 1188 ppm and both lead stearate and lead palmitate that have similar NMR parameters (spans of 700 ppm, skews of 0.5, and isotropic chemical shifts near 2130 ppm). Lead heptanoate has similar span and skew values as lead azelate but a difference of 100 ppm for the isotropic chemical shift. ^{207}Pb NMR results depend on the length of carboxylate chain, however the presence of cis-double bonds induces a curve in the acyl chain causing alterations in crystal packing as in the case of oleate which has the same number of carbon as stearate but the ^{207}Pb chemical-shift tensor of oleate has a span at 2350 ppm, a skew of 0.66, and an isotropic chemical shift at 1277 ppm. The ^{13}C ssNMR spectra shows a doubling in the resonance of carbons located in the position C1, C2 and C3 near the lead atom. This doubling in resonance is due to the presence of two fatty acid chains with two possible geometric coordination to the lead ion.

The sensitivity of these experiments was further enhanced by Dynamic Nuclear Polarization DNP, in which the proton polarization is increased by a microwave-driven transfer of polarization between unpaired electrons and protons. Recently, Kobayashi *et al*. demonstrated that DNP could be used to record the ^{207}Pb spectrum of lead carbonate phase in the white lead pigment. A mixture of TEKPoL biradical and 1,1,2,2 tetrachloroethane: methanol-d4 (96/4) was added to the sample and play the role of polarization source. DNP enhances the signal by a factor of eight under static conditions in the case of white lead.

Kehlet et *al.* applied the ultrafast spinning solid-state NMR spectroscopy, which offers higher resolution in comparison to the conventional solid-state NMR. This technique demands only few milligrams of sample making it a suitable method for the analysis of art oil paint. The ^{13}C showed a shift in the carbonyl signal from 173 ppm in the linseed oil reference sample to 182 ppm in oil paint sample, which corresponds more to a carboxylate rather than an ester bond. Those results indicate that triglycerides ester bonds were hydrolyzed during polymerization and aging process.

6. Gas chromatography mass spectrometry pyrolysis

GC-MS provides information on the organic compounds present in paint. It consists on the coupling of gas chromatography (GC) and a mass spectrometer (MS). GC-MS separates the constituents of a sample by chromatography and collects their mass spectrum in order to identify them. The presence of oil, waxes, resins, polysaccharide gums and animal glues can thus be demonstrated in paint samples.[32] However, this technique does not allow the analysis of non-volatile products, which often make up the majority of old paintings. In the absence of volatile compounds, it may be used after pyrolysis of the materials. Gas chromatography techniques are used and applied for the analysis of non-cross-linked compounds of linseed oil paint films. Methanolic extracts of the soluble part of a linseed oil film were investigated by GC-MS following an offline or online derivatization. The two strategies give reproducible and comparable results, online method is faster however the offline one is more suitable for a mixture of binding media that demands separation steps.[33] The offline methylation was done by methylation or trimethylsilyl derivatization. On the other hand, the offline derivatization is based on thermally assisted (trans)methylation with tetramethylammonium hydroxide using Curie-point pyrolysis–GC–MS.[13] Both modes of derivatization allowed the detection by GC-MS of a series of short-chain fatty (di)acids and C_{16} and (oxidised) C_{18} fatty acids. In another study, GC-MS techniques were applied to investigate the lipids based paint film degradation after irradiation with UV light and exposition to NO_x and SO_2 gases.[34] The obtained results showed the cleavage of fatty acids chains and the formation of oxalic acid. The developed method was later applied on Cimabue, Raffaello and Boucher paintings, and the analysis by GC-MS indicates the presence of oxalic acid and oxidized carboxylic acids. This study focused on the understanding of oil paint aging behavior, highlighting on the fatty acids chains degradation and the formation of free carboxylic acids. GC-MS allows as well the identification of lipid binders used in oil paintings by calculating the ratio between the

areas of stearic and palmitic acid peaks (S/P) as it is shown in Figure 13. Saturated fatty acids as palmitic and stearic acids, in contrary to the unsaturated fatty acids, are more stable during aging of oil paints, do not participate in the polymerization and are less influenced by the present pigments in the sample process.[35,36] The effect of pigments on the cross-linking mechanism of siccative oils was also under investigation using GC-MS.[37] In this study, they compared the composition of linseed oil paints layers without pigments, in the presence of lead white, zinc white and cinnabar (HgS). Fatty acids distribution was obtained after pyrolysis/silylation with hexamethyldisilazane (HMDS) as it is shown in Figure 14. The obtained results show that the presence of lead white and zinc white contributes to the formation of octanoic and nonanoic acids.[37]
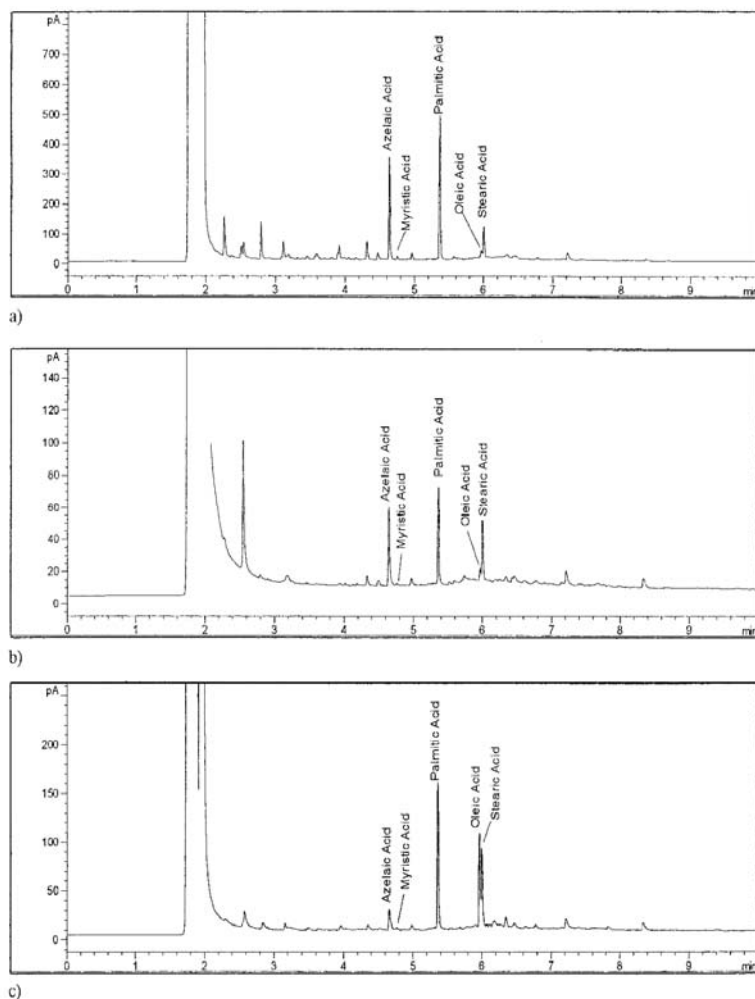
Figure 13. Chromatograms of ethyl esters of fatty acids from drying oils: (a) poppy oil, (b) linseed stand oil and (c) linseed stand oil in presence of cadmium red pigment[36]
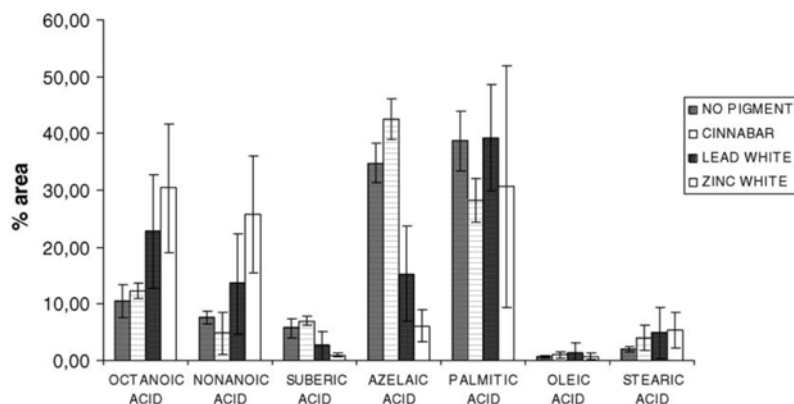
Figure 14. Fatty acids distribution obtained from pyrolysis/silylation of linseed oil paint layers with and without pigment[37]

7. Mass spectrometry

Mass spectrometry is an accurate and robust technique for the identification of siccative oil composition such as linseed oil.[38] *Van den Berg et al.*[3] applied MALDI-TOF MS and FT-ICR techniques to study the effect of linseed oil processing on its triglycerides composition. Results showed that the degree of oxidation increases after oil heating, and is enhanced by the presence of lead pigment. They also succeeded to identify triglycerides oligomers. MALDI-TOF MS approach was used for the discrimination of egg and oil binders in painted artworks by fingerprinting. The identification of specific markers belonging to various lipid classes, such as triacylglycerols (TAGs) and phospholipids (PLs), and their oxidation by-products allows the differentiation between egg and oil binders.[39] However, the analysis of dried siccative oil is more challenging, since siccative oils transform into a highly cross-linked and insoluble polymer upon autoxidation. *Muizebelt et al.* worked on the identification of cross-linked fatty acids by ESI-MS techniques.[40] In their studies, they prepared layers of ethyl ester of linoleic acid and methyl ester of ricinoic acid (MR) mixed with Co/Ca/Zr drier, which were allowed to react with air. The recovered oligomer from the polymerization mechanism of unsaturated fatty acids was analyzed with ESI-MS equipped with a quadrupole analyzer. The mass spectrum (Figure 15) show the presence of dimers, trimers and tetramers of linoleic acid. The identified compounds indicate the formation of C-C, ether and peroxide crosslinks. *Zovi et al.*[41] investigated the stand oil reactions by identifying the resulting products using NMR and mass spectrometry. In their work, they heated the linseed oil at 270 to 360 °C under nitrogen flux, and then they cleaved the bonds between the glycerol and the fatty

acids by saponification in order to recover only the cross-linked fatty acids. The NMR and MS analysis confirmed the formation of monounsaturated ring of six carbon atoms resulting from a Dials-alders addition. Furthermore, the MS analysis, signals the addition of an allylic radical on double bonds, followed by combination or elimination reactions. Secondary ion mass spectrometry (SIMS) provides several advantages in comparison to other mass spectrometry techniques. SIMS allows the identification of both organic and inorganic compounds of paintings, and is able to detect metallic soaps. However, this technique has some limitations when it comes to diacids and other polar compounds.[16b] HPLC-ESI-Q-ToF allows the acquisition of triglycerides profile and the characterization of lipids present in oil paints. Unlike the GC-MS which is limited by the identification of the composition of fatty acids only.[42]
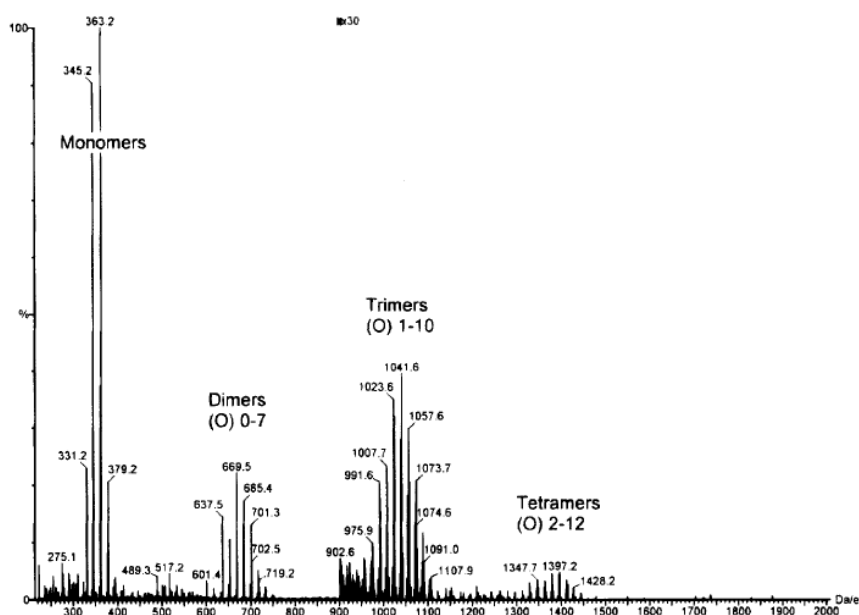
Figure 15. ESI-MS spectrum of cross-linked linoleic acid[40]

Van Loon et al.[43] proposed the direct temperature-resolved TOF-MS techniques as a fingerprinting strategy for the identification of oils, resins, waxes and other compounds present in complex samples in paintings. Modern time-of-flight mass spectrometers can offer high resolution and sensitivity. The acquisition of accurate mass permits to calculate the Kendrick mass defect (difference between the nominal and accurate mass) which can be graphically represented by Kendrick plot (Figure 16). The Kendrick plots are a graphical representation that can be served as fingerprint for fast identification of binding media.
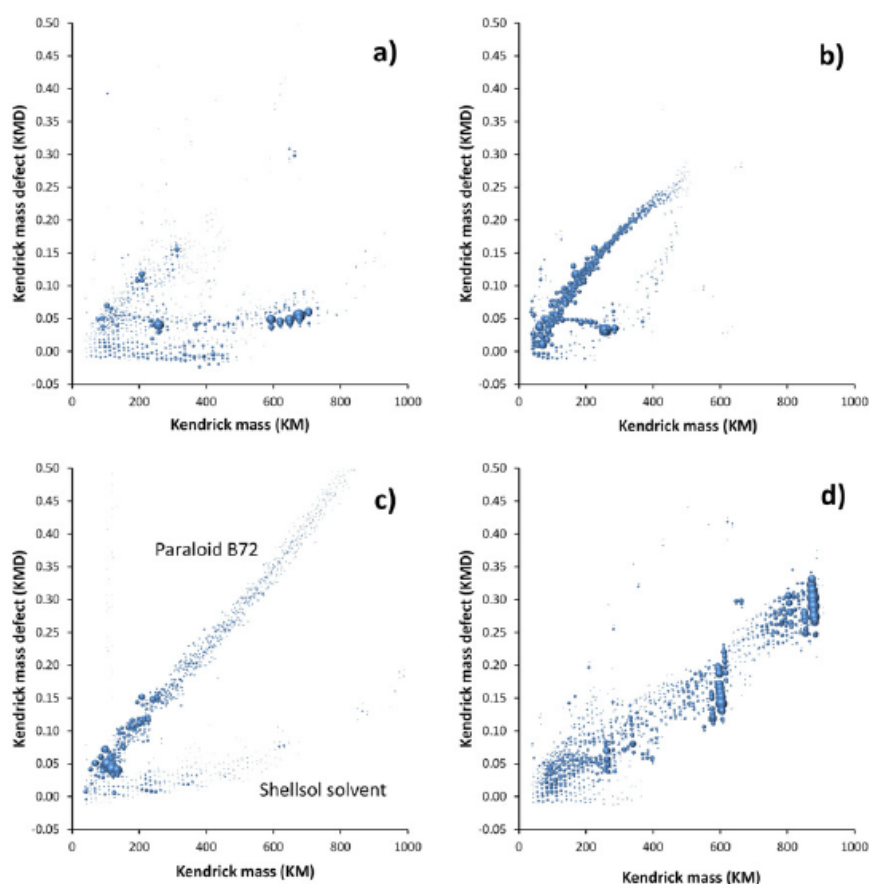
Figure 16. Kendrick plots of paintings and conservation reference materials, beeswax (a), rabbit skin glue (b), Paraloid B72 in Shellsol A (c), fresh linseed oil (d).[43]

V.   Conclusion and thesis outlines

Several techniques have been used for the characterization of the cross-linked polymer formed by the polymerization of drying oils but until now, these studies have only provided fragmentary information. The most widely used technique is Fourier Transform Infrared Spectroscopy (FTIR). The major advantage of this technique is that the sample does not need a pretreatment and can be analyzed in its solid form. However, it can detect only the formation or disappearance of functions without attribution of structures. Raman spectroscopy has also been applied in the analysis of lipids and presents the same limitations as FT-IR. Gas Chromatography coupled to Mass Spectrometry (GC-MS) is the technique usually used to determine and quantify the fatty acid composition of the triglycerides constituting the oils after trans-esterification in acid medium by BF_3-methanol. Unfortunately, for a polymerized oil, mass spectrometry (GC-MS) only gives access to the fatty acids that are not involved in the cross-linked network. ^{1}H and ^{13}C NMR liquid spectroscopy was also used on model samples because of its low sensitivity it was not applied on oil painting. NMR in solution is limited to the analysis of the soluble fraction of the polymer. Solid or in gel NMR does not allow the study of the cross-linked polymer considering the complexity of the sample and the large width of the obtained signals.

Our current work aims to characterize the structure of the network formed from the siccativation of linseed oil, identify the intermediates formed during the polymerization and finally understand the degradation process of this film and its interaction with the different pigments present. High-resolution mass spectrometry is the only technique that can give us access to the cross-linked structures formed between the different unsaturated fatty acids and the different aging-related changes in the very small amounts of available sample (less than one milligram). To perform this analysis, we proposed a chemical treatment that allows the cleavage of our polymer at the level of glycerol without altering the changes in the network formed between the fatty acids and at the same time to derivatize the fatty acids to improve the sensitivity of detection.

Results and discussion

I.   Linseed oil analysis by FT-ICR

First, we studied the composition of linseed oil before the drying process. We analyzed a fresh linseed oil sample purchased from Sigma-Aldrich using FT-ICR high-resolution mass spectrometry. The mass spectrum (Figure 1) shows the complexity of the fresh linseed oil. Triglycerides are the major components in linseed oil; they are formed by different combinations of five different fatty acids: saturated acids (palmitic acid (C16:0) and stearic acid (C18:0)) mono-unsaturated acid (oleic acid (C18:1)) and polyunsaturated acids which make up the major triglycerides such as linoleic acid (C18:2) and linolenic acid (C18:3). Some of these triglycerides are oxidized and one or two more oxygen are added to the carbon chain. Trilinolenin, which has nine unsaturation, is the major triglyceride present in linseed oil (Table 3). This analysis shows the heterogenic and complex composition of linseed oil. Moreover, it offers a prevision on the challenge of analyzing the polymerized linseed oil.
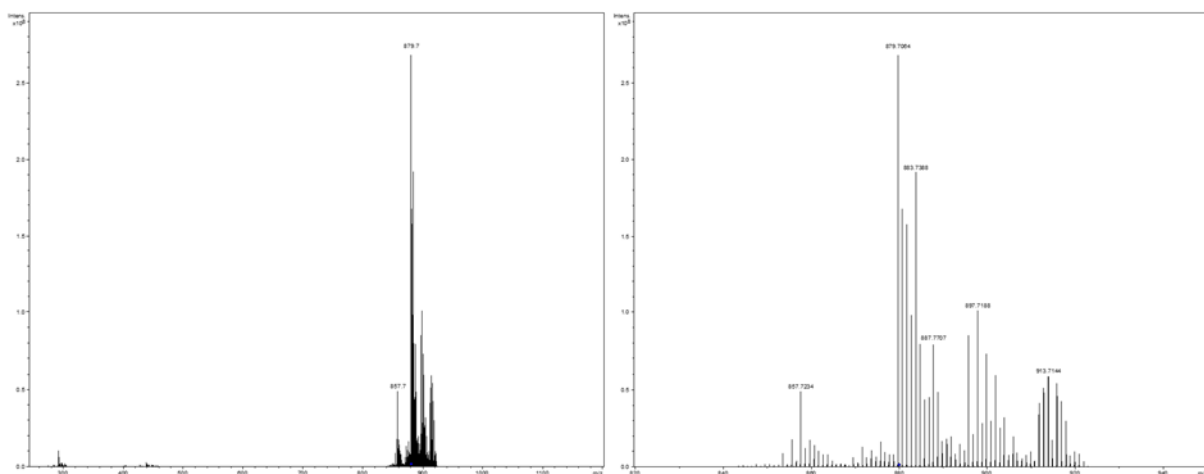
Figure 17. FT-ICR analysis of (Sigma Aldrich) linseed oil, on the left the entire MS spectrum and on the right zoom on the triglycerides zone.

Table 3. List of the triglycerides molecules present in the analyzed linseed oil

TAG	$C_xH_yO_zLi$	$[M + {}^7Li^+]$	Δm ppm	CN : DB	ECN	I
PLnLn	$C_{55}H_{94}O_6Li$	857,7234	2,2	52 : 6	40	49354162
LnLnLn	$C_{57}H_{92}O_6Li$	879,7233	1,5	54 : 9	36	268283447
LLnLn	$C_{57}H_{94}O_6Li$	881,7205	2,7	54 : 8	38	158314050
LLnLn/OLnLn	$C_{57}H_{96}O_6Li$	883,7388	1,9	54 : 8	38	191671885
OLLn/SLnLn/LLL	$C_{57}H_{98}O_6Li$	885,7518	1,2	54 : 8	38	43526744
OOln	$C_{57}H_{100}O_6Li$	887,7674	0,2	54 : 5	44	79969891
LnLnLn1O	$C_{57}H_{92}O_7Li$	895.7030	1,5	54 : 9	36	85261963
LLnLn1O	$C_{57}H_{94}O_7Li$	897,7154	2,1	54 : 8	38	101021333
OLnLn1O	$C_{57}H_{96}O_7Li$	899,7311	2,6	54 : 7	40	73852574
OLLn1O/LLL1O	$C_{57}H_{98}O_7Li$	901,7467	3,6	54 : 6	42	59558568
LnLnLn2O	$C_{57}H_{92}O_8Li$	911,6947	1,5	54 : 9	36	41368275
LLnLn2O	$C_{57}H_{94}O_8Li$	913,7103	2,1	54 : 8	38	59356891

II.   Development of depolymerization method

No study has succeeded in characterizing the detailed structure of the formed polymer, neither the process responsible for the hydrolysis of ester bonds and the release of fatty acids that cause the degradation of the solid film. The characterization of the structure as well as the knowledge of all the reactions that occur during the aging of the painting will allow us to evolve the techniques of conservations and restorations. Polymerized linseed oil forms a very complex and insoluble solid network, which makes its analysis and characterization a challenge for analytical chemistry. In addition, these complex materials are generally available only in very small quantities due to strict limits imposed on the sampling of works of art. Despite all these difficulties, several studies were carried out for the characterization of these "cross-linked" structures and several analytical techniques were proposed. Actually, all these studies have provided general information on the polymerization process and none of these techniques has succeeded in unveiling the structure of the formed network.

High resolution mass spectrometry is the only technique that can give us the opportunity, starting from minimal quantities of samples, to identify the cross-linked structure formed between different unsaturated fatty acids as well as the different modifications that may have occurred on this structure under the influence of aging and other factors like cleaning. However, in spite of that, this technique faces some limitations; the film of polymerized oil is insoluble and the free fatty acids ionize negatively, which makes the analysis more complex and their detection less sensitive. Johnson *et al*. already proposed a mechanism for derivation of fatty acids by forming Alkyldimethylaminoethyl[44] ester. An amine function ionizes well in positive mode and improves the analysis of acids in mass spectrometry. The first step is to convert the free fatty acids to acyl chloride by reacting with an oxalyl chloride, than a nucleophilic addition/elimination reaction with dimethylaminoethanol lead to the esterification of the fatty acid. In our case, the fatty acids are linked to glycerol, and it is preferred to avoid hydrolyzing the triglyceride ester linkages, which causes side reactions able to bring changes in our fatty acid chains. For these reasons, we have chosen to carry out a trans-esterification of our triglycerides, this reaction is well known in the field of biodiesel production, used to obtain methyl esters of fatty acids from triglycerides. Starting from this notion, we replaced the methanol used in the production of biodiesel by an excess of amine containing molecule

(dimethylaminoethanol, 3-pyridylcarbinol and 3- (Dimethylamino) -1-propylamine) (Figure 18) in the presence of sodium hydride which plays the role of a base. The base will deprotonate the alcohol or the amine which in turn will cleave the ester bond between fatty acids and glycerol, and reform an ester or amide bond with the fatty acid.
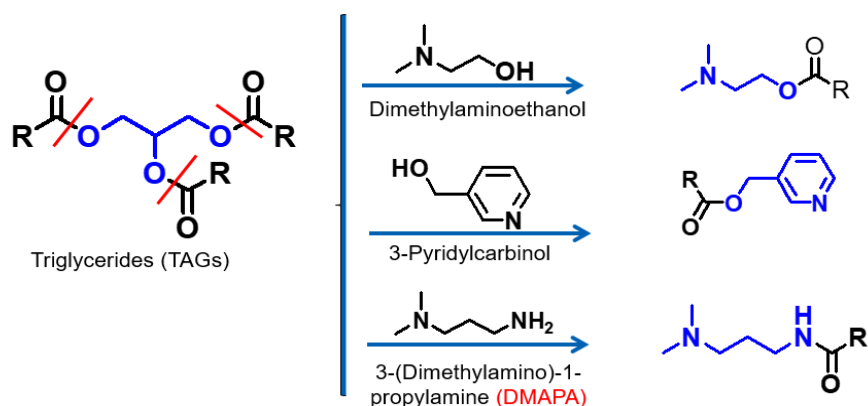
Figure 18. Trans-esterification and trans-amidation reactions of triglycerides.

1. Trans-esterification reaction with dimethylaminoethanol

Our first reactions were carried out using fresh linseed oil, in order to optimize our transesterification conditions. ^{1}H NMR analysis (Figure 20) of the obtained product following the transesterification reaction of linseed oil with 2-dimethylaminoethanol, shows the presence of characteristic peaks of the free carboxylic acid function (triplet at 2.4 ppm) and the disappearance of the characteristic peaks of the triglycerides (the quadruple doublet at 4.15 ppm represents the characteristic peaks of the glycerol molecule (Figure 19)). These results show that ester bonds between 2-dimethylaminoethanol and fatty acids are hydrolyzed due to the presence of H_2O molecules.
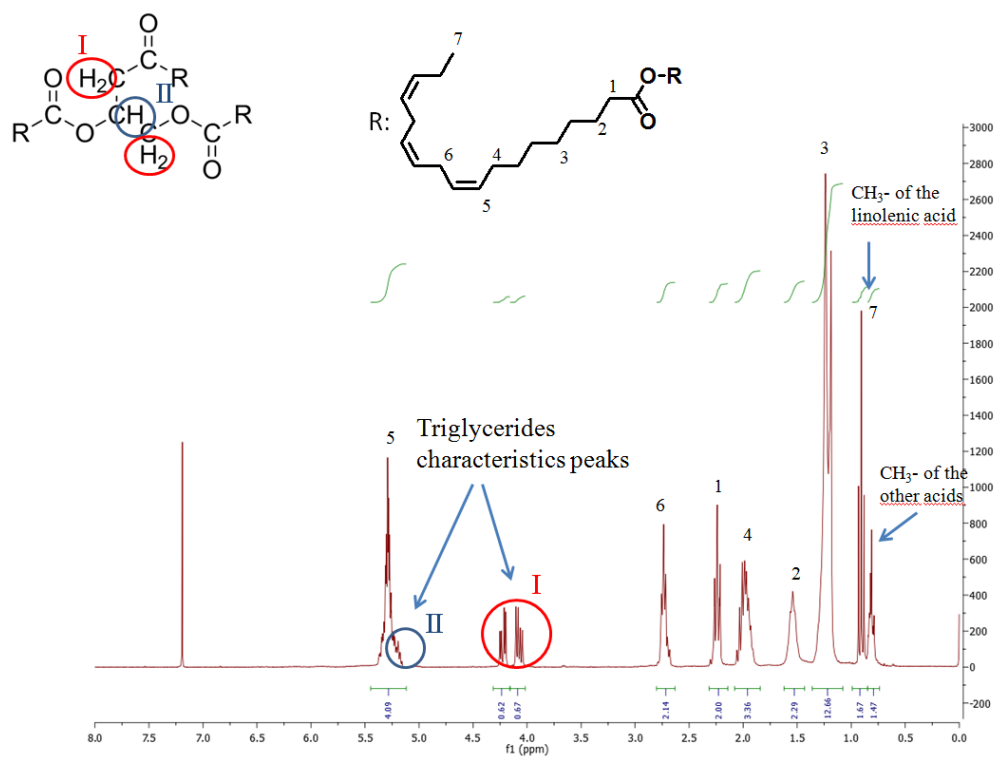
Figure 19 ^{1}H NMR spectrum of linseed oils in CDCl$_3$
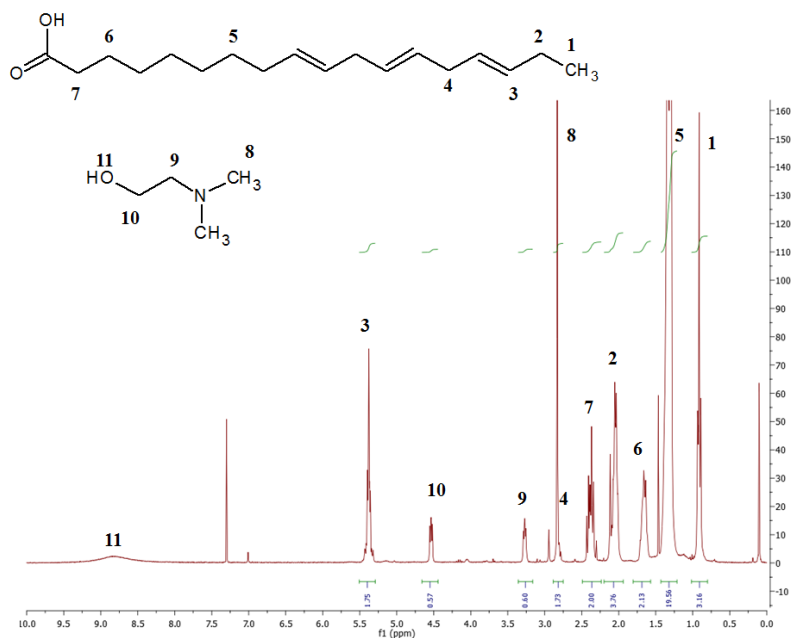
Figure 20. ^{1}H NMR spectrum in CDCl$_3$ of the products obtained after transesterification of linseed oil with 2-dimethyleaminoethanol after 90 min of reaction

2. Transesterification reaction using 3-pyridylcarbinol

In the case of 3-pyridylcarbinol, ^{1}H NMR analysis (Figure 21) indicates similar results to those obtained with 2-dimethylaminoethanol. The characteristic peaks of triglycerides (in the zone of 4-4.5 ppm) have disappeared and those of free carboxylic acid function are present at (2.4 ppm and 9 ppm). The presence of free fatty acids as products shows that the ester linkage between the glycerol and the fatty acids has been successfully cleaved, whereas the ester bond between the fatty acids and the derivatization molecules is hydrolyzed. This is caused by water molecules most probably formed by the conversion of glycerol to acrolein under the effect of the base present in the reaction medium since we worked in anhydrous conditions.
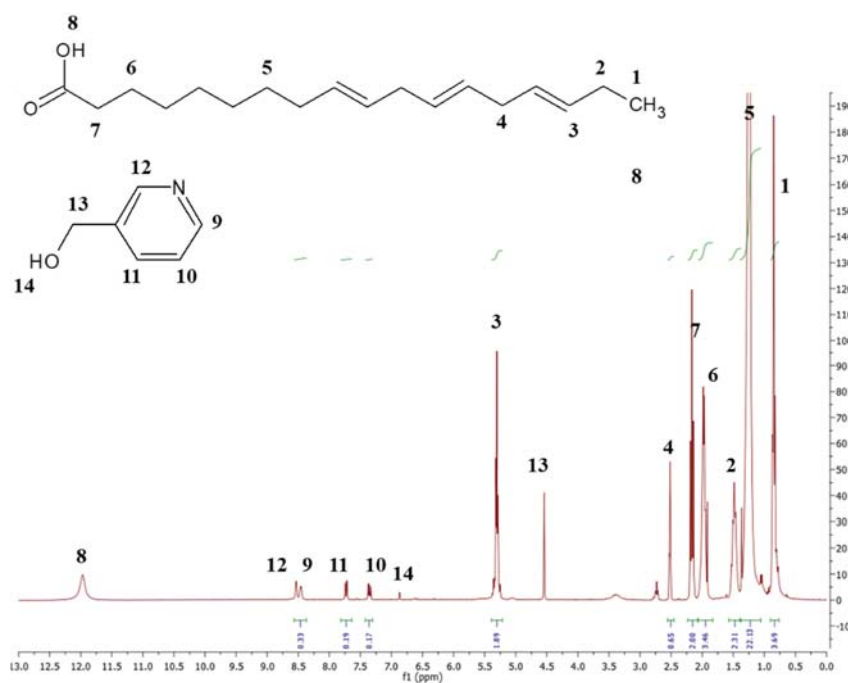
Figure 21. ^{1}H NMR spectrum in DMSO of the products obtained after transesterification of linseed oil with 3-pyridicarbinol after 90 min of reaction

3. Transesterification reaction using 3-(dimethylamino)-1-propylamine

The NMR spectrum (Figure 22) of the resulting products from the reaction of 3-(dimethylamino)-1-propylamine and linseed oil shows a sharp decrease in the intensity of glycerol characteristic peaks at 4 ppm, and the absence of carboxylic acid characteristic peaks. The shift of peaks corresponding to the amine group hydrogen of 3-(dimethylamino)-1-

propylamine from 1.2 ppm to 7.5 ppm which corresponds to an amide function confirms that the linseed oil trans-amidation was successful.

Between these 3 molecules that carry the tertiary amine function, the 3-(dimethylamino)-1-propylamine compound showed a better yield (100%) since the amide bond is more resistible to the hydrolysis reactions that can pass through the release of 2 H_2O by a glycerol molecule during its conversion to acrolein. In this work, we developed a new strategy that will allow us for the first time to analyze and identify the network structure formed between unsaturated fatty acids as well as developed a new derivation technique. This technique can be used in other areas of lipidomics and is much simpler and more efficient compared to other derivation methods that have already been proposed in the literature. The obtained product from linseed oil trans-amidation was also analyzed with FT-ICR MS. The mass spectrum (Figure 23) shows that triglycerides were completely converted to derivatized fatty acids. The spectrum also indicates that the linolenic acid is the main fatty acid in linseed oil. Moreover, MS spectrum confirms that the fatty acids carbon chain is intact and the trans-amidation reaction does not generate any alteration on their carbon chain.
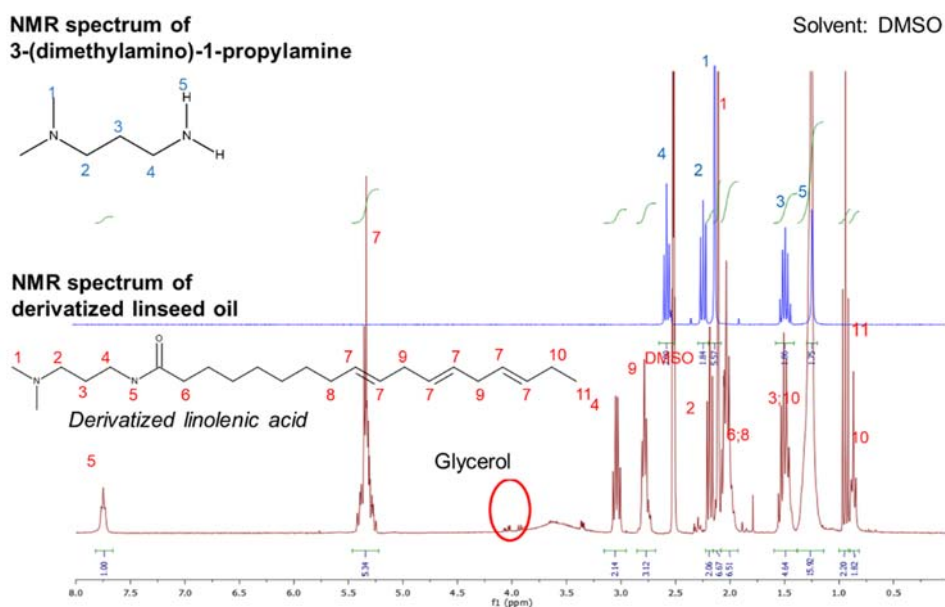
Figure 22. On the top, ^{1}H NMR spectrum in DMSO of 3-(dimethylamino)-1-propylamine and on the bottom ^{1}H NMR spectrum in DMSO of products obtained after 12 hours of reaction between linseed oil and 3-(dimethylamino)-1-propylamine
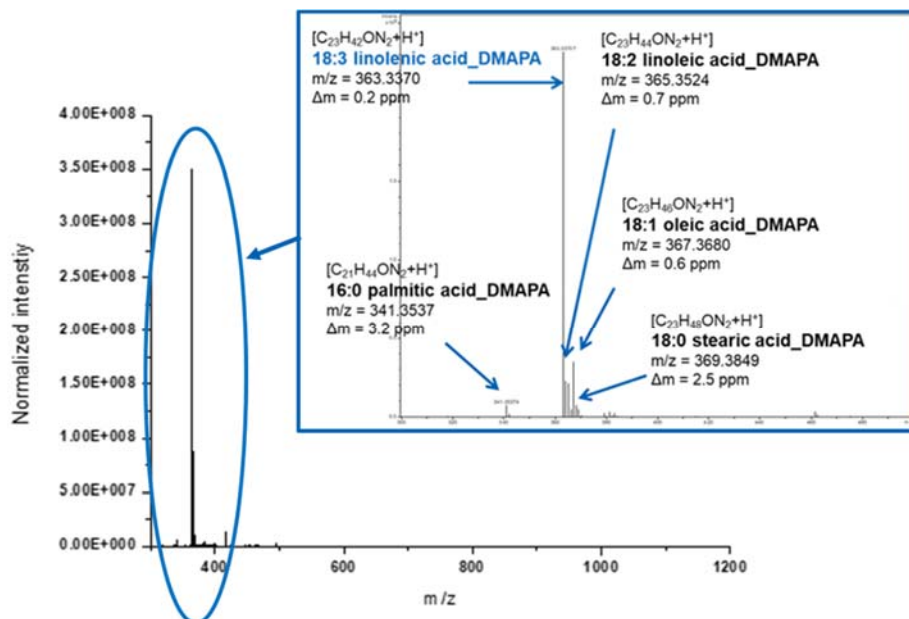
Figure 23. Linseed oil FT-ICR MS spectrum after trans-amidation

III.   Internal standard synthesis

Mass spectrometry analysis shows a complex and heterogeneous mixture of products composed of a mixture of fatty acid monomers and dimers, hence the need to have internal standards composed of fatty acid monomers and dimers. These molecules will allow us to understand and investigate the trans-amidation reaction on the oil paint film and calibrate our spectra during the FT-ICR analysis.

During the paint-film trans-amidation reaction, an exact amount of trimyristin triglycerides are added to the reaction mixture in order to release derivatized myristic acid which will be referred as internal standard for the quantification and mass spectrum calibration especially for monomers at low mass range (m / z = 300-500).

In the case of dimers, a strategy for the synthesis of methyl-oleate dimers bound with a carbon-carbon bond or a peroxide bond has been developed in order to reproduce the dimers formed during oil paint polymerization.

1. Methyl oleate dimer (C-C bond)

Our aim is to synthesize a dimer formed by two methyl-oleate molecules linked by a carbon-carbon bond. Dimeric molecules attract lots of interest in the pharmaceutical fields. Therefore, several methods of synthesis have been developed, among them Diels-Alders cycloaddition reaction.[45] An alternative method based on the transition-metal-catalyzed reductive homocoupling of organohalides lead to the formation of dimeric molecules with an intramolecular carbon-carbon bond. Thus, in the first step we have to synthesize allylic bromide functional fatty acids that can be used later in a homocoupling reaction. Wohl-Ziegler is a well-known reaction for the synthesis of allylic bromides. The addition of bromine on the allylic position is achieved with the help of N-bromosuccinimide (NBS) and 2,2'-azobis(2-methylpropionitrile) (AIBN) through a radical chain mechanism. Winkler *et al.*[46] have synthesized fatty acids containing allylic bromides in order to be destined for atom transfer radical polymerization (ATRP). The highest obtained yield was 87% including 85% of mono allyl bromides, 10 % diallyl bromides and 5 % of saturated alkyl bromides obtained under optimal conditions with a temperature of 80 °C, time of reaction of 240 min and a 1/1 Methyloleate/NBS ratio.

In our case, we aim to synthesize only mono allyl bromides and avoid the formation of other byproducts such as diallyl bromides and saturated alkyl bromides to have a better control of the homocoupling reaction in the next step. For this reason, we optimized the reaction conditions by decreasing the reaction time to 60 min and by changing the Methyloleate/NBS ratio to 1/4. We obtained a yield of 30% of mono allyl bromides without the formation of diallyl bromides and saturated alkyl bromides Figure 25 rather than a yield of 23% of dibromide and 55% of monobromide when following the literature conditions Figure 24.
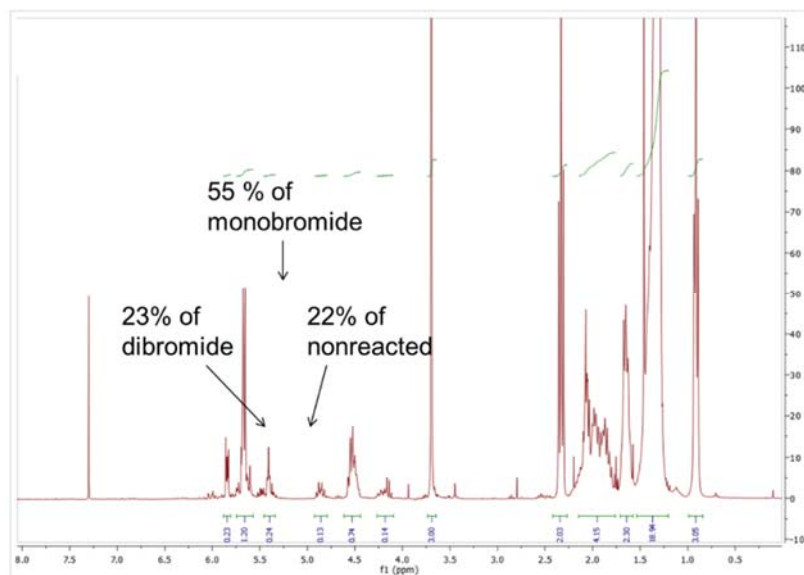
Figure 24. NMR spectrum of the obtained product from Wohl-Ziegler bromination under the literature conditions
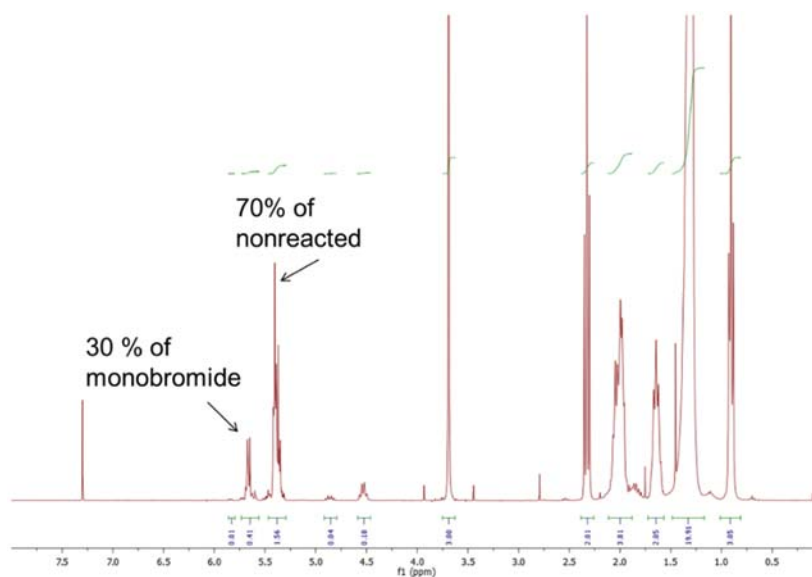
Figure 25. NMR spectrum of the obtained product from Wohl-Ziegler bromination under the optimized conditions

The next step was based on a study done by *Peng et al.*[47] in which they developed a Ni-catalyzed reductive approach for the homocoupling of alkyl bromides. The obtained product was submitted to a homocoupling reaction catalyzed with Ni(0)·2EC·Py, prepared in situ just before the reaction by mixing Zn, NiCl$_2$, ethyl crotonate (π ligand to Ni), and pyridine. After the preparation of the catalyst, mono allyl bromides were added and stirred for 4 hours at room

temperature. After 4 hours, the reaction was quenched and the recovered product was purified on a silica column. NMR analysis shows a full conversation of mono allyl bromides fatty acids into methyl-oleate dimers (Figure 26). The sample was also analyzed using Orbitrap MS and the mass spectrum confirmed the result obtained by NMR analysis (Figure 27).

In the following step, the isolated dimer was submitted to a trans-amidation reaction using the same conditions as in the case of linseed oil and oil paint film and by replacing the 3-dimethylaminopropylamine with amylamine. The obtained product was further analyzed by Orbitrap MS (Figure 29). The analysis shows that the majority of the dimers where derivatized on just one monomer of methyl-oleate, while only 10% of the dimers were derivatized on both fatty acid chains. The rest of monomers were only hydrolyzed and have a free carboxylic acid function.

In order to investigate if the free carboxylic function was produced during the electro-spray ionization or during the trans-amidation reaction, the obtained product was submitted to an amidation reaction with 3-dimethylaminopropylamine through a carbodiimide. The MS spectrum of the resulted products shows a full conversion into two derivatized monomers Figure 30. This result indicates that the trans-amidation reaction occurs on one fatty acid chain monomer only.
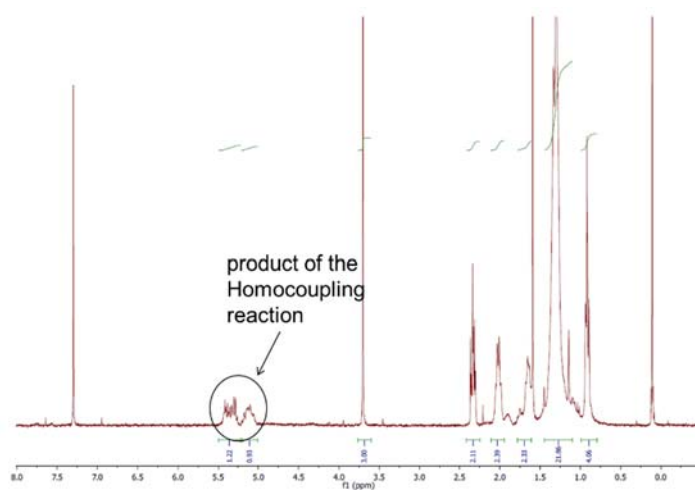
Figure 26. NMR spectrum of the pure methyl oleate dimer with carbon-carbon bond
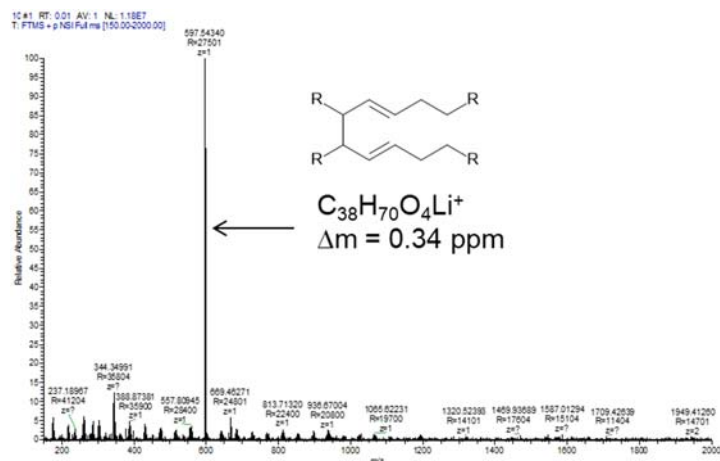
Figure 27. Orbitrap MS spectrum of the purified methyl-oleate dimer with carbon-carbon bond
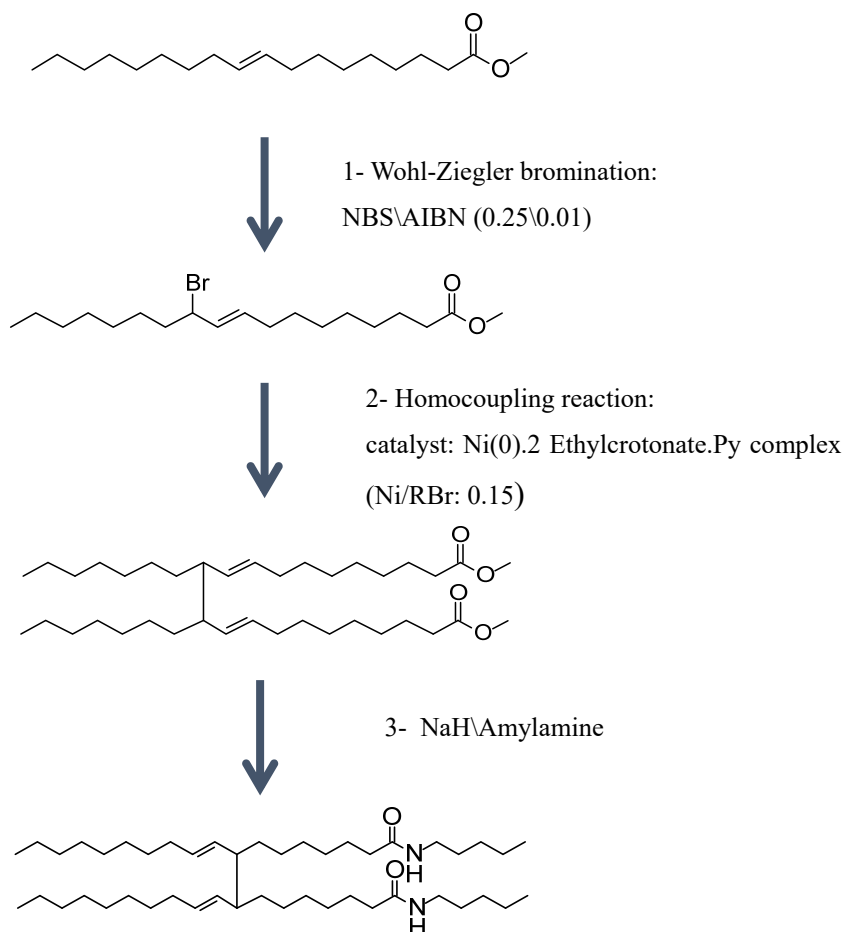
Figure 28. Synthesis mechanism of derivatized methyl oleate dimer with carbon-carbon bond
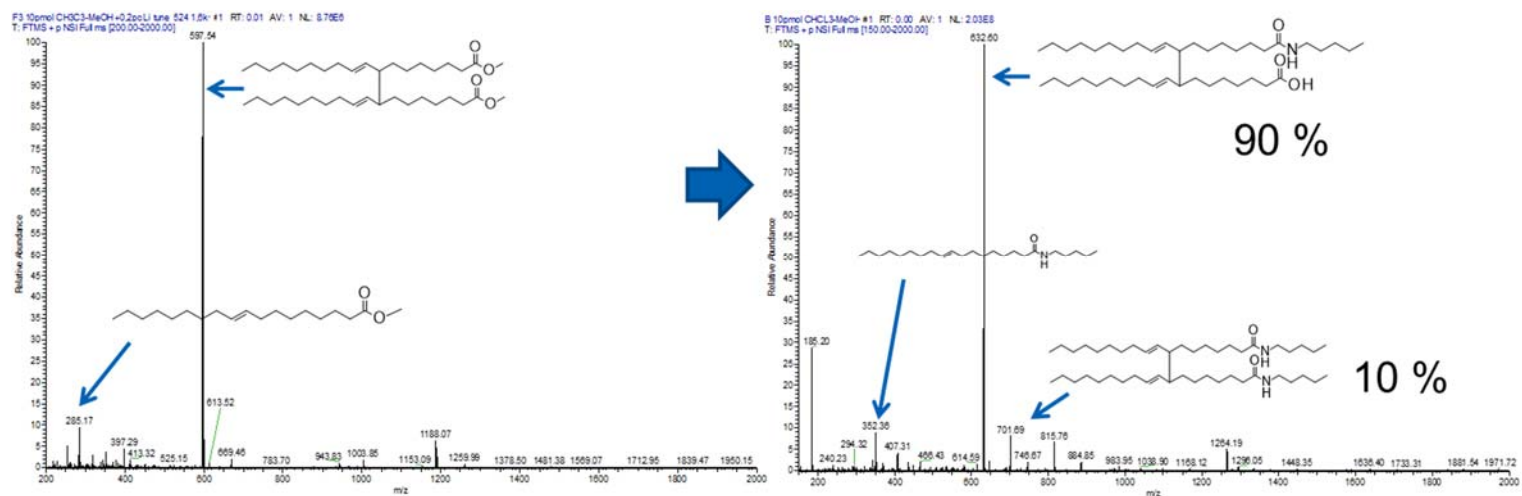
Figure 29. Orbitrap MS spectrum of the purified methyl-oleate dimer with carbon-carbon bond after derivatization
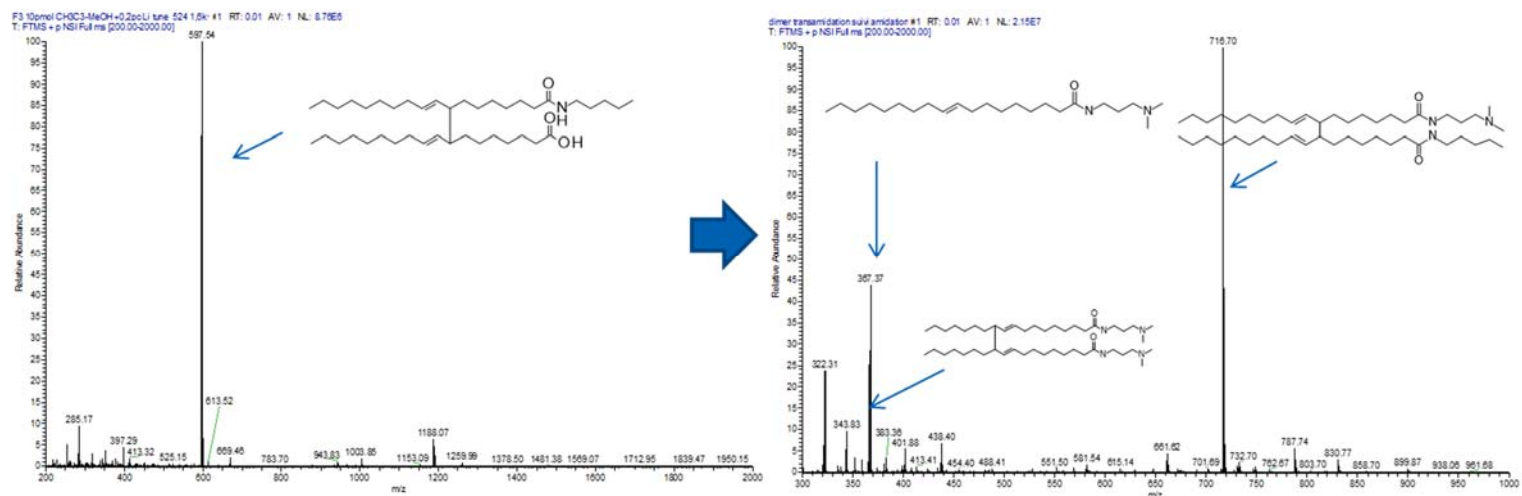
Figure 30. Orbitrap MS spectrum of the derivatized methyl-oleate dimer with carbon-carbon bond after amidation reaction

2. Methyl-oleate dimer (peroxide bond)

The work in this part was based on the method developed by *Foglia et al.*[48] for the synthesis of symmetrical dialkyl peroxides, in order to produce dimethyl oleate peroxide. In a phase transfer reaction, potassium superoxide reacts with tetramethylammonium bromide and forms tetramethylammonium superoxide in anhydrous (DMF). The alkyl bromide in our case is the methyl-oleate bromide added to the mixture. Methyl-oleate bromide was fully converted to dimethyl oleate peroxide with the presence of coproducts as alcohol Figure 32. The highest conversion rate is obtained with an excess of potassium superoxide and tetramethylammonium bromide. This reaction was done only once and we did not go further in our experiments due to risks of manipulation with the potassium superoxide.
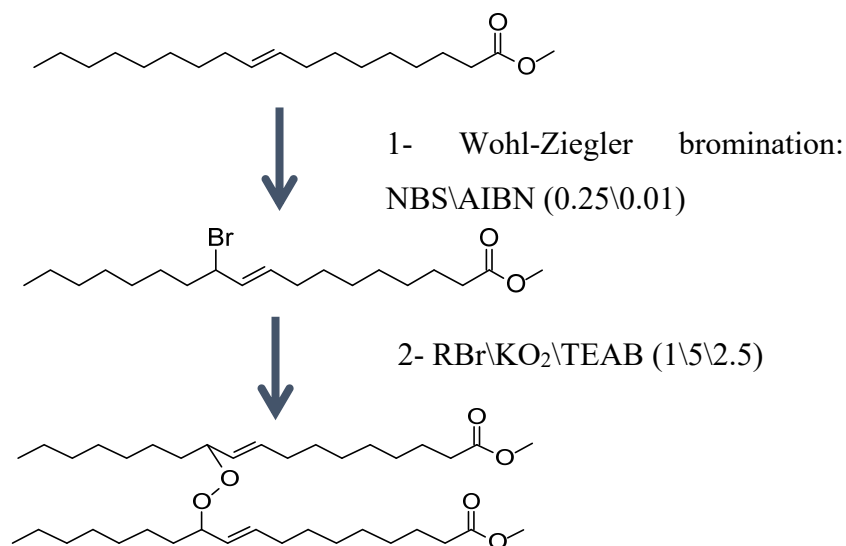
Figure 31. Synthesis mechanism of derivatized methyl-oleate dimer with peroxide bond
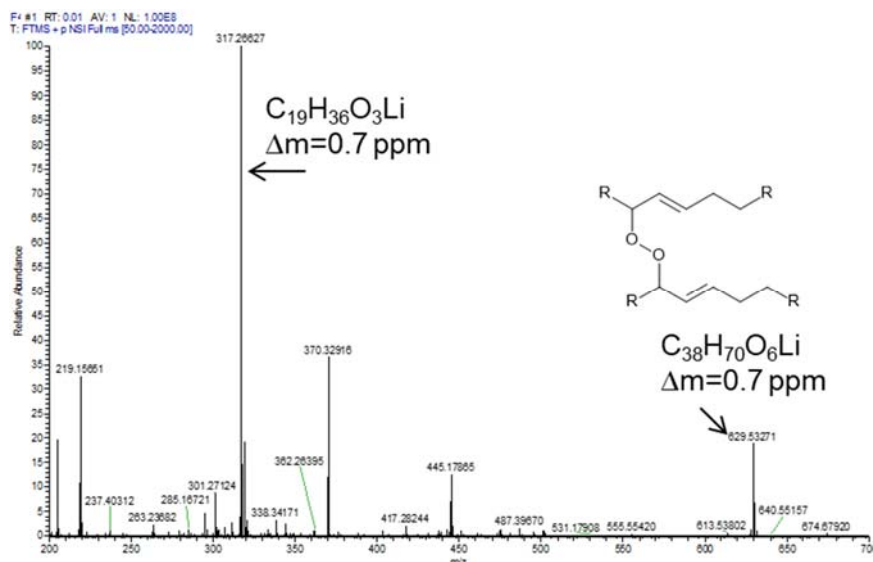
Figure 32. Orbitrap MS spectrum of the purified methyl-oleate dimer with peroxide bond

IV.   Mobile phase analysis

1.   Free Fatty acid derivatization

During oil paint drying process, β-scission mechanism, together with the hydrolysis of the ester bonds between the fatty acids and the glycerol lead to the release of free carboxylic acids that react with the metallic pigment and form metal soaps. Metal soaps are the main reason of paint degradation and the analysis of the free fatty acids recovered from the painting mobile phase, allows determining the degradation state of oil paintings. In order, to improve the detection of free fatty acids by mass spectrometry in the positive mode, we developed a method for fatty acids derivatization by adding tertiary amino group. The coupling reaction between the carboxylic acids and the amine is done via the intermediate of carbodiimides, such as 1-ethyl-3-(3-dimethylaminopropyl) carbodiimide (EDCI) in the presence of N-hydroxybenzotriazole (HOBt) to optimize the amides bond formation (Figure 33)[49].

Figure 33. Typical Reaction of coupling Acid with Amine in the Presence of EDCI/HOBt[49]

Standard myristic acid was derivatized with 3- dimethyl-aminopropyl and analyzed with FT-ICR MS. The MS spectrum shows that the reaction of derivatization was done successfully Figure 34.

Figure 34. FT-ICR MS spectrum of derivatized myristc acid

The mobile phase contains the soluble part of the paint film, which is composed by majority of the free fatty acids released during oil paint polymerization. In order to analyze the mobile phase, 1 mg of linseed oil paint film dried in the presence of 0.1% Co was swollen in MeOH for 12 hours. The solvent is then extracted and evaporated, free fatty acids are recovered and myristic acid was added (0.1 mg) as an internal standard for calibration and quantification. The mixture of carboxylic acids was derivatized with 3-dimethylaminopropylamine through carbodiimide as intermediate. The analysis of derivatized fatty acids was done with FT-ICR MS in positive mode, 0.1 % of formic acid was added to enhance the positive ionization. Mass spectrum (Figure 35) indicates that the mobile phase is composed by majority from saturated fatty acids as palmitic and stearic acids, and the more remarkably is the presence of oleic acids. These results signal that saturated fatty acids and even oleic acid are more likely to be released during oil paint drying by hydrolysis of the ester bond between the glycerol and fatty acids. The free fatty acids form complexes with the cations of the pigments present in the paint. These complexes are known as metal soaps.
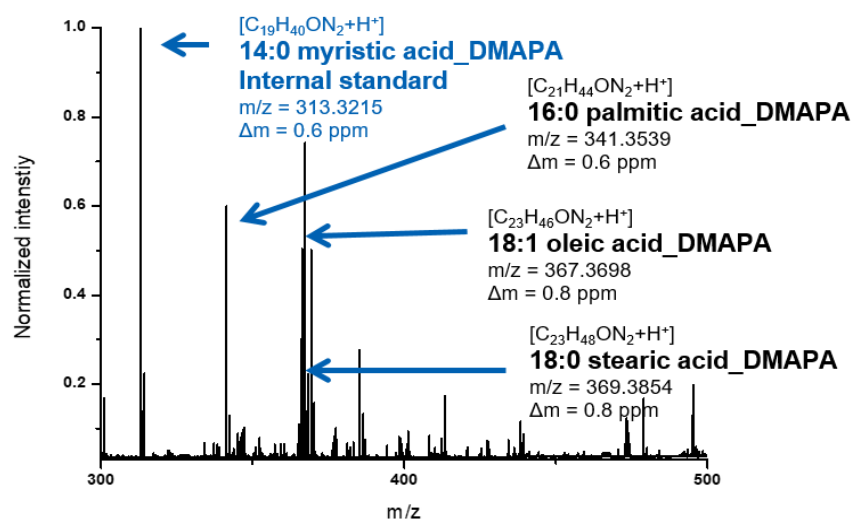
Figure 35. Mass spectrum of the mobile phase

V.   Solid model paint film

The binding media of historical oil paints is made up of drying oils rich in polyunsaturated fatty acids such as linseed oil. Upon drying, oil autoxidation, also known as siccativation, induces the formation of a tridimensional reticulated polymer. Until now, no study has succeeded to characterize the cross-linked polymer structure and the processes responsible for the degradation of solid films. This work is focused on the characterization and identification of the network structure of polymerized linseed oils by soft depolymerization and high- resolution mass spectrometry (FT-ICR) analysis. To perform this analysis, we designed a chemical treatment which cleaves the polymer at the ester bond between glycerol and the fatty acids without altering the network formed between these fatty acids. At the same time, derivatization of the fatty acids by adding a tertiary amine group was performed to improve their detection in positive mode. The developed and optimized strategy on fresh linseed oil was later applied on 1 mg of linseed oil paint film (dried in the presence of 0.1 % Co). The obtained products from trans-amidation were analyzed by FT-ICR. The spectrum shows thousands of peaks corresponding to the resulting products from the polymerization and degradation process (Figure 366). To decrease the complexity of the obtained MS spectrum, we devised the spectrum into two zones. The first zone corresponds to the fatty acids monomers with their different degrees of oxidation. The second zone is more complex and represents the resulted products from the drying process as dimers, trimers and others. We should mention that two internal standards were added for spectrum calibration and quantification. First internal standards is the trimyristin triglyceride which was added prior to the trans-amidation reaction, and it was converted into derivatized myristic acid (myristic acid_DMAPA, m/z = 313.3213). This internal standard is used for the calibration of monomers part of spectrum. For the calibration of the dimers zone, the synthesized methyl-oleate dimer linked with C-C bonds (m/z= 716.) was added to the mixture before the analysis.
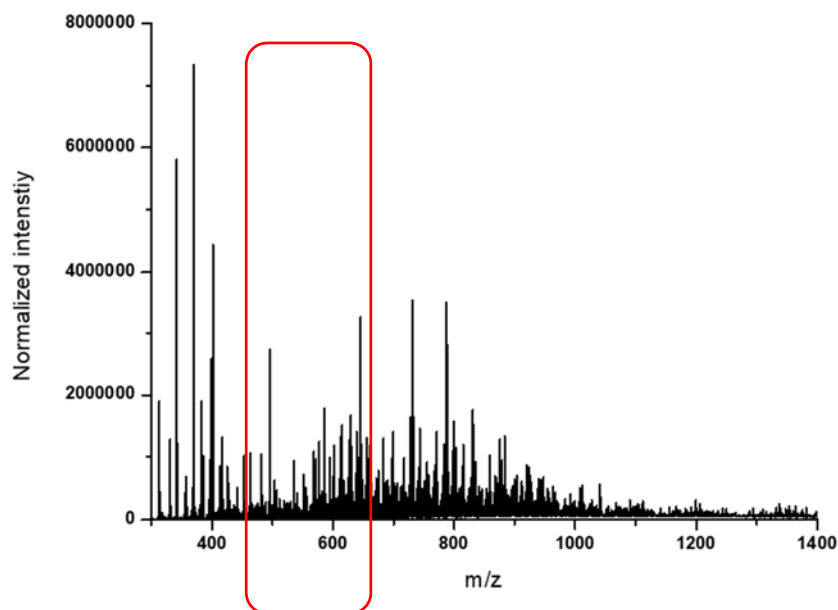
Figure 36. FT-ICR MS spectrum of derivatized linseed oil film

1. Study of monomers modifications

Zooming in on the monomers zone of the spectrum (Figure 37), we can notice that the proportion of polyunsaturated fatty acids such as linoleic acid and linolenic acid has remarkably decreased in comparison with fresh flaxseed oil after derivatization. These results confirm the contribution of polyunsaturated acids in the oil polymerization process. This spectrum indicates as well the presence of oleic acid with different degrees of oxidation (Table 4).
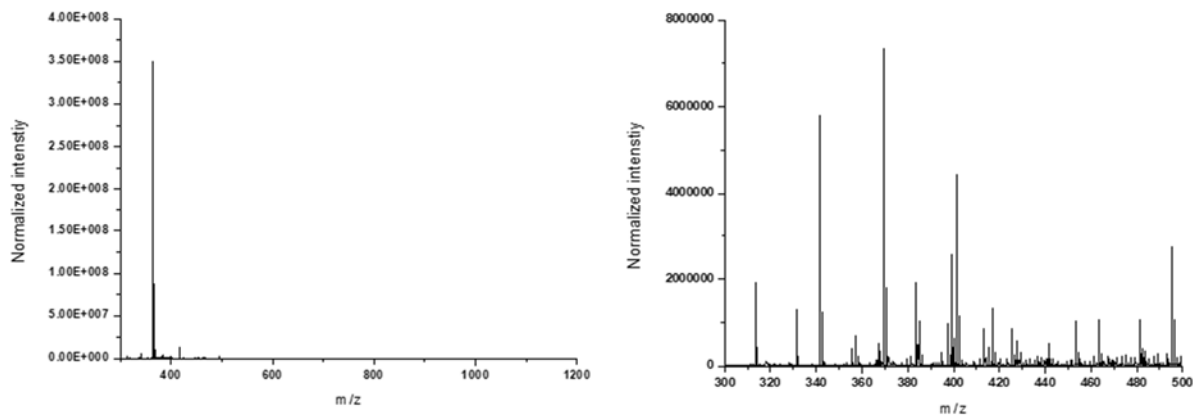
Figure 37. On the left FT-ICR MS spectrum of derivatized linseed oil and on the right spectrum of linseed oil film derivatized monomers

Table 4. Derived Fatty acids after linseed oil paint film transamidation

F.A._DMAPA	$C_xH_yO_zN_2$	[M + H$^+$]	Δm ppm	CN:DB	ECN	I
Plamitic acid_DMAPA	$C_{21}H_{45}ON_2$	341.3532	3.2	16 : 0	16	362660395
Linolenic acid_DMAPA	$C_{23}H_{43}ON_2$	363.3370	0.2	18 : 3	12	183282092
Linolenic acid_DMAPA	$C_{23}H_{45}ON_2$	365.352	0.7	18 : 2	14	137595472
Oleic acid_DMAPA	$C_{23}H_{47}ON_2$	367.3680	0.6	18 : 1	16	903721712
Stearic acid_DMAPA	$C_{23}H_{49}ON_2$	369.3849	2.5	18 : 0	18	422597517
Oleic acid 1O_DMAPA	$C_{23}H_{47}O_2N_2$	383.3644	3.1	18 : 0	18	301376381
Oleic acid 2O_DMAPA	$C_{23}H_{47}O_3N_2$	399.3597	3.9	18 : 0	18	97524578
Oleic acid 3O_DMAPA	$C_{23}H_{47}O_4N_2$	415.3530	3.9	18 : 0	18	78316228

2. Cross-linking products

FT-ICR MS technique offers high-resolution spectra and a mass accuracy in parts-per-billion, which leads to the generation of complicated spectra with thousands of peaks. This high amount of data makes the interrogation, interpretation and visualization of results a challenging task. Using a specific software can be a tool to manage the generated results.[50] Several modifications were introduced on the python script to suit our type of analysis because the original script was dedicated for the analysis of whisky samples.[51]

The software is divided into four modules:

The first part is responsible for the generation of a chemical formulas dictionary for m/z (z=1) between 100-1200 Da (the range of masses can be modified on demand). In this part, we indicate the type of atoms present in our compounds (in our case C, H, O and N) and we define the maximum and the minimum number of each atom presents in the molecules at defined range of m/z.

In the next modules, the code assigns automatically the input peak list to the chemical formula. For this part of the script, we added two more conditions. For the first condition, we set the relative mass error between the experimental and the theoretical mass at $\Delta m =< 1$ ppm to limit the false positives. Moreover, formula identification was based on odd-mass ions, and the mass of the proton that came from the ionization was subtracted.

The tool is based on the Kendrick mass defect (KMD), the easiest way to identify ions that differ from each other only in number of CH_2 and they are considered members of homology sequences. The KMD is the difference between the Nominal Mass and the Kendrick Mass [6a]

$$KM = IUPAC\ mass_{mesured}[14.0000/14.01565]$$

$$KMD = [NM-KM]$$

However, the number of possible formulas for each measured mass increases with molecular weight and it is possible for different homologous series to have similar KMDs. Therefore, it is necessary to calculate another independent parameter z*:

$$Z^*= (modulus[NM/14]) - 14$$

Ions that differ from each other by multiples of 14 will produce identical reminders. It means that ions with identical KMD and Z* value can differ only in number of CH_2. Unassigned peaks are then checked against the H_2O, and finally H_2 Kendrick mass units. Remaining unassigned peaks are then checked against the assigned peaks for being isotopes. For example, if we have an unassigned peak X m/z, we check if there is a peak at X - 1.003355 m/z, if so, X is likely to be the ^{13}C isotope.

Ions can be characterized by the number of double bonds

$$DBE = 1 + 1/2(2C - H + N)$$

In the fourth module, Van Krevlen plots were produced to simplify the results visualization.

Peaks are assigned based on the Kendrick mass defect and z* approach to formulae assignment, and the attributed compounds were classified in function of their number of Nitrogen, CH_2, DBE and oxygen.
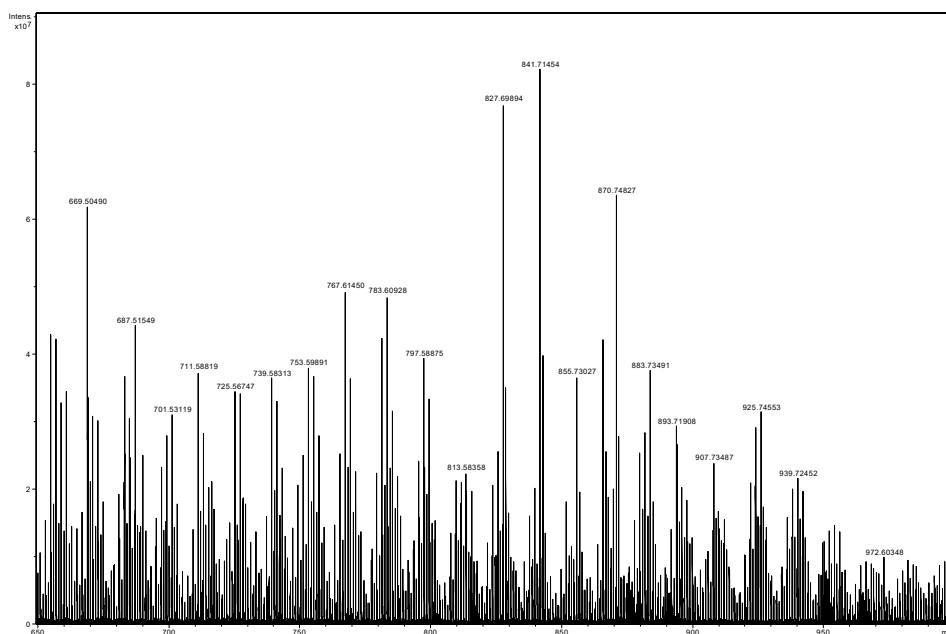
Figure 38. FT-ICR MS spectrum of linseed oil derivatized dimers, trimers and tetramers

The mass spectrum represents the chemical complexity of the sample. We have detected 7650 peaks with a signal-to-noise ratio > 4. The spectrum was linearly calibrated based on a mass

reference. This mass reference was made of five known masses (m/z: 313.3213; $C_{19}H_{41}ON_2$ (DMAPA-Myristic acid-internal standard)/ m/z: 341.3526; $C_{21}H_{45}ON_2$ (DMAPA-palmitic acid)/ m/z: 367.3683; $C_{23}H_{49}ON_2$ (DMAPA-oleic acid)/ m/z: 369.3839; $C_{23}H_{47}ON_2$ (DMAPA-stearic acid)/ m/z: 716.7028; $C_{46}H_{90}N_3O_2$ (synthesized methyl-oleate dimer)). For the linseed oil paint film dried in the presence of 0.1% Co, 6056 peaks were detected, but only 1299 peaks were identified as a monoisotopic formula with a mass error less than 1 ppm. Moreover, 336 peaks were identified as $^{13}C_1$ isotopologues and 4421 peaks were unassigned. The unassigned peaks may be secondary isotope peaks, e.g. with two ^{13}C atoms or a single ^{18}O.

3. Study of the DBE variations
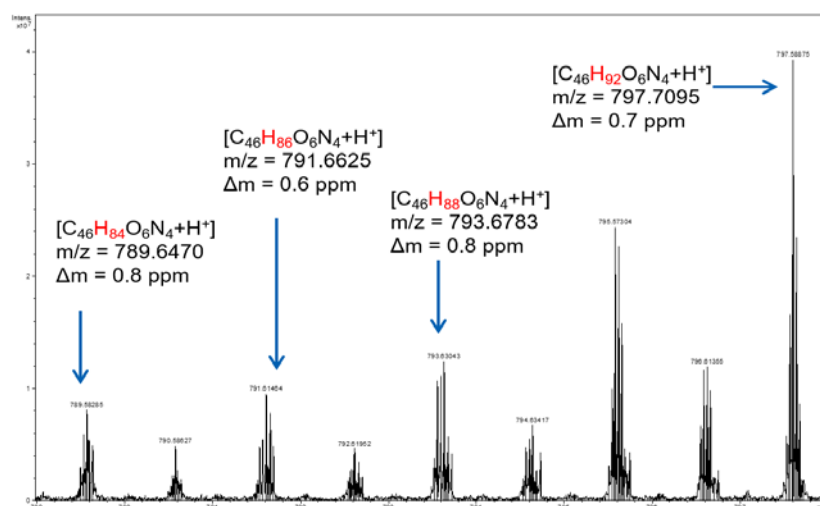
Figure 39. Zoom on the peaks in the region of 788-798 m/z

Table 5. Identified peaks in the mass range between 788-798 m/z

m/z [M+H]$^+$	Error (ppm)	DBE	Formula
789.6470	0.8	7	$C_{46}H_{84}N_4O_6$
791.6625	0.6	6	$C_{46}H_{86}N_4O_6$
793.6783	0.8	5	$C_{46}H_{88}N_4O_6$
797.7095	0.7	3	$C_{46}H_{92}N_4O_6$

When we zoom in on the MS spectra (Figure 39), we can remark a difference of 2H between two consecutive peaks. A same class of molecules that have the same number of carbon, oxygen

and nitrogen but different hydrogen number. This difference in hydrogen number is illustrated with the variation of DBE. In our case, the DBE indicating the number of unsaturation within the molecules represents an indication of the degree of polymerization and gives an inside look on the cross-linked structure of oil paint film. Double bonds are involved in the polymerization process of siccative oils, the abstraction of allylic hydrogen located between the two double bonds lead to a radical addition combination or radical addition elimination. The two ways of radical addition generates dimers, trimers and tetramers but with different number of unsaturation, as it is shown in Figure 40. An example of products of radical addition combination is the molecule $C_{46}H_{92}N_4O_6$ with a DBE of 3 and only one double bond in the fatty acid dimers. This indicates that during radical addition, allylic radical attracts a hydrogen from another fatty acid leading to less unsaturation.
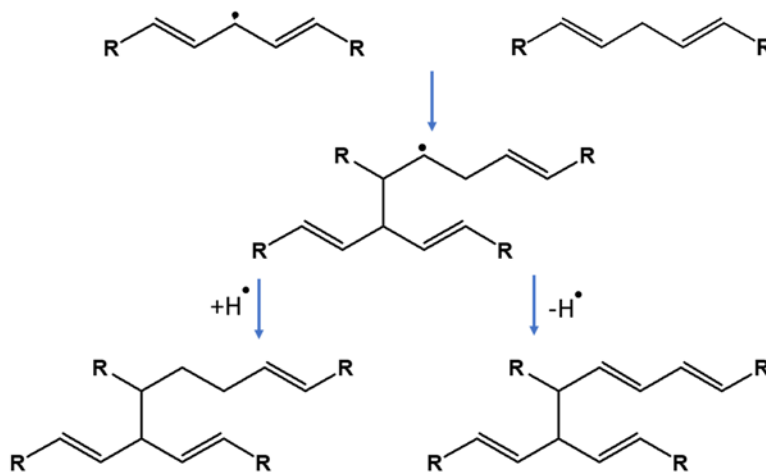
Figure 40. Mechanism of radical addition combination on the left and radical addition elimination on the right

4. Study of oxygen number variation
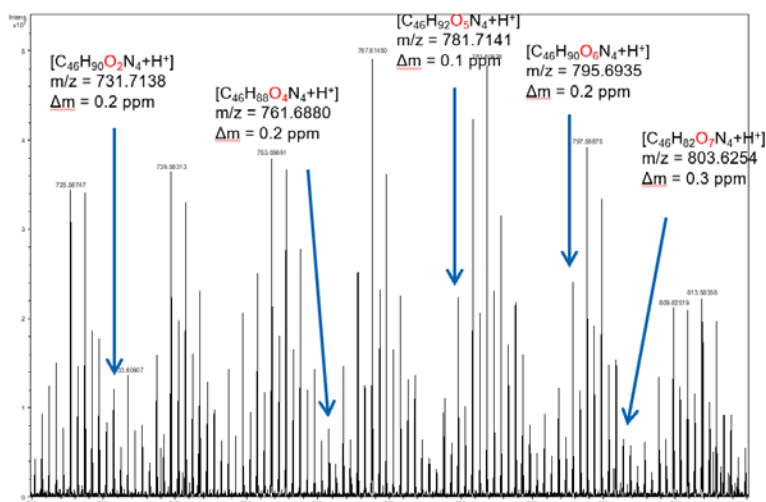
Figure 41. Zoom in on the peaks in the region of 720-820 m/z

On the other hand, we found that some peaks in the spectra are correlated between each other and the difference of masses corresponds to oxygen atoms (Figure 41). Table 6 represents an example of the identified derivatized fatty acids dimers, which shows that those dimers can have a degree of oxidation that vary from 0 to 5. Oxygen number is an important parameter that offers information about the degree of oxidation and the cross-linked structure of the polymer. For example, the identified molecule $C_{46}H_{90}N_4O_2$ (m/z = 731.7138 Da) have no oxidation leading to conclude that this dimer is linked by a carbon-carbon bond. Linseed oil drying is a chemical process that incorporate oxygen in the polymer structure in form of peroxide, alcohol, carbonyl and carboxylic acid. We succeeded to establish a relation between the oxygen and the DBE that allows the determination of the presence of peroxide function in the molecular structure. When the fatty acid carbon chain gains oxygen atoms, the number of hydrogen should decrease and the DBE should increase. However, if the number of oxygen is higher than the DBE (DBE-O < 0), oxygen is attached to another oxygen instead of carbon which indicates the presence of a peroxide function Figure 42.
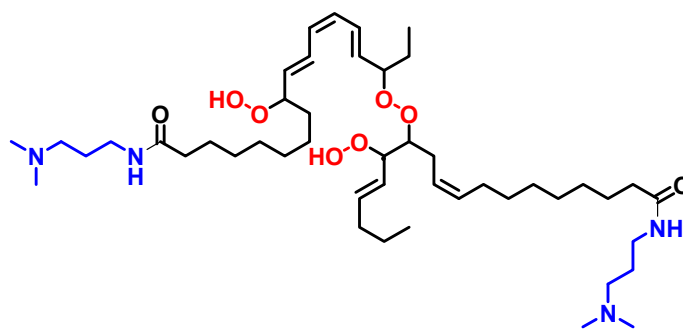
Figure 42. Fatty acids dimer contains peroxide functions

Table 6. Example of identified peaks in the mass range between 720-820 m/z

m/z [M+H]$^+$	Error (ppm)	DBE	Formula	DBE-O
731.7138	0.2	4	$C_{46}H_{90}N_4O_2$	2
761.6880	0.2	5	$C_{46}H_{88}N_4O_4$	1
781.7141	0.1	3	$C_{46}H_{92}N_4O_5$	-2
795.6935	0.2	4	$C_{46}H_{90}N_4O_6$	-2
803.6254	0.3	8	$C_{46}H_{82}N_4O_7$	1

5. Study of CH$_2$ variation

The identified ions in the MS spectrum of the linseed oil paint film have a difference of one CH$_2$ or more Table 7. For example, the two molecules $C_{46}H_{90}N_4O_4$ (m/z = 763.7037) and $C_{44}H_{86}N_4O_4$ (m/z = 735.6721) have a difference of C_2H_4. During oil paint drying process, beside the reticulation process, a degradation mechanism known as β-scission mechanism takes place. After the hydroperoxide decomposition and alkoxy radical formation, instead of reacting with fatty acids by radical addition, the radical species react within themself and cause the degradation of the fatty acid carbon chain producing volatile organic compounds and carboxylic acids. The β-scission mechanism is the main form of oil paint film degradation that releases free carboxylic acids functions which react with the pigments present in the painting and form metallic soaps.
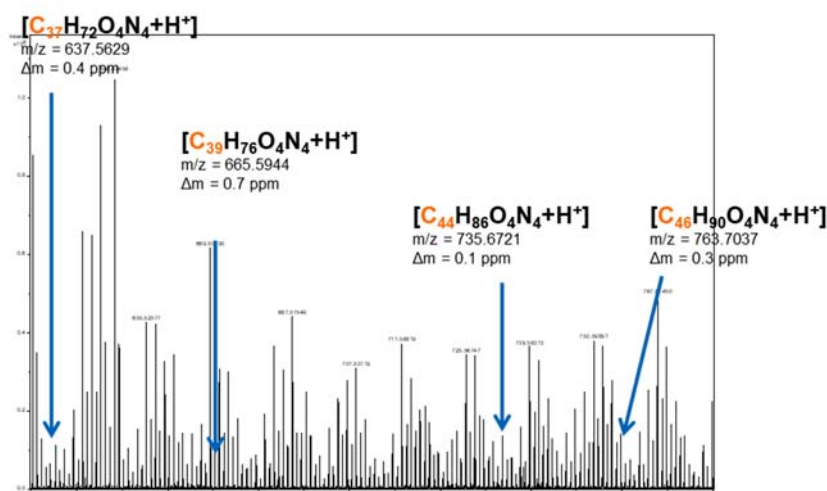
Figure 43. Zoom in on the peaks in the region of 630-780 m/z

Table 7. Example of identified peaks in the mass range between 630-780 m/z

m/z [M+H]$^+$	Error (ppm)	DBE	Formula
763.7037	0.3	4	$C_{46}H_{90}N_4O_4$
735.6721	0.1	4	$C_{44}H_{86}N_4O_4$
665.5944	0.7	4	$C_{39}H_{76}N_4O_4$
637.5629	0.4	4	$C_{37}H_{72}N_4O_4$

6. Study of nitrogen number variation

Each 3-dimethylaminopropylamine molecule contains two nitrogen atoms, and as it was mentioned before, DMAPA cleaves the ester bond between the fatty acid and the glycerol, forming an amide bond with the acid functions. The number of nitrogen atomes present in the molecule determines the number of cross-linked fatty acids. For example, 2 N is a monomer, 4 N is a dimer, 6 N is a trimer and 8 N is a tetramer.

Table 8. Represents an example of identified monomers, dimers and trimers

m/z [M+H]$^+$	Error (ppm)	DBE	Formula
367.3683	**0.0**	2	**$C_{23}H_{46}N_2O$**
731.7138	**0.2**	4	**$C_{46}H_{90}N_4O_2$**
1131.9503	**0.4**	12	**$C_{69}H_{122}N_6O_6$**
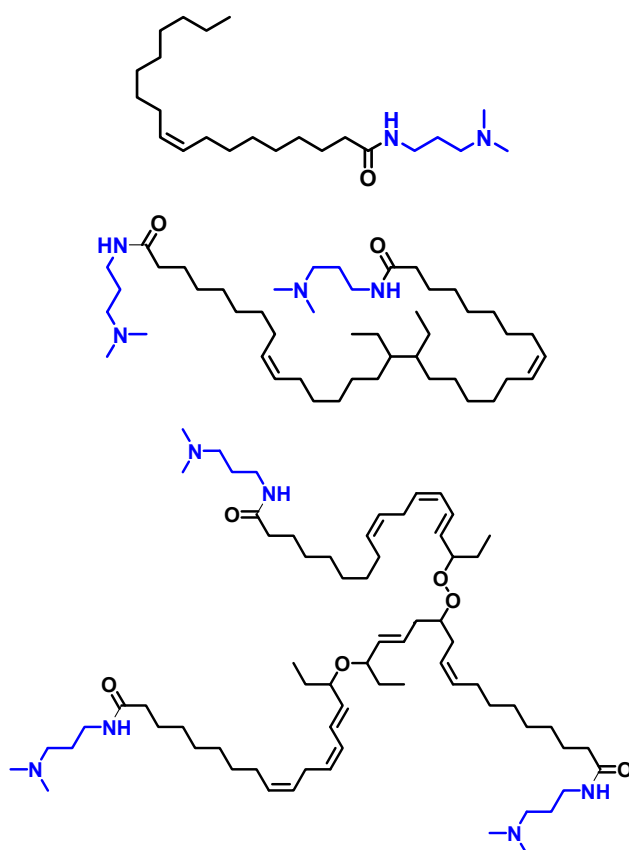
Figure 44. Schematic representation of fatty acid monomer, dimer and trimer

However, the plot representing the number of nitrogen versus the number of carbon as a function of mass (Figure 45), demonstrates clearly the presence of dimer and trimer fatty acids

with only two nitrogen atoms. The trans-amidation reaction occurs between DMAPA and the ester bond linking the fatty acid to the glycerol. The presence of free fatty acids in the final product proves the hydrolysis of the ester bond before the trans-amidation reaction. This hydrolysis is responsible for the mechanism of release of saturated fatty acids and the formation of metallic soaps. The saturated free fatty acids were identified in the mobile phase in the precedent study.
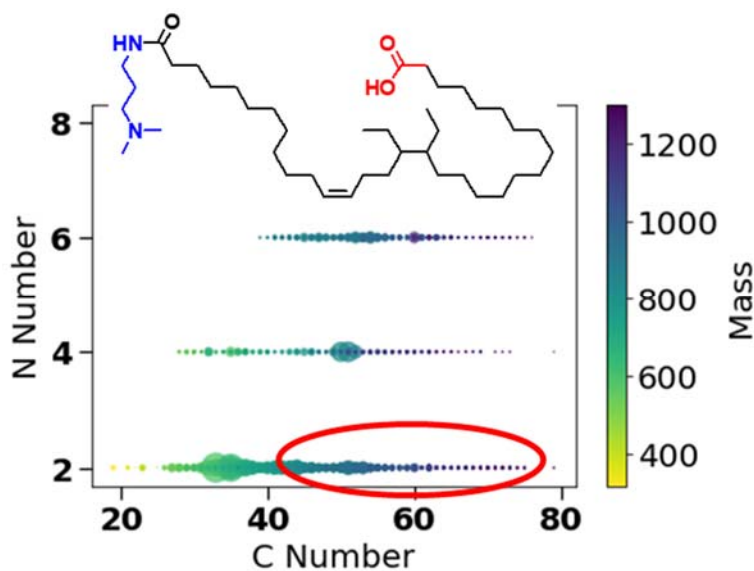
Figure 45. Plot representing the number of nitrogen versus the number of carbon as a function of mass

VI.   Comparison between modern and old model paint films

In the next study, we compared two types of models paints films. The first one is the same oil paint film used in the previous study where the drying process is similar to modern alkyd paint polymerization and it was catalyzed by 0.1% of cobalt salts. The second oil paint film is more representing to the old oil paint film and is composed of linseed oil and 50% of lead white [$(PbCO_3)_2 \cdot Pb(OH)_2$]. Both oil paints films were allowed to dry in the air at room temperature for 3 months.

The old model sample mass spectrum represents also a chemical complexity as the modern oil paint sample. For the old paint film, we detected 6854 peaks with a signal-to-noise ratio > 4. The spectrum was linearly calibrated based on the same mass reference. From the 6854 detected

peaks, only 2248 were identified as a monoisotopic formula with a mass error less than 1 ppm. Moreover, 738 peaks were identified as $^{13}C_1$ isotopologues and 4142 peaks were unassigned. The unassigned peaks may be secondary isotope peaks, e.g. with two ^{13}C atoms or a single ^{18}O.
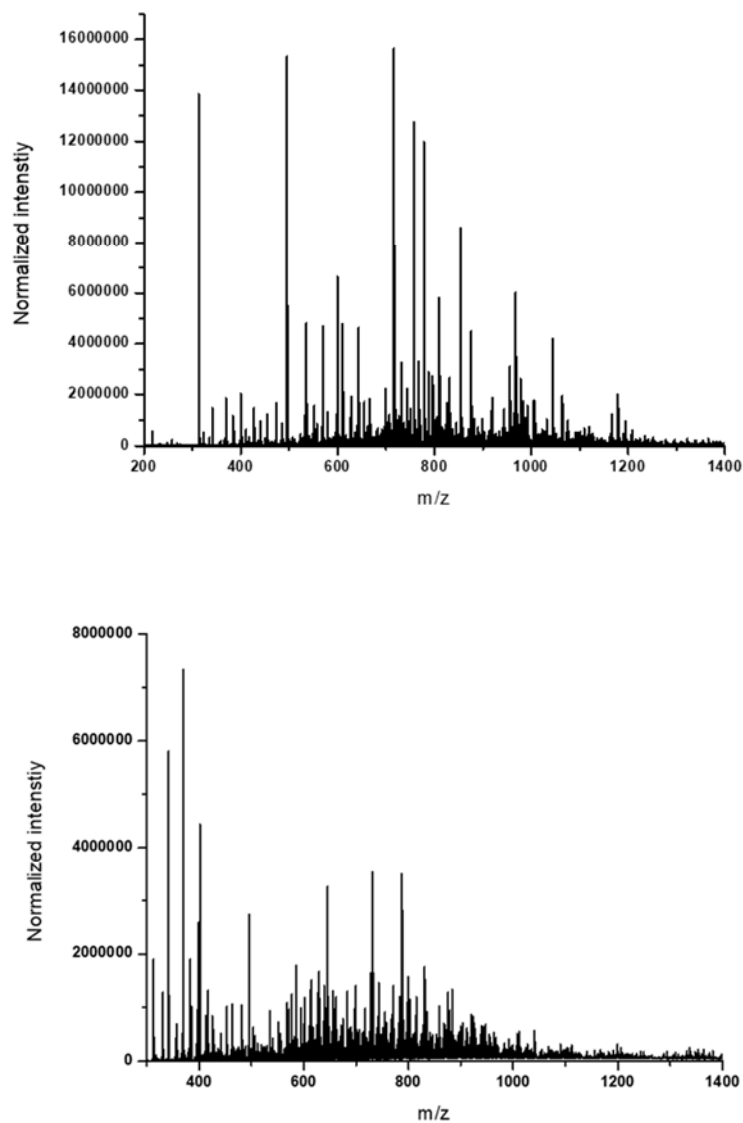
Figure 46. On the top the FT-ICR MS spectrum of an old model paint film, and on the bottom the FT-ICR MS spectrum of a modern model paint film

By comparing the mass spectra of the two painting samples Figure 46, we can see a slight difference. However, when we zoom in on a closer range of one nominal mass at 763-764 Da (Figure 47), we detect the presence of only one common compound ($C_{46}H_{90}O_4N_4$; m/z

763.7035 Da) between both paint films and 4 different compounds. These results demonstrate the influence of pigments on the polymerization process and on the cross-linked products.
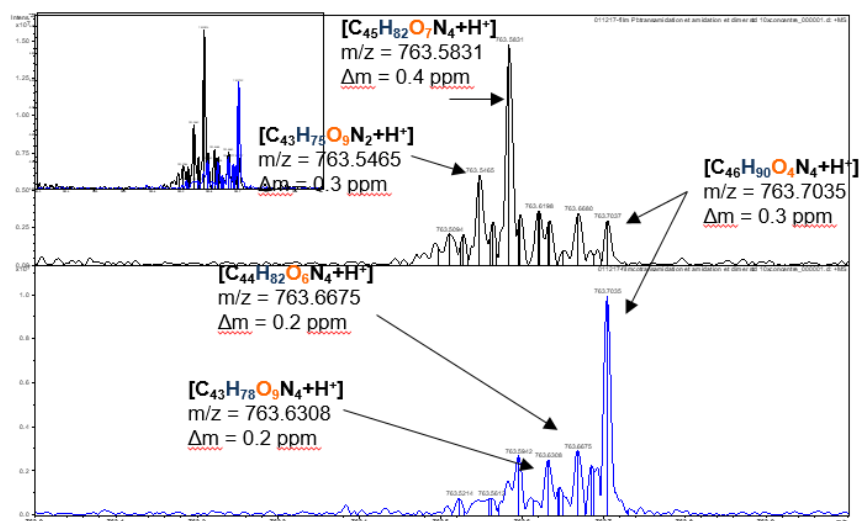
Figure 47. Zoom in on the peaks in the region of 763-764 m/z showing the common and different peaks between the two model paint films

The obtained data from both samples were graphically represented as a Van Krevelen and DBE versus carbon number plots.

Van Krevelen diagram highlights the identified species based on the assigned molecular formulas and the hydrogen to carbon (H/C) versus the oxygen-to-carbon ratios (O/C) as a function of the masses (Figure 48). The intensity of the peaks in the mass spectrum are reflected by the size of the points on the plots. In order to have a clearer view on compounds abundance in the sample, another Van Krevelen plot representing the hydrogen to carbon (H/C) versus the oxygen-to-carbon ratios (O/C) as a function of peak intensity was illustrated.

The comparison of Van Krevlen plots between the two samples shows that the oxygen to carbon ratio is higher in the case of old model sample. By checking the mass distribution, we can remark that the modern model sample contains more compounds with masses > 1000 Da that correspond to trimers and tetramers. If we compare the hydrogen to carbon ratio, we notice a higher abundance of compounds at low H/C ratio in comparison of the modern sample. It

indicates that in the case of modern sample, the carbon chains are longer so the H/C is lower or the carbon chains have more instauration which means less hydrogen. Those results can direct us to conclude, that lead pigments contribute to the oxidation process more than modern driers as cobalt salts, and lead pigments allow more incorporation of oxygen into the cross-linked structure of siccative oil. Furthermore, Lead pigments seem to increase the rate of β-scission mechanism which causes the degradation of fatty acids carbon chains.
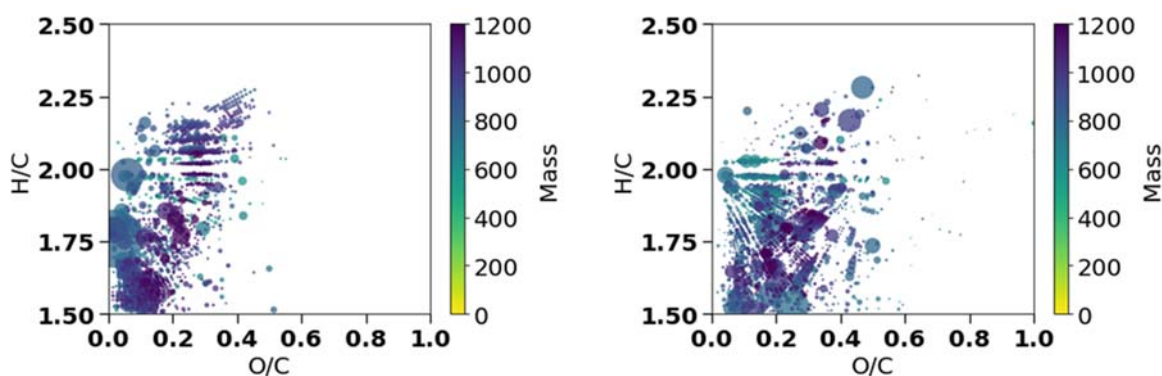
Figure 48. Van Krevelen diagrams highlighting the identified species based on the hydrogen to carbon (H/C) versus the oxygen-to-carbon ratios (O/C) as a function of the mass (old model paint sample on the right and modern paint sample on the left)
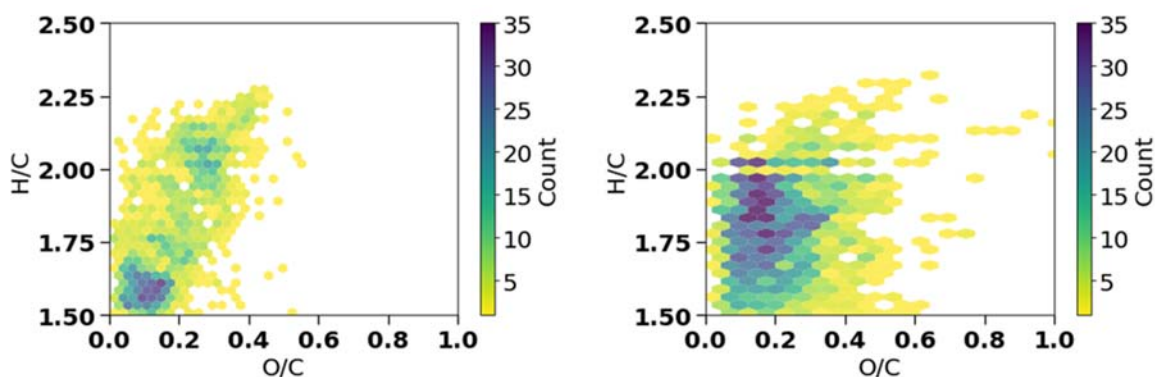
Figure 49. Van Krevelen diagrams highlighting the identified species based on the hydrogen to carbon (H/C) versus the oxygen-to-carbon ratios (O/C) as a function of the intensity (old model paint sample on the right and modern paint sample on the left)

The study of DBE versus carbon number plots as a function of compounds abundances shows that fatty acids dimers and trimers have higher DBE value in the case of old paint.

In the previous study, we demonstrated that the following equation DBE – O < 0 allows to identify the presence of peroxide functions in our compounds.

The plot DBE versus carbon number as a function of oxygen number illustrates the distribution of oxygen number as a function of DBE and carbon number per compound. When the oxygen number is higher than DBE value, the molecules contain peroxide. The plot shows that more peroxide functions are present in the old model paint sample
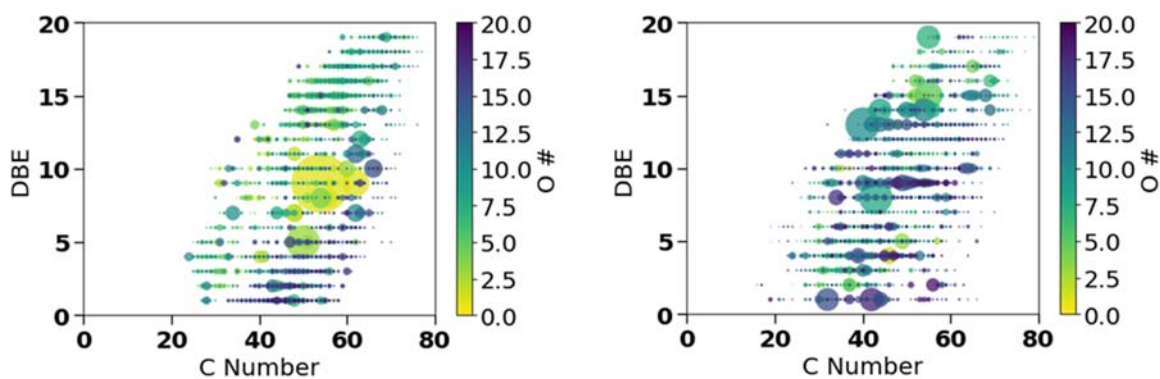
Figure 50. Plot DBE versus carbon number as a function of oxygen number (old model paint sample on the right and modern paint sample on the left)
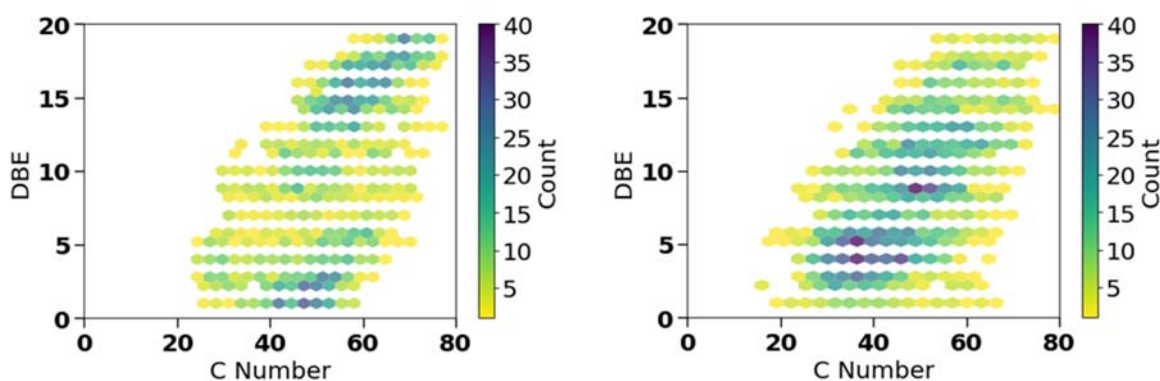
Figure 51. Plot DBE versus carbon number as a function of intensity (old model paint sample on the right and modern paint sample on the left)

VII.   Application on oil art painting

Figure 52. Oil painting dating from the 19th century "Portrait de femme Ecole française" painted by Louis Philippe

We applied the optimized and developed method on an oil painting dating from the 19th century called "*Portrait de femme Ecole française*" and has the signature of *Louis Philippe*. We extracted 1 mg of paint film that contains both organic and inorganic parts from four different spots of the painting with different colors (green, black, white and red-yellow).

In the first step, samples were analyzed with XRF in order to characterize the present pigments and with thermogravimetry to characterize the amount of organic material. These experiments were provided at Politecnico di Milano in the Department of Physics for XRF and in the Department of Chemistry, Material and Chemical Engineering for thermogravimetry.

1. Study of the inorganic part

a. X-ray fluorescence (XRF)

The used XRF spectrometer is ELIO (XGLab srl, Italy) based on a 25 mm^2 active area silicon drift detector and on a 40 kV-4W X-ray tube generator, which employs a Rh anode. The excitation X-ray beam is collimated to a ~1.2 mm spot diameter on the sample surface. The typical energy resolution of the spectrometer is below 135 eV. For all measurements, the following experimental conditions were used: working distance ~1.4 cm, tube voltage = 40 kV, tube anode current = 80 microA, acquisition time = 60 s.
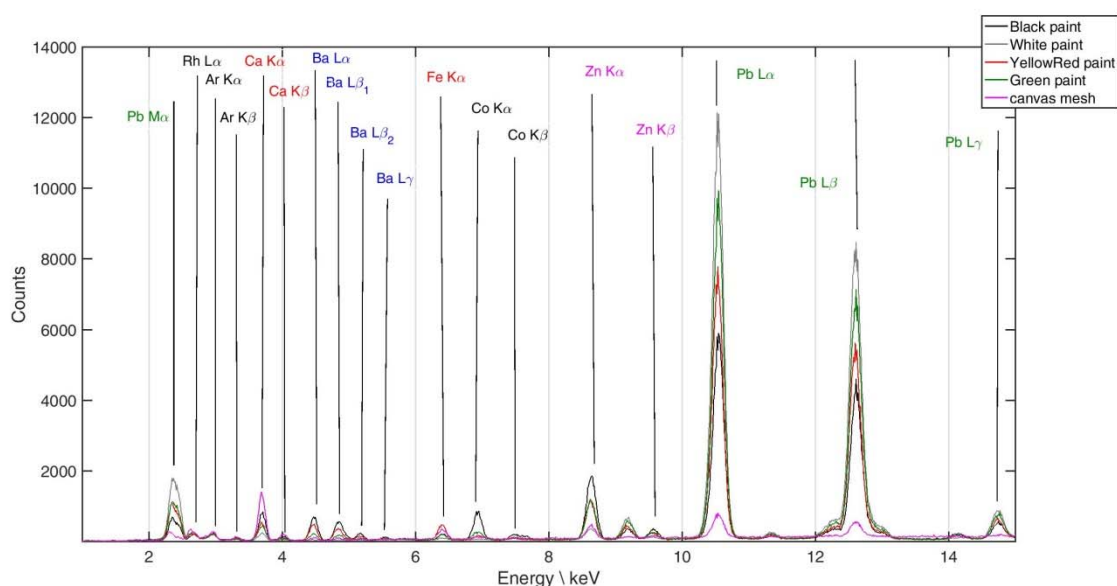
Figure 53. Example of an XRF analysis

The canvas mesh separated from the black sample was also analyzed, and we detected the presence of calcium and chlorine (elements detected in higher relative amounts with respect to the nearby black paint), the canvas mesh could have been treated with some materials such as gypsum. Interestingly, we detected an amount of iron (in relative concentration higher than the one detected in the black paint). The other detected elements (lead and zinc) have to be ascribed to the close black paint (residuals of the paint in the apparently free mesh).

The white paint is mainly composed of lead (possibly lead white) and minor amounts of zinc (possibly zinc white). Colored paints are made of lead, zinc (in higher relative quantities than

the white paint) and barium (probably ascribed to the use of barium sulphate). Moreover, in the yellow-red paint, the coloring matter is iron (possibly ascribed to the use of a yellow ochre).

In the black and green paints, beside iron was detected (in smaller relative quantities than the yellow-red paint), but also cobalt, which can come from cobalt blue ($CoOAl_2O_3$), cobalt green ($Zn_{1-x}Co_xO$) or smalt ($CoOKSi$).

b. TGA Analyses

Thermogravimetric analysis was done to determine the organic amount in each sample. In order to avoid the contribution of the canvas tissue to the total organic amount of the samples, the painted material was carefully separated from the tissue and analyzed.

Tests were carried out in air at temperatures ranging between 35-900 °C, with a temperature increase of 10°C/min. The TGA curve, which represents the percentage of weight loss as a function of temperature, is shown in green. The curve relating to the heat flow, in blue, provides indications on the thermal phenomena related to weight loss. The weight derivative, in red, was used in order to identify the beginning and the end of the thermic phenomena (which correspond to the minima of the curve).

For each sample, the weight loss at (150-375°C), which is not characterized by an intense endo/exothermic phenomenon, was probably related to the vaporization (or decomposition) of some organic compounds, such as solvents or some oils. The next loss (375-500°C) was related to a marked exothermic phenomenon, and it is reasonably attributable to the non-volatile organic fractions contained in the samples. The first loss (30-100°C) was related to water evaporation, while that between 500-700°C is typically associated to the decomposition of carbonates.

Table 9. The total organic amount present in the samples

Pigment	Organic amount (%)
Black	26.82
White	21.78
Green	24.26
Yellow-red	23.00
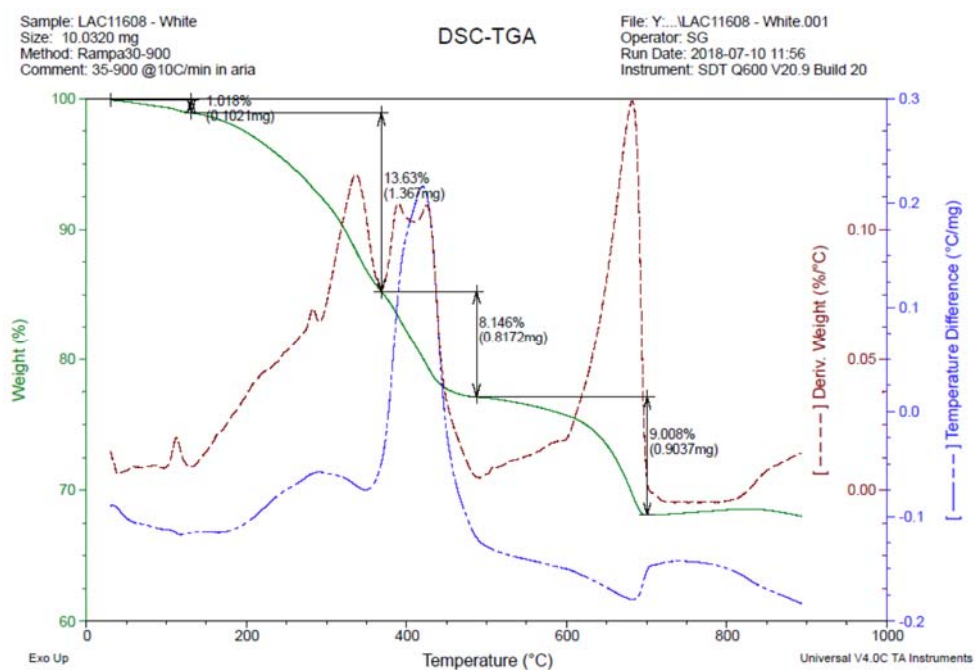
Figure 54.TGA of white sample

2. Study of the organic part

a. Oil pint film analysis and depolymerization

The same strategy developed earlier for oil paint depolymerization based on trans-amidation using 3-dimethylaminopropylamine was applied on the artistic oil paint. Samples were first swollen in THF overnight, the soluble part known by the mobile phase was extracted, derivatized and analyzed. The insoluble paint film was subjected to the depolymeriszation process without any separation of the organic phase from pigments. The inorganic phase was later isolated by a liquid-liquid (water-ethyl acetate) extraction; the resulting products of depolymerization were recovered from the organic phase and analyzed by FT-ICR MS.

As in the case of the model paint simples, mass spectrum of art oil paintings samples showed high chemical complexity. Spectra were calibrated using 4 reference compounds and the peaks were detected with a signal to noise ratio > 4. The reference compounds were composed of five known fatty acids: m/z 313.3213 ($C_{19}H_{41}ON_2$ DMAPA-Myristic acid-internal standard), m/z 341.3526 ($C_{21}H_{45}ON_2$ DMAPA-palmitic acid), m/z 367.3683 ($C_{23}H_{49}ON_2$ DMAPA-oleic acid), m/z 369.3839 ($C_{23}H_{47}ON_2$ DMAPA-stearic acid) and m/z 716.7028 ($C_{46}H_{90}N_3O_2$ (synthesized methyl oleate dimer). Myristin triglycerides having a mass equal to 2% of the initial sample mass were added to the samples before the transamidation reaction and used as internal standard for calibration and quantification. Referring to the internal standard $C_{19}H_{41}ON_2$ DMAPA-Myristic acid at m/z: 313.3213, we focused our work on the quantification of the total organic amount present in the sample considering the initial weight of the studied sample as well as the quantification of the different classes of molecules present in the sample (monomers, dimers, trimers and their degradated forms).

The Table 10 informs on the number of assigned/unassigned peaks in the studied spectra (i.e. assigned peaks are corresponding to molecular formula discussed in previous paragraphs) as well as monomers, dimers and trimers percentages and the ones of their degradated forms. The Figures 55 and 56 are showing the composition of the studied samples in term of multimers and their degradated forms. The degraded forms of multimers were identified *via* the molecular composition of the ions presents in the spectra considering the initial composition of linseed oil (main component linolenic acid; i.e. chain of 18 carbon atoms, 3 insaturations) and the

transamidation reaction (+ $C_5H_{14}N_2$). Monomers are thus composed of 23 carbons (or less in the case of fatty acid chain degradation) and 2 nitrogen atoms. The dimers correspond to two fatty acids linked to each other by a carbon-carbon, ether or peroxide bond and are thus composed of 46 carbon atoms and 4 nitrogen atoms (e.g.: $C_{46}H_{84}O_2N_4$), or 41 C and 2 N if one fatty acid is derivatized and the second one keep a free carboxylic acid function (e.g.: $C_{41}H_{72}O_3N_2$). A molecular formula based on 4 N and a number of carbon between 23 and 46 (e.g.: $C_{44}H_{80}O_2N_4$) signs the presence of a dimer with a degraded carbon chain. On the other hand, a degraded dimer czn be composed of 2 nitrogen atoms and a number of carbon between 41 and 23 (e.g.: $C_{39}H_{68}O_3N_2$). Trimer is formed with three fatty acids resulting in 69 C and 6 N (e.g.: $C_{69}H_{124}N_6O_3$), or 64-59 C and 4-2 N respectively (e.g.: $C_{64}H_{110}N_4O_4$; $C_{59}H_{96}N_4O_5$); a degraded trimer is thus composed from 6 nitrogen atoms and a number of carbons varying between 69 and 46 (e.g.: $C_{65}H_{116}N_6O_3$), or 64-59 and 46 in the case of 4 and 2 N respectively (e.g.: $C_{60}H_{102}N_4O_4$; $C_{55}H_{88}N_4O_5$). We also detected, compounds with a carbon chains between 92 and 68 with a number of nitrogen varying between 6,4 and 2 which corresponds to degraded tetramers (e.g.: $C_{77}H_{126}N_4O_4$). These molecular compositions were detected using a home-made program based on Python code.

Following the attribution of the molecular composition and their quantification using the internal standard, we observed that the amounts of organic part in both white and green samples are correlated with the obtained results from TGA analysis. However, in the case of the black and yellow-red samples, the percentages of the organic components were lower than the ones detected with TGA technique. This difference may be attributed to a loss of the organic material during sample preparation procedure or to interferences in the sample preparation procedure due to the sample composition. As shown in the Figures 55 and 56, we observed that the four samples are majorly composed of the degraded dimers and trimers, which prove that during the linseed oil polymerization, beside the reticulation process, the degradation mechanisms (e.g. β-scission) play an important role in oil painting reticulation and causes the fatty acids carbon chain degradation.

Table 10. Composition of the four art oil paints samples

	White	Green	Black	Yellow-red
Number of assigned peaks	3709	3314	3592	1146
Number of $^{13}C1$ isotopologues	797	727	777	211
Number of unassigned peak	15147	14238	14025	6741
Organic phase % (referring to the whole sample)	24%	23 %	10 %	7 %
Monomers %	4%	1%	5%	4%
Dimers %	4%	4%	4%	2%
Trimers %	1%	1%	1%	1%
Degraded dimers %	33%	20%	45%	18%
Degraded trimers %	43%	59%	30%	65%
Degraded tetramers %	15%	15%	15%	10%

White
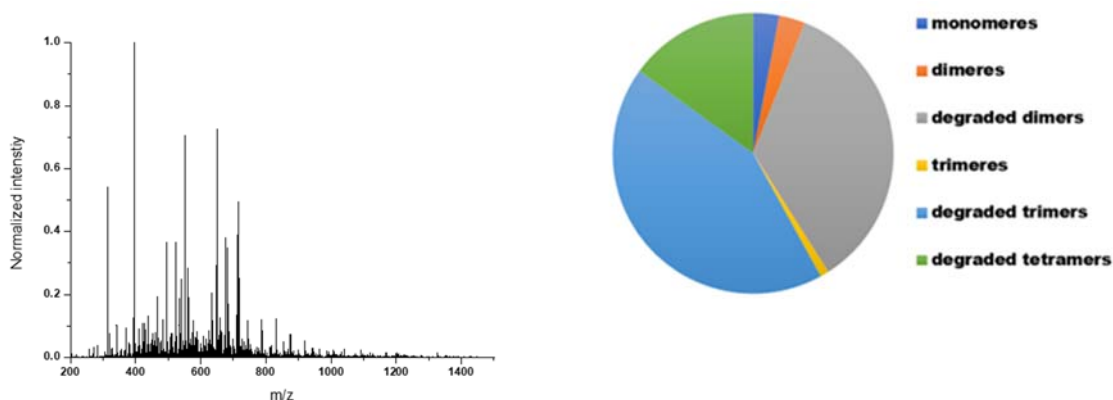
Green
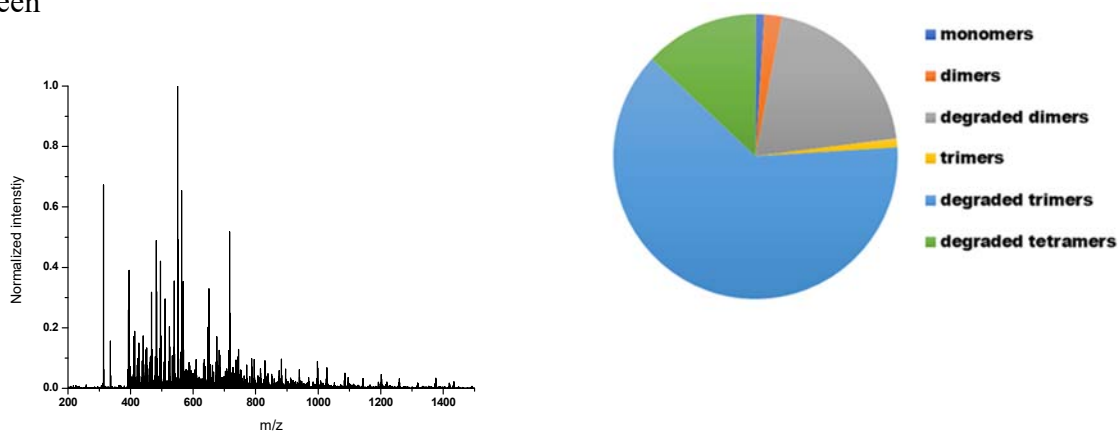
Figure 55. Mass spectra and compositions of the white and the green art oil paint samples

Black
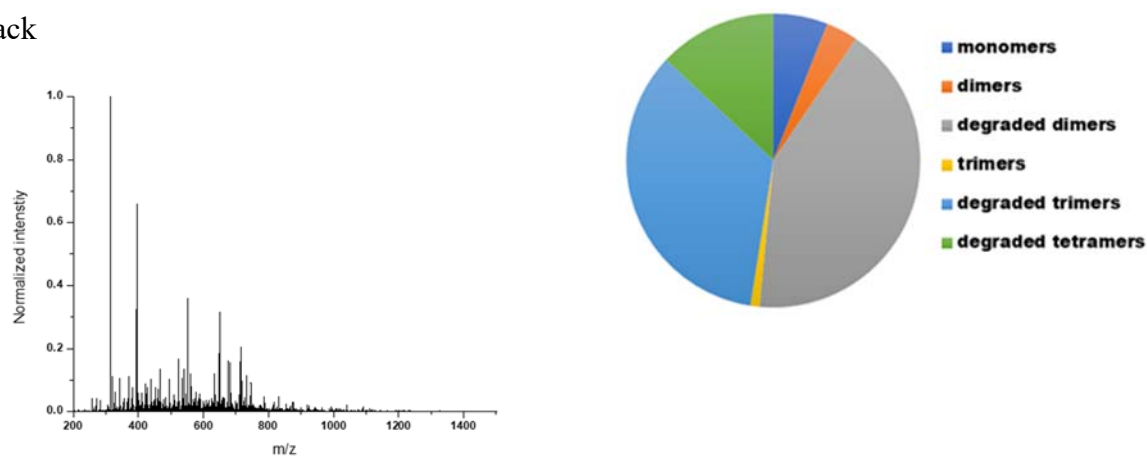
Red-yellow
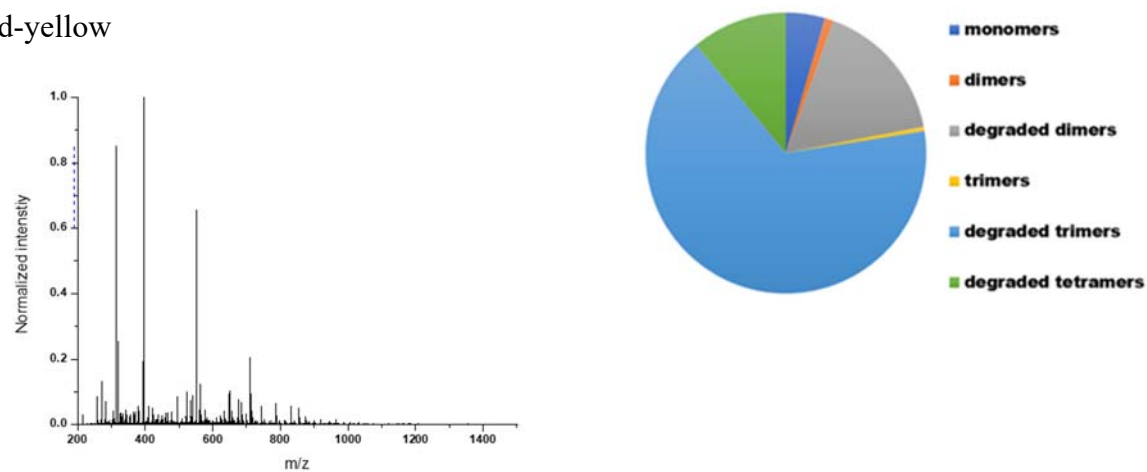
Figure 56. Mass spectra and compositions of the black and the red-yellow art oil paint samples

b. Van Krevelen plots

White
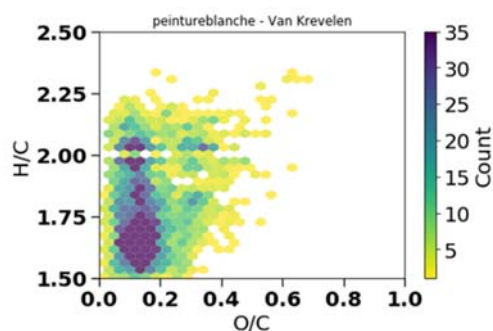
Black
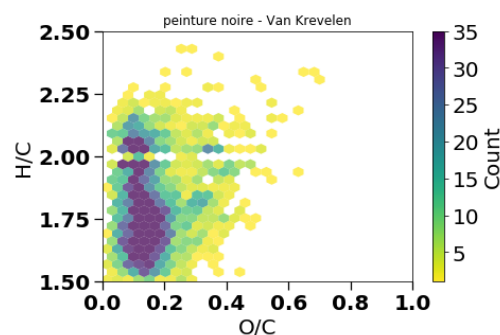
Green
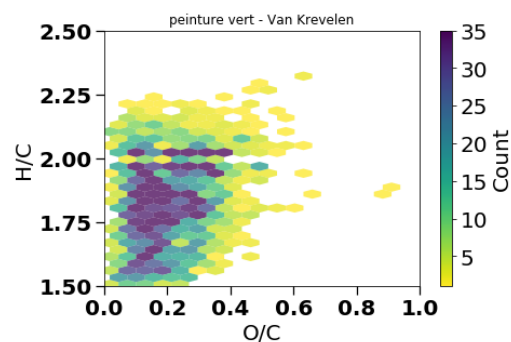
Red-yellow
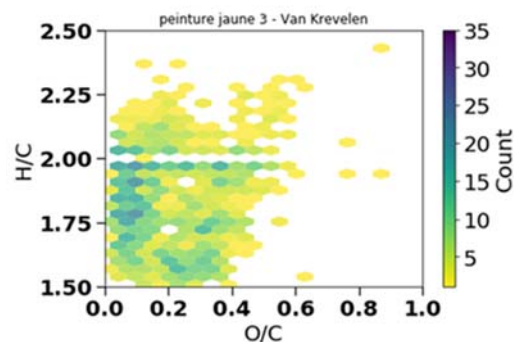
Figure 57. Van Krevelen diagrams highlighting the identified species based on the hydrogen to carbon (H/C) versus the oxygen-to-carbon ratios (O/C) as a function of the intensity of the four art oil paint samples

Van Krevlen plots show that the oxygen to carbon ratio is higher in the case of the green sample, however white and black samples contain more compounds with lower hydrogen to carbon ratio. It also indicates that black and white samples contain more compounds with shorter carbon chain than the green sample.

c. Experimental protocol reproducibility

In order to prove the reproducibility of our analysis, we repeated the same procedure on each sample several times and/or sampled in various locations of the artworks as in the case of the yellow-red sample. The Van Krevlen plots (Figure 59) show that the analyses of the yellow sample are similar, expecially when compared to another samples (for example here from black zone of the artwork). Moreover, zoom regions of the obtained mass spectra (Figure 58) inform on the presence of similar peaks for both analyses of the yellow samples. However when we compare this spectra with the one obtained from the black sample, we notice the presence of commom peaks but also of other peaks corresponding to different compounds.
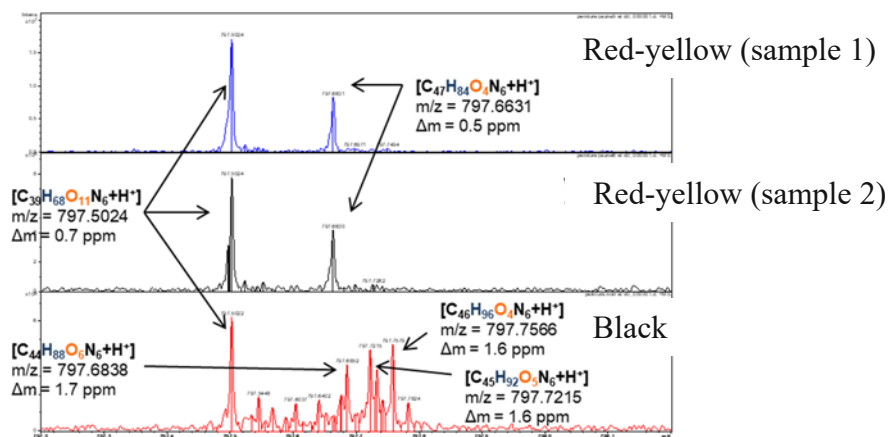
Figure 58. Zoom in on the peaks in the region of 797-798 m/z showing the common and different peaks between the yellow-red sample analyzed twice and the black sample.

Red-yellow (sample 1)
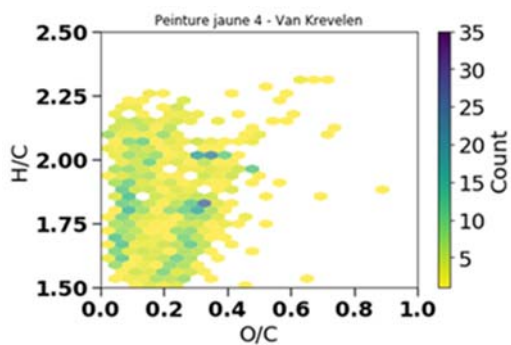
Red-yellow (sample 2)
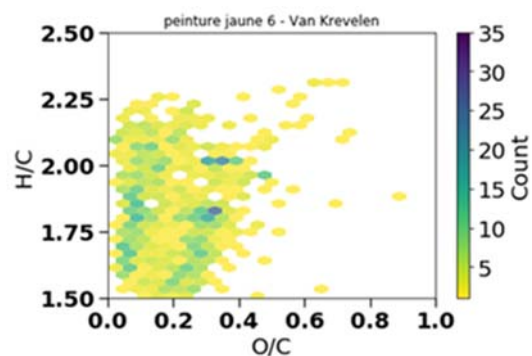
Black
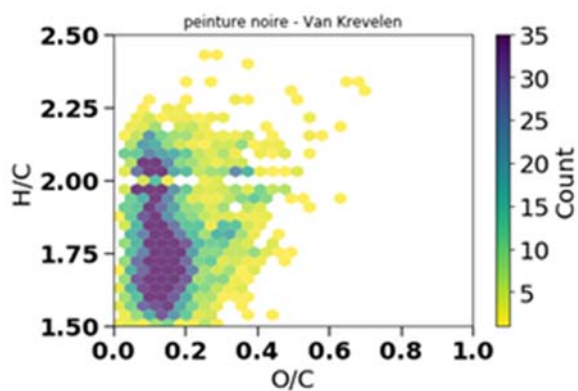
Figure 59. Van Krevelen diagrams highlighting the identified species based on the hydrogen to carbon (H/C) versus the oxygen-to-carbon ratios (O/C) as a function of the intensity: 2 red-yellow samples versus one black sample.

Conclusion

In this work, we developed a new and simple method to derivatize native and polymerized cross-linked solid films formed by linseed oil auto-oxidation based on the transamidation reaction. The FT-ICR analysis showed a higher sensitivity after derivatization in positive ionization mode due to the presence of an amine group. We succeeded to optimize our experimental protocol in order to derivatize and analyze less than 1 mg of paint sample. Moreover, we developed a new method for the synthesis of fatty acid dimers with carbon-carbon bond and peroxide bond.

This work is the first experimental characterization of the cross-linked polymer formed by the drying of siccative oils, we succeeded to show the occurrence in the studied samples of dimers, trimers and tetramers with a carbon-carbon, ether and peroxide bonds. Furthermore, several results during this study have highlighted the degradation mechanisms represented by the β-scission degradation and hydrolysis of the ester bonds between the fatty acids and the glycerol molecules.

We also studied the different compounds present in our derivatized paint samples, i.e. multimers and their degradated forms. We focused our methodology to classify the compounds present in the spectra regarding their molecular formula and we made an attempt of quantification of these compounds. We have also initiate a study of the influence of various parameters such as pigments. The developed methodology was applied on models but also on an oil art painting from the 19th century.

This experimental protocol will be optimizedin order to decrease the starting amount of sample used for the analysis. This methodology will be later applied on precious oil painting samples from Modigliani artworks within the National Modigliani project (cosupervised by the LaM Museum, Villeneuve d'Ascq, the C2RMF, Paris and our lab MSAP).

Material and methods

I.   Preparation of model paint film

1.   Model paints with cobalt salt as drier

A mixture of 1 g of linseed oil (Sigma Aldrich) with 0.1% Cobalt 2-ethylhexanoate (65% in white spirit) (Sigma Aldrich) which acts as a catalyst for the oxidation reaction of linseed oil and 200 μl of toluene. The mixture is spread over a glass surface for 3 days at ambient temperature.

2.   Paint models in presence of lead white pigments (($PbCO_3$)$_2$·$Pb(OH)_2$)

The paint films were prepared by stirring 1.0 g of linseed oil (Sigma Aldrich) with 2 mmol of pigment (534.42 mg ($PbCO_3$)$_2$·$Pb(OH)_2$) (Sigma-Aldrich) and 1 ml of deionized water. The mixture is spread over a glass surface for 3 days at ambient temperature.

II.   Transesterification of linseed oil film

All reagents were supplied by Sigma Aldrich. To test and optimize the transesterification reaction, we chose three derivatization reagents (2-dimethylaminoethanol ($C_4H_{11}NO$, 98.0%), 3-pyridylcarbinol ($C_6H_7NO_2$, 97.0%) and 3- (Dimethylamino)-1-propylamine ($C_5H_{14}N_2$, 99.0%)(DMAPA). These molecules can be positively charged because of their tertiary amino group and can be attached to the carboxyl acid by an ester or amide linkage.

The paint film was swelled with THF overnight, and the solvent (mobile phase) was separated from the film (solid phase). In a 100ml flask, 272.23mg (6.8mmol) of sodium hydride (NaH, 60% dispersed in mineral oil) were added and allowed to react for 15 minutes while stirring at room temperature with an excess of derivatization reagent (9ml). Then 1g of linseed oil film is added and the mixture is left to react for overnight while stirring under argon. Then the reaction is quenched by adding 2 ml of acetic acid followed by ammoniac until pH = 9. In the next step, the products were separated by liquid-liquid extraction with ethyl acetate and brine. Products present in the organic phase were recovered, evaporated, re-solubilized with (H_2O and 0.1% formic acid) and analyzed by NMR and high-resolution mass spectrometry FT-ICR.

III.   Derivation of free fatty acids

1-Ethyl-3- (3-dimethylaminopropyl) carbodiimide hydrochloride (EDCI) ($C_8H_{17}N_3HCl$), N-hydroxybenzotriazole hydrate (HOBt) ($C_6H_5N_3O.xH_2O,> 97\%$) and 3- (Dimethylamino) -1-propylamine ($C_5H_{14}N_2$, 99.0%) are supplied by Sigma Aldrich. The mobile phase recovered above was evaporated, it is supposed to contain free fatty acid, which will be derivatized in order to have a better detection by mass spectrometry in positive mode. 10 mg of the recovered free fatty acid were re-solubilized in 1 ml of ice-cold acetonitrile and N, N-dimethylformamide (4/1), followed by adding 67.1 mg of EDCI Dissolved in 1 ml of ice-cold purified water vortexed and kept in an ice bath. After 20 min, a mixture of HOBt (9.45 mg) and DMAPA (26.43 µL) in 2 ml of acetonitrile was added to the preceding mixture and the final solution is incubated at 60 °C for 4 hours. Finally, the derivatized fatty acids were evaporated and recovered in 1 ml of acetonitrile.

IV.   Synthesis of methyl oleate dimers

1.   Wohl–Ziegler bromination of methyloleate

All reagents were supplied by Sigma Aldrich. In a round bottom flask charged with 250 mg methyloleate (3.37 mmol), 3.5 mL of the solvent Cyclohexane was added. Then, N-Bromosuccinimide (NBS) (0.8 mmol) and Azobisisobutyronitrile (AIBN) (0.04 mmol) were added and the reaction mixture was stirred under a nitrogen for 1 hour at 80°C. Then, the reaction mixture was filtered and the solvent was evaporated at 30 °C. The products weredispersed in ethyl acetate and stored in dark at -20°C

2.   Carbon-Carbon Homo-coupling reaction of bromide methyl oleate

All reagents were supplied by Sigma Aldrich. In a round bottom flask charged with Zn (9.75 mg, 0.75 mmol) in pyridine (0.5 ml), ethyl crotonate (30 µl, 0.225 mmol) was added at room temperature and under vigorous stirring. $NiCl_2$ (9.5 mg, 0.075 mmol) was also added to the above mixture. Then, the temperature was rose to 55 °C while stirring for 15 min. The resulting red-brown Ni(0).2EC.Py complex was cooled down to room temperature. After the formation of the catalyst complex, methyl-oleate bromide (0.5 mmol) in CH_3CN (2 ml) was added drop

wise over a 10 sec period to realize the homocoupling reaction of bromide methyl-oleate. After 4 hours, the mixture was filtered with a short plug (elution with 30 ml of Et$_2$O), washed with brine, dried over Na$_2$SO$_4$, filtered, and concentrated. The product was purified by column-chromatography (petroleum ether/ethyl acetate = 97.5/2.5).

3. Synthesize of methyl-oleate dimer with peroxide bond

All reagents were supplied by Sigma Aldrich. 0.61 g (8.58x10^{-3} mol; 3.3 equiv) of potassium superoxide (KO$_2$) were introduced in an Erlenmeyer flask under N$_2$ flow. Then 60 mL of Dimethylformamide (DMF) and Tetraethylammonium bromide (TEAB) (0.87 g; 4.16x10^{-3} mol; 1.6 equiv) were added. The flask was capped and while stirring for 10 min to dissolve the solids. 1 g of methyl-oleate (2.6x10^{-3}mol) was added to the mixture and stirred for 3 hours at room temperature. Next, 50 mL of brine solution with 100 mL of hexane were cautiously added to control the exothermic and oxygen evolution from hydrolysis of excess KO$_2$. The hexane phase was separated. The aqueous phase and the middle milky layer were separated and washed with hexane and diethyl ether to recover the more polar species. The organic phases were then dried on Na$_2$SO$_4$ and concentrated. The final product was separated and purified by column-chromatography (petroleum ether/ethyl acetate = 95/5). The aqueous phase was treated with an excess of iodine solution in order to neutralize the KO$_2$ excess and avoid its reaction with acetone.

V. Mass spectrometry analysis

All the mass spectrometry analyses in this chapter were done on a 9.4 T nanoESI-hQh-ApexQE FT-ICR (Bruker Daltonics, Bremen, Allemagne) in positive mode. Samples were injected at a rate of 10 µL/hour using a syringe pump (Cole Parmer®, US) and a 250 µL syringe (Gastight, Hamilton). The acquisition was carried out with 1M points and a mass range of m/z 144.38 - 2500.

Linseed oil samples were diluted in a chloroform/methanol (1/1) solution with 2% of lithium chloride (^{7}Li) solution in methanol (10 mg/mL) for positive ionization. The derivatized lipids were diluted in ACN/H$_2$O (75/25) and 1% of formic acid was added to enhance the positive ionization.

VI.   Data processing and visualization

MS spectra were processed, visualized and calibrated using the Data Analysis software (Bruker Daltonics, Bremen, Germany). The calibration list was based on a number of known compounds as well the internal standards. A modified python script was used for peaks assignment and data visualization. The selected peaks for assignment have a Signal to Noise Ratio (SNR) threshold of 4 and a $\Delta m =< 1$ ppm to limit the false positives. Moreover, formula identification was based on odd-mass ions, and the mass of the proton that came from the ionization was subtracted. Peaks masses were assigned based on the Kendrick mass defect and z* approach to formulae assignment, and the attributed compounds were classed as a function of their number of Nitrogen, CH_2, DBE and oxygen. Van Krevelen plots were genertaed at the end in order to have a better data visualization.

References

1.   Dlugogorski, B. Z.; Kennedy, E. M.; Mackie, J. C., Roles of peroxides and unsaturation in spontaneous heating of linseed oil. *Fire Safety Journal* **2013,** *61*, 108-115.
2.   (a) Mills, J.; White, R., Organic chemistry of museum objects. BH Series. Conservation and Museology. Oxford: 1994; (b) Lazzari, M.; Chiantore, O., Drying and oxidative degradation of linseed oil. **1999,** *65*, 303-313; (c) Ordonez, E.; Twilley, J., Peer Reviewed: Clarifying the Haze: Efflorescence on Works of Art. *Analytical chemistry* **1997,** *69* (13), 416A-422A.
3.   Van Den Berg, J. D.; Vermist, N. D.; Carlyle, L.; Holčapek, M.; Boon, J. J., Effects of traditional processing methods of linseed oil on the composition of its triacylglycerols. *Journal of separation science* **2004,** *27* (3), 181-199.
4.   Gorkum, R. V.; Bouwman, E., The oxidative drying of alkyd paint catalysed by metal complexes. **2005,** *249*, 1709-1728.
5.   Meneghetti, S. M.; de Souza, R. F.; Monteiro, A. L.; de Souza, M. O., Substitution of lead catalysts by zirconium in the oxidative polymerization of linseed oil. *Progress in organic coatings* **1998,** *33* (3-4), 219-224.
6.   (a) Schaich, K., Metals and lipid oxidation. Contemporary issues. *Lipids* **1992,** *27* (3), 209-218; (b) Tumosa, C. S.; Mecklenburg, M. F., The influence of lead ions on the drying of oils. *Studies in Conservation* **2005,** *50* (sup1), 39-47.
7.   Zhang, Q.; Saleh, A. S. M.; Chen, J.; Shen, Q., Chemical alterations taken place during deep-fat frying based on certain reaction products : A review. *Chemistry and Physics of Lipids* **2012,** *165*, 662-681.
8.   Mallégol, J.; Gonon, L.; Commereuc, S.; Verney, V., Thermal (DSC) and chemical (iodometric titration) methods for peroxides measurements in order to monitor drying extent of alkyd resins. **2001,** *41*, 171-176.
9.   (a) Tanase, S.; Bouwman, E.; Reedijk, J., Role of additives in cobalt-mediated oxidative crosslinking of alkyd resins. **2004,** *259*, 101-107; (b) Muizebelt, W. J.; Hubertb, J. C.; Venderboschb, R. A. M., Mechanistic study of drying of alkyd resins using ethyl linoleate as a model substance. **1994,** *24*, 263-279; (c) Black, J., Metal-catalyzed autoxidation. The unrecognized consequences of metal-hydroperoxide complex formation. *Journal of the American Chemical Society* **1978,** *100* (2), 527-535.
10.   (a) Reviews, C.; Science, F., Chemistry of Deep-Fat Frying Oils. **2015,** *72*; (b) Boer, J. W. D.; Wesenhagen, P. V.; Wenker, E. C. M.; Maaijen, K.; Gol, F.; Gibbs, H.; Hage, R., The Quest for Cobalt-Free Alkyd Paint Driers. **2013**, 3581-3591.
11.   (a) Higgitt, C.; Spring, M.; Saunders, D., Pigment-medium interactions in oil paint films containing red lead or lead-tin yellow. *National Gallery Technical Bulletin* **2003,** *24*, 75-95; (b) Keune, K.; Boon, J. J., Analytical imaging studies of cross-sections of paintings affected by lead soap aggregate formation. *Studies in Conservation* **2007,** *52* (3), 161-176; (c) Keune, K.; van Loon, A.; Boon, J. J., SEM backscattered-electron images of paint cross sections as information source for the presence of the lead white pigment and lead-related degradation and migration phenomena in oil paintings. *Microscopy and Microanalysis* **2011,** *17* (5), 696-701.
12.   (a) Osmond, G.; Boon, J. J.; Puskar, L.; Drennan, J., Metal stearate distributions in modern artists' oil paints: surface and cross-sectional investigation of reference paint films using conventional and synchrotron infrared microspectroscopy. *Applied Spectroscopy* **2012,** *66* (10), 1136-1144; (b) Keune, K.; Boevé-Jones, G., Its surreal: zinc-oxide degradation and misperceptions in Salvador Dalí's Couple with Clouds in their Heads, 1936. In *Issues in Contemporary Oil Paint*, Springer: 2014; pp 283-294.
13.   Berg, J. D. J. V. D.; Berg, K. J. V. D.; Boon, J. J., Identification of non-cross-linked compounds in methanolic extracts of cured and aged linseed oil-based paint films using gas chromatography – mass spectrometry. **2002,** *950*, 195-211.

14.   (a) Mazzeo, R.; Prati, S.; Quaranta, M.; Joseph, E.; Kendix, E.; Galeotti, M., Attenuated total reflection micro FTIR characterisation of pigment–binder interaction in reconstructed paint films. *Analytical and bioanalytical chemistry* **2008,** *392* (1-2), 65-76; (b) Hermans, J. J.; Keune, K.; Loon, A. V.; Iedema, P. D., An infrared spectroscopic study of the nature of zinc carboxylates in oil paintings †. *Journal of Analytical Atomic Spectrometry* **2015,** *30,* 1600-1608; (c) Monico, L.; Janssens, K.; Cotte, M.; Sorace, L.; Vanmeert, F.; Giovanni, B.; Miliani, C., Chromium speciation methods and infrared spectroscopy for studying the chemical reactivity of lead chromate-based pigments in oil medium ☆. *Microchemical Journal* **2016,** *124*, 272-282; (d) Otero, V.; Sanches, D.; Montagner, C.; Vilarigues, M.; Carlyle, L.; Lopes, A.; Melo, M. J., Characterisation of metal carboxylates by Raman and infrared spectroscopy in works of art †. **2014**, 1197-1206.

15.   Robinet, L.; Corbeil-a2, M.-C., The characterization of metal soaps. *Studies in conservation* **2003,** *48* (1), 23-40.

16.   (a) Keune, K.; Boon, J. J., Imaging secondary ion mass spectrometry of a paint cross section taken from an early Netherlandish painting by Rogier van der Weyden. *Analytical Chemistry* **2004,** *76* (5), 1374-1385; (b) Keune, K.; Hoogland, F.; Boon, J. J.; Peggie, D.; Higgitt, C., International Journal of Mass Spectrometry Evaluation of the " added value " of SIMS : A mass spectrometric and spectroscopic study of an unusual Naples yellow oil paint reconstruction. **2009,** *284*, 22-34.

17.   (a) Catalano, J.; Murphy, A.; Yao, Y.; Alkan, F.; Zumbulyadis, N.; Centeno, S. A.; Dybowski, C., 207Pb and 119Sn Solid-State NMR and Relativistic Density Functional Theory Studies of the Historic Pigment Lead–Tin Yellow Type I and Its Reactivity in Oil Paintings. *The Journal of Physical Chemistry A* **2014,** *118* (36), 7952-7958; (b) Catalano, J.; Yao, Y.; Murphy, A.; Zumbulyadis, N.; Centeno, S. A.; Dybowski, C., Nuclear magnetic resonance spectra and 207Pb chemical-shift tensors of lead carboxylates relevant to soap formation in oil paintings. *Applied spectroscopy* **2014,** *68* (3), 280-286.

18.   Derrick, M. R.; Stulik, D.; Landry, J. M., *Infrared spectroscopy in conservation science*. Getty Publications: 2000.

19.   (a) Mallégol, J.; Gardette, J.-l.; Lemaire, J., Long-Term Behavior of Oil-Based Varnishes and Paints I . Spectroscopic Analysis of Curing Drying Oils. **1999,** *76*, 967-976; (b) Mallégol, J.; Lemaire, J.; Gardette, J.-l., Drier influence on the curing of linseed oil. **2000,** *39,* 107-113; (c) Mallégol, J.; Gardette, J.-l.; Lemaire, J., Long-Term Behavior of Oil-Based Varnishes and Paints . Photo- and Thermooxidation of Cured Linseed Oil. **2000,** *77*, 257-263.

20.   De Viguerie, L.; Payard, P.; Portero, E.; Walter, P.; Cotte, M., The drying of linseed oil investigated by Fourier transform infrared spectroscopy: historical recipes and influence of lead compounds. *Progress in Organic Coatings* **2016,** *93*, 46-60.

21.   Osmond, G.; Boon, J. J.; Puskar, L., Metal Stearate Distributions in Modern Artists ' Oil Paints : Surface and Cross-Sectional Investigation of Reference Paint Films Using Conventional and Synchrotron Infrared Microspectroscopy. **2012,** *66*, 1136-1144.

22.   Kaszowska, Z.; Malek, K.; Pa, M.; Mikołajska, A., Vibrational Spectroscopy A joint application of ATR-FTIR and SEM imaging with high spatial resolution : Identification and distribution of painting materials and their degradation products in paint cross sections. **2013,** *65*, 1-11.

23.   Ko, V.; Hradil, D.; Hradilová, J.; Ivan, N.; Schreiner, M., Spectrochimica Acta Part A : Molecular and Biomolecular Spectroscopy The ef fi ciency of micro-Raman spectroscopy in the analysis of complicated mixtures in modern paints : Munch ' s and Kupka ' s paintings under study. **2016,** *156*, 36-46.

24.   Daher, C.; Paris, C.; Le Hô, A. S.; Bellot-Gurlet, L.; Échard, J. P., A joint use of Raman and infrared spectroscopies for the identification of natural organic media used in ancient varnishes. *Journal of Raman Spectroscopy* **2010,** *41* (11), 1494-1499.

25.   Oyman, Z. O.; Ming, W.; Linde, R. V. D., Oxidation of 13 C-labeled ethyl linoleate monitored and quantitatively analyzed by 13 C NMR. **2006,** *42*, 1342-1348.

26. Manzano, E.; García-atero, J.; Dominguez-vidal, A.; Ayora-cañada, M. J.; Capitán-vallvey, F., Discrimination of aged mixtures of lipidic paint binders by Raman spectroscopy and chemometrics. **2012**, 781-786.

27. Mosca, S.; Frizzi, T.; Pontone, M.; Alberti, R.; Bombelli, L.; Capogrosso, V.; Nevin, A.; Valentini, G.; Comelli, D., Identification of pigments in different layers of illuminated manuscripts by X-ray fluorescence mapping and Raman spectroscopy. *Microchemical Journal* **2016,** *124*, 775-784.

28. Zidan, E. H.; Mosca, S.; Bellei, S.; Frizzi, T.; Gironda, M.; El-Rifai, I.; Mahgoub, H.; Sadik, S.; Rashed, M. G.; Osticioli, I., In situ imaging, elemental and molecular spectroscopy for the analysis of the construction and painting of a Late Period coffin at the Egyptian Museum of Cairo. *Measurement* **2018,** *118*, 379-386.

29. Spyros, A.; Anglos, D., Study of Aging in Oil Paintings by 1D and 2D NMR. **2004,** *76*, 4929-4936.

30. Cipriani, G.; Salvini, A.; Dei, L.; Macherelli, A.; Saverio, F.; Giannelli, C., Recent advances in swollen-state NMR spectroscopy for the study of drying oils. **2009,** *10*, 388-395.

31. Physics, A., Studies of organic paint binders by NMR spectroscopy. **2006,** *708*, 705-708.

32. Colombini, M. P.; Andreotti, A.; Bonaduce, I.; Modugno, F.; Ribechini, E., Analytical Strategies for Characterizing Organic Paint Media Using Gas Chromatography / Mass. **2010,** *43*, 715-727.

33. Piccirillo, A.; Scalarone, D.; Chiantore, O., Comparison between off-line and on-line derivatisation methods in the characterisation of siccative oils in paint media. **2005,** *74*, 33-38.

34. Colombini, M. P.; Modugno, F.; Fuoco, R.; Tognazzi, A., A GC-MS study on the deterioration of lipidic paint binders. **2002,** *73*, 175-185.

35. Manzano, E.; Rodriguez-simón, L. R.; Navas, N.; Checa-moreno, R., Talanta Study of the GC – MS determination of the palmitic – stearic acid ratio for the characterisation of drying oil in painting : La Encarnación by Alonso Cano as a case study. *Talanta* **2011,** *84*, 1148-1154.

36. Identification of lipid binders in paintings by gas chromatography. **2001,** *922*, 385-390.

37. Chiavari, G.; Fabbri, D.; Prati, S., Effect of pigments on the analysis of fatty acids in siccative oils by pyrolysis methylation and silylation §. **2005,** *74*, 39-44.

38. Loutelier-bourhis, C.; Zovi, O.; Lecamp, L.; Bunel, C.; Lange, C. M., Contribution of two approaches using electrospray ionization with multi-stage mass spectrometry for the characterization of linseed oil. **2009**, 3743-3752.

39. (a) Calvano, C. D.; Werf, I. D. V. D.; Palmisano, F., Fingerprinting of egg and oil binders in painted artworks by matrix-assisted laser desorption ionization time-of-flight mass spectrometry analysis of lipid oxidation by-products. **2011**, 2229-2240; (b) Werf, I. D. V. D.; Calvano, C. D.; Palmisano, F.; Sabbatini, L., Analytica Chimica Acta A simple protocol for Matrix Assisted Laser Desorption Ionization- time of flight-mass spectrometry (MALDI-TOF-MS) analysis of lipids and proteins in single microsamples of paintings. *Analytica Chimica Acta* **2012,** *718*, 1-10.

40. Muizebelt, W. J.; Nielen, M. W. F., Oxidative Crosslinking of Unsaturated Fatty Acids Studied with Mass Spec t rornet r y. **1996,** *31*, 545-554.

41. Zovi, O.; Lecamp, L.; Loutelier-bourhis, C.; Lange, C. M.; Bunel, C., Stand reaction of linseed oil. **2011**, 616-626.

42. La, J.; Zanaboni, M.; Uldanck, D.; Degano, I.; Modugno, F.; Kutzke, H.; Storevik, E.; Topalova-casadiego, B.; Perla, M., Analytica Chimica Acta Novel application of liquid chromatography / mass spectrometry for the characterization of drying oils in art : Elucidation on the composition of original paint materials used by Edvard Munch (1863 e 1944). **2015,** *896*, 177-189.

43. Loon, A. V.; Genuit, W.; Pottasch, C.; Smelt, S.; Noble, P., Analysis of old master paintings by direct temperature-resolved time-of- fl ight mass spectrometry : Some recent developments ☆. *Microchemical Journal* **2016,** *126*, 406-414.

44.   Johnson, D. W., Alkyldimethylaminoethyl ester iodides for improved analysis of fatty acids by electrospray ionization tandem mass spectrometry. *Rapid Communications in Mass Spectrometry* **2000,** *14* (21), 2019-2024.

45.   Snyder, S. A.; Kontes, F., Explorations into neolignan biosynthesis: Concise total syntheses of Helicterin B, Helisorin, and Helisterculin A from a common intermediate. *Journal of the American Chemical Society* **2009,** *131* (5), 1745-1752.

46.   Winkler, M.; Steinbiß, M.; Meier, M. A., A more sustainable Wohl–Z iegler bromination: Versatile derivatization of unsaturated FAME s and synthesis of renewable polyamides. *European Journal of Lipid Science and Technology* **2014,** *116* (1), 44-51.

47.   Peng, Y.; Luo, L.; Yan, C.-S.; Zhang, J.-J.; Wang, Y.-W., Ni-catalyzed reductive homocoupling of unactivated alkyl bromides at room temperature and its synthetic application. *The Journal of organic chemistry* **2013,** *78* (21), 10960-10967.

48.   Foglia, T. A.; Silbert, L. S., Preparation of di-n-alkyl peroxides: phase-transfer reaction of potassium superoxide with primary alkyl bromides. *Synthesis* **1992,** *1992* (06), 545-547.

49.   Chan, L. C.; Cox, B. G., Kinetics of amide formation through carbodiimide/N-hydroxybenzotriazole (HOBt) couplings. *The Journal of organic chemistry* **2007,** *72* (23), 8863-8869.

50.   Kew, W.; Blackburn, J. W.; Clarke, D. J.; Uhrín, D., Interactive van Krevelen diagrams–Advanced visualisation of mass spectrometry data of complex mixtures. *Rapid Communications in Mass Spectrometry* **2017,** *31* (7), 658-662.

51.   Kew, W.; Goodall, I.; Clarke, D.; Uhrín, D., Chemical diversity and complexity of scotch whisky as revealed by high-resolution mass spectrometry. *Journal of the American Society for Mass Spectrometry* **2017,** *28* (1), 200-213.

Chapter IV: Photochemical synthesis of metallic nanoparticles in flow

Table of contents

List of figures

List of tables

Introduction

I.   Nanoparticles: Definition

Interest in nanoscale materials has particularly increased over the last twenty years in areas such as chemistry,[1-3] physics, electronics,[4-5] optics,[6] magnetism[7] and even biology.[8]

Nanoparticles are particles that are between 1 and 100 nanometers in size. Nanoparticles are considered as an intermediate state between the solid bulk state and the atomic state.[1] Solid bulk materials have constant physical properties that do not depend on their size and their geometry, unlike nanoparticles. Thus, the properties of materials change as their size approaches the nanoscale and the percentage of atoms on the surface of a material becomes significant. For massive products ("bulk") of more than one micrometer (or micron), the percentage of atoms on the surface is negligible compared to the number of atoms in the volume of the material. The interesting and sometimes unexpected properties of nanoparticles are therefore largely related to the high surface/volume ratio as the size of the nanoparticles decreases. As a result, great efforts have been made in recent decades to develop synthetic methods to produce small nanoparticles (nm range) with a controlled size and shape.

Regarding the formation of metallic nanoparticles, there are two main synthetic approaches. On one hand, the physical method of dissociation called "top-down" consists on breaking up a solid metal in species of nanometric size. On the other hand, the chemical method of association called "bottom-up" is a chemical reduction of ionic salt precursor resulting in the formation of metal atoms associated into a particle.[9]

The Top-down approach essentially consists on the gradual reduction of the size of the current systems until reaching nanometric dimensions.

High energy grinding is one of the many techniques for obtaining nanocrystalline structures. In a sealed enclosure, under the effect of a succession of mechanical shocks, the powder grains are alternately plastically deformed, invoiced and bonded to each other, leading to a mixture of various constituents. The ratio of billing and bonding frequencies sets the final size of the powder aggregates.[10]

The Top-down approach also includes other synthetic methods such as photolithography,[11] laser ablation,[12-13] cathode sputtering.[14] They are based on the evaporation of a metal target respectively by heating with the aid of resistance, or by the bombardment of the target using a laser or ions of an inert gas.
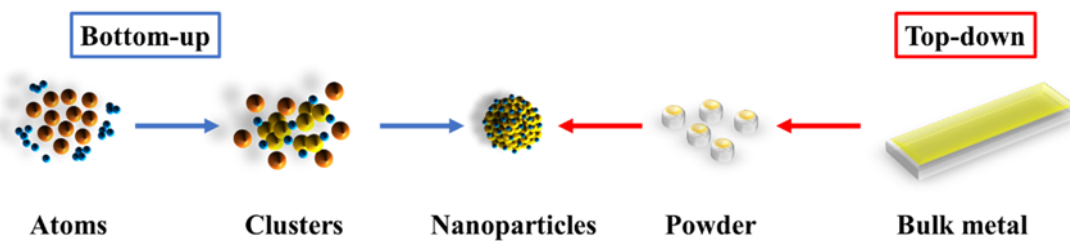
Figure 1. Schematic representation of the two Top-down and Bottom-up approaches for the synthesis of metallic nanoparticles

II. Nanoparticles formation mechanism

In our study, we are more concerned with the bottom-up approach. Various studies have been carried out in order to understand the molecular mechanisms involved in the synthesis of these nano-sized materials. The mechanism proposed for nanoparticles formation comprises two stages; nucleation and growth. It is very important to understand and control the different parameters that influence nanoparticles formation in order to obtain the lowest possible dispersity in size and shape.

M^{n+} :
Protecting ligand :
M_0 :

1st step:
formation of clusters

2nd step:
nucleation: formation of MNPs $+ nM^+$

3rd step:
growth: reduction of M^+ ion on the surface of nanoparticles
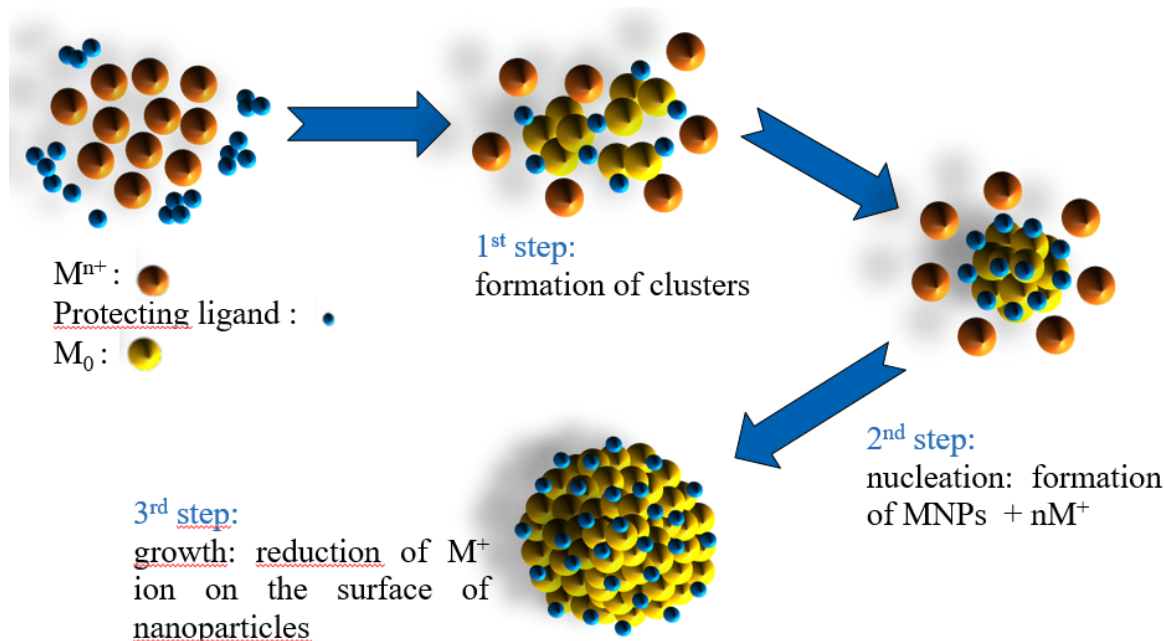
Figure 2. Schematic representation of metal nanoparticles formation following the bottom-up approach

1. Nucleation

Organo-metallic precursors are first dissolved and then reduced into metallic atoms with no charge. The oversaturation in insoluble metallic atoms and the collision between them leads to the formation of clusters in a first step. The next step is the nucleation, in which metallic atoms regroup in a thermodynamically stable solid phase, which constitutes the nucleus for later addition of metallic atoms on its surface during the growth step. Most of the theoretical studies are based on the classical nucleation theory.[15-18]There are two types of nucleation: (i) homogenous and (ii) heterogeneous. (i) When nuclei are formed spontaneously in the same phase uniformly, it is called

homogenous nucleation. (ii) Heterogeneous nucleation happens when the nucleation occurs at preferential sites of a solid particle surface.

We are interested in homogeneous nucleation, which takes place in a medium consisting of a single supersaturated phase where nucleus formation is spontaneous. The liquid/solid passage has an energy cost because it requires formation of an interface between the liquid and the solid phase. The Gibbs free energy of a nanoparticle formation with a radius r is given by the following equation:

$$\text{Equation 1: } \Delta G = 4\pi^2\gamma + \frac{4}{3}\pi r^3 \Delta G_V$$

The Total Gibbs free energy is the result of the sum of the surface Gibbs free energy γ and the bulk Gibbs free energy ΔG_V given by the following equation. Where k_B is Boltzmann's constant, T is the temperature and S the super-saturation of the solution. When the solution is supersaturated, ΔG_V becomes negative and the reaction becomes spontaneous.

$$\text{Equation 2: } \Delta G_V = \frac{-k_B T ln(S)}{v}$$

The surface Gibbs free energy γ is always positive and the bulk Gibbs free energy ΔG_V is negative as long as the solution is supersaturated. For this reason, the total Gibbs free energy ΔG depend on the nanoparticle radius r as it is shown in Figure 3. In order to form a stable nanoparticle, the radius of the nucleus should be equal to or higher than the critical radius (r*). When r < r*, the surface term is higher than the volume term, the nucleus is becomes unstable and re-dissolves. However, when r > r* the volume term compensates the energy applied on the surface of the nucleus and allows its surviving in the solution. The maximum free energy required for the formation of a stable nucleus and the critical radius are calculated by the following equations:

$$\text{Equation 3: } r^* = -2\gamma/\Delta G_V$$

$$\text{Equation 4: } \Delta G^* = \frac{16\pi\gamma}{3(\Delta G_V)^2}$$

As it is shown in the equations 3 and 4, the r* and ΔG^* can be decreased by decreasing the surface energy or by increasing the bulk free energy. ΔG_V increases with the supersaturation of the solution, however γ depends on the temperature, the solvent and the presence of ligands in the solution.
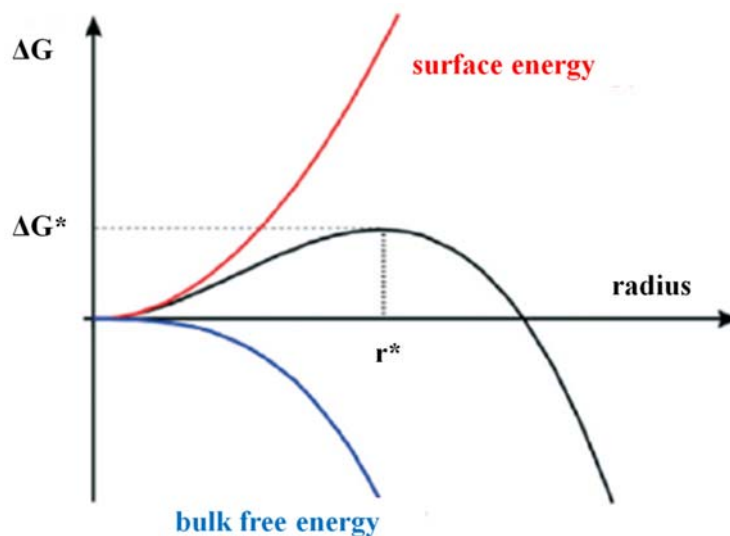
Figure 3. Variation of the Gibbs free energy as a function of the nucleus radius [17]

The nucleation rate is the number of formed nucleus as a function of time, and it is illustrated by the use of an Arrhenius type equation, where A is a pre-exponential factor:

$$\text{Equation 5: } \frac{dN}{dt} = A\, exp\left(-\frac{\Delta G^*}{k_B T}\right)$$

$$\text{Equation 6: } \frac{dN}{dt} = A\, exp\left(\frac{16\pi\gamma^3 v^2}{3k_B{}^3 T^3 (\ln S)^2}\right)$$

The nucleation rate depends on the temperature, the supersaturation and the surface free energy which also depends on the temperature, the solvent and the presence of ligands in the solution.[19]

2. Nanoparticles growth

The nucleus having reached the critical radius (r*) will be able to grow by consumption of the monomers in solution. This growth stage is thermodynamically favored, any increase in size will result in a decrease in free energy. However, two physical processes govern and can limit this phenomenon: the diffusion of the monomers of the solution towards the surface of the particle and the reaction of the monomers on the surface of the particles.[20] The higher the concentration of monomers in the solution, the faster the particles will grow.

In order to obtain a population of monodispersed particles, the nucleation and growth steps should ideally be decoupled.[16] Indeed, if the nucleation is brief and fast, the particles will then grow simultaneously, and the final size distribution will be narrow. In practice, solutions contain

complex chemical species that go against well-defined nucleation. An overlap between the two stages thus occurs during the synthesis, leading to a larger size distribution than in theory.

III.   Nanoparticles stabilization modes

The stability of the particles in solution results from a balance between the attractive Van der Waals forces and the repulsive electrostatic forces. In the absence of these repulsive forces opposed to the Van der Waals forces, the colloids aggregate to give the solid metal. There are three types of nanoparticle stabilization: 1) Electrostatic stabilization by anions and adsorbed cations on the surface. 2) Steric stabilization by large, congested molecules such as polymers or ligands. and 3) Electrosteric stabilization combining both steric and electrostatic effects.

1. Electrostatic stabilization

Ions adsorbed on the metal surface such as carboxylates, halides or polyoxoanions in aqueous solution and their respective counter-anions, form a double ionic layer around the particle at the origin of electrostatic stabilization. This creates a Coulomb repulsion between metal clusters. If the associated electrical potential is large enough, then the electrostatic repulsion prevents the agglomeration of the particles.[21]
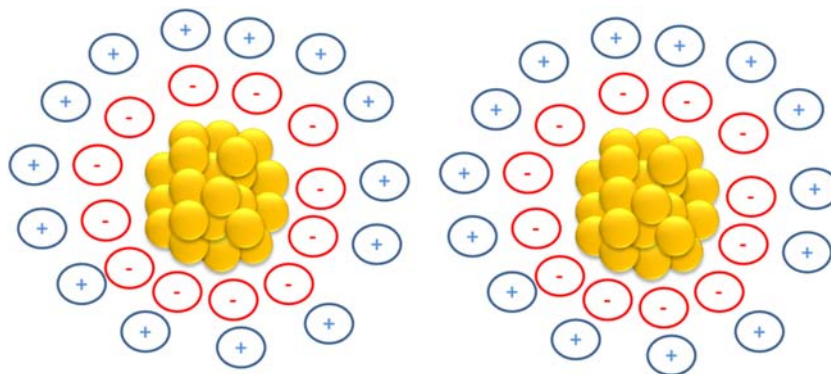
Figure 4. Schematic representation of the nanoparticles electrostatic stabilization

2. Steric stabilization

The adsorption of macromolecules, such as polymers, oligomers, or other organic molecules on the surface of the particles forms a protective layer. Those molecules prevents the agglomeration of particles in two different ways: 1) the movement is restricted in the inter-particle space causing a decrease in entropy and an increase in free energy and 2) the high concentration of stabilizing agent in this space prevents the two layers from interpenetrating.[22]

Different types of organic ligands were used for the stabilization of nanoparticles due to their coordination properties towards metals. The most used ligands are phosphines,[23-25] thiols,[26-28] and amines.[29-31] The choice of the ligand depends on its attended application. For example, in the case of catalytic applications, the organic molecules must not be introduced in too large excess to not block the active sites of the metal surface. On the other hand, polymers are also used to create a steric barrier between the particles, such as poly (N-vinyl-2-pyrrolidone) (PVP),[32-33] polyvinyl alcohol (PVA)[34-36] or cyclodextrins.[37-38]

3. Electro-Steric stabilization

Electro-steric stabilization is the combination of the two previous stabilization mechanisms. The ligands commonly used are charged organic compounds which benefit from the effect of both charge and steric hindrance. The most used molecules are charged polymers and ionic surfactants.[39-40]

IV.   Methods of nanoparticles synthesis

1.   Turkevish method

This protocol is based on the use of sodium citrate ($Na_3C_6H_5O_7$) for its reducing and stabilizing properties.[41-42] At first a part of the molecules present in the medium reduces the metallic ions to metallic atoms and then the other part adsorbs on the surface of the neoformed nanoparticles to stabilize them and avoid the creation of agglomerates.[42-43] The obtained particles have an average size of the order of 15 nm.[44-46] The advantage of this synthetic route is the presence of various experimental conditions that can be modified and parameterized to modulate the particles in terms of size and shape with controlled dispersion.[47-48]

Since then, other synthetic routes have been developed to obtain gold nanoparticles with increased control in terms of stability, size and particle size distribution around the average size. To do this, various reducing agents (e.g. azacryptand)[26, 49] as well as stabilizers PVA (polyvinyl alcohol)[50] or PVP (Poly (N-vinyl-2-pyrrolidone))[51] were used.

2.   Brust method

Developed by Brust in the 1990s for the synthesis of gold nanoparticles,[26] it consists on transferring a gold salt ($AuCl_4^-$), solubilized in the aqueous phase, into an organic phase (toluene) *via* a phase transfer agent, tetraoctylammonium bromide (TOAB). After addition of a stabilizing agent (decanethiol), the gold salt is reduced with sodium borohydride ($NaBH_4$). Several successive washes help to remove residual surfactant and precipitation size selection refines the size distribution. The gold nanoparticles dressed with thiols are finally obtained and they are thermodynamically stable with a diameter of 2.5 nm. In the case of silver, the synthesis protocol is the same as for gold, and the used silver salts are nitrate ($AgNO_3$) or perchlorate ($AgClO_4$).[52-53] Multiple variants have also been developed, allowing to control the final size of the nanoparticles as well as their dressing by different ligands such as amines, phosphines or polymers.[54] This method of synthesis has subsequently been adapted to different elements: Pd,[55] Cu,[56] Pt,[57] CoPt.[58]

3. Reverse Micellar Way

Inverse micelles (IM) are water droplets in a solvent, stabilized with a surfactant. The latter is an amphiphilic molecule that will be placed at the water-solvent interface, thus lowering the interfacial tension. IMs are used as a microreactor to achieve nanoparticle synthesis. At first inverse micellar solution contains the metal salt(s). We can then distinguish two procedures for the reduction: either the direct introduction of a reducing agent from aqueous phase into the micellar medium, or the introduction of another micellar solution containing the reducing agent. Under the effect of Brownian motion, multiple and incessant collisions occur, the aqueous hearts exchange and the reaction then takes place. Then there is separation and reconstitution of new independent droplets, containing in their heart the nanoparticles. A stabilizing agent is added to the solution and is adsorbed on the surface of the nanoparticles, ensuring their stability and thus allowing their extraction from the synthesis medium. Several successive washes remove the residual surfactant and precipitation size selection refines the size distribution. The size of the micelles and, consequently, the size of the nanoparticles, can be controlled by the ratio of both water and surfactant concentrations. Nanoparticles of many materials have been synthesized by this method such as silver,[59,60] gold[61] or bimetallic nanoparticles (AuAg, AuPd, PdPt ...).[62]

4. Nanoparticles synthesis *via* thermolysis

Another way for synthesizing nanoparticles is to decompose a precursor at high temperatures (between 150 and 350 °C). This decomposition takes place in the presence of ligands in a high-boiling solvent, most often under an inert atmosphere. The complex $[C_{14}H_{29}(CH_3)_3N]$ $[Au(SC_{12}H_{25})_2]$ is itself a good precursor for the synthesis at 180 °C of gold nanoparticles dressed with thiol, with a relatively large size distribution (26 ± 20 nm).[63] Navaladian et *al*. succeeded in synthesizing spherical silver nanoparticles 10 nm in diameter, via the decomposition of silver oxalate at 140°C, the polyvinyl alcohol being chosen as a stabilizing agent.[64] The synthesis of ultra-small AgNPs (> 3.5 nm) capped with oleylamine was reported by Park et *al*.[65] using the thermolysis method. Stable, small monodispersed palladium nanoparticles were obtained by thermolysis of Pd-thiolate cluster $[Pd(SC_{12}H_{25})_2]_6$, the Pd-thiolate precursor was heated at 298 °C for 3 hours.[29]

5. Photochemical synthesis

Photochemistry is considered as a key method in green chemistry since the generation of photons generates no waste. Light has considerable control over the formation of nanoparticles and the growth process control is performed by simply varying the volume, the duration and the exposure intensity.

This photochemical technique is based on the Norrish type I reaction.[66] In this type of reaction, benzoines are used as a source of radicals to reduce the soluble metal ions to their neutral (atomic) form to next generate nanostructures. The benzoin widely used by Scaiano *et al.* is Irgacure-2959® which generates ketyl radicals. He succeeded in the synthesis of aqueous unprotected gold nanoparticles.[67] A further study, from our laboratory has succeeded in optimizing the synthetic protocol by using high power UV sources which allowed to decrease the size of these gold nanoparticles down to 2 nm in order to be used as catalysts for aldehydes oxidative esterification reaction.[68]

Scaiano *et al.* described the photochemical synthesis of spherical silver nanoparticles with a diameter of 3 nm stabilized by citrate ligands.[69] They used Irgacure 2959® and low-power LEDs sources as in the case of gold nanoparticles. These nanoparticles could be photochemically modified in the visible range and lead to the formation of other nanoparticles having a larger size and different shapes (hexagonal, triangular and tubular). Scaiano showed that the shape of the nanoparticles depends on the excitation source and especially the wavelength.

Scaiano also described the possibility of using Irgacure 2959® in non-aqueous media with silver trifluoroacetate ($AgCO_2CF_3$) as a precursor in the presence of cyclohexylamine in tetrahydrofuran (THF), to form small AgNPs in few minutes (d = 3.4 nm).[70] The irradiation of AgNPs during the growth phase at different wavelength allowed the shape conversion. Moreover, the use of microfluidic approach permitted to reduce the conversion time and increase the control on the geometry of AgNPs.[71]

Hafermann et *al*. developed a photochemical synthesis of PdNPs in flow, using Irgacure 2959® as a photo-initiator to reduce palladium nitrate. They showed that the photochemical synthesis gives access to nanoparticles of better quality than those obtained by other synthetic techniques.[72]

6. Metallic nanoparticles synthesis in microfluidic system

The classical nucleation theory is based on two major steps (nucleation and growth).[73] In the nucleation step, metallic ions present in the precursor solution are reduced into atoms and create small particles called nucleons. In the next step, after the decrease of precursor concentration bellow the required minimum for the nucleation, soluble metallic ions are reduced on the surface of formed nucleons and achieve their growth. However, nucleation and growth can take place at the same time, which causes a broad size distribution of the final particles. Moreover, the size and dispersity of the nanoparticles depends on the experimental conditions as concentration, time, temperature/luminosity (in the case of photochemical reaction) and pressure. Microreactors allow a better control of the different reaction parameters than batch, and attain a shorter nucleation period. Which leads to the formation of nanoparticles with a narrow size distribution.[74-76]

Many studies were done on the synthesis of metallic particles in flow and different microfluidics systems designs were reported. In general, microreactors were made from glass, silicon, poly (dimethylsiloxane) (PDMS), stainless steel, ceramics, or polytetrafluoroethylene (PTFE).[75, 77] Two types of microreactors exist, single-phase continuous-flow microreactors and emulsion (two-phase) microdroplet/segmented-flow microreactors. The continuous-flow microreactors are easier to handle, more practical and faster, but the two phase reactors generates particles with less size dispersion.[74]

Several studies exist on synthesis of gold, silver and palladium nanoparticles in microfluidic systems. In our laboratory, the synthesis of gold nanoparticles by the Turkevich method with a diameter less than 2 nm protected by continuous sodium citrate has been described. A microfluidic system based on fused silica capillaries allows a high control of the synthesis parameters such as the mixing of the reagents, the temperature and the reaction time. This small size of gold nanoparticles was never been obtained using the conventional balloon Turkevich process. These nanoparticles were subsequently applied in catalysis.[78-79]

Regarding silver nanoparticles, some microfluidic system tests have been described in the literature.[71, 80] Using a PTFE capillary tube, well-dispersed silver nanoparticles with different sizes were synthesized by modifying the precursor solution flow rates. The authors demonstrated that the use of smaller diameter tubes is more suitable to achieve controllable synthesis of silver nanoparticles at different sizes. Concerning the synthesis of PdNP fluxes, several studies in the

literature describe the synthesis of ¨PdNPs, according to different techniques such as the photochemical method,[72] or NaBH$_4$[81] reduction. The synthesis of PdNPs in microfluidic system allows to obtain small and mono-dispersed NPs.

V.   Nanoparticles characterization

1. UV-Vis spectroscopy (plasmon band)

Optical properties are the main characteristic of noble metal nanoparticles. When a metal particle is subjected to an electromagnetic field and the size of the particles is smaller than the wavelength, free electrons of the conduction band undergo the same field and oscillate collectively and coherently under the effect of the electric field of the incident radiation. This phenomena is called Surface Plasmon Resonance.[14] This resonance occurs in the visible domain, only for gold, silver and copper. For example in water, spherical nanoparticles (size between 3-80 nm) exhibit an plasmon absorption at 567-570 nm, 390-400 nm and 500-550 nm respectively. The plasmon resonance frequency depends on the nature of the metal, the size and the geometry of nanoparticles, the ligands and the medium in which the particles are dispersed. For this reasons it is possible to study the optical properties by UV-Vis spectroscopy in order to characterize and identify Au, Ag and Cu nanoparticles.[82]
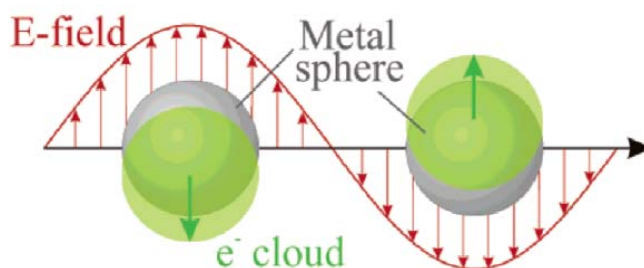
Figure 5. Schematic representation of the cloud oscillation of conduction electrons (localized surface plasmon) for a metal sphere subjected to an electric field.[83]

In 1908, Mie presents a solution to Maxwell's equations for describing absorption spectra of spherical particles of arbitrary size. This theory remains important because it is the only one to propose a simple and exact solution to Maxwell's equations.[83]

The UV-visible absorption spectrum of a dilute solution of nanoparticles can be calculated from this theory.[59] For a dilute colloidal solution, containing N particles per unit volume, the absorbance is given by the following equation.

$$\text{Equation 7: } A = \frac{CNl}{2.303}$$

Where C is the absorption cross-section and l is the length of the optical path.

In the case of spherical nanoparticles with a size of $2\pi R < \lambda$ (R is the NP radius and λ the incident wavelength), the electric dipole term of the Mie's theory becomes dominant. The cross section is described by the following equation.[84]

$$\text{Equation 8: } C = \frac{18\pi V \epsilon_2(\omega)\epsilon_m^{3/2}}{\lambda[(\epsilon_1(\omega)+2\epsilon_m)^2+\epsilon_2(\omega)^2]}$$

V corresponds to volume of spherical nanoparticle, ϵ_m is the permittivity of the medium and λ is the incident wavelength with a frequency ω.

Example of solvent's relative permittivity:

Solvent	Relative permittivity
Water	1.75^{78}
Toluene	2.38^{85}
THF	7.52^{86}

The complex relative permittivity of the metal is given by:

$$\text{Equation 9: } \epsilon(\omega) = \epsilon_1(\omega) + i\epsilon_2(\omega)$$

The absorption reaches its maximum for $\epsilon_1(\omega) = -2\ \epsilon_m$ when ϵ_2 is small. The wavelength of the plasmon resonance depends on $\epsilon_1(\omega)$ which implies that the surface plasmon band position depend on the solvent in which the nanoparticles are dispersed. The ϵ_2 determines the width and the height of the resonance plasmon band. The dielectric function is composed of two terms. The first term corresponds to the interband contribution (gold: 5d; silver: 4d) and the second term corresponds to the almost free conduction electrons based on Drude expression (D).[87]

$$\text{Equation 10: } \epsilon_1(\omega) = \epsilon_{1IB}(\omega) + \epsilon_{1D}(\omega)$$

And

$$\text{Equation 10: } \epsilon_2(\omega) = \epsilon_{2IB}(\omega) + \epsilon_{2D}(\omega)$$

$\epsilon_{1D}(\omega)$ is given by:

$$\text{Equation 11: } \epsilon_{1D}(\omega) = 1 - \left\{ \frac{\omega_p^2}{(\omega^2 + \omega_0^2)} \right\}$$

And $\epsilon_{2d}(\omega)$ is given by:

$$\text{Equation 12: } \epsilon_{2D}(\omega) = \frac{\omega_p^2 \omega_0}{\omega(\omega^2 + \omega_0^2)}$$

ω_0 is the frequency of the inelastic collision of the free electrons within the metal. ω_p is the frequencies of the plasma oscillation of free electron given by the following equation.

$$\text{Equation 13: } \omega_p^2 = \frac{\pi N e^2}{m}$$

N stands for the density of free electron, e for the electron charge and m is the effective mass.

a. The influence of size on optical properties of nanoparticles.

UV-Vis spectroscopy is an important techniques for the characterization of nanoparticles that possess optical properties such as gold, silver and copper. It allows not only a kinetic monitoring of M^{n+} reduction into M^0 but it gives also an indication on the nanoparticles sizes and geometry based on the wavelength, the height and the width of surface plasmon band. You et al.[88] showed the variation of wavelength (λ_{max}) as a function of the gold nanoparticles size (Figure 6).
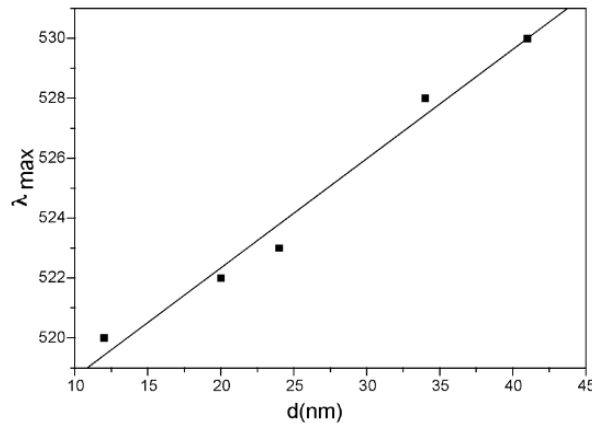
Figure 6. λ_{max} variation as a function of Au-NPs diameter[88]
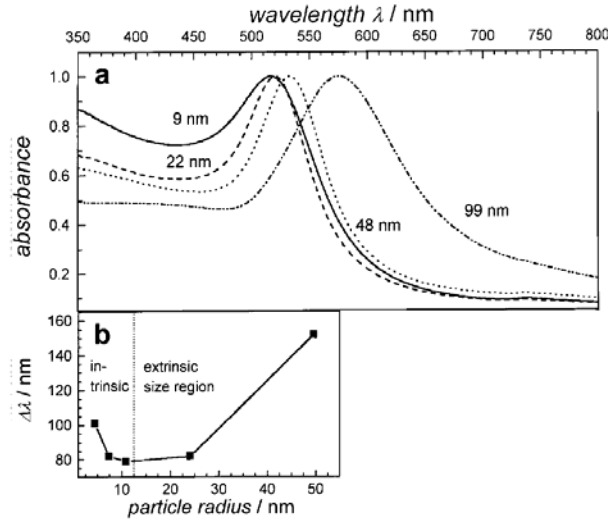
Figure 7. a) UV-visible spectra of the AuNPs with different sizes in water. (b) Variation of λ_{max} as a function of AuNPs radius[89]

In another study done by Link et *al.*,[89] they demonstrated that the absorption bands positions of nanoparticles cannot be correlated with the size for NPs that have a diameter < 20 nm. However, the width of plasmon band increases when the size of Au-NPs decreases (Figure 7). The width of the surface plasmon band increases until it becomes invisible for nanoparticles less than 3 nm.

However, due to the small size of nanoparticles, the rate of scattering from particles surfaces ω_s dominates ω_0 and the size influence on the surface plasmon band. ω_s is given by:[87]

$$\text{Equation 14:} \omega_s = \frac{v_f}{R}$$

R is the particle radius and v_f is the Ferni velocity

The reduction in size of the metal induces an increase in the imaginary part of its dielectric function ε_2. We can therefore observe an increase in the damping of the resonance and consequently an enlargement of the absorption band.

b. The influence of ligands on optical properties of nanoparticles

The adsorption of molecules on the surface of nanoparticles also leads to a decrease in resonance intensity and a significant displacement of its wavelength position (Figure 8).[90] This phenomenon is not only explained by a change in the dielectric function of the medium but rather by a modification of the local electronic density on the surface of the metal.
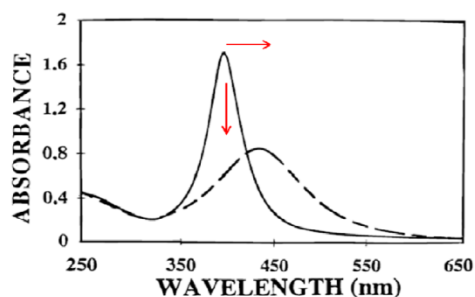
Figure 8. UV-visible spectrum driving the damping and the displacement of the plasmon resonance due to the hanging of the thiols on silver nanoparticles synthesized in inverse micelles[90]

c. The influence of shape on optical properties of nanoparticles

Chen et *al.*,[91] for their part, were interested in the influence of the nanoparticles shape on their UV-visible spectrum. They started by synthesizing gold nanoparticles of different shapes like spheres, cubes, stars, sticks and bipyramids. Then they compared the UV-visible spectra obtained for each of the morphologies. MET and UV-visible spectra are shown in Figure 16. The absorption peak at surface plasmon varies depending on the geometry of the nanoparticles,
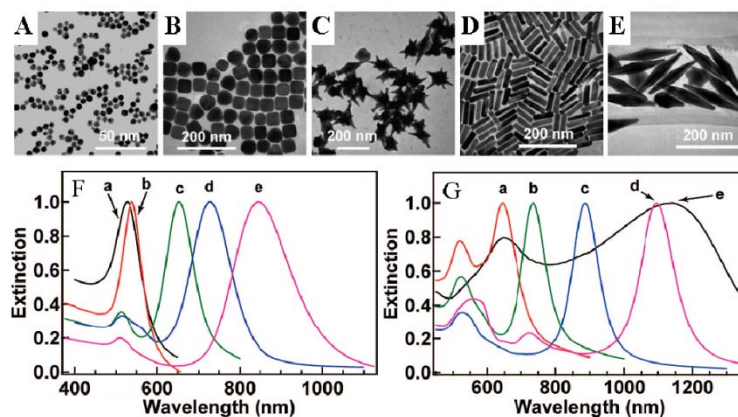
Figure 9. Evolution of the UV-Vis spectrum of AuNPs as a function of their shape[91]

In another study, Silvestrini *et al.[71]* also showed that in the case of silver nanoparticles the absorption peak at surface plasmon varies as function of AgNPS shape.
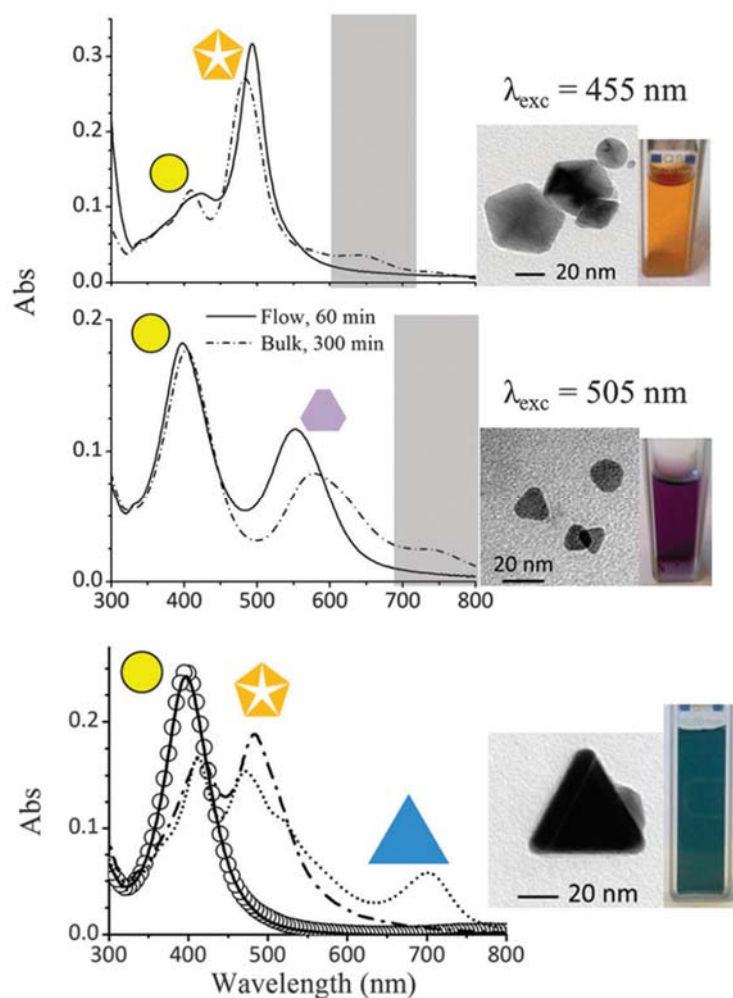
Figure 10. Evolution of the UV-Vis spectrum of silver NP colloids as a function of their shape[71]

2. **Dynamic light scattering (DLS)**

Dynamic Light scattering (DLS) is a relatively recent characterization technique that is becoming increasingly popular in research laboratories specializing in nanotechnology. This technique provides access to the size distribution of suspended nanoparticles.[92]

During the implementation of this technique, the colloidal solution is illuminated by a monochromatic light beam (LASER). Part of this light scattered by the particles is then detected by a photomultiplier. The Brownian motion within the solution constantly upsets the distances between the particles. The displacement of the particles then generates fluctuations in the constructive and destructive interactions of the scattered light. The treatment of these fluctuations by a digital correlator makes it possible to obtain an autocorrelation function of the signal which represents the probability for a particle to be at a given instant $(t + \tau)$ at the same point of space as at moment (t). The smaller a particle, the lower the probability. Conversely, the probability increases with particle size.

The intensity correlation function $(G_2(\tau))$ represents the particles motions. It corresponds to the variation in scattering intensity by comparing the intensity at time T to a later time $(T+\tau)$ and expressed by an integral over the intensity product at different times.

$$\text{Equation 15: } G_2(\tau) = \langle I(t)I(t + \tau) \rangle$$

And the normalized form of $G_2(\tau)$;

$$\text{Equation 16: } g_2(\tau) = \frac{\langle I(t)I(t+\tau)\rangle}{\langle I(t)\rangle^2}$$

It is almost impossible to identify the movement of each particle from the flickering. However, the electric field correlation function $(G_1(\tau))$ describes the correlated particles movement

$$\text{Equation 17: } G_1(\tau) = \langle E(t)E(t + \tau) \rangle$$

And the normalized form of $G_1(\tau)$;

$$\text{Equation 18: } g_1(\tau) = \frac{\langle E(t)E(t+\tau)\rangle}{\langle E(t)E(t)\rangle}$$

The two correlation functions are associated following the Seigert relationship.

$$\text{Equation 19: } G_2(\tau) = B[1 + \beta|g_1(\tau)|^2]$$

B and β are both constants. B corresponds to the baseline and β is an instrumental response which depends on detector area, optical alignment and scattering properties.

In the case of monodispersed particles which also undergo a Brownian motion, the electric field correlation factor, $G_1(\tau)$ decays exponentially as a function of a decay constant Γ as it is represented in Equation 20

$$\text{Equation 20: } G_1(\tau) = exp^{-\Gamma\tau}$$

The relation between the Brownian motion and the decay constant is represented by Equation 21.

$$\text{Equation 21: } \Gamma = -Dq^2$$

D corresponds to the diffusion behavior of particles and q is the Bragg wave factor calculated by the equation 22.

$$\text{Equation 22: } q = \frac{4\pi n}{\lambda} \sin\left(\frac{\theta}{2}\right)$$

λ is the wavelength of incident light, n is the solvent refractive index and θ is the angle of the detector. The particles hydrodynamics radius is obtained following the Stokes-Einstein equation:

$$\text{Equation 23: } D = \frac{kT}{6\pi\mu r}$$

- r= hydrodynamic radius
- D = translational diffusion coefficient
- k = Boltzmann's constant
- T = temprature
- η = viscosity

3. Transmission electron microscopy (TEM)

Transmission electron microscopy (TEM) is a fundamental tool for the study of nanoscale materials. Used in conventional mode, this technique allows determining the morphology, size, polydispersity and crystallinity of synthesized nanoparticles. The resolution of electronic microscopes is greater than that of optical microscopes due to the use of an accelerated electron beam. For example, if the electrons are accelerated with a voltage of 100 kV the theoretical resolution will be 0.0037 nm. On the other hand, the aberrations of the electromagnetic lenses reduce the resolution to ~ 0.3 nm.

Electrons accelerated at a voltage between 100-1000 kV will be proportioned by the cathode, a filament made from tungsten (W) or hexaboride of lantane (LaB$_6$) which is heated at high temperatures to excite electrons.

The accelerated electrons are directed toward the sample by electromagnetic lenses, these electrons will pass through the sample (which should have a minor thickness of 30 nm) and create an image using the transmitted electrons.

VI.   Nanoparticles applications

In recent years, metallic nanoparticles have attracted considerable interest due to their intriguing physicochemical properties, small size and surface plasmon behavior. Nanoparticles have been used in diverse domains including optoelectronics, biosensors, catalysis, and, as antimicrobials.

1.   Catalytic applications

One of the main applications of metal nanoparticles remains catalysis.[93-95] These nanomaterials soluble in aqueous or organic media have a surface reactivity giving them intermediate properties between heterogeneous and homogeneous catalysts. In addition, their small size (between 1 and 10 nm) gives them a very large specific surface and therefore potentially a high number of active sites available for the transformation of substrates.[1, 22] Their high selectivity can be modulated by the choice of stabilizing agents present on their surface. Also, in recent years, transition metal particles have become increasingly interesting, highlighting the need to control their size, shape, organization and the nature of chemical species on their surface.[1] For this reason, criteria for distinguishing nanoclusters from traditional colloids have been proposed by Finke.[2] These particles are generally: between 1 and 10 nm in size, isolable and redissolvable, soluble in organic or aqueous solvents as well and have a well-defined surface composition.

Nanoparticles were applied as catalyst in different number of reactions as hydrogenation,[2, 93, 96-97] oxidation[68, 98-100] and the formation of carbon-carbon bonds reactions[101] as Suzuki-Miyaura reactions. In our study, we are particularly interested in gold, silver and palladium nanoparticles.

Gold is considered to be chemically inert and was classified as inactive or inactive as a catalyst, but in 1980 Haruta demonstrated that 5 nm diameter gold particles were effective for the oxidation of carbon monoxide.[102] Hutchings found that gold can be a good catalyst for the hydrochlorination of acetylene to vinyl chloride.[103] Moreover, poly-(2-aminothiophenol)-stablized AuNPs have been applied as catalyst for or Suzuki− Miyaura cross-coupling reaction of aryl halides with arylboronic acids in water.[104] More recently, our laboratory showed the photocatalytic activity of gold nanoparticles supported over PTFE microbeads in the oxidative esterification reaction of aldehydes.[68] Several studies have investigated the catalytic activity of AgNPs for 4-nitrophenol reduction.[105-106] In another publication, the shape of AgNPs plays a role in their catalytic activity. The cubic form of nanoparticles showed the best result for styrene oxidation.[107]

Palladium is considered as one of the most effective metals as catalysts for carbon-carbon bond formation such as cross-coupling reactions; Suzuki, Sonogashira, Heck, Stille. Palladium nanoparticles (PdNPs) have attracted great interest recently. Their large surface area to volume ratio and the high activity of surface atoms make PdNPs an alternative catalyst for coupling reactions under greener conditions. In addition, the use of solid-grafted PdNPs makes it possible to reduce costs, simplify procedures and facilitate the separation of the final product as well as the recovery of catalysts and their recycling. Palladium nanoparticles stabilized by poly-(N-vinyl-2-pyrrolidone) (PVP) showed to be efficient catalyst for Suzuki reaction in water.[108] The PVP has an essential role in stabilizing PdNPs and prevents them precipitating during chemical Suzuki reactions. However the excess of PVP decreases the catalytic activity of PdNPs.[109] PVP–Pd nanoparticles were also supported on activated carbon and applied as catalyst for Suzuki reaction. The activated carbon support increases the stability of PdNPs and prevents their precipitation and agglomeration. It allows also an easy recovery of the catalyst. The recycling and reuse of PdNPs as catalyst for several reactions permits to maintain $73 \pm 3\%$ of its catalytic activity during the fifth next cycles of the reaction.[110] PdNPs supported on TiO_2 exhibit a photocatalytic activity under 465 nm illumination wavelength toward Sonogashira coupling reaction in mild conditions.[111]

Bimetallic nanoparticles have interesting catalytic properties. Gold and palladium bimetallic nanoparticles exhibited higher catalytic activities for organic reactions such as Stille, Hiyama, Butchwald-Hartwig and Ullmann cross-coupling than the gold and palladium monometallic nanoparticles.[112] As well Au-Ag alloy nanoparticles showed exceptionally high activity in catalysis for low-temperature CO oxidation.[113]

2. Anti-bacterial applications

For a long time silver was used due to its antibacterial properties, Herodotus mentioned that Persian kings only drank water if it was in a silver vase, so Hippocrates used it for wound healing and treatment of ulcers and burns.[114] The antibacterial properties of silver have been extensively studied, its effectiveness against *Streptococcus mutans* (S. *mutans*), the microorganism that causes caries, has been verified by Cristóbal et *al.*[115] as well as its reaction against gram negative bacteria like *Escherichia coli* and gram-positive bacteria such as *Staphylococcus aureus*.[116-117]

Generally, these nanoparticles are more reactive because of their surface area ratio and the volume radius, i.e. a particle is more reactive when it is smaller, yet it is more likely that it interacts with

bacteria. The mechanism of action of nanoparticles in the cell is not yet established, with scientists proposing various hypotheses.

A study by Feng et *al.* suggests that nanoparticles penetrate the cell membrane of the bacteria, where sulfur-containing proteins are found. Silver nanoparticles interact with these proteins in the cell as well as with phosphorus-containing compounds such as DNA. When the silver nanoparticles enter the bacterial cell, they form a region of low molecular weight in the center of the bacteria on which the bacteria cluster, thus protecting the DNA from silver ions. Nanoparticles preferentially attack the respiratory chain, cell division eventually leading to cell death. In addition, nanoparticles release silver ions into bacterial cells and enhance their bactericidal activity.[118]

Gold nanoparticles have also antibacterial properties. In the investigation of M.Mohamed *et al.* these nanoparticles are capable of penetrating the cell membrane of the bacterium *Corynebacterium pseudotuberculosis* (causing *caseous lymphadenitis*) and inhibiting it. These nanoparticles can be irradiated with a beam of light of 520 nm so that they absorb the energy and an increase of temperature occurs to cause the death of the bacteria, this technique is called photo thermal therapy.[119]

Functionalization of gold nanoparticles is also a good way to increase antimicrobial activity. Li et *al.* reported a relationship between the antimicrobial effect and the surface functionalization of the nanoparticles, they found that the most hydrophobic have a major efficiency against the bacteria *Escherichia coli*, *Enterobacter cloacae* complex, *Pseudomonas aeruginosa* and *Staphylococcus aureus*.[120]

3. Nanoparticles in cultural heritage, for coloration, diagnosis and restoration

Historically, the synthesis of nanoparticles is not as recent as one imagines, because in the fourth century AD, Roman craftsmen made glasses that contained nanoscale metals. An object dating from this period; called *Lycurgus* cup is exposed at the British museum in London. The cup, which represents the death of King *Lycurgus*, is made from glass that contains nano particles of silver and gold. The color of the cup changes according to the lighting: if it is illuminated by the interior (transmitted light), its color becomes red and if it is illuminated by the outside (reflected light) its color becomes green.[121] In the medieval churches, the large varieties of the beautiful colors of windows, are due to the presence in the glass of copper metal nanoparticles, having a size comparable to the wavelength of the light. Particles of different sizes disperse different wavelengths of light, giving the glass different colors.[122-123] On the other hand, noble metal nanoparticles as AgNPs and AuNPs were used to enhance Raman signals for the identification of organic pigments and dyes in works of art and cultural heritage material.[124]

Nanomagnetic sponge was applied to clean the surfaces of damaged painting, this sponge is composed of magnetic nanoparticles ($CoFe_2O_4$) linked to polyethylene glycol-acrylamide gel matrix. The magnetic nanoparticles ensure the removal of all the cleaning gel residue from the painting surface.[125]

Alkaline earth metal hydroxide nanoparticles are widely used in consolidation and deacidification of cultural heritage objects. Many monumental art works are made from calcium carbonate material, for this reason calcium hydroxide nanoparticles ($Ca(OH)_2$) present the best choice to be applied for consolidation.[126] However, in presence of large amount of soluble sulfates in a wall painting, sulfate ions can react with calcium hydroxide to form gypsum (white glaze on the painted surface). Studies show that a mixture of $Ca(OH)_2$ NPs and barium hydroxide nanoparticles ($Ba(OH)_2$) gave better results in consolidation.[127] Magnesium hydroxide ($Mg(OH)_2$) nanoparticles have been used for the deacidification of paper, canvas, and wood. They play a role in stabilizing the pH around neutrality and in the inhibition of both metal catalyzed oxidation and the acid hydrolysis of paper.[128] In another study, ZnO nanoparticles were mixed with acrylic varnish and applied as coating layer to protect the oil painting against dirt, fungal attack and UV aging.[129]

Figure 11 The upper picture represents the Lycurgus Cup. The cup on the right is in reflected light and on the left in transmitted light, department of Prehistory and Europe, The British Museum.[121] And the picture below represents Panel 8e from the Great East Window (1405e1408) at York Minster.[122]

Results and discussion

The applications of NPs depend strongly on their size, shape, protecting ligand and stability all of which can be defined depending on the synthesis method. Turkevich et *al* developed the first, and the most common, protocol for the synthesis of stable gold and silver nanoparticles in aqueous medium using thermal energy and sodium citrate which serves as a reducing agent of HAuCl₄.[41] Despite its high efficiency, this protocol can only be performed under aqueous conditions since the formed hydrophilic NPs are unstable in organic solvents. Moreover, the removal of the aqueous solvent generally leads to the complete loss of the ability to reform a colloidal solution.[130]

To overcome this limitation, Brust-Schiffrin et *al*, succeeded in developing two-phase liquid-liquid system for the synthesis of gold and silver nanoparticles with alkanethiol stabilization.[26] Nonetheless there are few reports that describe the synthesis of stable silver NPs in the organic solvent toluene.[131]

In order to obtain NPs of lower dispersity and higher stability, protocols using electrochemistry, [132-133] laser ablation[134-135] and microwave heating[136-137] as forms of energy for nucleation along with using different types of polymers and organic molecules for stabilizing the NPs are reported.[138]

In addition, using photochemistry can provide many advantages compared to the other protocols due to their excellent spatial and temporal control, their execution at room temperature and their substitution of the strong reducing agents whose chemical residuals might adhere to the formed NPs. Despite these advantages, synthesis of NPs based on photochemical processes have exhibited low yields and high dispersity. For instance, a general photochemical synthesis of stable metal nanoparticles has been described by the Scaiano's group based on the reduction of metal salts by ketyl radicals. However, the formed nanoparticles had low production yields along with poor size control and polydispersity.[67, 70] These limitations can be overcome by using microfluidic systems that have recently shown potentials in the synthesis of NPs of controlled sizes.[139] This is due to their high heat and mass transfer compared to batch reactors. Moreover, the small path length compared to batch reactors leads to improved homogeneous illumination of the reaction mixture that would lead to better yields. Microreactors have easier control over the reaction conditions, for instance by changing the flow rate, both the mass transfer and the residence time are modified. This flexibility in tuning the reaction conditions makes it more favorable to have highly controlled NPs

in flow than in batch.[140] For instance, our research group already synthesized gold NPs using the Turkevich method in flow where a size range of 1.5 to 3 nm of NPs was obtained for a residence time of 35 to 94 s.[78] Baber et *al* 2017 also synthesized nanoparticles in flow using the Turkevich method where the size was controlled by changing the flow rate.[141] This level of control over mass transfer is not easily achieved using batch reactors. As a result, many studies focus on preparing various noble NPs using the flow technology.[72, 142-143] Other studies have succeed to develop a photochemical synthesis of gold, silver and noble metal nanoparticles in flow, the microfluidic system applied to the photochemical synthesis of metal nanoparticles promotes a fast nucleation and allows to obtain small and mono-dispersed nanoparticles. However, the synthesis of ultra-stable metallic nanoparticles in organic solvent in order to expand their applications, is considered a challenge. In this work, we demonstrate the photochemical synthesis of small mono-dispersed metallic nanoparticles in organic solvents in a lab designed microfluidic system.

I.   Silver nanoparticles synthesis by photochemistry

1. Mechanism of photochemical synthesis

The silver nanoparticles of Turkevich are unstable in organic solvents, thus unusable for the desired application. As described in the first chapter, Scaiano has proposed a new method for synthesizing silver nanoparticles into organic solvents by batch photochemistry using alkylamines (cyclohexylamine) as a protective agent. We have adopted the conditions used by Scaiano using three different amines: amylamine, cyclohexylamine and oleylamine.

The particles are not stable in THF, nanoparticles agglomerate and precipitate after a short period of time, they are stable only for one week away from light and at 4°C. The literature describes this instability in THF and attributes it to desorption on the surface of the nanoparticles of the ammonium trifluoroacetate salt which forms an important part of the stabilization layer of the particles, then their precipitation. This lack of long-term stability limits the use of these nanoparticles. Scaiano et *al* described the replacement of THF with toluene after evaporation which leads to a higher polydispersity but a better stability.[70] In this study, we used microreactor technology that accelerateds photochemical reactions and provided better control over size and polydispersity when synthesizing these nanoparticles directly in toluene. Silver trifluoroacetate salt was replaced with silver tetrafluoroborate since it was found that is more stable in toluene. We performed a systematic kinetic study and evaluated the influence of protective ligands (amylamine and oleylamine) on size and dispersion. Nanoparticles synthesized in the presence of cyclohexylamine were unstable and they precipitated after few minutes from their synthesis.

Figure 12. AgNPs coated with amylamine in toluene

Table 1 represents the different flow rates and irradiation times applied to complete the kinetic study of formation of AgNPs in a microfluidic system.

Table 1. Different flow rates and irradiation times used in our kinetic study.

flow rate (µl.min⁻¹)	Irradiation time (min.sec)	Time of reaction (min.sec)
4500	0.30	1.20
2250	1.00	2.40
1500	1.30	4.00
1125	2.00	5.20
750	3.00	8.00
450	5.00	13.20
225	10.0	26.40

After optimization of the reagents (photoinitiator, silver salt, amine), it turned out that silver tetrafluoroborate combined with Irgacure 907® (instead of Irgacure 2959®) leads to the best results. The concentrations of injected reagents were: 5 mM for the AgBF4 silver precursor, 50 mM for the amine (amylamine and oleylamine) and 5 mM for the Irgacure 907® photoinitiator. An Amine/Ag⁺ molar ratio greater than 10 is necessary, with a smaller ratio, we observe a precipitation of the nanoparticles in the microfluidic system. The formation mechanism of AgNPs is shown in Figure 13.
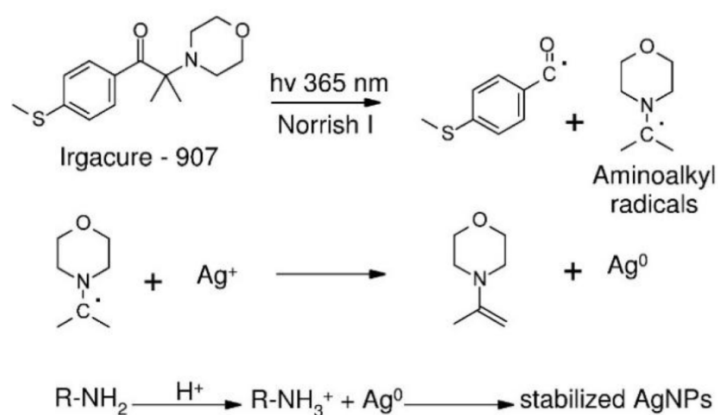
Figure 13. Mechanism of AgNPs synthesis

Irgacure 907 generates amino alkyl radicals following a Norrish type I reaction after UV irradiation at 365 nm. Generated radicals reduce Ag⁺ into Ag⁰ and the formed nanoparticles are stabilized with the amine ligands.

205

After optimization, the photochemical protocol transposed into a microfluidic system making it possible to obtain a significant reduction in the sizes and the polydispersity of the silver particles compared with what has been observed with the classical Turkevich method. These nanoparticles are monodispersed, stable in organic solvent, and have a small size.

2. Amylamine

a. Characterization using UV-Vis spectroscopy

UV-Vis spectroscopy allows the determination of the Surface Plasmon Band (SPB) and the intensity of its absorbance (Figure 14). The λ_{max} of silver nanoparticles with amylamine maintains the same value ($\lambda_{max} = 438$ nm) during the different irradiation times and it shows a variation only at 1 min of irradiation accompanied with a decrease in absorbance which can be caused by AgNPs agglomeration. Absorbance increases with the increase of the irradiation time to reach its maximum after 1.5 minutes then it remains constant with the increase in irradiation time. We can conclude that at 1 minute and 30 seconds all the Ag^+ ions have been reduced into Ag^0 and assembled in stable nanoparticles. It is assumed that the concentration of AgNPs is equal to that of the silver ions (5 mM).
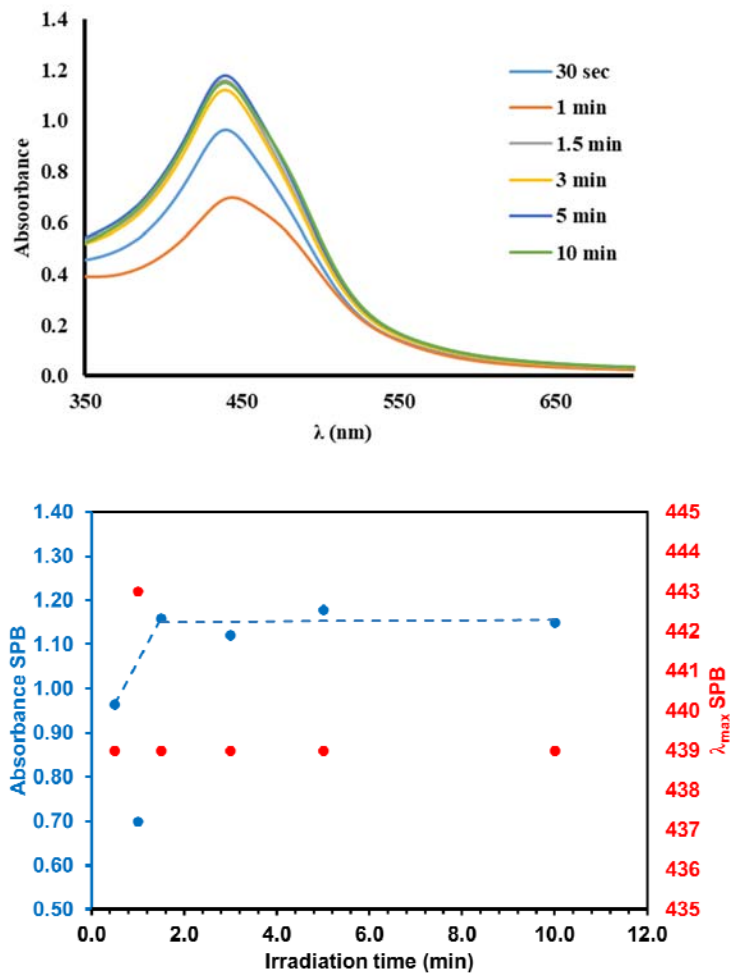
Figure 14. (a) UV-visible spectra of the AgNPs-amylamine obtained in flow at different irradiation times using the 1:10 Ag$^+$/amylamine ratio. (b) Variation of the absorbance (blue) and surface plasmon band wavelength (red) of the prepared Ag-NPs at different irradiation times.

b. Characterization by DLS (Dynamic Light Scattering)

In the next step, we carried out a kinetic follow-up of the reaction as a function of the size and polydispersity of the nanoparticles synthesized with the different amines based on DLS (Dynamic Light Scattering) technique. For each sample, five independent measurements were made. For each measurement, 10 to 14 sub-measurements with a duration of 10 seconds were carried out. The software calculates the size of the different particle populations that are present in the sample as well as the average value of the hydrodynamic diameter of our nanoparticles. From these information, we can calculate the polydispersity index which is a measure of the width of the particle size distribution. Polydispersity indices less than 0.1 are typically referred to as "monodisperse". The formula for polydispersity is established according to the standard deviation:

PDI = square of the standard deviation / mean diameter.

For example, a particle with an average diameter of 2.7 nm and a standard deviation of 0.64 nm has a PDI of 0.055 (Figure 15).
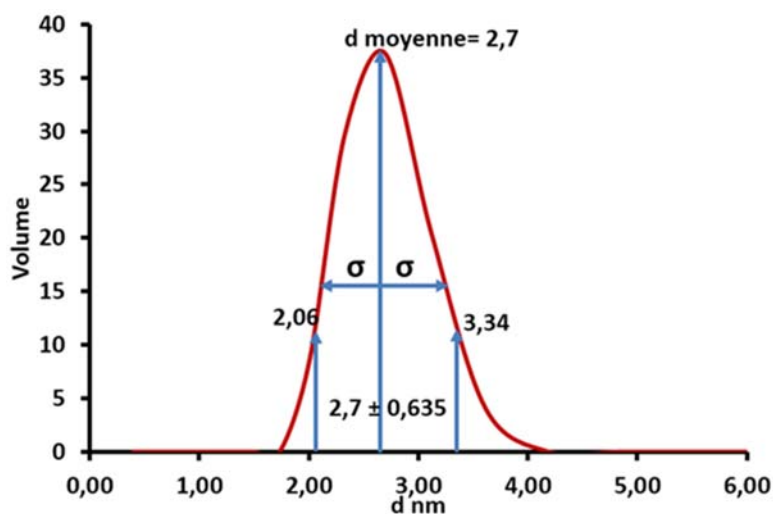
Figure 15. Example of polydispersity variation
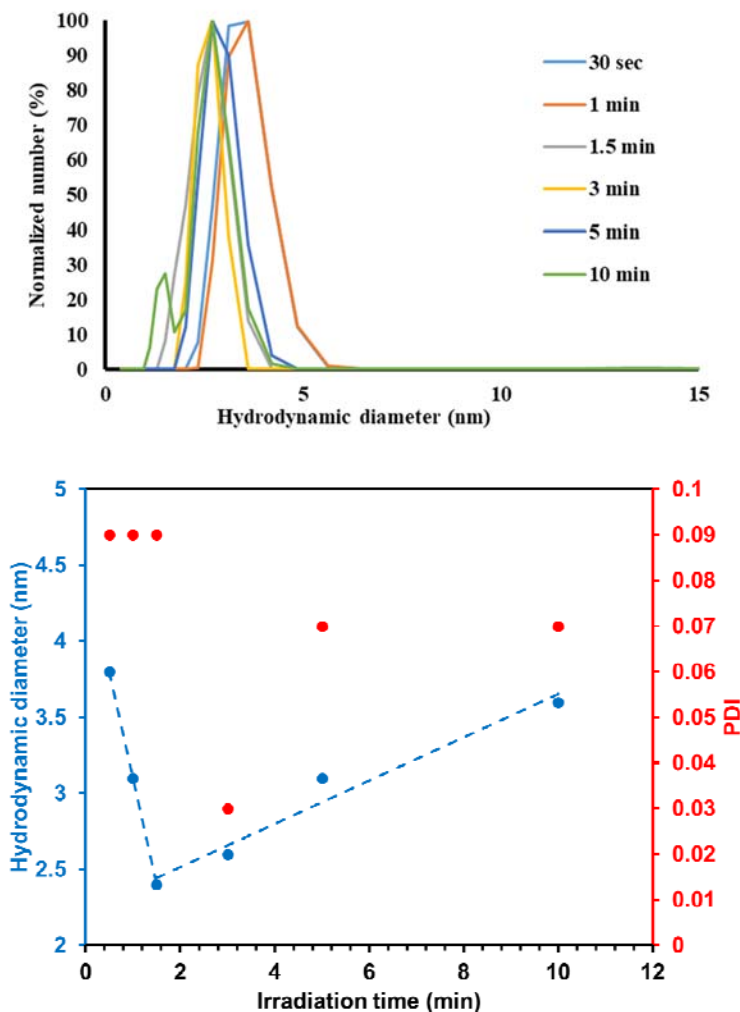
Figure 16. DLS distribution of AgNPs-amylamine prepared in flow at different irradiation times using the 1:10 Ag$^+$/amylamine ratio. (b) Variation of average diameter (blue) and PDI (red) of the prepared Ag-NPs at different irradiation times

After only 30 sec of irradiation, silver clusters are formed and have a size of 3.7 nm with a polydispersity of 0.09. The hydrodynamic diameter decreases and attends its minimum at 1 min 30 sec. Then the size of nanoparticles increases with increasing irradiation time, reaching a size of 4.2 nm after 5 minutes of irradiation. The PDI is less than 0.1 at the different irradiation times, which shows that the nanoparticles formed are monodispersed. In addition, it was noted that between 30 seconds and 1.5 minutes the value of the PDI falls from 0.09 to 0.05 (Figure 16). This shows that in the nucleation stage, particles become more and more monodispersed. During the growth phase the PDI remains practically constant and AgNPs size grow slightly. (Table 2. This variation in size as a function of the irradiation time is in agreement with the nanoparticle formation theory. As we explained before, the mechanism of formation of silver nanoparticles consists of 3 steps. The first

step is the formation of silver colloids. In this step and under UV irradiation, Irgacure -907 generates aminoalkyl radicals, which reduce the Ag^+ ion to Ag^0. Metallic silver atoms gather together to form colloids that are polydispersed and have an irregular size and shape which correspond to the phase between 0.3 and 1.5 min of irradiation. In the second stage, the nucleation step, the colloids formed reorganize into particles that have a well-defined and regular size and shape between 1.5 and 3 min of irradiation. The nanoparticles formed in this stage are called nucleons for two reasons, firstly they are monodispersed and they have a minimum size, and secondly these nanoparticles will be the assembly core for nanoparticles of the larger size. The small nanoparticles formed in the second stage are surrounded by ions of Ag^+, these ions will be reduced on the surface of the nanoparticles to complete their growth and this is the third and last stage. In this step after 3 min of irradiation, the nanoparticles grow in size but they retain their monodispersities. It should be noted that protective ligands such as amylamine in this case play an initial role since they prevent the aggregation of nanoparticles.

Table 2. AgNPs-Amylamine variation of Absorbance, λ_{max}, Hydrodynamic diameter, and PDI

	Flow rate ($\mu L.min^{-1}$)	Irradiation time (min)	λ_{max}	Absorbance at λ_{max}	Average diameter	PDI
AgBF₄/amylamine = 1/10	4500	0.5	439	0.96	3.6	0.09
	2250	1.0	443	0.7	3.3	0.07
	1500	1.5	439	1.16	2.3	0.05
	750	3.0	439	1.21	2.6	0.03
	450	5.0	439	1.18	3.1	0.04
	225	10.0	439	1.15	3.6	0.05

c. Characterization by Transmission Electron Microscopy (TEM)

TEM image of AgNPs obtained after 3 minutes of irradiation in the microfluidic system (Figure 17) shows that particles are clearly separated. On the other side, size distribution in TEM confirm the results obtained with the DLS. AgNPs nanoparticles capped with amylamine are mono-dispersed and have a small size around 2 nm.
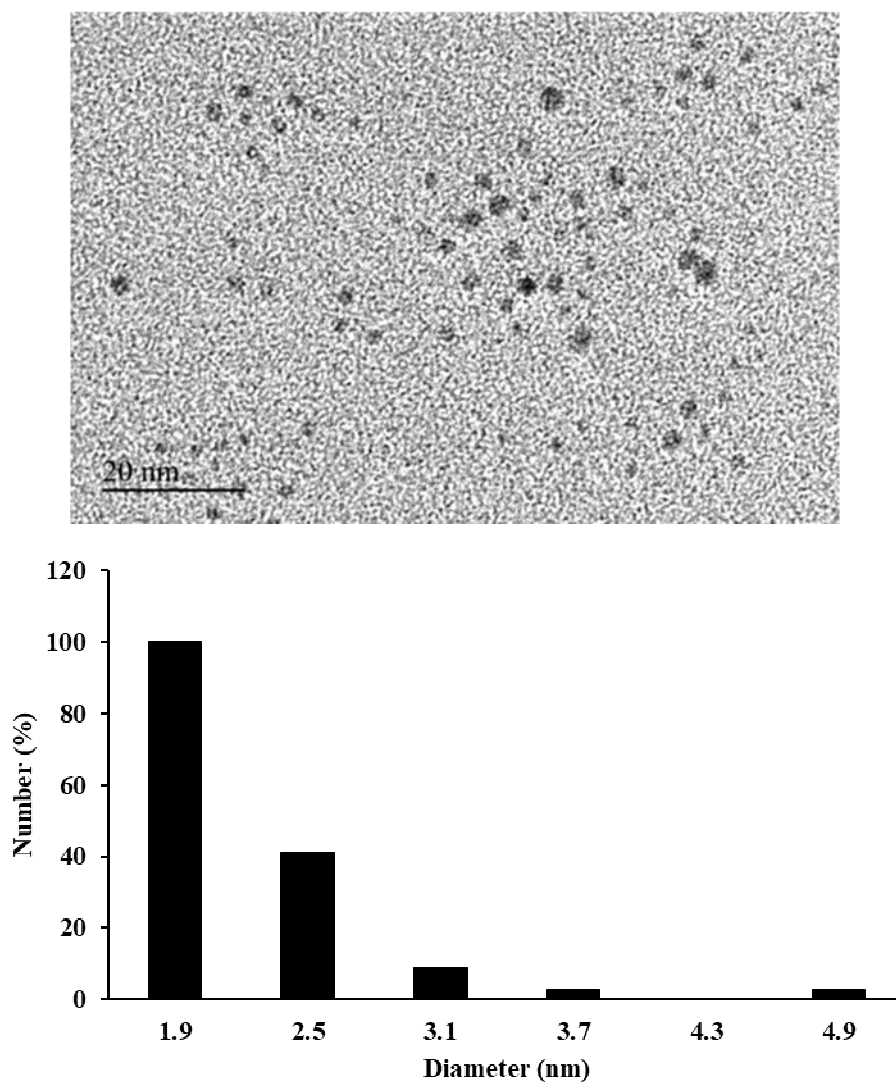
Figure 17. . Transmission Electron Microscopy (TEM) images and size distribution of Ag-NPs obtained after 3 minutes of irradiation

3. Oleyamine

For silver nanoparticles capped with oleylamine, the plasmon band is at 455 nm (Figure 18), and the absorbance increases with increasing irradiation time to reach its maximum around 3 minutes, then it decreases with the increase in irradiation time. This is due to the formation of aggregates and some of the nanoparticles are precipitated in the system.

Figure 18. (a) UV-visible spectra of the AgNPs-oleylamine obtained in flow at different irradiation times using the 1:10 Ag$^+$/ oleylamine ratio. (b) Variation of the absorbance (blue) and surface plasmon band wavelength (red) of the prepared Ag-NPs at different irradiation times.

In the case of silver nanoparticles with oleylamine, the same mechanism for forming nanoparticles as seen previously with amylamine is observed. The minimum size of the nanoparticles (3.6 nm) is reached after 1.5 minutes of irradiation, and the nanoparticles are larger than the previous ones (Figure 19). However, the PDI is greater than or equal to 0.1, which shows that the nanoparticles obtained are polydispersed. The PDI increases in parallel with the irradiation time, reaching its

maximum of 0.16 after 2 minutes and remains constant for up to 5 minutes. It should be noted that, if the irradiation time is increased, the particles precipitate in the system after 5 minutes. As it shown in Table 3, the best are obtained between 1.5 – 3 min of irradiation, when the AgNPs size and dispersity are the lowest with a maximal absorbance at $\lambda_{max.}$
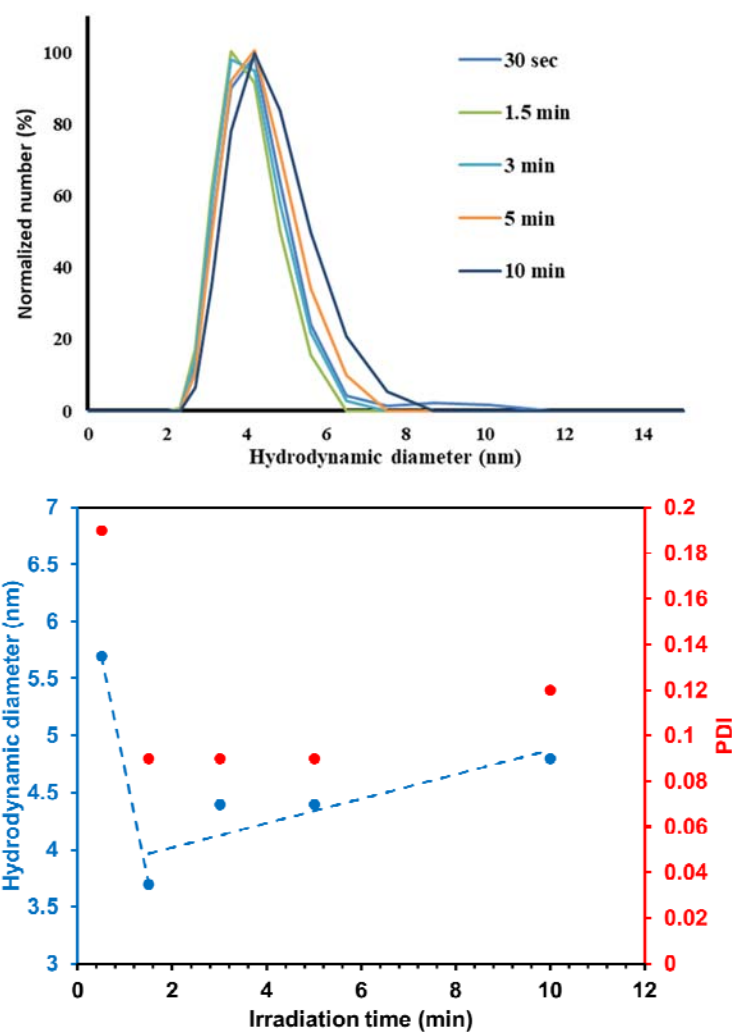
Figure 19. (a) DLS distribution of AgNPs-oleylmine prepared in flow at different irradiation times using the 1:10 Ag$^+$/oleylamine ratio. (b) Variation of average diameter (blue) and PDI (red) of the prepared Ag-NPs at different irradiation times

Table 3. AgNPs-Oleylamine variation of Absorbance, λ_{max}, Hydrodynamic diameter, and PDI

	Flow rate ($\mu L.min^{-1}$)	Irradiation time (min. sec)	λ_{max}	Absorbance at λ_{max}	Average diameter	PDI
AgBF₄/oleylamine = 1/10	4500	0.5	462	0.83	5.7	0.19
	1500	1.5	457	0.90	3.7	0.09
	750	3.0	455	1.99	4.4	0.09
	450	5.0	454	1.97	4.4	0.09
	225	10.0	459	0.87	4.8	0.12

During the study, we showed that it is possible to synthesize small, monodispersed and stable nanoparticles in organic medium. The optimal conditions for synthesizing these nanoparticles are:

a- Using amylamine as a protective ligand for nanoparticles.

b- A molar ratio amylamine/AgBF₄ equal to 10.

c- The ideal injection volume flow rate in a FEP reactor 4.8 m long and 800 µm in diameter for the synthesis is between 1500 and 750 µl.min-1 which corresponds to a time of irradiation between 1.5 and 3 minutes.

II.   Antibacterial application of silver nanoparticles

Silver is well known for its antibacterial properties; however, AgNPs applications for antibacterial coating and paints are still limited, due to their instability in the organic solvent when they are synthesized using the classical methods in aqueous medium. Even the preparation of stable nanoparticles in organic solvent is a complicated process (e.g. Burst method) and it is difficult to control the size and dispersity. On the other hand, these methods are not adopted for an industrial high scale production.

We mixed commercial 1g of alkyd paint with different ratios of silver nanoparticles and we supposed that the obtained mass of AgNPs is equal to Ag^+ ions mass introduced into the microfluidic system. The dried paints films were tested later for their antibacterial activity against gram negative *Escherichia Coli.* in LB-TOP 10 Agar (Figure 20). The paint film without AgNPs did not show any antibacterial activity, even when 5 µg of AgNPs were added. However, the paint film embedded starting from 10 µg of AgNPs shows clearly an antibacterial activity and inhibits the growth of *Escherichia Coli.*

In this work, we present a new method to synthesize small and ultra-stable silver nanoparticles. Our approach is the fastest synthesis method of AgNPs with a full control on size, dispersity and shape. Based on photochemistry our strategy is considered as a green method and produce zero waste. Moreover, the synthesis in flow allows to scale up the production of AgNPs, and make our technique suitable for industrial application. We also used the synthesized AgNPs in the conception of effective antibacterial coating, which can be applied to coat different type of surfaces and to protect them from bacterial proliferation.
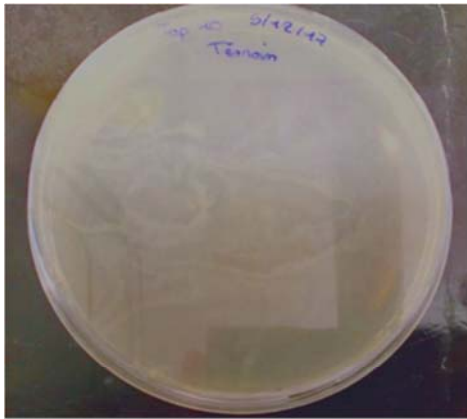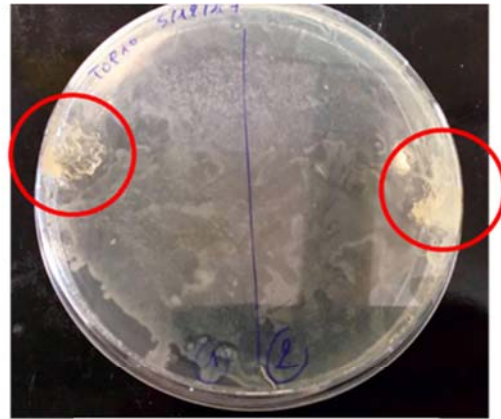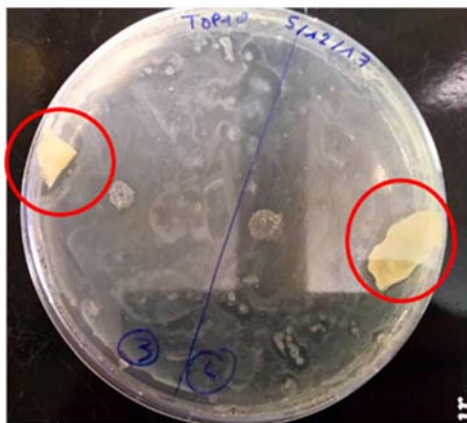
Figure 20. Antibacterial activity of alkyd paints embedded with AgNPs

III. Synthesis of gold nanoparticles

1. Mechanism of photochemical synthesis

Upon absorption of UV irradiation (365 nm), Irgacure 2959 generates acetone ketyl radical *via* a Norrish type I cleavage reaction which acts as a reducing agent formed *in-situ* (Figure 21). The complete reduction of Au^{3+} (tetrachloroaurate, $HAuCl_4$) to Au^0 requires three equivalents of ketyl radicals. It should be noted that the mechanism involves a dismutation step of unstable Au^{2+} ion to both Au^{3+} and Au^+, this step doesn't influence the number of ketyl radicals intermediates necessary for complete reduction.[66] Compared to aqueous conditions for which no particular ligand is usually required, the formation of gold nanoparticles in organic solvent needs an appropriate stabilizing ligand, such as amines described in this study. The stabilization of NPs surface by capping with ligands is crucial to prevent aggregation by guiding the growth of the crystal during the colloidal syntheses.[144] For this reason, the nitrogen based ligands, cyclohexylamine, amylamine and oleylamine were assessed. However, only oleylamine provided ultra-stable gold nanoparticles when used.
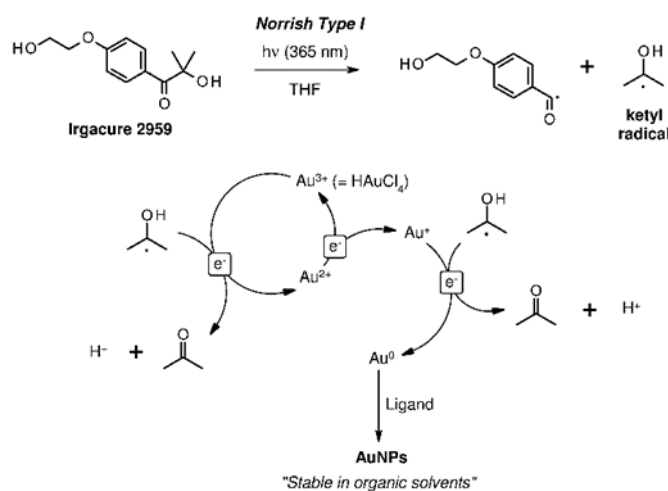
Figure 21. Mechanism of the photoinduced formation of stabilized gold nanoparticles using Irgacure2959®

2. Effect of ligand concentration

To explore the impact of the HAuCl$_4$/oleylamine ratio on the AuNPs size and distribution, we conducted three experiments by increasing the quantity of oleylamine and keeping the molar concentration of HAuCl$_4$ constant at 0.33 mol.L^{-1} giving the following ratios: 1:3, 1:5, 1:10. The irradiation time was fixed at 15 minutes.

The surface plasmon absorption band is observed in the three spectra around 535 +/- 5 nm by UV-Vis spectroscopy for every studied ratios and red-shifted with the increase in the quantity of the added ligand, so that λmax of 528, 537 and 538 nm were obtained for the ratios 3:1, 5:1 and 10:1 respectively (Figure 22).
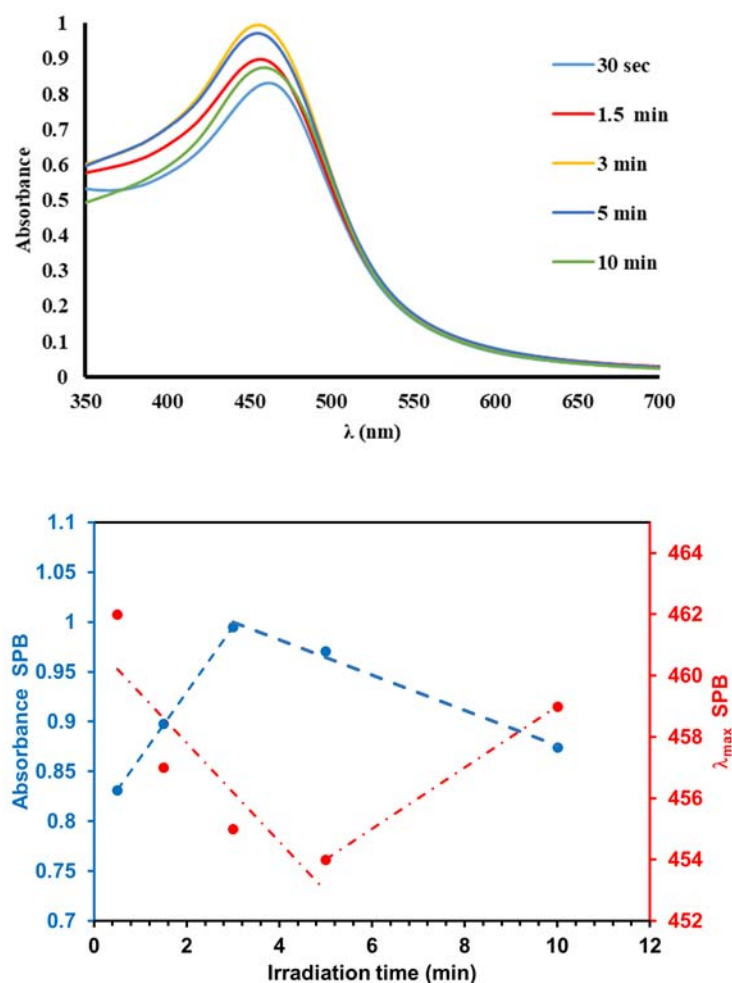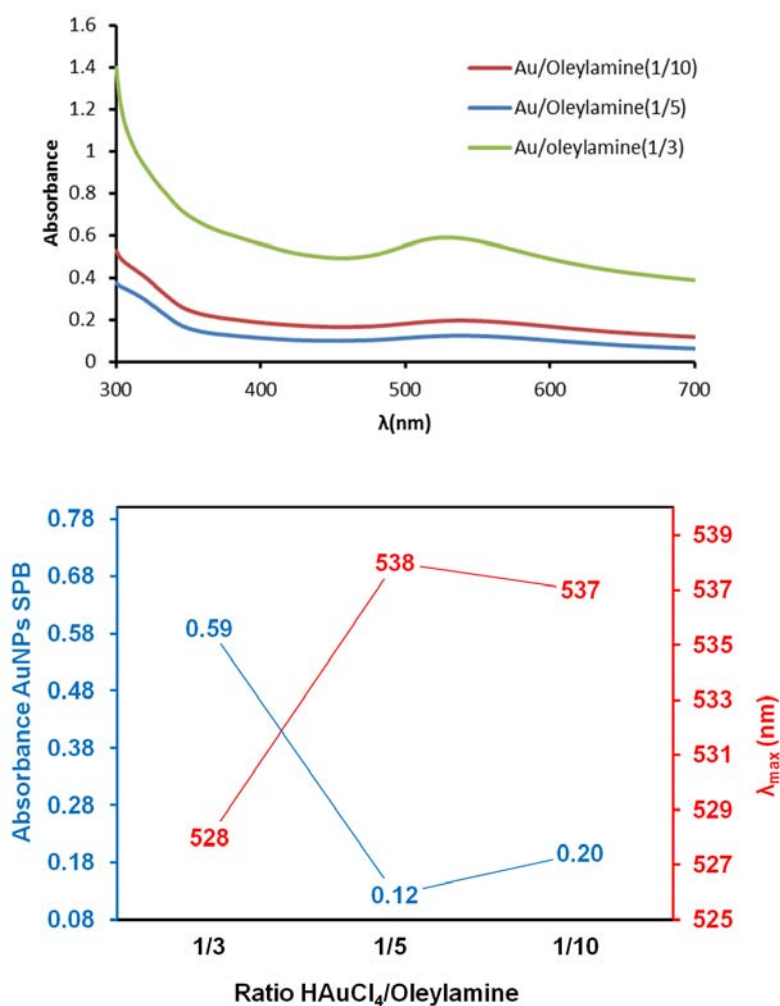

Figure 22 UV-visible spectra of the gold nanoparticles obtained in flow at different irradiation times using the 1: 10 Au^{3+}/oleylamine ratio. (b) Variation of the absorbance (blue) and surface plasmon band wavelength (red) of the prepared Au-NPs at different irradiation times

The amount of the capping ligand also influences the dispersity and the size of the formed NPs. By using DLS, it was found that both the hydrodynamic diameter and the dispersity decrease with the increase in the ligand quantity (Figure 23). The ratio of 3:1 gave Au-NPs an average hydrodynamic diameter of 10.3 nm and larger polydispersity index (PDI) of 0.13. Au-NPs of slightly smaller average size (10.1 nm) and improved PDI (0.05) were obtained when increasing the ratio of oleylamine to 5; the best results in terms of size and dispersity were obtained when having the 10:1 ratio where the formed Au-NPs were as small as 8.8 nm in size and with a PDI of 0.03. The particles produced were stable for at least several months, even in the presence of air and without protection. These results are in accordance with literature for silver nanoparticles synthesis under similar conditions, where the increase in the ligand concentration induces the formation of small, monodispersed and ultra-stable NPs (Figure 22).[70] The sizes and poly-dispersity indices of the different NPs obtained also justify the absorbance intensity of the three NPs surface plasmon bands as the NPs of relatively largest average size (10.3 nm) had the strongest absorbance. Similar results were obtained in previous studies where, for a given gold concentration the absorbance increases linearly with size.[141, 145]

However, according to El-Sayed et al, the peak wavelength red-shifts with the increase in the size of the NPs.[146-147] This is in contrast with the results of this study where the smallest (7.5 nm) and the least dispersed (PDI = 0.03) Au-NPs were obtained when having the ratio of 10:1 of the ligand that had the peak wavelength at 538 nm. Many studies also support our findings where the maximum blue-shifts with increasing particle diameter. Nevertheless, there are predictions of shifts of the peak absorptions of Au NPs into both directions.[148]

Table 4. Study of Au^{3+}/oleylamine effect on Au-NNPs synthesize

Au^{3+}/oleylamine	λ_{max}	Absorbance at λ_{max}	Average diameter	PDI
1/3	528	0.59	3.6	0.09
1/5	538	0.12	3.3	0.07
1/10	537	0.20	2.3	0.05
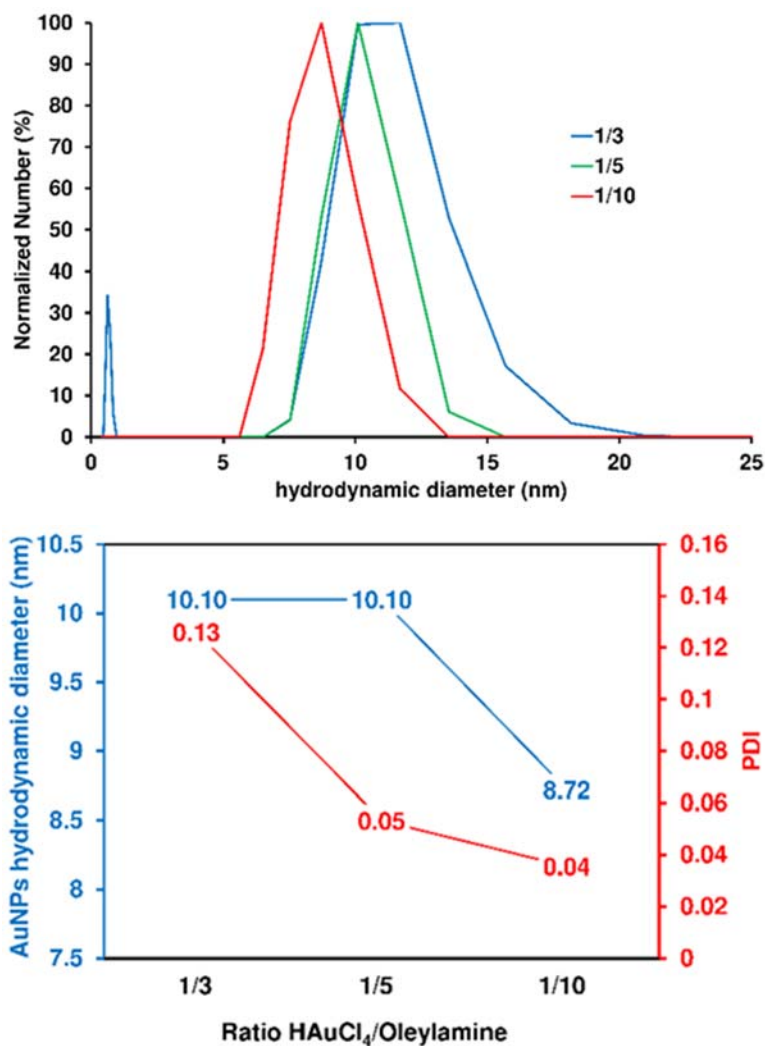
Figure 23. (Upper panel) DLS distribution of gold nanoparticles prepared in flow at the three Au^{3+}/oleylamine ratios; 1:3 (blue), 1:5 (green) and 1:10 (red). (Bottom panel) Variation of the hydrodynamic diameter (blue) and polydispesity index (red) of the prepared Au-NPs as function of Au^{3+}/oleylamine ratio.

3. Effects of irradiation times on AuNPs formation

After determining the best ligand to gold precursor ratio to deliver small and monodispersed NPs, we further explored the impact of the irradiation time on the size and dispersity of AuNPs. The residence time was varied between 3 and 45 minutes (flow rates ranging between 42 and 635 µL.min^{-1}) in the UV irradiated microfluidic reactor while all other parameters were kept unchanged.

Figure 24 indicated the UV-Vis spectra of samples produced with exposure to UV light for indicated times at room temperature. All samples present a visible SPB absorption whose intensity increases with the increase in the irradiation time. Approximately 75% of the maximum absorption is reached within 10 min of exposure. The wavelength of SPB also fluctuates with time. The maximum of absorption is initially at 423 nm red shift to 434 nm after 15 min of irradiation to reach a maximum which next decreases for longer times (Figure 24). Such a variation reflects the underlying modifications in light scattering following the nucleation and growth steps of NPs formation as indicated by Scaiano *et al.*[67] In parallel, the reaction was monitored by DLS and both hydrodynamic diameter and polydispersity have been determined (Figure 25). The distribution is much sharper at low residence time and widens after 10 min. On the other hand, when the residence time was increased, the diameter started to decrease slightly from 10.5 nm down to 8.8 nm and then increased again up to 14 nm after 45 min. The transition at 10 minutes is similar to that obtained by our group when preparing gold nanoparticles in flow using Turkevich protocol.[78] It corresponds to the changes in the physical parameters as it shows the transfer from the nucleation to the growth step.
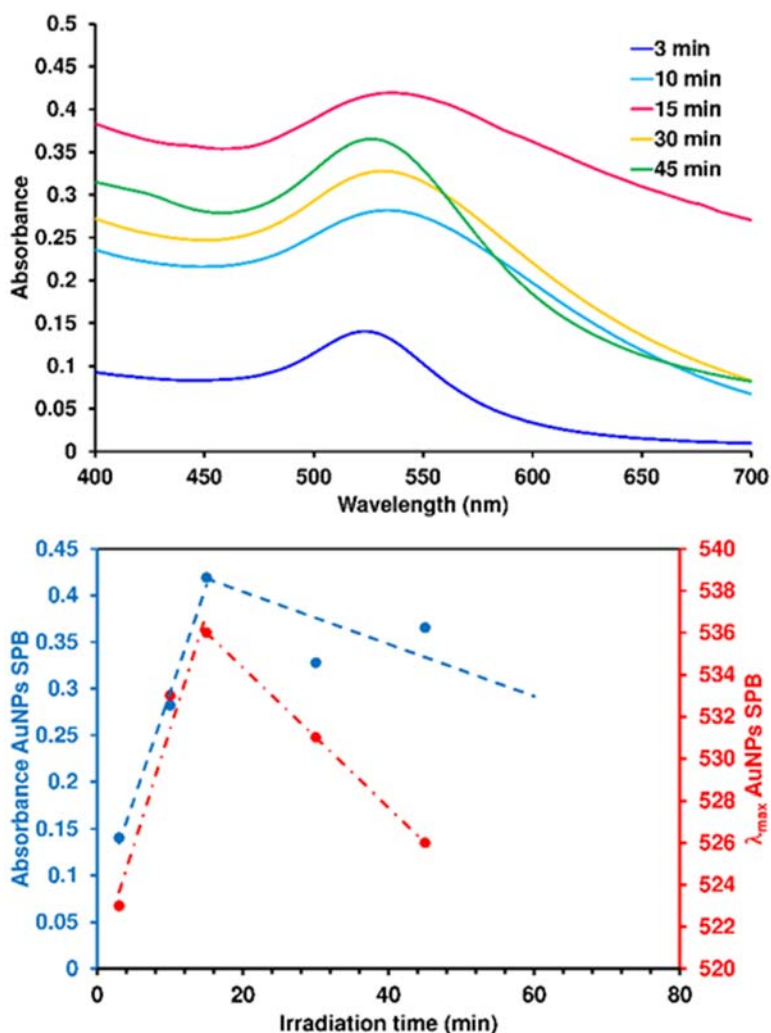
Figure 24 (a) UV-visible spectra of the gold nanoparticles obtained in flow at different irradiation times using the 1: 10 Au^{3+}/oleylamine ratio. (b) Variation of the absorbance (blue) and surface plasmon band wavelength (red) of the prepared Au-NPs at different irradiation times

As explained in previous papers, the curve that corresponds to the variation of the NPs size as function of the irradiation time can be divided into two parts where the point that corresponds to 10 min of irradiation is the shift point.[78, 149] Before this point, there were not enough NPs, thus slightly faster growth is observed. As for the second part, the NP size increases linearly in accordance with the two step Finke–Watzky model.[150] The curve can be further explained when referring to the stages of nanoparticles formation described by Compton & Osterloh.[151]
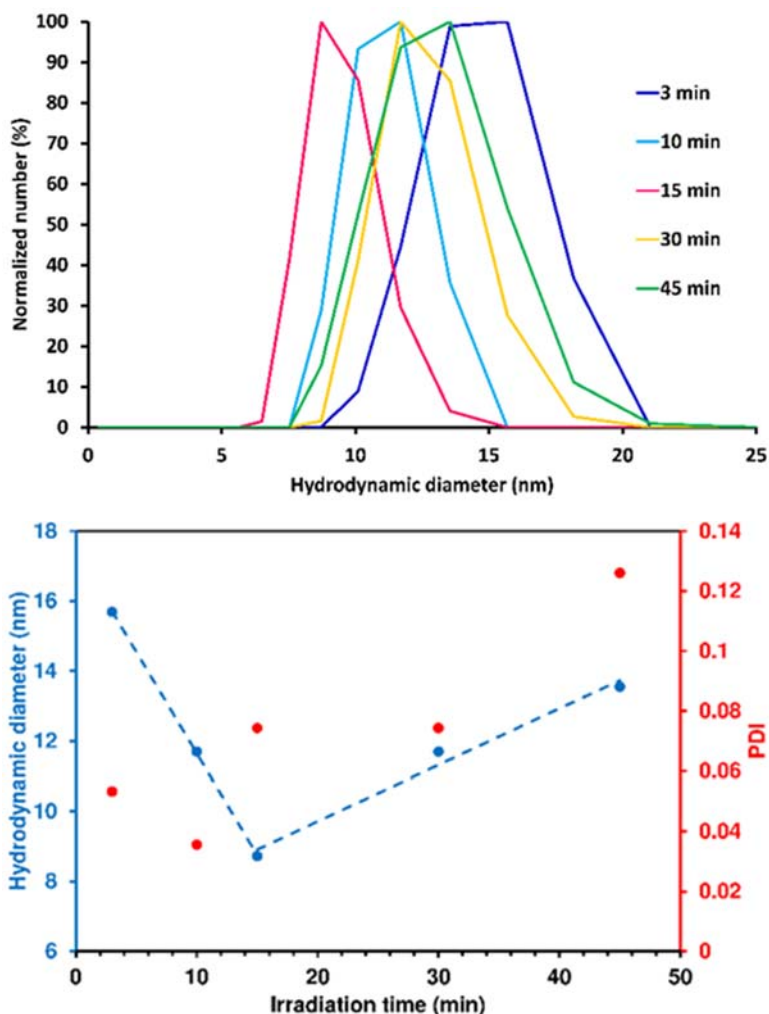
Figure 25. (a) DLS distribution of gold nanoparticles prepared in flow at different irradiation times using the 1: 10 Au^{3+}/oleylamine ratio. (b) Variation of average diameter (blue) and PDI (red) of the prepared Au-NPs at different irradiation times

In the early stages of formation of stable nanoparticles, the few and the newly formed M^0 aggregate next to each other to form clusters (first section). Nucleation starts when these clusters constitute 20% of the initial M^{n+} that is converted to M^0 (at t irradiation = 10 minutes). The formed NPs cores continue to grow in this growth step by the controlled diffusion of the formed M^0 from the constant reduction of M^{n+} within the solution. The final step involves the rapid consumption of the remaining salt ions left in solution *via* an autocatalytic reduction that takes place at the surface of the NPs.
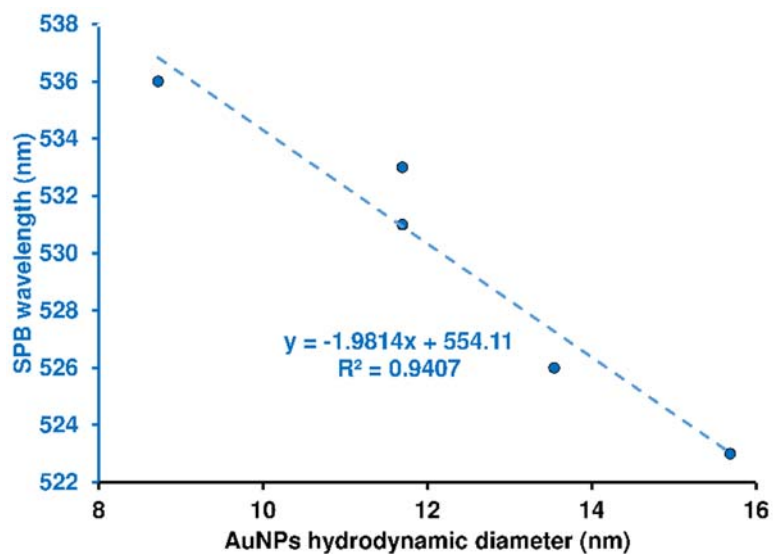
Figure 26. AuNPs SPB wavelength [134] vs. AuNPs hydrodynamic diameter.

Interestingly, both hydrodynamic diameters measurement and SPB wavelength variation measured through the residence time variation are linearly fitted (Figure 26) which demonstrates the high level of precision of flow techniques combined with off-line DLS and UV-Vis measurements for nanoparticle formation studies.

Table 5. AuNPs-Oleylamine variation of Absorbance, λ_{max}, Hydrodynamic diameter, and PDI

HAuCl₄/oleylamine = 1/10					
Flow rate (µL.min⁻¹)	Irradiation time (min)	λ_{max}	Absorbance at λ_{max}	Average diameter	PDI
628.3	3	523	0.14	4.2	0.09
188.5	10	533	0.28	3.1	0.14
125.6	15	536	0.42	3.6	0.16
62.8	30	531	0.33	4.1	0.14
41.9	45	526	0.36	4.2	0.16

As introduced before, the synthesis of Au-NPs has already been described in flow but never in organic solvents. In most of the cases, stable nanometric Au-NPs were obtained with sizes as small as 2 nm. However, all of the preparations were done in aqueous solution so the comparison is not valid. Similarly, previous attempts to prepare NPs of 1-3 nm size range in organic solutions involved two-phase (water–toluene) systems using tetraoctylammonium bromide as the phase-transfer reagent in a batch reactor.[26] So this is the first reported attempt using a single phase system, under continuous flow, to prepare hydrophobic Au-NPs. Literature shows that hydrophobic silver nanoparticles can be precipitated and re-dissolved in a new solvent without any significant change in their properties.[130] In this study, such ultra-stable AuNPs can be re-dispersed in toluene after THF evaporation preserving their size, dispersion and stability (Figure 27).
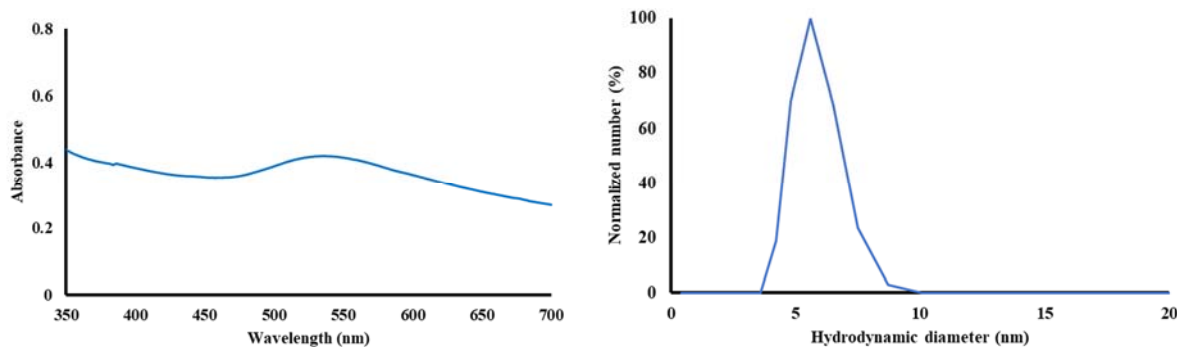
Figure 27. On the left UV-visible spectra of the gold nanoparticles re-dispersed in toluene and on the right DLS distribution of gold nanoparticles re-dispersed in toluene

To determine the influence of the flow technology on the properties of the formed NPs, batch experiments were performed. The same solution of gold precursor in THF that was used for the flow experiments was placed in an optical transparent quartz cuvette (12.5 × 12.5 × 45 mm) and was then homogeneously irradiated by a 365 nm UV LED of equal irradiance (320 mW.cm^{-2}). The smallest NPs obtained were of an average size of 12.9 nm with a PDI of 0.02, and that after 45 min of irradiation (Figure 28 and Figure 29). Thus working in flow, that ensures improved illumination, made it possible to have smaller (8.8 nm) NPs with the same level of dispersity (0.018) after only 15 minutes of residence time.
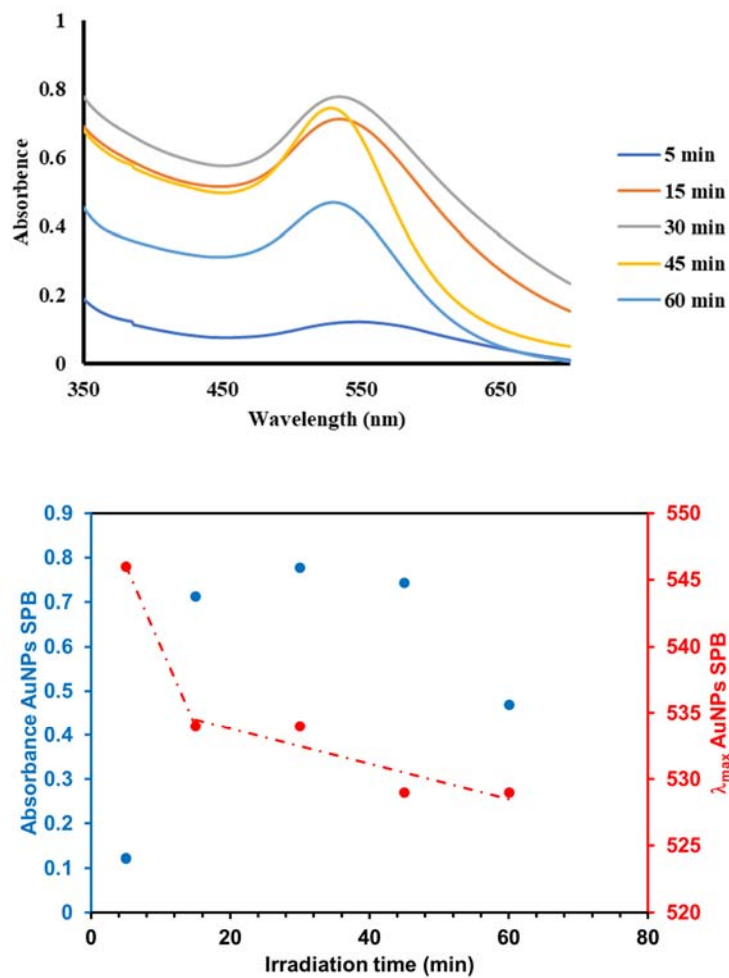
Figure 28. UV-visible spectra of the gold nanoparticles obtained in batch at different irradiation times using the 1: 10 Au^{3+}/oleylamine ratio. (b) Variation of the absorbance (blue) and surface plasmon band wavelength (red) of the prepared Au-NPs at different irradiation times
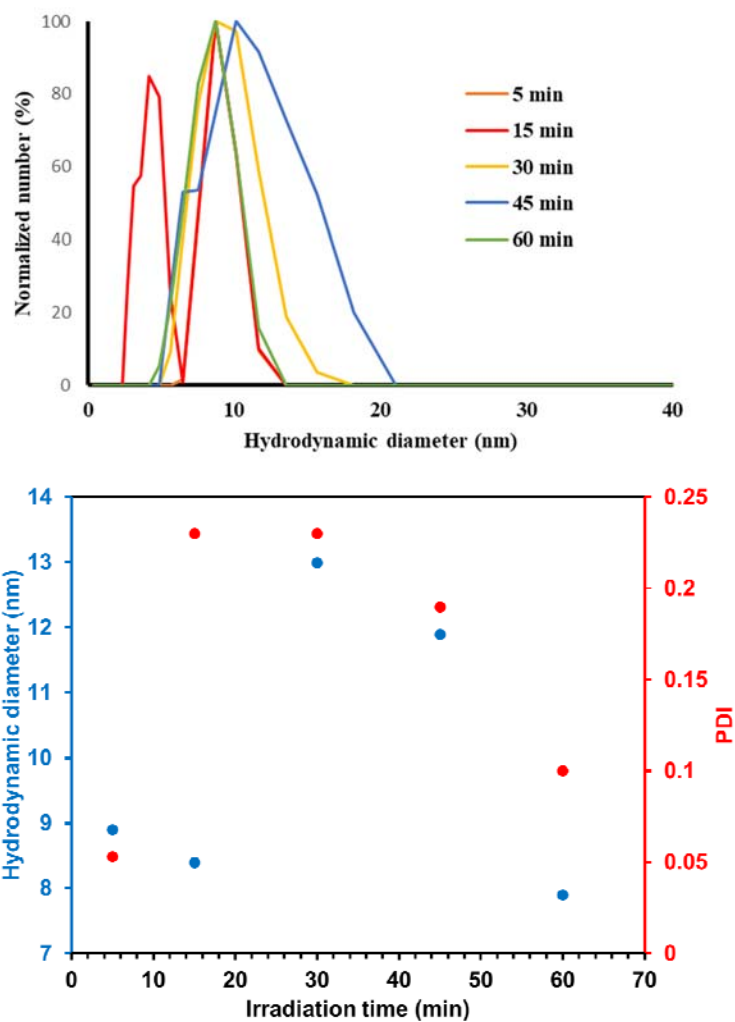
Figure 29. (a) DLS distribution of gold nanoparticles prepared in batch at different irradiation times using the 1: 10 Au^{3+}/oleylamine ratio. (b) Variation of average diameter (blue) and PDI (red) of the prepared Au-NPs at different irradiation times

4. Transmission electron microscopy (TEM) characterization of AuNPs

Nanoparticles were further analyzed by transmission electron microscopy (TEM) (Figure 30) in order to confirm the DLS analysis. No centrifugation or any other kind of filtration was performed prior to the TEM analysis. TEM pictures clearly show the nanoparticles with a mean diameter centered on 5 nm for the particles obtained within the microfluidic device at a flow rate of 125.7 µL.min-1 corresponding to 15 min of irradiation. These results are in good agreement with the DLS analysis. Indeed, electron microscopy gives access to the size of the inner gold core since only electron rich atoms can be observed and the DLS method takes into account the oleylamine stabilizing layer based on overall particle diffusion in organic solution. As it can be seen on the TEM image, particles are clearly separated and the distance observed between them corresponds to the oleylamine chains which can't be observed using such microscopic technique.
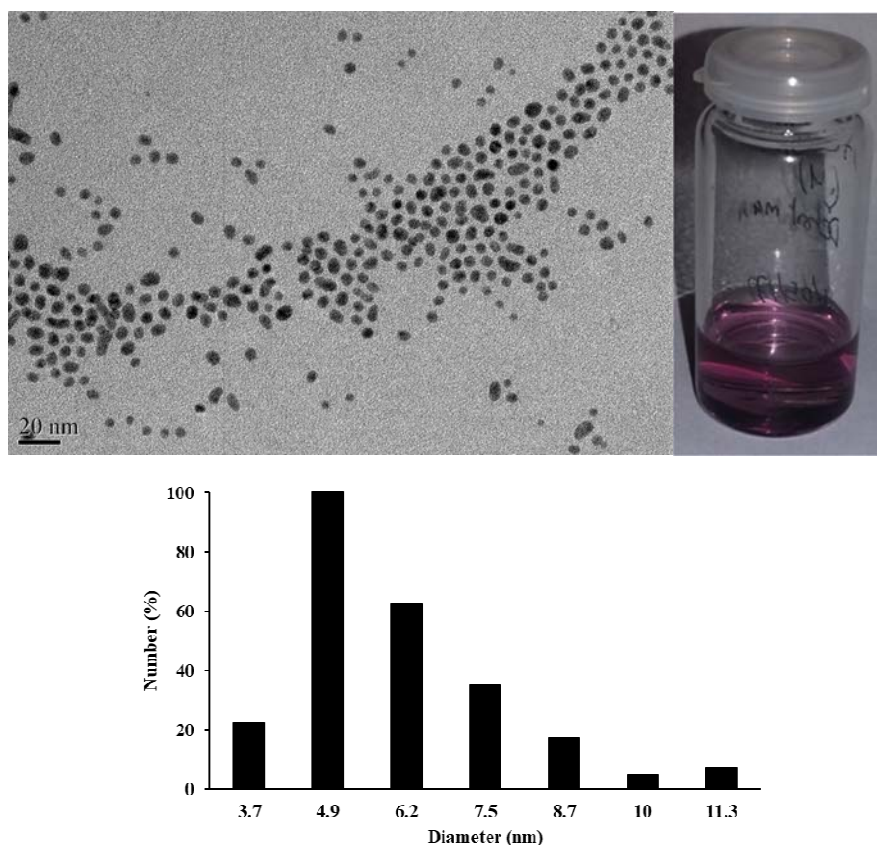
Figure 30. Transmission Electron Microscopy (TEM) images and size distribution of Au-NPs obtained at a flow rate of 125.7 µL.min-1

IV. Palladium nanoparticles synthesis

After successfully synthesizing ultra-stable AuNPs and AgNPs in organic solvents, we applied the same strategy used above in order to synthesize PdNPs.

The photochemical synthesize of small PdNPs in flow has been described.[72] However, in this study, we propose to synthesize stable PdNPs in organic solvents in order to expend their application as homogenous catalysts for Carbon-Carbon coupling reactions.

For the synthesis of PdNPs, we chose palladium acetylacetonate as a metallic precursor, THF as a solvent, oleylamine as ligand to stabilize the formed particles and Irgacure-2959® was used as photoinitiator.
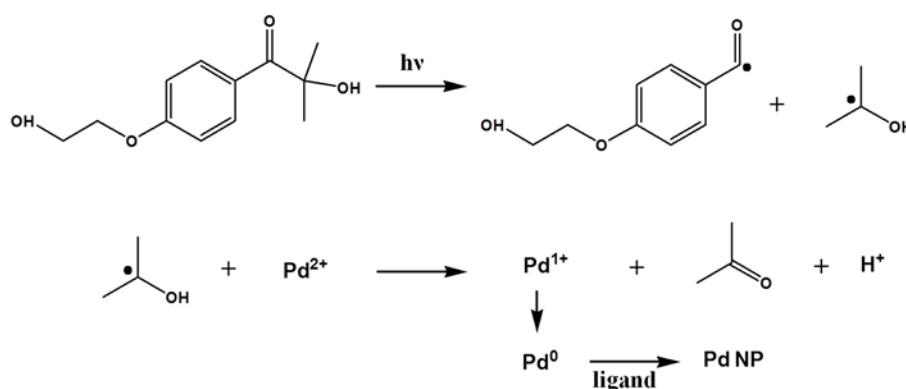
Figure 31. Mechanism of the photoinduced formation of stabilized palladium nanoparticles using Irgacure2959®

Under UV irradiation, Irgacure-2959® undergoes a Norrish I-type reaction, in which it will have a break in an α carbon of the carbonyl group and will generate a ketyl radical. The ketyl radical is well known to be a powerful reducing agent, which will reduce Pd^{2+} into Pd^0 as it is detailed in the mechanism scheme (**Error! Reference source not found.**).

For our studies, we injected into the microfluidic system 3 mL of a solution composed of the metal precursor palladium acetylacetonate ($C_{10}H_{14}O_4Pd$) with a fix concentration of 5 mM. The solvent used in this experiment was the THF. Our aim was to investigate the influence of the Pd^{2+}/oleylamine and Pd^{2+}/I2959, as well the irradiation time on the formation of PdNPs, in order to control the size and the dispersity of the NPs.

The microfluidic system was designed in our lab. It was mad of a transparent FEP tube (FluorinatedEthylenePropylene) with an internal diameter of 800 μm and a length of 375 cm with

a volume of 1.885 ml. The FEP tube was fixed on a metal grid and faced to a UV LED source (365 nm, irradiance up to 3 W.cm^{-2}) model Omnicure AC7300. The distance between the UV LED source and the microfluidic system was about 15 cm in order to have a homogeneous irradiation. At the end of the tube, a vial is placed to recover the synthesized nanoparticles and is covered with aluminum paper to prevent irradiation parasite.

The Harvard Apparatus Syringe Pump (Holliston, MA, USA) PHD ULTRA equipped with an 8 ml stainless steel syringe was used to program the flow and the volume of injected reagents.
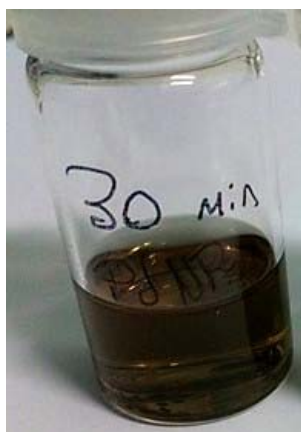
Figure 32. PdNPs capped with oleylamine in THF

1. Effect of ligand concentration

In the first step, we studied the influence of oleylamine concentration on the synthesis of PdNPS as well as their size and polydispersity. The ratio of Pd^{2+}/I-2959 was fixed at1/2, and the irradiation time at 30 min. The Pd^{2+}/oleylamine ratio was tested for 1/1, 1/3, 1/6 and 1/10.

Table 6. Study of Pd^{2+}/oleylamine influence on PdNPs synthesize

Fixed parameters: Pd^{2+}/I-2959® ratio: 1/2 • Flow rate: 62.85 µL.min⁻¹ • Irradiation time: 30 min		
Pd^{2+}/Oleylamine	**Hydrodynamic diameter [134]**	**PDI**
1/1	14.6	0.14
1/3	11.3	0.15
1/6	10.4	0.08
1/10	10.3	0.05

The synthesized nanoparticles are recovered and analyzed by DLS, in order to measure the diameter and to determine the polydispersity index as shown in Table 6. For each sample, five independent measurements are made with 10 to 14 sub-measurements for each measurement. Then we calculated the average diameter and we deduced the PDI based on the width of size distribution.

The obtained results show that the PdNPs size and dispersity decreases with increasing ligand (oleylamine) concentration (Figure 33). Pd^{2+}/Oleylamine ratios of 1/6 and 1/10 have the smallest diameters (10.4 and 10.3 respectively) and the most monodispersed nanoparticles (0.08 and 0.05 respectively). Those results indicates that increasing ligand concentration leads to increasing the steric stabilization of PdNPs and results in formation of smaller and more mono-dispersed nanoparticles.
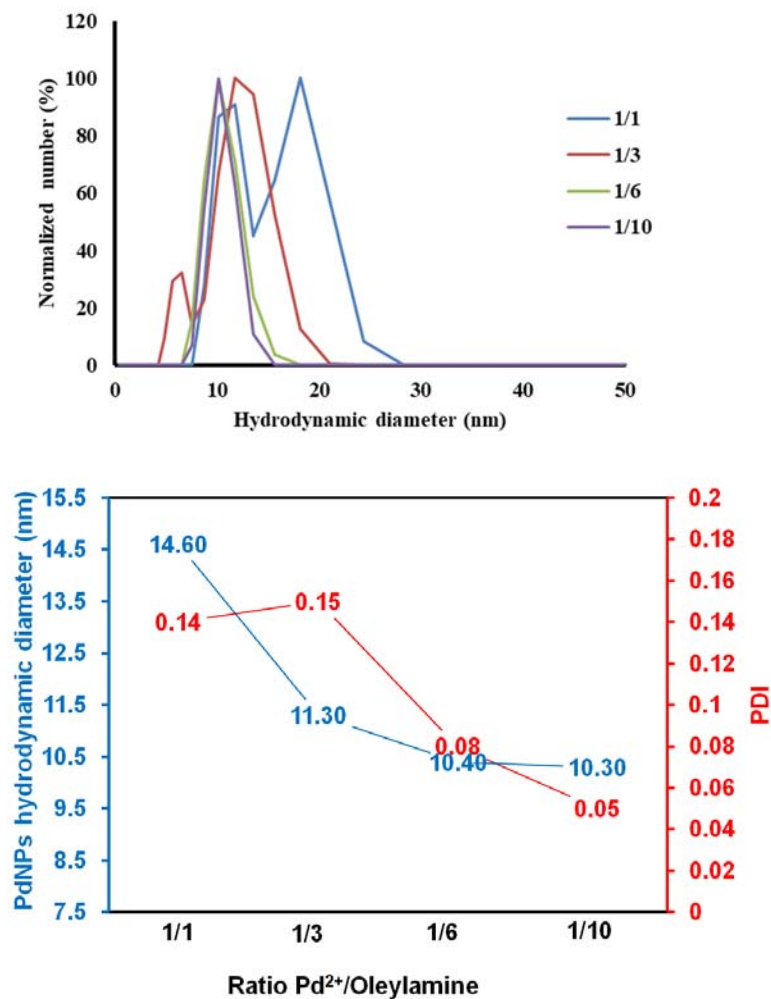
Figure 33. (upper panel) DLS distribution of PdNPs prepared in flow at the four Pd^{2+}/oleylamine ratios; 1:1 (blue), 1:3 (red), 1:6 (green) and 1:10 (violet). (bottom panel) Variation of the hydrodynamic diameter (blue) and polydispesity index (red) of the prepared PdNPs as function of Pd^{2+}/oleylamine ratio.

2. Effect of Photo-initiator concentration

Following the optimization of the ligand concentration in order to obtain small, stable and mono-dispersed NPs, we worked next on the determination of the optimal I-2959® concentration. The ratio Pd^{2+}/oleylamine is set at 1/10, and the irradiation time at 30 min. The different Pd^{2+}/I-2959® ratios tested are 2/1, 1/1, 1/2, 1/4, 1/8.

Table 7. Study of Pd^{2+}/ I-2959® influence on PdNPs synthesize

Fixed parameters:		
• Pd^{2+}/Oleylamine ratio: 1/10 • Flow rate: 62.85 µL.min⁻¹ • Irradiation time: 30 min		
Pd^{2+}/Irgacure-2959	**Hydrodynamic diameter [134]**	**PDI**
2/1	9.7	0.06
1/1	7.5	0.05
1/2	10.3	0.05
1/4	12.9	0.06
1/8	14	0.05

We monitored the size and dispersity variation as a function of different Pd^{2+}/I-2959® ratio variations (Table 7, Figure 34). The photo-initiator concentration does not show any influence on the dispersity of the nanoparticles which is almost stable (PDI = 0.05) at different Pd^{2+}/I-2959® ratios. The smallest size (7.5 nm) of PdNPs is obtained at Pd^{2+}/I-2959® ratio equal to 1. However, the hydrodynamic diameter of PdNPs increases with increasing the photo-initiator concentration to reach 14 nm at a Pd^{2+}/I-2959® ratio equal to 1/8. The photo-initiator plays the role of a reductive agent, ketyl radicals reduce Pd^{2+} into Pd^{+} ions which are not stable and they are involved into dismutation mechanism to form Pd^{0} and/or Pd^{2+}. The fast reduction of palladium ions and the fast nucleation lead to the formation of smaller nanoparticles. However, when increasing the I-2959® concentration, the PdNPs size is increasing which means that the reduction reaction becomes slower. Pd^{+} ions in presence of an excess of photo-initiator may react with phenyl groups to create C_6H_5-Pd^{+} intermediates instead of its reduction into Pd^{0},[152] which slows down the nucleation step and leads to the formation of bigger PdNPs.
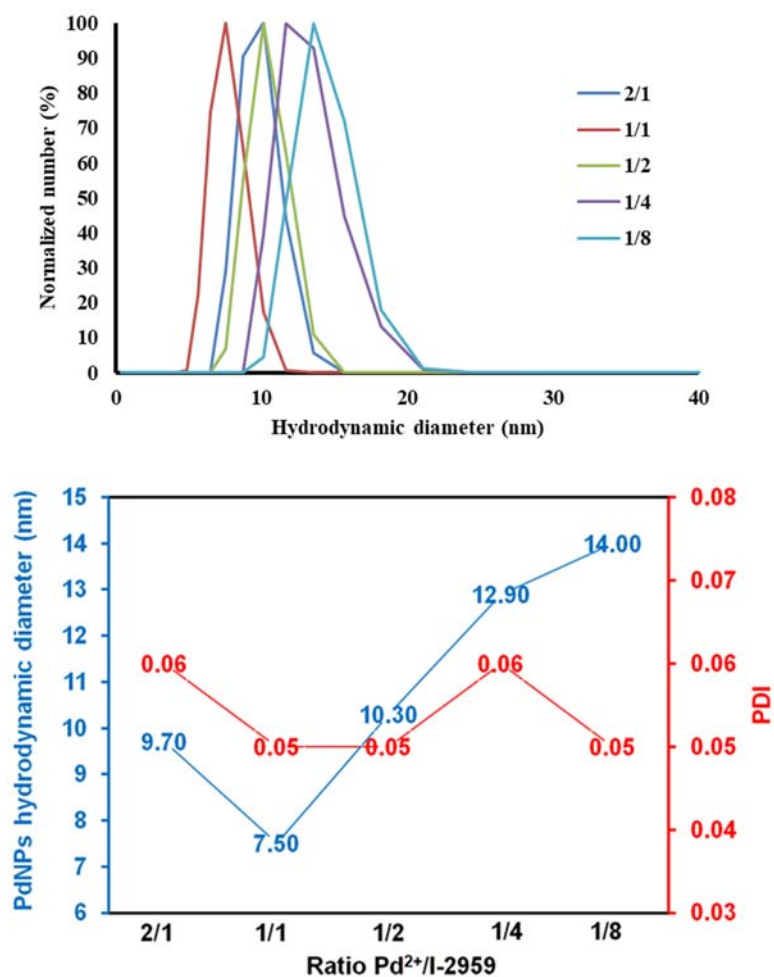
Figure 34. (upper panel) DLS distribution of PdNPs prepared in flow at the four Pd^{2+}/I-2959® ratios; 2:1 (blue), 1:1 (red), 1:2 (green), 1:4 (violet) and 1:8 (light blue). (bottom panel) Variation of the hydrodynamic diameter (blue) and polydispesity index (red) of the prepared PdNPs as function of Pd^{2+}/I-2959® ratio

3. Effects of irradiation times on PdNPs formation

After the optimization of the Pd^{2+}/oleylamine and Pd^{2+}/I-2959® ratios, we investigated the irradiation time influence on the Hydrodynamic diameter and PDI variations. In order to determine the optimal irradiation time that lead to the formation of stable, small and mono-dispersed NPs. The synthesized PdNPs were aimed to be used as a catalyst so we fixed a 1/1 ratio for Pd^{2+}/I-2959 and 1/6 for Pd^{2+}/oleylamine even if the optimal ratio was 1/10. For this reason, we were interested in synthesizing small and mono-dispersed PdNPs with the minimum required concentration of ligand in order to increase their catalytic activity.

Results represented in the Table 8 and Figure 35 show a drastically decrease in the size and the polydispersity between the first 2 min (d = 86 nm and PDI = 0.15 at 1 min) and the third minute of irradiation (d = 6 nm and PDI = 0.05). This size drop corresponds to the passage from the first step of nanoparticles formation mechanism which is the formation of aggregates to the second step which corresponds to the nucleon formation. On the other hand, the size of the PdNPs (6-7 nm) remains constant approximately with the increase in irradiation time between 3 and 20 min.

Table 8. Study of hydrodynamic diameter and PDI variation as a function of irradiation time

Fixed parameters:			
• Pd^{2+}/Oleylamine ratio: 1/6			
• Pd^{2+}/Irgacure-2959 ratio: 1/1			
Flow rate (μL.min^{-1})	**Irradiation time (min)**	**Hydrodynamic diameter** [134]	**PDI**
1885	1	86	0.15
942.5	2	89	0.07
628	3	6	0.05
377	5	7.3	0.03
188.5	10	7.7	0.05
125.7	15	6	0.08
94.3	20	6.1	0.16

We can also notice that the polydispersity index decreases with increasing the irradiation time from 0.15 at 1 min to a minimum of 0.03 after 5 minutes of irradiation. This decrease corresponds to the passage from the aggregation stage where the aggregates formed have a large and polydispersed size to the formation of nucleons which are smaller in size and more monodispersed. On the other

hand, the PDI rises with the increase of the irradiation time to reach 0.16 after 20 min which showing that there is no uniformity during the growth step and the size of PdNPs changes to form populations with different sizes.
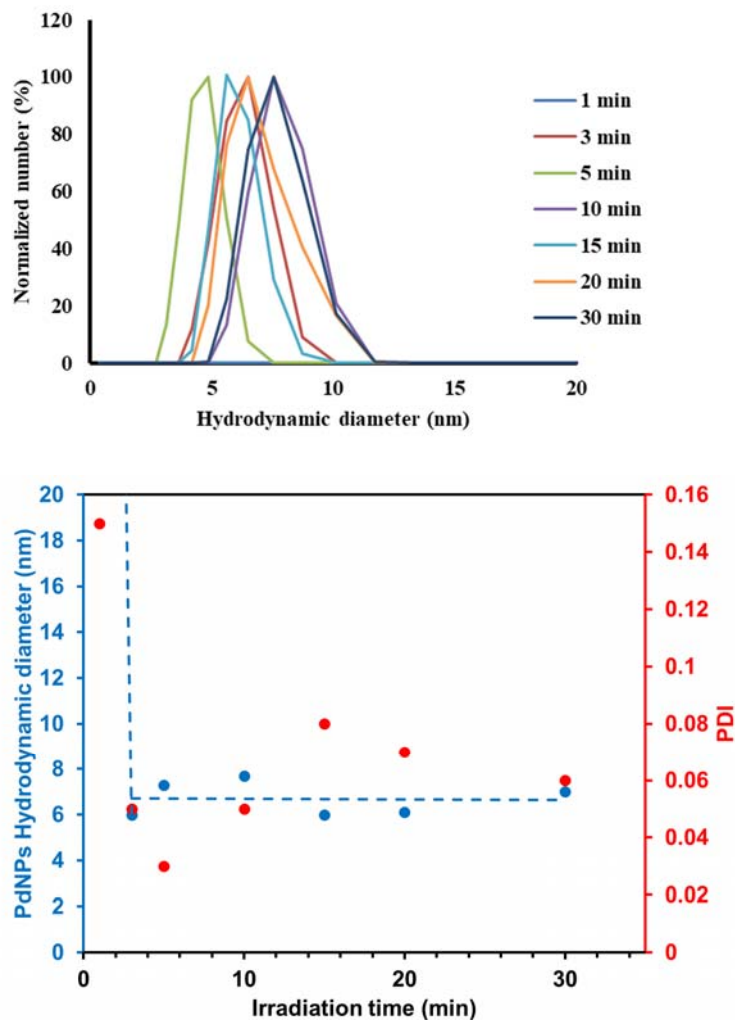
Figure 35. (a) DLS distribution of PdNPs prepared in flow at different irradiation times using the 1:10 Pd^{2+}/oleylamine ratio. (b) Variation of average diameter (blue) and PDI (red) of the prepared PdNPs at different irradiation times

From these results, it can be deduced that the optimal conditions for synthesizing of ultra-stable palladium nanoparticles in organic solvents such as THF with a diameter of 6-7 nm and with a low PDI are:

- Pd^{2+}/oleylamine ratio: 1/6
- Pd^{2+}/Irgacure-2959 ratio: 1/1
- Irradiation time between 3 to 5 min

When, we compare the results obtained from the three different studies, we can notice that:

In the first study, we fixed the Pd^{2+}/I-2959® ratio at 1/2 and we changed the ligand concentration. We noticed that by increasing the ligand concentration from 5 mM to 50 mM the PDI decreased from 0.14 to 0.05 and the size decreased from 14.6 nm to 10.3 nm. Those results indicate that ligands have influence on both size and dipersity of NPs.

In the second study, we fixed the Pd^{2+}/oleylamine at the optimal ratio of 1/10 and we varied the photoinitiator concentration. The PDI stayed stable around 0.05 at different Pd^{2+}/I-2959® values. On the other hand, the PdNPs size depended on the Pd^{2+}/I-2959 ratio, the smallest NPs (7.5 nm) obtained at a ratio of Pd^{2+}/I-2959 equal to 1 and the NPs with the bigger hydrodynamic diameter (14 nm) are obtained at Pd^{2+}/I-2959 ratio of 1/8. Based on those results, we can conclude that photoinitiators have more influence on the NPs size than ligands; however, they do not have any impact on the dispersity of NPs.

The irradiation time monitoring shows that nucleon are formed after 3 min of irradiation and the formed PdNPs are ultra-stable and their size does not vary significantly with increasing the irradiation time and neither their dispersity.

4. Transmission Electron Microscopy (TEM) characterization of PdNPs
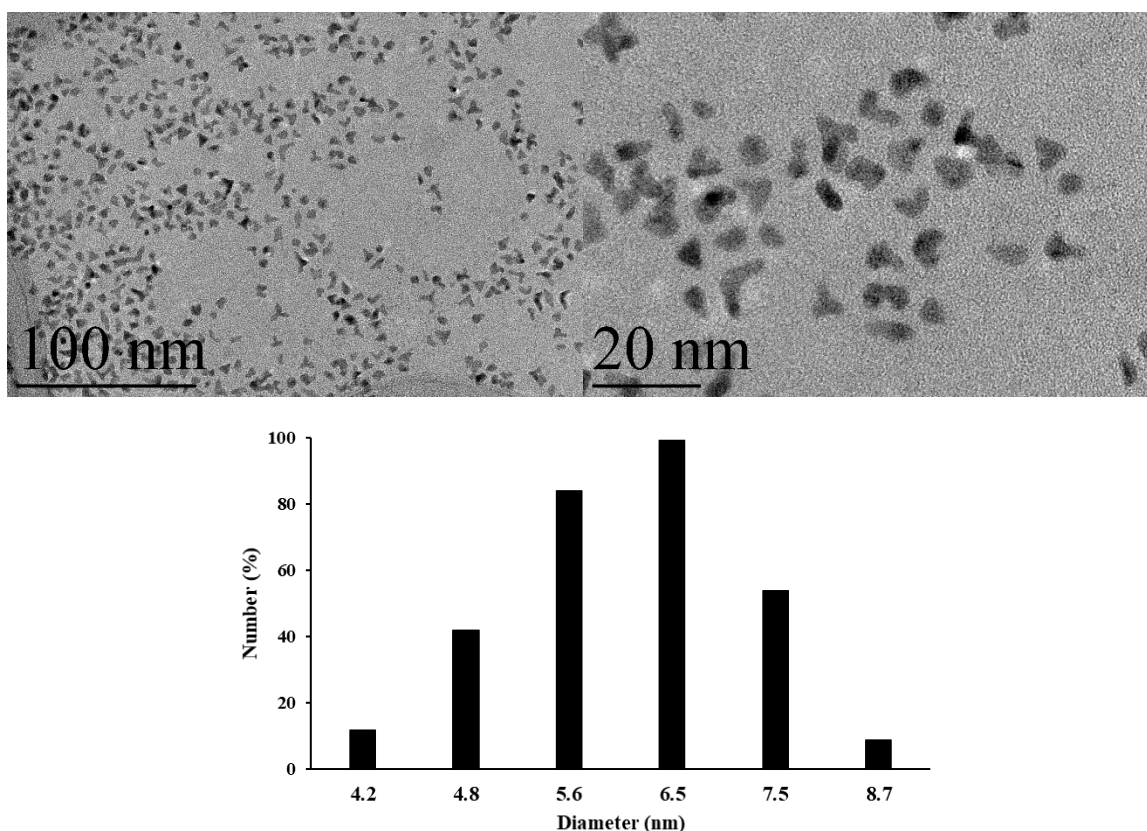
Figure 36. Transmission Electron Microscopy (TEM) images and size distribution of PdNPs obtained at 3 min of irradiation

Palladium nanoparticles were synthesized according to the optimal conditions (Pd^{2+}/oleylamine ratio: 1/6; Pd^{2+}/I-2959 ratio: 1/1; Irradiation time: 3min) and analyzed by transmission electron microscopy (TEM) (Figure 36) in order to confirm the DLS analysis. No centrifugation or any other kind of filtration was performed prior to the TEM analysis. The TEM pictures clearly show the nanoparticles with a mean diameter centered at 6 nm for the particles obtained within the microfluidic device at a flow rate of 628 µL.min^{-1} corresponding to 3 min of irradiation. These results match the DLS analysis. Moreover, TEM analysis shows that PdNPs are mono-dispersed and have a uniform shape corresponding to a prism.

Conclusion

The classical synthesis of Turkevish, generates nanoparticles stable only in aqueous medium. On the other hand, thermolysis and Brust methods suffer from a low control on the size, shape and dispersity of nanoparticles. Based on Scaiano's photochemical synthesis of nanoparticles, we succeeded to develop a photochemical method for the synthesis of ultra-stable metallic nanoparticles (silver, gold and palladium) in organic medium and in microfluidic system. Our homemade designed microfluidic system offers high advantages for the synthesis of metallic nanoparticles. It allows having a better control on the size, shape and dispersity of nanoparticles. Moreover, the flow system permit to increase 10 times more the final concentration of solution in metallic nanoparticles by comparing with batch systems. Another advantage of the microfluidic system is that it allows to obtain nanoparticles after few minutes of irradiation and permit scaling up the nanoparticles synthesis for industrial applications.

On the other hand, the photochemical synthesis is a greener method that offers a better and more homogenous transfer of energy in comparison to other methods. Another important point is that this approach does not produce any chemical wastes.

Moreover, we described the use of silver nanoparticles as stable antibacterial additive for commercial available alkyd paints. AgNPs embedded in alkyd paints films showed a high antibacterial activity against Gram-negative bacteria *Escherichia coli*.

Material and methods

I.   Photochemical synthesis of nanoparticles

1.   Reagents

Silver Tetrafluoroborate (AgBF$_4$, 99.0%) were supplied by ACROS ORGANICS® (Geel, Belgium), palladium(II) acetylacetonate (C$_{10}$H$_{14}$O$_4$Pd, 99%) purchased from Flourochem® and gold (III) chloride hydrate (HAuCl$_4$.xH$_2$O, 99.9%) from Alfa Aesar®. Amylamine (C$_5$H$_{13}$N, 99.0%) and oleylamine (C$_{18}$H$_{37}$N, 80-90%) are supplied by ACROS ORGANICS (Geel, Belgium). Photoinitiators such as Irgacure 2959® 98.0% [2-Hydroxy-4′-(2-hydroxyethoxy)-2-methylpropiophenone.(C$_{12}$H$_{16}$O$_4$)], and Irgacure 907® 98.0% [2-Methyl-4′-(methylthio)-2-morpholinopropiophenone (C$_{15}$H$_{21}$NO$_2$S)] are marketed by Sigma-Aldrich (St. Louis, USA). Toluene (C$_7$H$_8$, 99%) and tetrahydrofuran (C$_4$H$_8$O, 99%) were purchased from Sigma-Aldrich (St. Louis, USA) as well.

2.   Photochemical synthesis of AgNPs-amylamine/oleylamine at different irradiation times

In a first step, three solutions of volume 33 ml in toluene are prepared. The first solution contains the silver precursor silver tetrafluoroborate AgBF$_4$ with a concentration of 15 mM. The second contains the photoinitiator Irgacure 907® at the same concentration as silver. The third solution has a concentration of 150 mM and contains the amine, which will act as a protective and stabilizing ligand. It was observed that the silver salt is not stable and tends to precipitate in the solution. To avoid this problem, the first solution containing the silver precursor is immediately mixed with the third solution containing the amine. Solutions should be stored in a refrigerator at 4 ° C and protected from light.

For photochemical reactions in a microfluidic system, a 6 ml mixture containing 5 mM Ag$^+$, 5 mM Irgacure 907® and 50 mM amine is prepared. After stirring, the solution was taken by 8 ml stainless steel syringe for injection into the microfluidic system. Different injection rates have been studied to establish the kinetics of the nanoparticle formation reaction as well as the variation of the size of nanoparticles. The irradiation time is inversely related to the flow rate and the duration of the experiment.

Irradiation time = Internal volume of the system / Flow rate

Experience Duration = Solution volume / Flow rate

After the injection of all the reagent solution, the same volume of solvent is injected at the same rate to ensure the total recovery of the products and to clean the system.

Table 9. Different flow rates and irradiation times used for the synthesis of AgNPs

Flow rate (μL.min^{-1})	Irradiation time (min.sec)	Experience duration (min.sec)
4500	0.5	1.2
2250	1.0	2.4
1500	1.5	4.0
1125	2.0	5.2
750	3.0	8.0
450	5.0	13.2
225	10.0	26.4

3. Photochemical synthesis of AuNPs and study of the influence of oleylamine concentration

6 ml mixture containing 0.33 mM HAuCl$_4$, 0.99 mM Irgacure 2959$^{®}$ and different concentrations of oleylamine (0.99, 1.65 or 3.30 mM) were injected into the microfluidic system *via* a 5 mL glass syringe and irradiated for 15 minutes with a flow rate of 125.7 μL.min^{-1}.

4. . Photochemical synthesis of AuNPs and study of the influence of irradiation times

To study the influence of the irradiation time on the synthesis of gold nanoparticles, 3 ml of the reaction mixture containing a concentration 0.33 mM HAuCl$_4$, 0.99 mM Irgacure 2959$^{®}$ and 3.3 mM of oleylamine was injected with various irradiation times and flow rates. The irradiation time was varied between 3, 10, 15, 30 and 45 minutes.

Table 10. Different flow rates and irradiation times used for the synthesis of AuNPs

Flow rate (μL.min^{-1})	Irradiation time (min.sec)	Experience duration (min.sec)
628.3	3.0	4.8
188.5	10.0	15.9

125.6	15.0	25.9
62.8	30.0	47.8
41.9	45.0	71.6

5. Photochemical synthesis of PdNPs and study of the influence of oleylamine concentration

A reaction mixture of 3 mL is injected into the microfluidic system, this solution is composed of palladium acetylacetonate ($C_{10}H_{14}O_4Pd$) with a concentration of 5 mM and the photoinitiator Irgacure-2959® with a concentration of 10 mM. The concentration of oleylamine was varied according to the ratios Pd^{2+}/oleylamine between 1/1, 1/3, 1/6 and 1/10. The irradiation time is set at 30 minutes and the flow rate is at 62.83 µL/min.

6. Photochemical synthesis of PdNPs and study of the influence of Irgacure-2959 concentration

In this experiment, the same volume of the reaction mixture was injected with the same flow rate as the previous reaction and with the same irradiation time of 30 min. Concentration of Pd(acac)$_2$ and the concentration of oleylamine are fixed at 5 mM and 50 mM respectively. The purpose of this study is to consider the effect of photoinitiator concentration. For this reason, the ratios of Pd^{2+}/Irgacure-2959 was varied between 2/1, 1/1, 1/2, 1/4 and 1/6.

7. Photochemical synthesis of PdNPs and study of the influence of irradiation times

To study the influence of the irradiation time on the synthesis of palladium nanoparticles, 3 ml of the reaction mixture containing a concentration of Pd(acac)$_2$ of 5 mM, oleylamine of 30 mM and Irgacure-2959 of 5 mM were injected with various irradiation times and flow rates. The irradiation time was varied between 1, 2, 3, 5, 10, 15 and 20 minutes.

Table 11. Different flow rates and irradiation times used for the synthesis of PdNPs

Flow rate (µL.min^{-1})	Irradiation time (min.sec)	Time of reaction (min.sec)
1885	1.0	1.6
942.5	2.0	3.2
628	3.0	4.8
377	5.0	8.0
188.5	10.0	15.9
125.7	15.0	23.9
94.3	20.0	31.8

II.   Description of the microfluidic photochemical montage

The irradiation source in our assembly is a Lumen Dynamics Model AC7300 UV (365 nm, irradiance up to 3W.cm^{-2}) LED (Mississauga, Canada). The microfluidic system is constructed from a transparent tube of FEP (Fluorinated Ethylene Propylene) with an internal diameter of 800 μm. On a metal grid 34 cm long and 14 cm wide, FEP tube was fixed with 3D PLA fixing rods and the length of FEP tube was 4.8 m during the AgNPs synthesize and 3.75 m during AuNPs and PdNPs synthesis. The system is terminated with 20 cm of FEP tubing that delivers our product to a vial for collection. This part is wrapped with aluminum foil to prevent parasitic irradiation and to stop the growth reaction of the nanoparticles. The metal grid is placed 15 cm from the UV LEDs providing uniform illumination for the entire microfluidic system with an irradiance of 320 mW.cm-2 measured with an X9-2 Gigahertz-Optik radiometer (Türkenfeld, Germany). The reagents were introduced using a Harvard Apparatus syringe pump (Holliston, MA, USA) PHD ULTRA equipped with an 8 mL stainless steel syringe in the case of AgNPs and PdNPs. In the case of AuNPs, harvard apparatus picoplus was used equiped with 5 mL glass syringue. Harvard Apparatus syringe pumps are modular and programmable. A worm rotates about its axis to advance the system and push the plunger of the syringe; the rotation of the screw is constant and depends on the volumetric flow previously chosen.

.
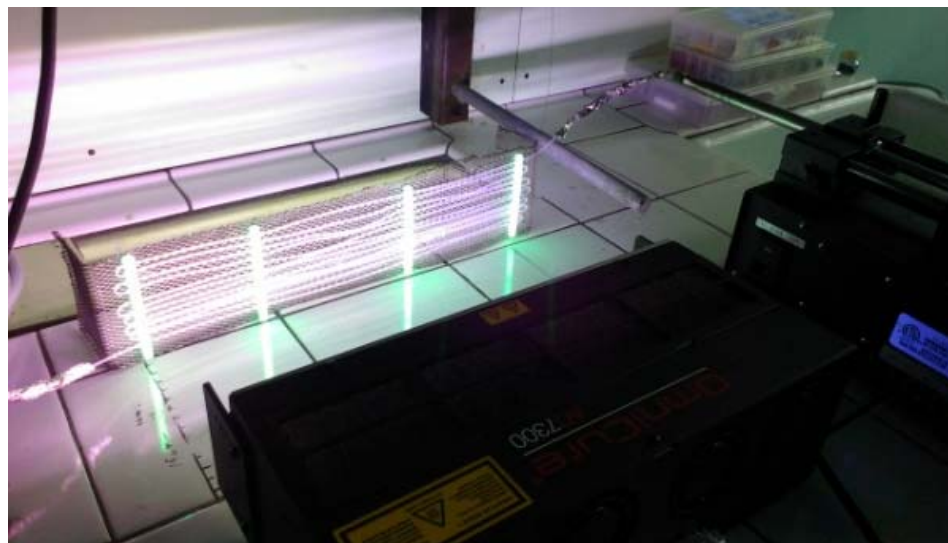
Figure 37.Homemade microfluidic system

References

1.	Aiken III, J. D.; Finke, R. G., A review of modern transition-metal nanoclusters: their synthesis, characterization, and applications in catalysis. *Journal of Molecular Catalysis A: Chemical* **1999,** *145* (1-2), 1-44.

2.	Widegren, J. A.; Finke, R. G., A review of the problem of distinguishing true homogeneous catalysis from soluble or other metal-particle heterogeneous catalysis under reducing conditions. *Journal of Molecular Catalysis A: Chemical* **2003,** *198* (1-2), 317-341.

3.	Pachón, L. D.; Rothenberg, G., Transition-metal nanoparticles: synthesis, stability and the leaching issue. *Applied Organometallic Chemistry* **2008,** *22* (6), 288-299.

4.	Schmid, G., Large clusters and colloids. Metals in the embryonic state. *Chemical Reviews* **1992,** *92* (8), 1709-1727.

5.	Schmid, G.; Chi, L. F., Metal clusters and colloids. *Advanced Materials* **1998,** *10* (7), 515-526.

6.	Caseri, W., Nanocomposites of polymers and metals or semiconductors: historical background and optical properties. *Macromolecular Rapid Communications* **2000,** *21* (11), 705-722.

7.	El-Sayed, M. A., Some interesting properties of metals confined in time and nanometer space of different shapes. *Accounts of chemical research* **2001,** *34* (4), 257-264.

8.	Kim, J. H.; Lee, S.; Park, K.; Nam, H. Y.; Jang, S. Y.; Youn, I.; Kim, K.; Jeon, H.; Park, R. W.; Kim, I. S., Protein-phosphorylation-responsive polymeric nanoparticles for imaging protein kinase activities in single living cells. *Angewandte Chemie International Edition* **2007,** *46* (30), 5779-5782.

9.	Toshima, N.; Yonezawa, T., Bimetallic nanoparticles—novel materials for chemical and physical applications. *New Journal of Chemistry* **1998,** *22* (11), 1179-1201.

10.	Muñoz, J. E.; Cervantes, J.; Esparza, R.; Rosas, G., Iron nanoparticles produced by high-energy ball milling. *Journal of nanoparticle research* **2007,** *9* (5), 945-950.

11.	Bhuvana, T.; Subramaniam, C.; Pradeep, T.; Kulkarni, G., Conducting nanocrystal patterns using a silver organic complex blended with polystyrene as e-beam resist. *The Journal of Physical Chemistry C* **2009,** *113* (17), 7038-7043.

12.	Amendola, V.; Polizzi, S.; Meneghetti, M., Free silver nanoparticles synthesized by laser ablation in organic solvents and their easy functionalization. *Langmuir* **2007,** *23* (12), 6766-6770.

13.	Amendola, V.; Meneghetti, M., Laser ablation synthesis in solution and size manipulation of noble metal nanoparticles. *Physical chemistry chemical physics* **2009,** *11* (20), 3805-3821.

14.	Okumu, J.; Dahmen, C.; Sprafke, A.; Luysberg, M.; Von Plessen, G.; Wuttig, M., Photochromic silver nanoparticles fabricated by sputter deposition. *Journal of Applied Physics* **2005,** *97* (9), 094305.

15.	Becker, R.; Doring, W., Kinetic treatment of the nucleation in supersaturated vapors. **1954**.

16.	LaMer, V. K.; Dinegar, R. H., Theory, production and mechanism of formation of monodispersed hydrosols. *Journal of the American Chemical Society* **1950,** *72* (11), 4847-4854.

17.	Polte, J., Fundamental growth principles of colloidal metal nanoparticles–a new perspective. *CrystEngComm* **2015,** *17* (36), 6809-6830.

18.	Thanh, N. T.; Maclean, N.; Mahiddine, S., Mechanisms of nucleation and growth of nanoparticles in solution. *Chemical reviews* **2014,** *114* (15), 7610-7630.

19.	Kwon, S. G.; Hyeon, T., Formation mechanisms of uniform nanocrystals via hot-injection and heat-up methods. *Small* **2011,** *7* (19), 2685-2702.

20.	Sugimoto, T., The theory of the nucleation of monodisperse particles in open systems and its application to AgBr systems. *Journal of colloid and interface science* **1992,** *150* (1), 208-225.

21.	Ott, L. S.; Finke, R. G., Transition-metal nanocluster stabilization for catalysis: a critical review of ranking methods and putative stabilizers. *Coordination Chemistry Reviews* **2007,** *251* (9-10), 1075-1100.

22.	Roucoux, A.; Schulz, J.; Patin, H., Reduced transition metal colloids: a novel family of reusable catalysts? *Chemical reviews* **2002,** *102* (10), 3757-3778.

23.	Duteil, A.; Schmid, G.; Meyer-Zaika, W., Ligand stabilized nickel colloids. *Journal of the Chemical Society, Chemical Communications* **1995,** (1), 31-32.

24.	Ramirez, E.; Jansat, S.; Philippot, K.; Lecante, P.; Gomez, M.; Masdeu-Bultó, A. M.; Chaudret, B., Influence of organic ligands on the stabilization of palladium nanoparticles. *Journal of Organometallic Chemistry* **2004,** *689* (24), 4601-4610.

25.	Weare, W. W.; Reed, S. M.; Warner, M. G.; Hutchison, J. E., Improved synthesis of small (d core≈ 1.5 nm) phosphine-stabilized gold nanoparticles. *Journal of the American Chemical Society* **2000,** *122* (51), 12890-12891.

26.	Brust, M.; Walker, M.; Bethell, D.; Schiffrin, D. J.; Whyman, R., Synthesis of thiol-derivatised gold nanoparticles in a two-phase liquid–liquid system. *Journal of the Chemical Society, Chemical Communications* **1994,** (7), 801-802.

27.	Brust, M.; Kiely, C. J., Some recent advances in nanostructure preparation from gold and silver particles: a short topical review. *Colloids and Surfaces A: Physicochemical and Engineering Aspects* **2002,** *202* (2-3), 175-186.

28.	Yee, C. K.; Jordan, R.; Ulman, A.; White, H.; King, A.; Rafailovich, M.; Sokolov, J., Novel one-phase synthesis of thiol-functionalized gold, palladium, and iridium nanoparticles using superhydride. *Langmuir* **1999,** *15* (10), 3486-3491.

29.	Kim, S.-W.; Park, J.; Jang, Y.; Chung, Y.; Hwang, S.; Hyeon, T.; Kim, Y. W., Synthesis of monodisperse palladium nanoparticles. *Nano Letters* **2003,** *3* (9), 1289-1291.

30.	Polavarapu, L.; Xu, Q.-H., A simple method for large scale synthesis of highly monodisperse gold nanoparticles at room temperature and their electron relaxation properties. *Nanotechnology* **2009,** *20* (18), 185606.

31.	Mourdikoudis, S.; Liz-Marzan, L. M., Oleylamine in nanoparticle synthesis. *Chemistry of Materials* **2013,** *25* (9), 1465-1476.

32.	Teranishi, T.; Kiyokawa, I.; Miyake, M., Synthesis of monodisperse gold nanoparticles using linear polymers as protective agents. *Advanced Materials* **1998,** *10* (8), 596-599.

33.	Teranishi, T.; Miyake, M., Size control of palladium nanoparticles and their crystal structures. *Chemistry of Materials* **1998,** *10* (2), 594-600.

34.	Roy, P. S.; Bagchi, J.; Bhattacharya, S. K., Size-controlled synthesis and characterization of polyvinyl alcohol coated palladium nanoparticles. *Transition metal chemistry* **2009,** *34* (4), 447-453.

35.	Khanna, P.; Gokhale, R.; Subbarao, V.; Vishwanath, A. K.; Das, B.; Satyanarayana, C., PVA stabilized gold nanoparticles by use of unexplored albeit conventional reducing agent. *Materials Chemistry and Physics* **2005,** *92* (1), 229-233.

36.	Pencheva, D.; Bryaskova, R.; Kantardjiev, T., Polyvinyl alcohol/silver nanoparticles (PVA/AgNps) as a model for testing the biological activity of hybrid materials with included silver nanoparticles. *Materials Science and Engineering: C* **2012,** *32* (7), 2048-2051.

37.	Pande, S.; Ghosh, S. K.; Praharaj, S.; Panigrahi, S.; Basu, S.; Jana, S.; Pal, A.; Tsukuda, T.; Pal, T., Synthesis of normal and inverted gold− silver core− shell architectures in β-cyclodextrin and their applications in SERS. *The Journal of Physical Chemistry C* **2007,** *111* (29), 10806-10813.

38.	Strimbu, L.; Liu, J.; Kaifer, A. E., Cyclodextrin-capped palladium nanoparticles as catalysts for the Suzuki reaction. *Langmuir* **2003,** *19* (2), 483-485.

39.	Reetz, M. T.; Maase, M., Redox-Controlled Size-Selective Fabrication of Nanostructured Transition Metal Colloids. *Advanced Materials* **1999,** *11* (9), 773-777.

40.	Kumar, C. G.; Mamidyala, S. K.; Das, B.; Sridhar, B.; Devi, G. S.; Karuna, M. S., Synthesis of biosurfactant-based silver nanoparticles with purified rhamnolipids isolated from Pseudomonas aeruginosa BS-161R. *J Microbiol Biotechnol* **2010,** *20* (7), 1061-1068.

41.	Turkevich, J.; Stevenson, P. C.; Hillier, J., A study of the nucleation and growth processes in the synthesis of colloidal gold. *Discussions of the Faraday Society* **1951,** *11*, 55-75.

42.	Turkevich, J.; Stevenson, P. C.; Hillier, J., The formation of colloidal gold. *The Journal of Physical Chemistry* **1953,** *57* (7), 670-673.

43.	Henglein, A.; Giersig, M., Formation of colloidal silver nanoparticles: capping action of citrate. *The Journal of Physical Chemistry B* **1999,** *103* (44), 9533-9539.

44.   Nguyen, D. T.; Kim, D.-J.; So, M. G.; Kim, K.-S., Experimental measurements of gold nanoparticle nucleation and growth by citrate reduction of HAuCl4. *Advanced Powder Technology* **2010,** *21* (2), 111-118.

45.   Wangoo, N.; Bhasin, K.; Boro, R.; Suri, C. R., Facile synthesis and functionalization of water-soluble gold nanoparticles for a bioprobe. *Analytica chimica acta* **2008,** *610* (1), 142-148.

46.   Uppal, M. A.; Kafizas, A.; Lim, T. H.; Parkin, I. P., The extended time evolution size decrease of gold nanoparticles formed by the Turkevich method. *New Journal of Chemistry* **2010,** *34* (7), 1401-1407.

47.   Sau, T. K.; Murphy, C. J., Room temperature, high-yield synthesis of multiple shapes of gold nanoparticles in aqueous solution. *Journal of the American Chemical Society* **2004,** *126* (28), 8648-8649.

48.   Sivaraman, S. K.; Kumar, S.; Santhanam, V., Monodisperse sub-10 nm gold nanoparticles by reversing the order of addition in Turkevich method–The role of chloroauric acid. *Journal of colloid and Interface Science* **2011,** *361* (2), 543-547.

49.   Lee, K. Y.; Hwang, J.; Lee, Y. W.; Kim, J.; Han, S. W., One-step synthesis of gold nanoparticles using azacryptand and their applications in SERS and catalysis. *Journal of colloid and interface science* **2007,** *316* (2), 476-481.

50.   Lignier, P.; Comotti, M.; Schüth, F.; Rousset, J.-L.; Caps, V., Effect of the titania morphology on the Au/TiO2-catalyzed aerobic epoxidation of stilbene. *Catalysis Today* **2009,** *141* (3-4), 355-360.

51.   Grace, A. N.; Pandian, K., One pot synthesis of polymer protected gold nanoparticles and nanoprisms in glycerol. *Colloids and Surfaces A: Physicochemical and engineering aspects* **2006,** *290* (1-3), 138-142.

52.   Heath, J. R.; Knobler, C. M.; Leff, D. V., Pressure/temperature phase diagrams and superlattices of organically functionalized metal nanocrystal monolayers: the influence of particle size, size distribution, and surface passivant. *The Journal of Physical Chemistry B* **1997,** *101* (2), 189-197.

53.   Korgel, B. A.; Fullam, S.; Connolly, S.; Fitzmaurice, D., Assembly and self-organization of silver nanocrystal superlattices: ordered "soft spheres". *The Journal of Physical Chemistry B* **1998,** *102* (43), 8379-8388.

54.   Yang, J.; Lee, J. Y.; Ying, J. Y., Phase transfer and its applications in nanotechnology. *Chemical Society Reviews* **2011,** *40* (3), 1672-1696.

55.   Chen, S.; Huang, K.; Stearns, J. A., Alkanethiolate-protected palladium nanoparticles. *Chemistry of Materials* **2000,** *12* (2), 540-547.

56.   Kanninen, P.; Johans, C.; Merta, J.; Kontturi, K., Influence of ligand structure on the stability and oxidation of copper nanoparticles. *Journal of colloid and interface science* **2008,** *318* (1), 88-95.

57.   Wikander, K.; Petit, C.; Holmberg, K.; Pileni, M.-P., Size control and growth process of alkylamine-stabilized platinum nanocrystals: a comparison between the phase transfer and reverse micelles methods. *Langmuir* **2006,** *22* (10), 4863-4868.

58.   Demortiere, A.; Petit, C., First Synthesis by Liquid− Liquid Phase Transfer of Magnetic Co x Pt100-x Nanoalloys. *Langmuir* **2007,** *23* (16), 8575-8584.

59.   Petit, C.; Lixon, P.; Pileni, M. P., In situ synthesis of silver nanocluster in AOT reverse micelles. *The Journal of Physical Chemistry* **1993,** *97* (49), 12974-12983.

60.   Courty, A.; Lisiecki, I.; Pileni, M., Vibration of self-organized silver nanocrystals. *The Journal of chemical physics* **2002,** *116* (18), 8074-8078.

61.   Wilcoxon, J.; Williamson, R.; Baughman, R., Optical properties of gold colloids formed in inverse micelles. *The Journal of chemical physics* **1993,** *98* (12), 9933-9950.

62.   López-Quintela, M. A.; Tojo, C.; Blanco, M.; Rio, L. G.; Leis, J., Microemulsion dynamics and reactions in microemulsions. *Current opinion in colloid & interface science* **2004,** *9* (3-4), 264-278.

63.   Nakamoto, M.; Yamamoto, M.; Fukusumi, M., Thermolysis of gold (I) thiolate complexes producing novel gold nanoparticles passivated by alkyl groups. *Chemical Communications* **2002,** (15), 1622-1623.

64.   Navaladian, S.; Viswanathan, B.; Viswanath, R.; Varadarajan, T., Thermal decomposition as route for silver nanoparticles. *Nanoscale research letters* **2007,** *2* (1), 44.

65.   Park, J.; Kwon, S. G.; Jun, S. W.; Kim, B. H.; Hyeon, T., Large-Scale Synthesis of Ultra-Small-Sized Silver Nanoparticles. *ChemPhysChem* **2012,** *13* (10), 2540-2543.

66.   Scaiano, J. C.; Stamplecoskie, K. G.; Hallett-Tapley, G. L., Photochemical Norrish type I reaction as a tool for metal nanoparticle synthesis: importance of proton coupled electron transfer. *Chemical Communications* **2012,** *48* (40), 4798-4808.

67.   McGilvray, K. L.; Decan, M. R.; Wang, D.; Scaiano, J. C., Facile photochemical synthesis of unprotected aqueous gold nanoparticles. *Journal of the American Chemical Society* **2006,** *128* (50), 15980-15981.

68.   Penhoat, M.; Vanbésien, T.; Cocud, A.; Addad, A.; Vezin, H.; Rolando, C., PTFE supported gold nanoparticles as photocatalysts for oxidative esterification of aldehydes. *New Journal of Chemistry* **2016,** *40* (11), 9460-9470.

69.   Stamplecoskie, K. G.; Scaiano, J. C., Light emitting diode irradiation can control the morphology and optical properties of silver nanoparticles. *Journal of the American Chemical Society* **2010,** *132* (6), 1825-1827.

70.   Maretti, L.; Billone, P. S.; Liu, Y.; Scaiano, J. C., Facile photochemical synthesis and characterization of highly fluorescent silver nanoparticles. *Journal of the American Chemical Society* **2009,** *131* (39), 13972-13980.

71.   Silvestrini, S.; Carofiglio, T.; Maggini, M., Shape-selective growth of silver nanoparticles under continuous flow photochemical conditions. *Chemical Communications* **2013,** *49* (1), 84-86.

72.   Hafermann, L.; Köhler, J. M., Photochemical Micro Continuous-Flow Synthesis of Noble Metal Nanoparticles of the Platinum Group. *Chemical Engineering & Technology* **2015,** *38* (7), 1138-1143.

73.   Kashchiev, D.; Vekilov, P. G.; Kolomeisky, A. B., Kinetics of two-step nucleation of crystals. *The Journal of chemical physics* **2005,** *122* (24), 244706.

74.   Abou-Hassan, A.; Sandre, O.; Cabuil, V., Microfluidics in inorganic chemistry. *Angewandte Chemie International Edition* **2010,** *49* (36), 6268-6286.

75.   Song, Y.; Hormes, J.; Kumar, C. S., Microfluidic synthesis of nanomaterials. *small* **2008,** *4* (6), 698-711.

76.   Makgwane, P. R.; Ray, S. S., Synthesis of nanomaterials by continuous-flow microfluidics: a review. *Journal of nanoscience and nanotechnology* **2014,** *14* (2), 1338-1363.

77.   He, S. T.; Liu, Y. L.; Maeda, H., Controlled synthesis of colloidal silver nanoparticles in capillary micro-flow reactor. *Journal of Nanoparticle Research* **2008,** *10* (1), 209-215.

78.   Ftouni, J.; Penhoat, M.; Addad, A.; Payen, E.; Rolando, C.; Girardon, J.-S., Highly controlled synthesis of nanometric gold particles by citrate reduction using the short mixing, heating and quenching times achievable in a microfluidic device. *Nanoscale* **2012,** *4* (15), 4450-4454.

79.   Jamal, F.; Jean-Sébastien, G.; Maël, P.; Edmond, P.; Christian, R., Gold nanoparticle synthesis in microfluidic systems and immobilisation in microreactors designed for the catalysis of fine organic reactions. *Microsystem technologies* **2012,** *18* (2), 151-158.

80.   Lin, X. Z.; Terepka, A. D.; Yang, H., Synthesis of silver nanoparticles in a continuous flow tubular microreactor. *Nano Letters* **2004,** *4* (11), 2227-2232.

81.   Sharada, S.; Suryawanshi, P. L.; Kumar, R.; Gumfekar, S. P.; Narsaiah, T. B.; Sonawane, S. H., Synthesis of palladium nanoparticles using continuous flow microreactor. *Colloids and Surfaces A: Physicochemical and Engineering Aspects* **2016,** *498*, 297-304.

82.   Tauran, Y.; Brioude, A.; Coleman, A. W.; Rhimi, M.; Kim, B., Molecular recognition by gold, silver and copper nanoparticles. *World journal of biological chemistry* **2013,** *4* (3), 35.

83.   Kelly, K. L.; Coronado, E.; Zhao, L. L.; Schatz, G. C., The optical properties of metal nanoparticles: the influence of size, shape, and dielectric environment. ACS Publications: 2003.

84.   Taleb, A.; Petit, C.; Pileni, M., Optical properties of self-assembled 2D and 3D superlattices of silver nanoparticles. *The Journal of Physical Chemistry B* **1998,** *102* (12), 2214-2220.

85.   George, J.; Sastry, N. V., Densities, excess molar volumes, viscosities, speeds of sound, excess isentropic compressibilities, and relative permittivities for C m H2 m+ 1 (OCH2CH2) n OH (m= 1 or 2 or

4 and n= 1)+ benzene,+ toluene,+(o-, m-, and p-) xylenes,+ ethylbenzene, and+ cyclohexane. *Journal of Chemical & Engineering Data* **2003,** *48* (4), 977-989.

86.   Guarino, V.; Cirillo, V.; Taddei, P.; Alvarez-Perez, M. A.; Ambrosio, L., Tuning size scale and crystallinity of PCL electrospun fibres via solvent permittivity to address hMSC response. *Macromolecular bioscience* **2011,** *11* (12), 1694-1705.

87.   Alvarez, M. M.; Khoury, J. T.; Schaaff, T. G.; Shafigullin, M. N.; Vezmar, I.; Whetten, R. L., Optical absorption spectra of nanocrystal gold molecules. *The Journal of Physical Chemistry B* **1997,** *101* (19), 3706-3712.

88.   He, Y. Q.; Liu, S. P.; Kong, L.; Liu, Z. F., A study on the sizes and concentrations of gold nanoparticles by spectra of absorption, resonance Rayleigh scattering and resonance non-linear scattering. *Spectrochimica Acta Part A: Molecular and Biomolecular Spectroscopy* **2005,** *61* (13-14), 2861-2866.

89.   Link, S.; El-Sayed, M. A., Spectral properties and relaxation dynamics of surface plasmon electronic oscillations in gold and silver nanodots and nanorods. ACS Publications: 1999.

90.   Taleb, A.; Petit, C.; Pileni, M., Synthesis of highly monodisperse silver nanoparticles from AOT reverse micelles: a way to 2D and 3D self-organization. *Chemistry of Materials* **1997,** *9* (4), 950-959.

91.   Chen, H.; Kou, X.; Yang, Z.; Ni, W.; Wang, J., Shape- and size-dependent refractive index sensitivity of gold nanoparticles. *Langmuir* **2008,** *24* (10), 5233-5237.

92.   Bhattacharjee, S., DLS and zeta potential–What they are and what they are not? *Journal of Controlled Release* **2016,** *235*, 337-351.

93.   Widegren, J. A.; Finke, R. G., A review of soluble transition-metal nanoclusters as arene hydrogenation catalysts. *Journal of Molecular Catalysis A: Chemical* **2003,** *191* (2), 187-207.

94.   Dyson, P. J., Catalysis by low oxidation state transition metal (carbonyl) clusters. *Coordination chemistry reviews* **2004,** *248* (21-24), 2443-2458.

95.   Astruc, D.; Lu, F.; Aranzaes, J. R., Nanoparticles as recyclable catalysts: the frontier between homogeneous and heterogeneous catalysis. *Angewandte Chemie International Edition* **2005,** *44* (48), 7852-7872.

96.   Bönnemann, H.; Braun, G. A., Enantioselectivity control with metal colloids as catalysts. *Chemistry–A European Journal* **1997,** *3* (8), 1200-1202.

97.   Yu, W.-Y.; Liu, H.-F.; Tao, Q., Modification of metal cations to metal clusters in liquid medium. *Chemical Communications* **1996,** (15), 1773-1774.

98.   Launay, F.; Roucoux, A.; Patin, H., Ruthenium colloids: A new catalyst for alkane oxidation by tBHP in a biphasic water-organic phase system. *Tetrahedron letters* **1998,** *39* (11), 1353-1356.

99.   Shiraishi, Y.; Toshima, N., Colloidal silver catalysts for oxidation of ethylene. *Journal of Molecular Catalysis A: Chemical* **1999,** *141* (1-3), 187-192.

100.   Ftouni, J.; Penhoat, M.; Girardon, J.-S.; Addad, A.; Payen, E.; Rolando, C., Immobilization of gold nanoparticles on fused silica capillary surface for the development of catalytic microreactors. *Chemical engineering journal* **2013,** *227*, 103-110.

101.   Moreno-Manas, M.; Pleixats, R., Formation of carbon− carbon bonds under catalysis by transition-metal nanoparticles. *Accounts of Chemical Research* **2003,** *36* (8), 638-643.

102.   Haruta, M.; Kobayashi, T.; Sano, H.; Yamada, N., Novel gold catalysts for the oxidation of carbon monoxide at a temperature far below 0 C. *Chemistry Letters* **1987,** *16* (2), 405-408.

103.   Nkosi, B.; Adams, M. D.; Coville, N. J.; Hutchings, G. J., Hydrochlorination of acetylene using carbon-supported gold catalysts: A study of catalyst reactivation. *Journal of Catalysis* **1991,** *128* (2), 378-386.

104.   Han, J.; Liu, Y.; Guo, R., Facile synthesis of highly stable gold nanoparticles and their unexpected excellent catalytic activity for Suzuki− Miyaura cross-coupling reaction in water. *Journal of the American Chemical Society* **2009,** *131* (6), 2060-2061.

105.   Yan, Z.; Fu, L.; Zuo, X.; Yang, H., Green assembly of stable and uniform silver nanoparticles on 2D silica nanosheets for catalytic reduction of 4-nitrophenol. *Applied Catalysis B: Environmental* **2018,** *226*, 23-30.

106.   Gangula, A.; Podila, R.; Karanam, L.; Janardhana, C.; Rao, A. M., Catalytic reduction of 4-nitrophenol using biogenic gold and silver nanoparticles derived from Breynia rhamnoides. *Langmuir* **2011,** *27* (24), 15268-15274.

107.   Xu, R.; Wang, D.; Zhang, J.; Li, Y., Shape-dependent catalytic activity of silver nanoparticles for the oxidation of styrene. *Chemistry–An Asian Journal* **2006,** *1* (6), 888-893.

108.   Li, Y.; Hong, X. M.; Collard, D. M.; El-Sayed, M. A., Suzuki cross-coupling reactions catalyzed by palladium nanoparticles in aqueous solution. *Organic letters* **2000,** *2* (15), 2385-2388.

109.   Narayanan, R.; El-Sayed, M. A., Effect of catalysis on the stability of metallic nanoparticles: Suzuki reaction catalyzed by PVP-palladium nanoparticles. *Journal of the American Chemical Society* **2003,** *125* (27), 8340-8347.

110.   Narayanan, R.; El-Sayed, M. A., Carbon-supported spherical palladium nanoparticles as potential recyclable catalysts for the Suzuki reaction. *Journal of Catalysis* **2005,** *234* (2), 348-355.

111.   Elhage, A.; Lanterna, A. E.; Scaiano, J. C., Light-Induced Sonogashira C–C Coupling under Mild Conditions Using Supported Palladium Nanoparticles. *ACS Sustainable Chemistry & Engineering* **2018,** *6* (2), 1717-1722.

112.   Xiao, Q.; Sarina, S.; Bo, A.; Jia, J.; Liu, H.; Arnold, D. P.; Huang, Y.; Wu, H.; Zhu, H., Visible light-driven cross-coupling reactions at lower temperatures using a photocatalyst of palladium and gold alloy nanoparticles. *Acs Catalysis* **2014,** *4* (6), 1725-1734.

113.   Liu, J.-H.; Wang, A.-Q.; Chi, Y.-S.; Lin, H.-P.; Mou, C.-Y., Synergistic effect in an Au− Ag alloy nanocatalyst: CO oxidation. *The Journal of Physical Chemistry B* **2005,** *109* (1), 40-43.

114.   Alexander, J. W., History of the medical use of silver. *Surgical infections* **2009,** *10* (3), 289-292.

115.   Espinosa-Cristóbal, L.; Martínez-Castañón, G.; Martínez-Martínez, R.; Loyola-Rodriguez, J.; Patino-Marin, N.; Reyes-Macias, J.; Ruiz, F., Antibacterial effect of silver nanoparticles against Streptococcus mutans. *Materials Letters* **2009,** *63* (29), 2603-2606.

116.   Mirzajani, F.; Ghassempour, A.; Aliahmadi, A.; Esmaeili, M. A., Antibacterial effect of silver nanoparticles on Staphylococcus aureus. *Research in microbiology* **2011,** *162* (5), 542-549.

117.   Martinez-Castanon, G.; Nino-Martinez, N.; Martinez-Gutierrez, F.; Martinez-Mendoza, J.; Ruiz, F., Synthesis and antibacterial activity of silver nanoparticles with different sizes. *Journal of Nanoparticle Research* **2008,** *10* (8), 1343-1348.

118.   Feng, Q. L.; Wu, J.; Chen, G.; Cui, F.; Kim, T.; Kim, J., A mechanistic study of the antibacterial effect of silver ions on Escherichia coli and Staphylococcus aureus. *Journal of biomedical materials research* **2000,** *52* (4), 662-668.

119.   Mohamed, M. M.; Fouad, S. A.; Elshoky, H. A.; Mohammed, G. M.; Salaheldin, T. A., Antibacterial effect of gold nanoparticles against Corynebacterium pseudotuberculosis. *International Journal of Veterinary Science and Medicine* **2017,** *5* (1), 23-29.

120.   Li, X.; Robinson, S. M.; Gupta, A.; Saha, K.; Jiang, Z.; Moyano, D. F.; Sahar, A.; Riley, M. A.; Rotello, V. M., Functional gold nanoparticles as potent antimicrobial agents against multi-drug-resistant bacteria. *ACS nano* **2014,** *8* (10), 10682-10686.

121.   Freestone, I.; Meeks, N.; Sax, M.; Higgitt, C., The Lycurgus cup—a roman nanotechnology. *Gold bulletin* **2007,** *40* (4), 270-277.

122.   Kunicki-Goldfinger, J. J.; Freestone, I. C.; McDonald, I.; Hobot, J. A.; Gilderdale-Scott, H.; Ayers, T., Technology, production and chronology of red window glass in the medieval period–rediscovery of a lost technology. *Journal of Archaeological Science* **2014,** *41*, 89-105.

123.   Colomban, P.; Tournie, A.; Ricciardi, P., Raman spectroscopy of copper nanoparticle-containing glass matrices: ancient red stained-glass windows. *Journal of Raman Spectroscopy: An International Journal for Original Work in all Aspects of Raman Spectroscopy, Including Higher Order Processes, and also Brillouin and Rayleigh Scattering* **2009,** *40* (12), 1949-1955.

124.   Chen, K.; Leona, M.; Vo-Dinh, T., Surface-enhanced Raman scattering for identification of organic pigments and dyes in works of art and cultural heritage material. *Sensor Review* **2007,** *27* (2), 109-120.

125.   Bonini, M.; Lenz, S.; Giorgi, R.; Baglioni, P., Nanomagnetic sponges for the cleaning of works of art. *Langmuir* **2007,** *23* (17), 8681-8685.

126.   Daniele, V.; Taglieri, G., Synthesis of Ca (OH) 2 nanoparticles with the addition of Triton X-100. Protective treatments on natural stones: Preliminary results. *Journal of Cultural Heritage* **2012,** *13* (1), 40-46.

127.   Chelazzi, D.; Poggi, G.; Jaidar, Y.; Toccafondi, N.; Giorgi, R.; Baglioni, P., Hydroxide nanoparticles for cultural heritage: consolidation and protection of wall paintings and carbonate materials. *Journal of colloid and interface science* **2013,** *392*, 42-49.

128.   Giorgi, R.; Bozzi, C.; Dei, L.; Gabbiani, C.; Ninham, B. W.; Baglioni, P., Nanoparticles of Mg (OH) 2: synthesis and application to paper conservation. *Langmuir* **2005,** *21* (18), 8495-8501.

129.   El-Feky, O. M.; Hassan, E. A.; Fadel, S. M.; Hassan, M. L., Use of ZnO nanoparticles for protecting oil paintings on paper support against dirt, fungal attack, and UV aging. *Journal of Cultural Heritage* **2014,** *15* (2), 165-172.

130.   Fratoddi, I., Hydrophobic and hydrophilic Au and Ag nanoparticles. Breakthroughs and perspectives. *Nanomaterials* **2017,** *8* (1), 11.

131.   Chaki, N. K.; Sudrik, S. G.; Sonawane, H. R.; Vijayamohanan, K., Single phase preparation of monodispersed silver nanoclusters using a unique electron transfer and cluster stabilising agent, triethylamine. *Chemical Communications* **2002,** (1), 76-77.

132.   Ma, H.; Yin, B.; Wang, S.; Jiao, Y.; Pan, W.; Huang, S.; Chen, S.; Meng, F., Synthesis of silver and gold nanoparticles by a novel electrochemical method. *ChemPhysChem* **2004,** *5* (1), 68-75.

133.   Cojocaru, A.; Brincoveanu, O.; Pantazi, A.; Balan, D.; Enachescu, M.; Visan, T.; Anicai, L., Electrochemical preparation of Ag nanoparticles involving choline chloride–glycerol deep eutectic solvents. *Bulg. Chem. Commun* **2017,** *49*, 194-204.

134.   Zhang, J.; Chaker, M.; Ma, D., Pulsed laser ablation based synthesis of colloidal metal nanoparticles for catalytic applications. *Journal of colloid and interface science* **2017,** *489*, 138-149.

135.   Correard, F.; Maximova, K.; Estève, M.-A.; Villard, C.; Roy, M.; Al-Kattan, A.; Sentis, M.; Gingras, M.; Kabashin, A. V.; Braguer, D., Gold nanoparticles prepared by laser ablation in aqueous biocompatible solutions: assessment of safety and biological identity for nanomedicine applications. *International journal of nanomedicine* **2014,** *9*, 5415.

136.   Kundu, S.; Wang, K.; Liang, H., Size-selective synthesis and catalytic application of polyelectrolyte encapsulated gold nanoparticles using microwave irradiation. *The Journal of Physical Chemistry C* **2009,** *113* (13), 5157-5163.

137.   El-Naggar, M. E.; Shaheen, T. I.; Fouda, M. M.; Hebeish, A. A., Eco-friendly microwave-assisted green and rapid synthesis of well-stabilized gold and core–shell silver–gold nanoparticles. *Carbohydrate polymers* **2016,** *136*, 1128-1136.

138.   Iravani, S.; Thota, S.; Crans, D., Methods for Preparation of Metal Nanoparticles. *Metal Nanoparticles: Synthesis and Applications in Pharmaceutical Sciences* **2018**, 15-31.

139.   Hafermann, L.; Köhler, J. M., Small gold nanoparticles formed by rapid photochemical flow-through synthesis using microfluid segment technique. *Journal of Nanoparticle Research* **2015,** *17* (2), 99.

140.   Bogdan, A. R.; Mason, B. P.; Sylvester, K. T.; McQuade, D. T., Improving Solid-Supported Catalyst Productivity by Using Simplified Packed-Bed Microreactors. *Angewandte Chemie International Edition* **2007,** *46* (10), 1698-1701.

141.   Baber, R.; Mazzei, L.; Thanh, N. T. K.; Gavriilidis, A., An engineering approach to synthesis of gold and silver nanoparticles by controlling hydrodynamics and mixing based on a coaxial flow reactor. *Nanoscale* **2017,** *9* (37), 14149-14161.

142.   Wu, K.-J.; Bohan, G. M. D. V.; Torrente-Murciano, L., Synthesis of narrow sized silver nanoparticles in the absence of capping ligands in helical microreactors. *Reaction Chemistry & Engineering* **2017,** *2* (2), 116-128.

143.   Okafor, O.; Weilhard, A.; Fernandes, J. A.; Karjalainen, E.; Goodridge, R.; Sans, V., Advanced reactor engineering with 3D printing for the continuous-flow synthesis of silver nanoparticles. *Reaction Chemistry & Engineering* **2017,** *2* (2), 129-136.

144.   Fontana, L.; Bassetti, M.; Battocchio, C.; Venditti, I.; Fratoddi, I., Synthesis of gold and silver nanoparticles functionalized with organic dithiols. *Colloids and Surfaces A: Physicochemical and Engineering Aspects* **2017**.

145.   Hendel, T.; Wuithschick, M.; Kettemann, F.; Birnbaum, A.; Rademann, K.; Polte, J. r., In situ determination of colloidal gold concentrations with UV–Vis spectroscopy: limitations and perspectives. *Analytical chemistry* **2014,** *86* (22), 11115-11124.

146.   Link, S.; El-Sayed, M. A., Size and temperature dependence of the plasmon absorption of colloidal gold nanoparticles. *The Journal of Physical Chemistry B* **1999,** *103* (21), 4212-4217.

147.   Jain, P. K.; Lee, K. S.; El-Sayed, I. H.; El-Sayed, M. A., Calculated absorption and scattering properties of gold nanoparticles of different size, shape, and composition: applications in biological imaging and biomedicine. *The journal of physical chemistry B* **2006,** *110* (14), 7238-7248.

148.   Kreibig, U.; Genzel, L., Optical absorption of small metallic particles. *Surface Science* **1985,** *156*, 678-700.

149.   Kimling, J.; Maier, M.; Okenve, B.; Kotaidis, V.; Ballot, H.; Plech, A., Turkevich method for gold nanoparticle synthesis revisited. *The Journal of Physical Chemistry B* **2006,** *110* (32), 15700-15707.

150.   Watzky, M. A.; Finney, E. E.; Finke, R. G., Transition-metal nanocluster size vs formation time and the catalytically effective nucleus number: A mechanism-based treatment. *Journal of the American Chemical Society* **2008,** *130* (36), 11959-11969.

151.   Compton, O. C.; Osterloh, F. E., Evolution of size and shape in the colloidal crystallization of gold nanoparticles. *Journal of the American Chemical Society* **2007,** *129* (25), 7793-7798.

152.   Heck, R. F., Mechanism of arylation and carbomethoxylation of olefins with organopalladium compounds. *Journal of the American Chemical Society* **1969,** *91* (24), 6707-6714.

General conclusion

This thesis work proposes new lipidomic and proteomic developments using very high resolution mass spectrometry for the analysis of cultural heritage.

In the first part of this work, our objective was to identify protein residues trapped into archaeological amphora Dressel 14 from shipwrecks (from the 2nd century). These amphorae were supposed to store and transport fish derivate products such as *Garum* and *Liquamen*. The proteomics workflow was firstly adapted to study *Garum* model fish sauces prepared from various fish species (e.g. sardines, mackerels). After the optimization of extraction, digestion and data-treatment procedures, both muscle proteins (e.g. tropomyosin, myosin) and blood proteins (e.g. hemoglobin) were successfully identified by sequence homology to other fish species (e.g. *Danio renio*, etc.). Due to the lack of fish protein sequences in proteomic/genomic databases, an internal proteomic database was established from several fresh fish muscles that belong to *Clupidae* and *Scombridae* families present in both Mediterranean Sea and Atlantic Ocean such as *Scomber scombrus*, *Sardina pilchardus, Auxis thazard, Euthynnus alletteratus and Thunnus alalonga*. For fish species authentication in *Garum* model sample, *de novo* species specific peptides were compared to the same peptides extracted from fresh fish samples. The developed protocol was applied to the study of an archeological amphora (116 AD) preserved in submarine context. A total of 157 proteins were successfully identified including 10 muscle proteins and 2 blood proteins with fish specific peptides. Considering the 10 muscle proteins identified, 32 peptides were specific for fish among which 7 for Scombridae. Considering the 2 blood proteins, 4 specific peptides for fish were identified among which 2 were specific for Scombridae. The trace of proteins identified in the archaeological sample showed similarities with *Thunnus thynnus* and *Thunnus allalunga* species and excluded the *Auxis thazard* and *Euthynnus alletteratus* species. However this result have to be taken with caution considering the important lack of fish databases and the trace level of organic component detected in the amphorae.

The second contribution of my thesis was focused on the characterization and identification of the network structure of polymerized linseed oils and the phenomena of degradation by soft depolymerization and high resolution mass spectrometry (FT-ICR) analysis. To perform this analysis, we designed a chemical treatment which cleaves the polymer at the ester bond between glycerol and the fatty acids without altering the network formed between these fatty acids. At the same time, derivatization of fatty acids by adding a tertiary amine group was performed to

improve their detection in positive mode. The obtained products from trans-amidation were analyzed with FT-ICR and had shown thousands of peaks corresponding to the resulting products from polymerization and degradation processes. Van Krevlen plots were produced to represent different classes of products and to visually represent the difference between oil paint films polymerized in the presence of different pigments. In this work, we present a new strategy, which allowed for the first time the analysis and identification of the network structure formed between unsaturated fatty acids in a real art oil painting that dates from the 19th century.

In the last part of this work, we describe a photochemical synthesis of metallic nanoparticles (silver, gold and palladium) dispersed in organic solvents (THF and toluene) in batch and microfluidic systems. We investigated the influence of different parameters (such as time of irradiation, ligand, ratio of metal/ligand and metal/photo-initiator) on nanoparticles generation. We succeeded in optimizing our experimental conditions in order to obtain small, mono-dispersed and ultra-stable nanoparticles in organic solvents.

Abstract

Mass spectrometry is a powerful analytical technique which allows to analyze different types of samples from different fields. In this work, we propose new developments in lipidomics and proteomics for the analysis of cultural heritage samples. The first part of this work describes a methodological development in proteomics applied to the analysis of archaeological samples. This work consists in optimizing the "bottom-up" strategy for the analysis of proteins residues trapped in archaeological ceramics preserved in unfavorable conditions for their conservation (for example: first century amphora preserved in a submarine environment). During this work, we studied non-sequenced organisms by adapting a *de novo* sequencing methodology and we succeeded to demonstrate by analytical evidence, and for the first time, the use of Dressel 14 amphorae for the transportation of fish belonging to Thunnus genus. In the second part, we present a new approach in lipidomics for the analysis and the identification of crosslinked polymer network present in linseed oil based paints. In this part, we developed a new method for soft depolymerization and derivatization of reticulated lipids, which are than analyzed with high resolution mass spectrometry (FT-ICR MS) to access into the 3D network formed by lipids in oil paint. The developed method was applied to an oil paint that dates back to the 19th century, and we also studied the interaction between lipids and pigments. The third part describes the development of a photochemical synthesis in flow of ultra stable metallic nanoparticles (silver, gold and palladium) in organic medium.

Key words: high resolution mass spectrometry, FT-ICR, orbitrap, lipidomics, proteomics, cultural heritage, microfluidics systems, photosynthesis, nanoparticles

Résumé

La spectrométrie de masse est une méthode analytique puissante qui permet l'analyse de différents types d'échantillons. Ce travail de thèse présente de nouvelles approches en lipidomique et en protéomique appliquées à l'analyse des échantillons de patrimoine culturel par spectrométrie de masse. La première partie de cette thèse propose un développement méthodologique en protéomique pour l'analyse des échantillons archéologiques. Ce travail consiste à optimiser la stratégie "bottom-up" pour l'analyse des traces de protéines piégées dans des céramiques archéologiques conservées dans des contextes très défavorables (exemple: amphore du 1er siècle conservée dans un environnement sous-marin). Au cours de ce travail, nous avons étudié des organismes non séquencés en adaptant une méthodologie de séquençage *de novo*. Nous avons réussi à démontrer par des preuves analytiques et pour la première fois, la présence de poisson du genre Thunnus au sein d'amphorae Dressel 14. La deuxième partie présente une nouvelle approche pour l'analyse et l'identification de la structure 3D du réseau de polymères réticulés de peintures d'huile de lin. Celle-ci repose sur le développement d'une technique de dépolymérisation douce et de dérivatisation des lipides réticulés afin de les analyser en spectrométrie de masse à haute résolution (FT-ICR MS) dans le but d'accéder au réseau 3D formé par les lipides dans la peinture. Puis, cette méthode a été appliquée à une peinture à l'huile datant du XIXe siècle. Une étude de l'interaction entre les lipides et les pigments a également été effectuée. Enfin, la troisième partie décrit le développement d'une nouvelle méthode de synthèse photochimique en flux des nanoparticules métalliques (argent, or et palladium) ultra-stables dans plusieurs solvants organiques.

Mots clés: spectrométrie de masse à haute résolution, FT-ICR, orbitrap, lipidomique, protéomique, héritage culturel, systèmes microfluidiques, photosynthèse, nanoparticules